Design and Computational Modelling for a Shape Memory Alloy-based Adaptronic Architecture

MSc Thesis P5 Report
For 2nd July 2018

Yufe Wong
4631579

Mentors:

Peter Eigenraam (1st, Structures)

Serdar Asut (2nd, Computation)

Kaspar Jansen (3rd, Material)

Tags: atria, adaptive, energy, consumption, sustainability, HVAC, adaptronic, smart, material, façade, responsive, thermal, computational, Grasshopper, modelling, nitinol, Shape Memory Alloy

P5 report for Master Thesis
in partial fulfilment of the requirements for the degree of
Master of Science in Building Technology,
at the Delft University of Technology,
to be defended publicly on 2nd July 2018

Author:
Yufe Wong,
yufe@hotmail.co.uk
4631579
Sustainability Studio, Building Technology Track

First Mentor:
P. (Peter) Eigenraam – Structural Mechanics

Second Mentor:
Dr. S. (Serdar) Aşut – Parametric Design

Third Mentor:
Prof. dr. ir. K.M.B. (Kaspar) Jansen – Material Science

Delegate of the Board of Examiners:
Dr.ir. M. (Marjolein) Spaans

Preface

From the start, I wanted to study something different and far from the menu of standard thesis topics, in hopes that something completely new might be explored. The subject of the thesis arose from a fascination of moving structures, mixed with a moral obligation to design for sustainable progress. I was thankful for the diverse activities and branching lines of study, as it lead to a lively project with many options to advance towards. There were many demanding moments where the comfort zone of building technology had to be left behind, which in the end is a good way to find novel solutions that make a contribution. Unfortunately, the field still lags behind compared to the aerospace, robotics and medical industries in terms of innovation, so makes use of trickle-down technologies that were innovated elsewhere years before.

Throughout the project, there was a desire to take Building Technology into what I think is unexplored and fruitful territory. I truly believe that adaptronics can greatly improve the way buildings regulate their indoor environment, but the technology and processes of today may not be conducive to deliver them smoothly. Fortunately, the academic community of TU Delft is full of innovative minds that like to discuss and discover.

I would like to thank my mentors, Peter Eigenraam and Serdar Aşut, who gave me freedom to roam around a multitude of topics and tasks, and faith to eventually deliver. I would also like to thank Kaspar Jansen, who was able to discuss the material science aspects of the design. Peter Engels also helped with literature studies regarding building physics. The support and feedback from all mentors have been invaluable.

Finally, a big thank you to family and friends. Particularly to my parents, who have kept me informed of the most recent trending social media articles as well as frequently asking if I need support, to the Parouses for their actual support and to my good friends Magdalena Ludwiczak and Amy Collins, who advised about friction within a pulley.

Abstract

In the EU, the heating and cooling of buildings consumes 14% of all energy. This is a major consumer for one type of activity, and it is compounded by the fact that 75% of it is sourced from fossil fuels. The thoughtful design of facades play a major role in the reduction of heating and cooling energy loads, and the reduction of both necessitates some form of adaptiveness between the cold season and the hot season.

This thesis investigates a subset of adaptiveness called adaptronic. It has been defined as "the integration of actuators, sensors and controls with a material or structural component", and it means that a device would be able to sense its surroundings and thoughtfully respond to it in a designed way, using the properties of its materials. Shape Memory Alloys (SMAs) were investigated to achieve adaptronic architecture, with the idea of designing a courtyard atrium that is able to sense the temperature of the outside and thereby open up in hot weather. Such a seasonal atrium could in theory result in a 21-30% heating energy saving for houses in Amsterdam, due to the Greenhouse Effect in the winter.

The aim of the thesis is therefore to investigate and design the adaptronic ability of an auto-responsive façade module, with regards to the structural and detailing aspects. Literature studies were carried out on the material behaviour and reference projects, which appreciated the complexity of the behaviour and the remoteness of the material towards designers with no specialist knowledge. A computational tool was produced in Grasshopper, a plug-in of Rhino 3D, to allow a designer with no specialist knowledge to track and predict the movement of an SMA structure as the temperature changes. The tool is now available online with a Creative Commons Attribution 4.0 International Licence.

Thereafter, a concept design was made followed by experiments and explorations with prototypes to produce and test an "engine" that could deliver the actuation for the adaptronic atrium. The prototype was able to successfully actuate a 61.3 degree rotation when electrically heated, and then return to the rest position when cooled. The prototype was also able to be actuated by the environment with the help of a constructed solar-heated chamber, under zero-stress conditions.

A final design was made for an adaptronic façade module, composed of a custom-made adaptronic engine that is fitted onto a set of 4 standard pivot-window profiles to animate them. The engine features an environmentally powered heat chamber which provides a pattern of temperature to the SMA piece. The entire module is prefabricated, so that the required precision of the hardware can be attained. In a future study, the for saving HVAC loads as a result of the modules can be quantified and thereafter the design can be optimized.

The thesis hopes to lay the foundation for both adaptronics and architecture animated by SMAs. Both show a promising future towards a smart-materials based adaptiveness for sustainable progress.

Contents

1. Introduction

Context

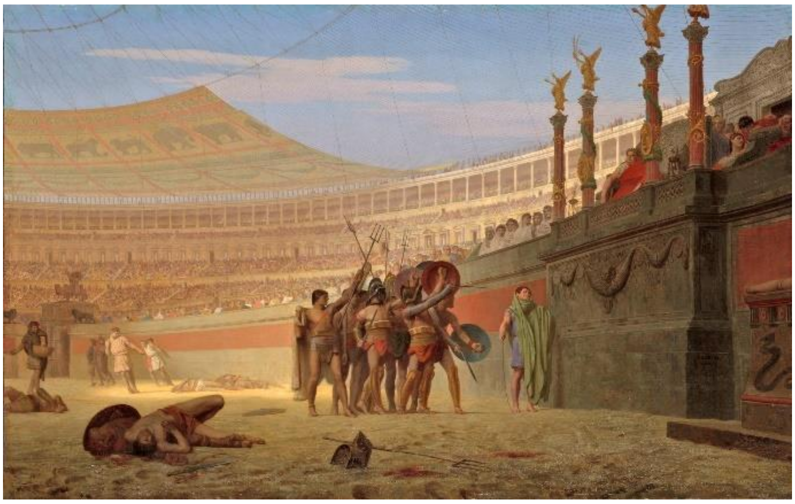

Figure 1: Jean-Léon Gérôme depicts retractable awning in Ave Caesar Morituri te Salutant (1859), his painting of a Colosseum battle[1]

Adaptive Architecture at a Glance

An early example of adaptive architecture is the Roman retractable awning known as the Velarium, which provided shading for the spectators at the Colosseum. The structure provided variable shading and some shelter from rain, but it is thought that the main use was to provide a ventilating updraft for the seating area. Teams of sailors operated the rope-and-pulley systems which opened and closed the structure (Langmead & Garnaut, 2001, p. 275). This is the same building which used an adaptive space for the theatre of battle: trapdoors, mechanical lifts and even a system to flood the central court for naval events (Castex, 2008, p. 93). Along with the static architecture, such adaptive capabilities would have been immensely impressive for any citizen of any time, thereby serving the purpose of showcasing the power of the Flavian Emperor Vespasian as well as the prowess of Roman engineering.

There is no doubt that the idea of an adaptive or dynamic architecture, able to change its physical features from one moment to the next, fires up the imagination of designers and potential users. In modern times, the idea of a 'living, breathing' architecture has driven the vision of some computational and conceptual designers, resulting in interesting prototypes and attractive renders but not many finished building projects (Beesley, 2006, p. 3). In a loose definition, these are building skins able to change its own properties, such as its geometry, colour or insulative value. A general goal seems to be to imbue biological qualities into the building system, especially that of responsiveness to people, climate and data (Loonen, 2015).

Two peculiar conditions have directed the course of a new and more promising generation of adaptive architecture. Firstly, that technologies in many different fields are emerging which might finally make dynamic adaptive skins both possible and feasible for built proposals, for example biology, materials science and computational/robotic developments. Secondly, that there is an enforced drive for sustainability, particularly in the reduction of energy and carbon footprint. This drive for sustainability will guide the research direction of this thesis, which will look at the emerging technologies to design an environmentally-responsive façade unit. The response would work to maintain the indoor comfort and thereby reduce the HVAC demands and

---

[1] Image by Jean-Léon Gérôme, "*Ave Caesar Morituri te Salutant*" 1859 as seen in the Yale University Art Gallery, Connecticut

thereby minimize building energy consumption. The focus will be on the feasibility, structure, detailing and the process of design for such a device, instead of the fine-tuning for environmental effects.

In the rest of this context subchapter, there will be a review of the global significance of building energy consumption, the role of atria on building HVAC (Heating, Air, Ventilation and Air Conditioning) demands and the concept of *adaptronics*. The first presents the fundamental problem of high energy consumption in buildings, the second presents the physical area of opportunistic improvement and the third presents the method for delivering an adaptive solution. Regarding the second, alternative areas were studied for potential improvement, namely dynamic shading and passive ventilation. These were not chosen as a focus of the thesis, but they can also benefit from the findings. Their literature reviews can be seen in the Appendix.

Building Energy Consumption

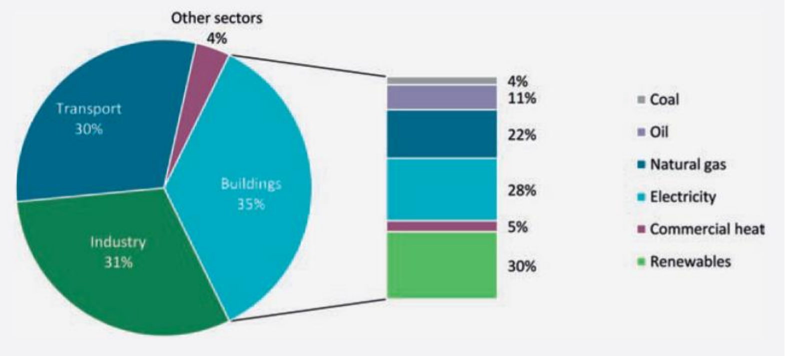

Figure 2: Final Energy Consumption by sector and breakdown of sources of energy for building sector in 2013, from International Energy Agency (International Energy Agency, 2013)

One of the most pressing issues of our century is the threat of climate change, caused by greenhouse gases which are the products of fossil fuel consumption. The European Commission has set out efforts to reduce energy consumption, carbon emissions and increase the share of renewable energy production in efforts to ensure sustainability. These measures are happening in the face of increasing global energy demands, which have gone up 101% in the period 1971 to 2015, following a roughly linear trend which shows no sign of retreat in recent years. Predictions show this trend will continue given rising population and the increasing GDP per capita for virtually all nations. Two targets of the EC relate directly to energy consumption, namely to achieve energy savings of 20% by 2020 compared to business-as-usual and 27% by 2030 (European Commission, 2010), (European Commission, 2014). This includes a strategy that prescribes all new buildings to be “nearly zero energy” by 2020. Figure 2 illustrates the significant role that the building sector plays in the final energy consumption of the EU, making up over a third.

Surveys by the U.S. Energy Information Administration give a breakdown of the energy end uses for offices and homes, as shown in Figure 3 and Figure 4. HVAC accounted for more than half of the total consumption in offices and almost half in homes. In 2012, the EC reported that heating and cooling accounted for 50% of final energy consumption, of which 75% is sourced from fossil fuels (European Commission, 2016). In Figure 5, (European Commission, 2016) shows the breakdown of this into the residential, industry and service sector whilst in Figure 6, (Heat Roadmap Europe 4, 2017) states that 13.5% of all energy in Europe was spent on heating of space in 2015, with another 0.5% on cooling. The dominance of space conditioning energy consumption becomes an even more pressing issue given the increased proliferation of HVAC systems and increasing amount of time spent indoors as nations develop (U.S. Energy Information Administration, 2017).

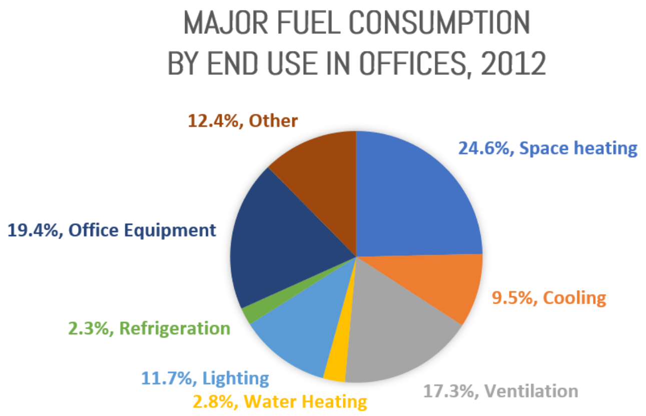

Figure 3: Breakdown of energy end uses for offices in the US (U.S. Energy Information Administration, 2016)

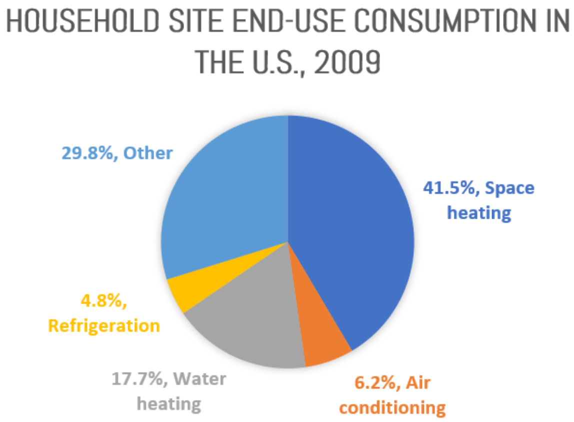

Figure 4: Breakdown of energy end uses for households in the US. The 'Other' category includes lighting, appliances and other electronic devices (U.S. Energy Information Administration, 2009)

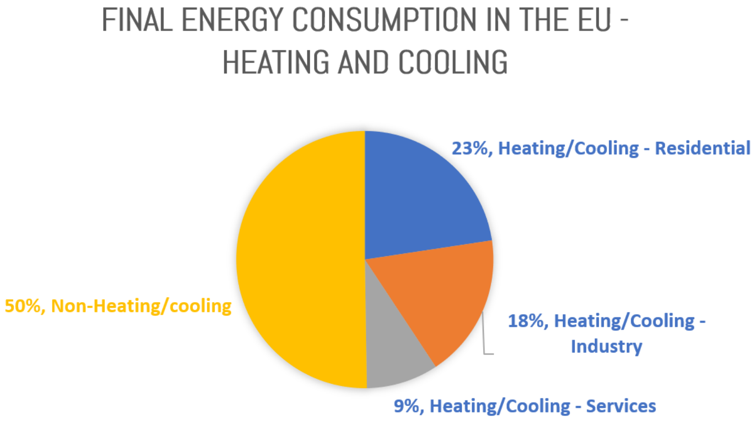

Figure 5: Final energy consumption with regards to heating and cooling in the EU (European Commission, 2016)

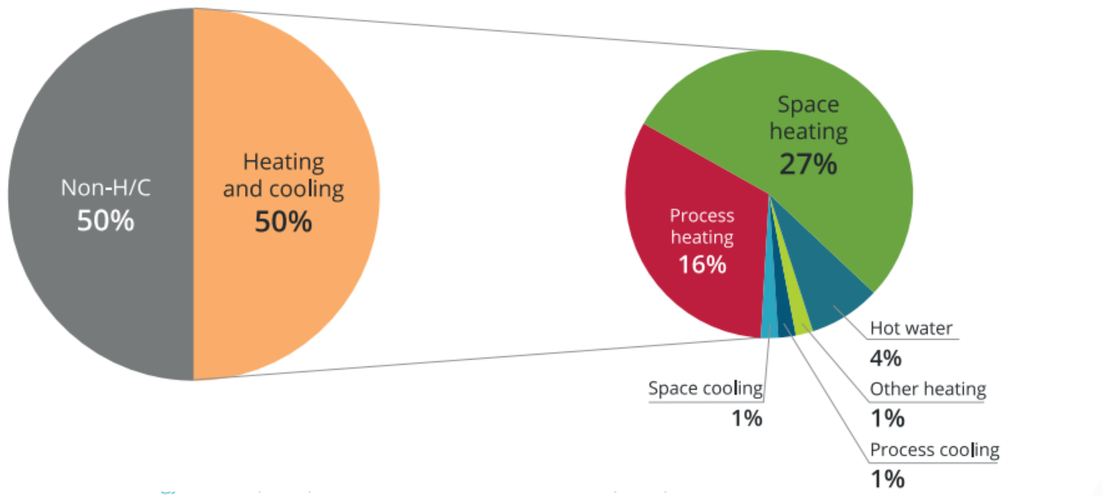

Figure 6: Final Energy use in 2015 in the EU (Heat Roadmap Europe 4, 2017). Half of all the energy used in the EU is spent on heating and cooling.

Given these findings of the immense impact of space conditioning, it can be seen that design for low-energy buildings can play a profound role in the reduction of energy and fossil fuel consumption on a global scale. The thoughtful provision of solar gain, natural ventilation and shading has potential to greatly reduce the HVAC demands, so much responsibility lies in the field of façade design, which plays a crucial role for the indoor environment (Knaack & Bilow, 2007).

The Energy-saving Atrium

> *The tenacious survival of the atrium in the face of increasing urban density at Pompeii, Herculaneum, and Ostia is all the more remarkable in that it is a relatively space-wasting configuration.*
>
> -John R Clarke
> in *A Companion to Roman Architecture*
> (Ulrich & Quenemoen, 2013)

Figure 7:Pompejanum, the Atrium, idealized replica of a Roman villa in Aschaffenburg, Germany. The pool of water, known as the Compluvium, connects to a cistern below, the Impluvium[2]

In ancient Roman housing, the atrium was arguably the most important room of the single-family *domus* and multi-family *insula.* It was central to the *fauces-atrium-tablinum* axis, which formed the backbone of the plan, and featured the "decadence of fresco painting" (Pollio & Morgan, 1960, p. 210). Historians agree that the initial purpose of the atrium was to provide air, light and water for the building, as well as to provide a space for greeting visitors (Ulrich & Quenemoen, 2013). The roofs around this tall space slanted inwards, causing rainwater to be collected in a central pool, the *compluvium*. In hot weather, this water could be splashed onto the floors to provide evaporative cooling, which in turn could drive a reverse stack-effect for ventilation.

In modern times, the atrium has again gained great significance following glass and metal innovations of the 19th century; it finds its most striking usage in large corporate, institutional and shopping mall buildings, where they can create immense, bright and airy spaces that visually tie the programme of a building together. Their popularity has occurred in all climates, the main appeal being its symbol of wealth, sophistication and power. Atria in recent times have gained a reputation for thermal discomfort and increased energy consumption, especially in cases where temperate or cold-climate atria designs are 'transplanted' into hot climates (Palma Rojas, 2014). This is due to excessive solar gain in the summer, which can significantly increase cooling loads.

The HVAC consequences of atria design are profound due to its large ratio of façade to floorspace, and the fact that they can be a buffer zone between heated adjoining rooms and the exterior. The consequence can be positive, as in Foster and Partner's 30 St Mary Axe, also known as the Gherkin, which utilises passive ventilation in the atria to draw fresh air into the offices of the skyscraper. Along with other environmental strategies, this helps the building consume half the energy of a similarly sized skyscraper (Foster and Partners). In the book *Sustainability, Energy and Architecture: Case Studies in Realizing Green Buildings*, 7 of the 10 exemplary sustainable projects had atria for positive climatic purposes (Sayigh, 2014, pp. 359-

---

[2] Image credit to Carpe Raddato
https://commons.wikimedia.org/wiki/File:Pompejanum,_the_Atrium,_idealized_replica_of_a_Roman_villa,_Aschaffenburg,_Germany_(14185443908).jpg

385). Of the examples in *Energy Manual: Sustainable Architecture,* 10 out of 20 featured atria-like spaces (Hegger, 2008, pp. 199-259). The following studies explain the impact of atria on building energy performance.

Four-sided open court vs glazed roof

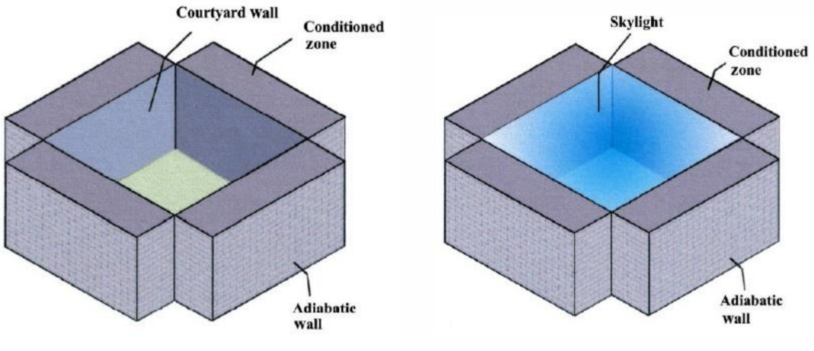

Figure 8: The simulation models by Alawould and Clark, studying energy consumption in a courtyard vs atrium building. The courtyard dimensions are 14.7 x 14.7m, so a building of 5 storeys would have about the same height and width

(Aldawoud & Clark, 2008) compared the energy consumption of a courtyard building to the same building with the courtyard roofed with glass to form an atrium, shown above. The simulations showed that an atrium with a double-glazed low-E skin would save energy in all four climate types if the building were to be five stories or taller. The benefit is more pronounced for taller buildings because an the atrium significantly reduces the amount of surface area of envelope that is exposed to the outside, and its reduction is much more significant for tall buildings; this greatly reduces the total heat transfer through the fabric in both hot and cold climates. For colder climates, the benefit is more pronounced because heating loads are more intensive, which is what atria are good at reducing.

Atrium Energy Performance Throughout the Year; Effect of Higher Insulation Glazing

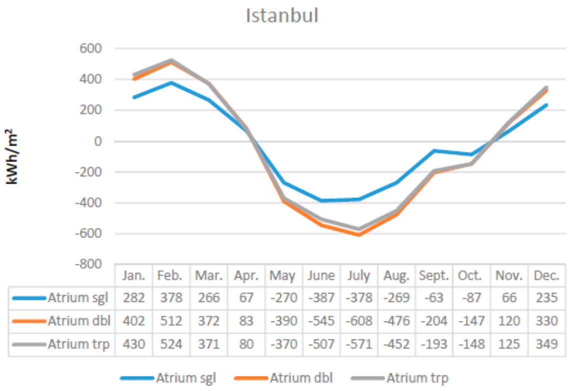

	Jan.	Feb.	Mar.	Apr.	May	June	July	Aug.	Sept.	Oct.	Nov.	Dec.
Atrium sgl	282	378	266	67	-270	-387	-378	-269	-63	-87	66	235
Atrium dbl	402	512	372	83	-390	-545	-608	-476	-204	-147	120	330
Atrium trp	430	524	371	80	-370	-507	-571	-452	-193	-148	125	349

Figure 9: The energy conserved due to having an atrium instead of open courtyard, in Istanbul, for single, double and triple glazed roof

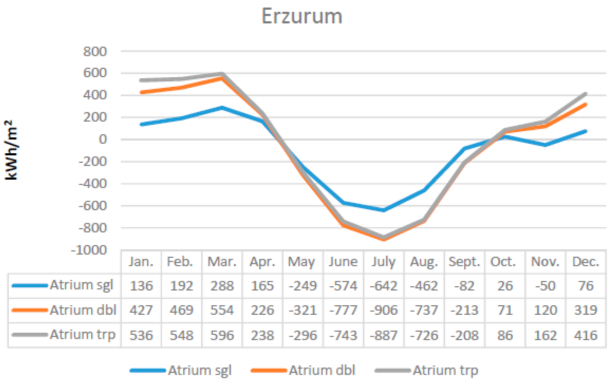

	Jan.	Feb.	Mar.	Apr.	May	June	July	Aug.	Sept.	Oct.	Nov.	Dec.
Atrium sgl	136	192	288	165	-249	-574	-642	-462	-82	26	-50	76
Atrium dbl	427	469	554	226	-321	-777	-906	-737	-213	71	120	319
Atrium trp	536	548	596	238	-296	-743	-887	-726	-208	86	162	416

Figure 10:The energy conserved due to having an atrium instead of open courtyard, in Erzum, for single, double and triple glazed roof

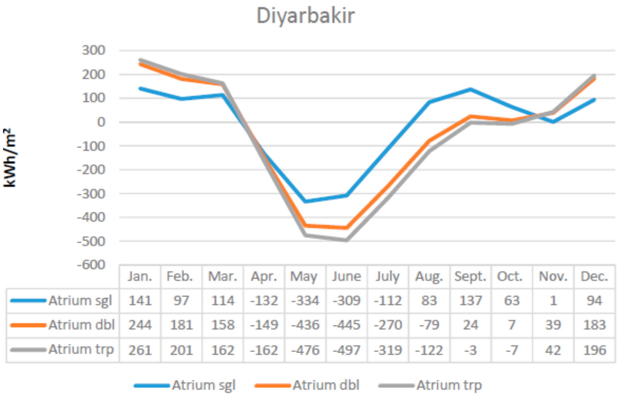

	Jan.	Feb.	Mar.	Apr.	May	June	July	Aug.	Sept.	Oct.	Nov.	Dec.
Atrium sgl	141	97	114	-132	-334	-309	-112	83	137	63	1	94
Atrium dbl	244	181	158	-149	-436	-445	-270	-79	24	7	39	183
Atrium trp	261	201	162	-162	-476	-497	-319	-122	-3	-7	42	196

Figure 11: The energy conserved due to having an atrium instead of open courtyard, in Diyarbakir, for single, double and triple glazed roof

(Tabesh & Sertyesilisik, 2016) simulated and mapped out the amount of energy conserved due to a glazed roof, which covered a courtyard with programme on all four sides, a building shape similar to the first case study of Alawould in Figure 8. The courtyard was 25 x 25 m and 3 storeys tall. This was experimented in three climates in Turkey: cold (Erzurum), mild/humid (Istanbul) and hot/dry (Diyarbakir). The atrium envelope was also variable, at single, double and triple glazing. The findings are shown in the figures above, where positive denotes energy saved and negative is denotes an increase in consumption compared to a base case of no atrium. As shown, atria have an effect of increasing the cooling load in Summer but decreasing the heating load in the Winter; more layers of glazing result in greater extremes of energy conserved/spent.

Atrium between houses with responsive shade and ventilation

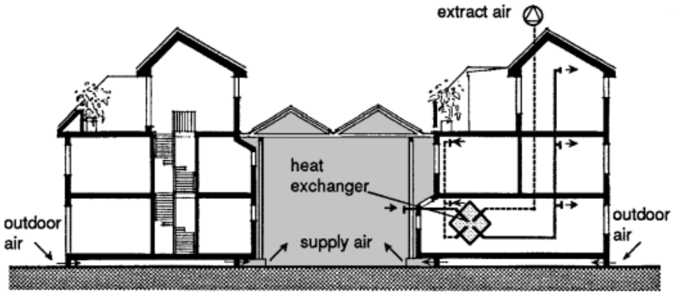

Figure 12: Tärnan, Sweden built in 1983.

(Wall, 1996) calculated the energy benefit of having an atrium that spans between two rows of terraces in Tärnan, located 45km North of Malmö in Sweden (Figure 12). Built in 1983, the atria was used as a climate experiment and it incorporates tailor-made responsive systems. Examples include vents which open at a set temperature point and closes during rain or strong winds, and curtains controlled by both a light and temperature meter. The atrium was intended to be unheated, but in real use the residents supply it with heat to keep plants alive. The study calculated the approximate energy saving due to the existence of the atrium to be the equivalent of 7% of the heating load.

Adding a Space Conditioned Atrium: Influence on Energy Performance

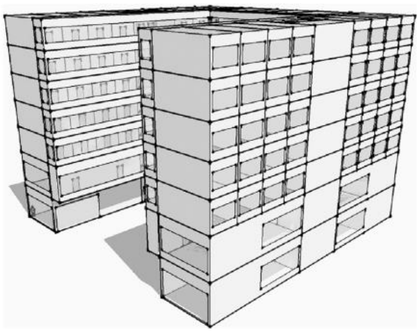

Figure 13: Hypothetical hotel building in Belgrade to receive an atrium for potential energy conservation. The courtyard opens into the Southwest direction

(Vujošević & Krstić-Furundžić, 2017) simulated the effect of adding an atrium to a hypothetical seven-storey hotel in Belgrade that was originally U-shaped in plan. The atrium had a Southwest-facing glazed façade, with three other sides of built programme. Unlike the other studies mentioned, this one featured a space conditioned atrium, so gets heated and cooled to reach thermal comfort levels of typical indoor spaces. Four alternative scenarios were tested for energy consumption:

1. the control variable of an open courtyard,
2. a glazed atrium to complete the block shape of the building,
3. same as the second but with increased infiltration from 0.5 to 1.2 air changes per hour, which is the maximum permitted by Serbian regulations and
4. same as the second but equipped with extensive fixed shading devices on the exterior of the atrium.

In all three cases, having a space conditioned atrium has drastic negative consequences for building energy performance as shown in Figure 14. There is an increase in both heating and cooling energy demand in all cases, compared to the control variable of an open courtyard. This shows the negative impact of treating an atrium space as indoor space; the space becomes a definite annual net consumer of energy instead of a possible contributor.

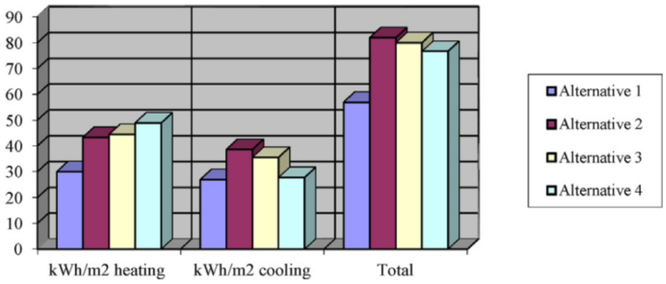

Figure 14: Results of the simulation for whole-year energy consumption. See above for explanation of each Alternative

Atrium with Variable Shading, Glazing Performance and Ventilation Strategies

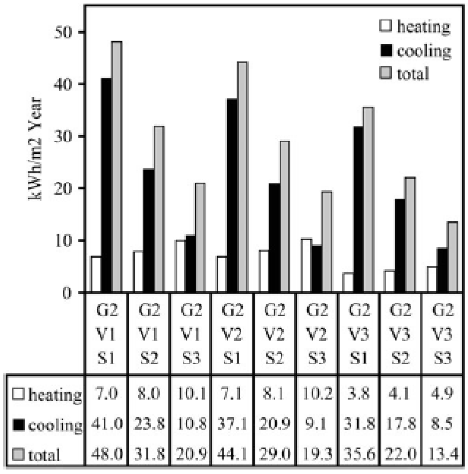

	G2 V1 S1	G2 V1 S2	G2 V1 S3	G2 V2 S1	G2 V2 S2	G2 V2 S3	G2 V3 S1	G2 V3 S2	G2 V3 S3
☐ heating	7.0	8.0	10.1	7.1	8.1	10.2	3.8	4.1	4.9
■ cooling	41.0	23.8	10.8	37.1	20.9	9.1	31.8	17.8	8.5
▨ total	48.0	31.8	20.9	44.1	29.0	19.3	35.6	22.0	13.4

Figure 15: The 9 permutations which used S2 glazing

(Rojas, 2014) modelled the cooling and heating energy consumption for an atrium in Santiago, Chile. There were three ventilation strategies that were tested: V1) windows always closed, V2) windows always opened and V3) windows open on summer nights and when 18°C<T<26°C. Results are shown in Figure 15, which also show different shading and glazing strategies as S1-S2-S3 and G1-G2-G3 respectively. V3 is the best performing; it shows that a “smart” temperature-responsive ventilation system in an atria can save around 27% in building energy consumption.

Atrium in the Winter with Open Courtyard in the Summer

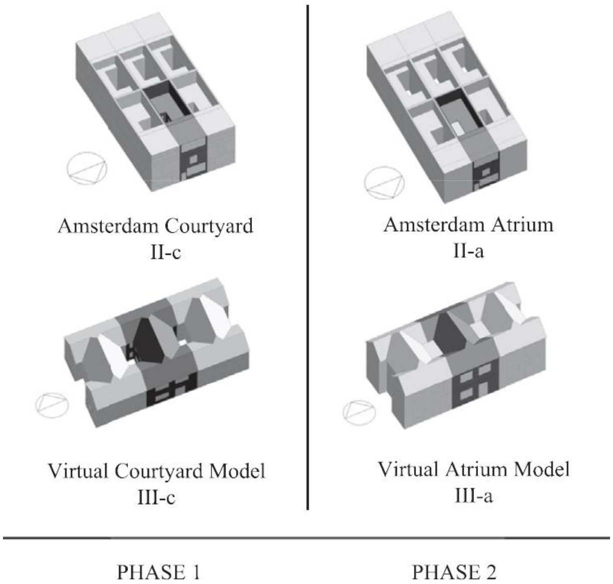

Figure 16: Research scenarios for studying the effect of adding atria to houses in Amsterdam. Model II-c is an existing house with an open court. Model II-a is the same building, but with an atrium

(Taleghani, Tenpierik, & van den Dobbelsteen, 2014) simulated the energy and thermal comfort effects of converting a courtyard into an atrium for two types of terraced houses in Amsterdam, as shown in Figure 16 (before and after labelled phase 1 and 2 respectively). Due to lack of cooling equipment in conventional homes, the annual number of discomfort hours is used instead. The atria were not heated for thermal comfort in the winter, effectively making it a buffer space. Interestingly, the concept of a seasonal atrium was studied, which involved the building having an atrium from October until April and an open courtyard from May until September. With these simulations, building II enjoyed a heating load reduction of 21% (from 33 to 26 kWh/m^2) compared to the year-round courtyard, and building III a 30% reduction. The number of discomfort hours for both buildings remained the same.

Summary

The literature shows that atria are not condemned to be an enemy of sustainability. On the contrary, these impressive and pleasurable spaces can be a tool of passive climatic intervention for the reduction of overall HVAC consumption (Tabesh & Sertyesilisik), (Hung & Chow, 2001), (Danielski, Nair, Joelsson, & Fröling, 2016). A significant overall energy saving can be ensured, so long as it is treated as a transitional space with less strict thermal comfort requirements, and that the devices to control climate are dynamic and sensibly controlled in response to changing conditions. The mechanism to improve the building energy performance via atria is to harvest solar heat energy in the winter (via the greenhouse effect) to reduce heating loads, and provide ventilation to reduce cooling loads in the summer. It would need some kind of dynamic mechanism to fulfil these two different functions in the two seasons; care must be taken in the Summer not to overheat due to solar gain. This could be done be seasonal shading or seasonal ventilation. (Rojas, 2014) showed that a smart, temperature-responsive ventilation system of an atrium can save around 27% in building energy consumption.

Mentioned in the final case study of (Taleghani et al., 2014), a very effective scenario would be an atrium that exists only for the heating months of the year and is an open courtyard for the other part of the year. The concept of a ‘seasonal’ courtyard-atrium space is interesting as a best-of-both-worlds solution, saving up to 30% for a house in Amsterdam. It is therefore quite a promising concept if a technology can implement it on a large scale without high operational costs.

Adaptronics

Figure 17: Arab World Institute facade, which features mechanical irises that open and close according to interior light quality.[3]

Any moving device is necessarily in the business of actuation: the act of putting something into motion, or more broadly, the act of making an object doing change. At the most primitive method of actuation, hand-controlled windows, doors and openings have been around as long as architecture itself; at the other end, algorithmic and data-driven computers orchestrate the movements of a thousand moving parts of a facade. The latter does not always function better in practice. A frequently mentioned example is the Arab World Institute (1987) of Jean Nouveu, which has on its South façade 240 units containing many irises which incrementally open and close based on sensors for the interior light quality. The majority of these units today are no longer functional, which shows the danger of relying on the unreliable.

Despite the wide abundance of them in a market, electric actuators do have some drawbacks. A typical mean lifetime of an actuator is 30 000 operations, or 25 years for an actuator working five times per day for 250 days of the year, but in practice some can fail after a year or two due to excessive use (Chartered Institution of Building Services, 2005). They are prone to breakage due to tendencies to overheat and the complexity from having a large number of parts, some of which are frictionally moving against each other by design. Commercial actuators for windows are also expensive; the cheapest electric upgrade for a Keylite center-pivot roof window is a motor and transformer switch, which costs 340 Euros (Keylite, 2017). In the robotics industry, electronic actuators are pervasive but they are seen as the bottleneck in the technology, and a long-lasting one of 70 years which yearns for a less space-intensive solution (Cianchetti, 2013).

There is one genre of device that can deliver motion whilst removing the need for electronic actuators: Adaptronics. The idea was put forward in the book *Adaptronics and Smart Structures: Basics, Material, Design and Application* (Janocha, 1999). The term is defined by as "the integration of actuators, sensors and controls with a material or structural component". A basic example conceived by D. Neumann involves a partially inflated balloon inside a pipe for fluid. At high temperatures, the balloon expands and stops the flow of liquid, thereby acting as a temperature-dependent valve. Such a simple mechanism replaces a thermocouple, computer, electric motor and power source that might otherwise have been used to achieve do the same job, and a similar anti-scalding valve was developed by the Memry Corporation with shape memory alloy (NASA, 2018).

---

[3] Image credit to MIMOA https://www.mimoa.eu/projects/France/Paris/Arab%20World%20Institute accessed on 7th January 2018

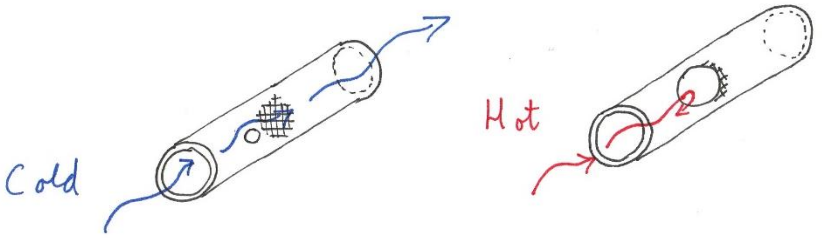

Figure 18: An example showing the simplicity of an adaptronic device. A material in a pipe expands when its temperature rises, stopping the flow in the pipe. It is effectively a temperature-dependent valve

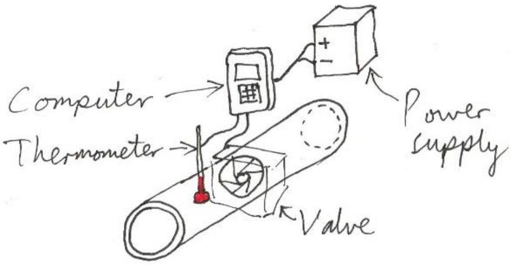

Figure 19: the traditional alternative to Figure 18, which involves a more complex set-up and combination of devices

This biological-like approach can also be referred to as 'smart' or 'intelligent', except those terms are more commonly referring to microelectronic or data-processing devices instead. The key differentiating ingredient in adaptronics are smart materials; they effectively sense a given input from the environment, and translate it into a response. In an adaptronic device, this response can be harnessed as part of a larger system, which translates the response into a more meaningful action in order to achieve a goal. In the earlier example, the gas in the balloon is effectively the smart material (that is multifunctionally both sensor and actuator), the membrane and pipe together make the rest of the adaptronic structure and the flow rate of the liquid is the output that needs to be changed, in response to the temperature of the environment. In this new design paradigm, the computer (or brain) of the system does not appear to be present; in fact, the boundary between sensor, brain and actuator has been blurred. On the level of a device governed by smart materiality, they become indistinguishable.

The following are examples of smart materials that could be utilized in adaptronic products:

- Shear-thickening non-Newtonian fluids: turn solid when compressed, for example starchy water
- Photochromic glass: opaque when electrified
- Piezoelectric materials: produce voltage when stress is applied
- Shape memory materials: revert back to a 'remembered' shape, normally due to heat but can also be magnetic

(Janocha, 1999) gives a number of design concepts for adaptronic devices, which do not necessarily eliminate all electronics but they do remove the microprocessor and computing hardware from the systems. At the time of writing, the adaptronic devices mentioned were largely in the development stage. Some have multiple materials and elements working in concert to deliver the sensing and reacting whilst others can be simple devices that deform when heated, as seen in Figure 20. Not all applications are industrial; the research and development company Grado Zero Espace developed a shirt which self-rolls the sleeves up in hot conditions, with a fabric cost of 1200 per meter. 'Absorbing' power from the environment instead of drawing it from a battery/grid is not a necessary criteria of adaptronics, but the true elegance of the concept comes from being a passive actuator.

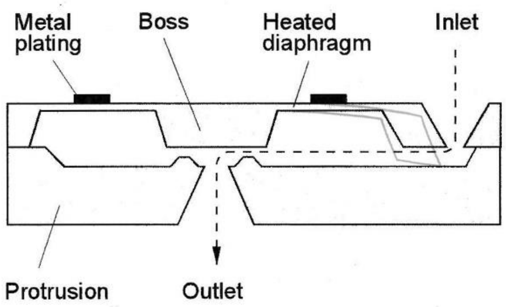

Figure 20: A thermomechanical gas valve by the American company IC-Sensors. The diaphragm is made of a bimetal strip which opens and closes based on temperature (Jerman, 1994). Image from Adaptronics and Smart Structures

Figure 21: A shirt developed by Grado Zero Espace that self-rolls its own sleeves up in hot temperatures, made of Shape Memory Alloy (Grado Zero Espace).

Overall, the material phenomena of the entities known as adaptronics and smart/intelligent structures can be an efficient way of delivering a high tech but low complexity actuation device. Michelle Addington and Daniel Schodeck call them the "answer for the twenty first century's technological needs" (Addington & Schodek, 2005). Craig A. Rogers, former Editor-in-Chief of *Journal of Intelligent Material Systems and Structures,* believes "Intelligent materials systems will be manifestations of the next materials and engineering revolution-the dawn of a new materials age".

The main focus of adaptronics today appears to be in vibration/ noise reduction and structural damage monitoring, but other promising fields include vehicle engineering, aerospace, medical engineering and façade engineering (Fraunhofer Adaptronics Alliance).

This thesis will be using Shape memory alloy as the focus of the study. They are a very promising material for the design of adaptronics, but the material is not commonly used in building technology. They can form structural components which respond to temperature changes, potentially leading to architecture that changes with the weather or season.

In the architectural field, only a small handful of facade researchers are working on adaptronic parts, at varying degrees of technical depth. Some utilize the properties of Shape Memory Alloys. These examples will be shown in Chapter 2, which contains an overview of reference projects regarding the intersection of adaptronics and architecture.

Research Framework

> “ *The inability of the passive inert building to provide comfortable conditions is the cause for the provision of environmental services systems, introduced to overcome the inadequacy of the static building. It is the amount of this servicing which provides the greatest justification for the intelligent building.* ”
>
> -Michael Wigginton and Jude Harris in *Intelligent Skins*[4]

Problem Statement

Heating and cooling account for 50% of all energy expenditure in the EU, of which 27% is space heating (Heat Roadmap Europe 4, 2017). There is enormous scope for energy savings in the cooling and heating demands by thoughtful design and construction of facades.

Atria are a popular architectural feature which many architects and clients desire for their visual and social experience. However, they can be either a significant drain on a building's energy performance or key weapon in the reduction of energy consumption. Effective design captures solar gain in the winter without increasing solar gain in the summer. In particular, a hypothetical seasonal atrium that becomes an open courtyard for the cooling seasons can save as much as 30% in heating load, based on a simulated house in Amsterdam (Taleghani et al., 2014).

Adaptronics is a method of designing the sensor, computer and actuator all into the materials itself. This removes many problems that are inherent with the electrical and mechanical systems of adaptive technologies. There are already a few recent projects that involve architectural adaptronics, but it has not yet been implemented in built projects. The concept has great potential to save energy as an auto-responsive solution that does not cost energy to operate. It can be a method for making facades adaptive without the clutter or electrical complexity of traditional motorized hardware, or the unreliable nature of manual control.

One of the most common smart materials to deliver adaptronic devices are Shape Memory Alloys (SMAs), which can change shape when the temperature changes. They are not commonly used in the building industry, but there is a wide scope of applications and benefits for this innovative smart material. The complex behaviour of the material is a barrier to designers with no specialist knowledge, so there is an opportunity to create a bridge between the two, for example with user-friendly modelling software.

There is much potential for SMAs to be used within an adaptronic façade module that opens itself in the warm season, to deliver a seasonal courtyard and thereby save energy by utilizing the greenhouse effect only when needed during the months of the year that require heating.

---

[4] (Michael Wigginton, 2002), p19

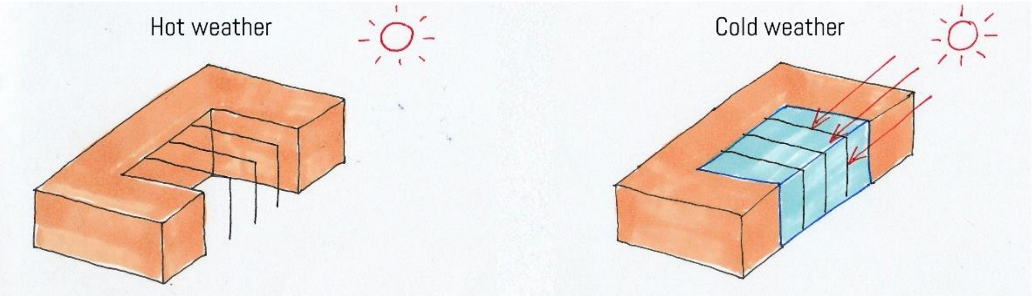

Figure 22: Concept for the main objective: façade modules to achieve a seasonally open adaptronic atrium/courtyard

Main Objective

This thesis aims to investigate the feasibility and process of designing and constructing an adaptronic façade module based on Shape Memory Alloy behaviour that can open itself in hot weather and remain closed in cold weather, to be used in an atrium situated in a temperate climate.

Sub Objectives

1. **To investigate Shape Memory Alloys and the process of incorporating it into the design of a temperature-sensitive façade module for an atrium**
2. **To deliver a design that allows the module to be easily manufactured and assembled**
3. **To provide a software tool to allow the behaviour of SMAs to be easily modelled, thereby empowering designers with no specialist knowledge of the material to work with it**

Main Research Question

In terms of structure and detailing, how can a Shape Memory Alloy-based adaptronic atrium be designed to self-actuate in response to external environmental conditions, for the purposes of energy consumption reduction, in temperate climate regions?

Sub-questions

To achieve the sub-objectives, sub-questions start from the smaller scale and generally work upwards, which has been seen as the more suitable approach in this study. The investigations can generally be categorized into three distinct areas of study/design: material, adaptronic 'engine' and module.[5] Some design is also done on the scale of the atrium, but it is not a key focus in this thesis.

1. **How can Shape Memory Alloys be used in building technology? What are the conditions and limits when structurally incorporating Shape Memory Alloys as an adaptive component in a façade module?**
2. **How can the behaviour of an SMA element be modelled computationally to predict the movement of the façade module given a stream of temperature data?**
3. **How can an adaptronic actuator 'engine' be designed to deliver the desired temperature-responsive change of the façade module?**
4. **How can a façade module incorporate the engine that delivers adaptronic abilities, and still function with all the usual requirements of a conventional facade? To what extent can it be done simply, with long-term reliability and with ease of manufacture/assembly?**

---

[5] The separation between the engine and the body design was seen as a logical choice, as they worked at different scales and had a very different set of demands. It is compared to the design of a car, in that the the engine and the the body would be two different design projects for much of the process, to be married at a key stage.

5. **To what extent can an adaptronic system deliver two extreme states of a fully transparent but insulated atrium to a fully open court, in response to a temperature change?**

Goal and boundaries

It should be noted that the thesis will look at the possibility of such a device, but not the fine-tuning for calculating the exact energy saving. Therefore, it will be a focus on the computational, feasibility and detailing aspects, which for now are the most pertinent questions for proving that it will work. A future study with a focus on building physics can look at the fine-tuning of the energy saving implications. The thesis is therefore setting the foundation for a future designer to be able to utilize findings to achieve the most energetically effective adaptronic atrium. Additionally, it will empower other designers to work with SMAs and exploit its phenomena to their own needs.

Output

The thesis will result in a design for an adaptronic façade module, along with prototypes to validate the concept and mechanisms, and a computational tool for SMA design. Regarding the last item, the tool could for example allow a designer to input the properties of a chosen SMA sample and design custom adaptronic modules that are optimized for the local climate. The program would animate an adaptronic structure as a function of temperature.

Design Brief

To address the research question, an existing housing complex in Amsterdam named the Gerschwin Brothers building, designed by LEVS Architecten and built in 2018, has been chosen as it has a courtyard open on its south side. The adaptronic atrium shall be built to fill in the courtyard, and the atrium will open up in hot conditions to behave as closely as possible to an open courtyard.

Figure 23: The Gerschwin Brothers Building by LEVS Architecten (2018) in Amsterdam will be design context

Methodology

The sub-questions inform the sequence of studies and produce the outputs. They are as follows:

Question	Action
1. How can Shape Memory Alloys be used in building technology? What are the conditions and limits when structurally incorporating Shape Memory Alloys as an adaptive component in a façade module?	• Literature study on the material behaviours, existing usages, and research projects for SMAs.
2. How can the behaviour of an SMA element be modelled computationally to predict the movement of the façade module given a stream of temperature data?	• Literature study on the past attempts at SMA behaviour modelling • Script-building in Grasshopper
3. How can an adaptronic actuator 'engine' be designed to deliver the desired temperature-responsive change of the façade module?	• Design and experimenting of parametric models in Grasshopper with dynamic features • Physical testing of SMA material • Design and moving prototypes for module concept and engine
4. How can a façade module incorporate the engine that delivers adaptronic abilities, and still function with all the usual requirements of a conventional facade? To what extent can it be done simply, with long-term reliability and with ease of manufacture/assembly?	• Design of module • Review of design
5. To what extent can an adaptronic system deliver two extreme states of fully closed and fully open, in response to a temperature change?	• Experimenting and review of parametric models • Construct and test prototypes based on SMA-driven elements

Relevance

Relevance for the Sustainability Studio and Society

An agent against the highly intensive energy costs of HVAC

The thesis fits into the Sustainability Studio, the only studio of the Building Technology Track, as it seeks to tackle a major contributor of carbon emissions and thereby also find societal relevance. Governments and international bodies are increasingly applying pressure on buildings and all other human activities to cut down on energy and fossil fuel consumption, in order to stave off the potentially catastrophic consequences of climate change. The situation places great responsibility on the thoughtful design of energetically sustainable facades, as the heating and cooling of spaces consume 14% of all energy in the EU. Designing against HVAC consumption would therefore be a very logical strategy, and the concept of a seasonal atrium has the potential to cut down heating load by about a quarter in the case of a home in Amsterdam. It would therefore be an agent against the highly intensive energy costs of HVAC.

Scientific Relevance

Adaptronics: a new method for adaptive facades

Currently, responsive architectural systems for regulating indoor comfort are largely based on electrical sensors, computer controllers and motors. They can be complex to build, as they require a large number of parts, are prone to failure and they take up a lot of space. This thesis explores the possibility of adaptronic technology in the façade, which replaces all the complex electrical hardware with smart materials integrated into a thoughtfully designed structure. Such a device is able to do the job of sensing, computing and reacting simply by harnessing the properties of the smart material as it responds to external stimuli. This has great potential for façade design, as it has the job of separating the stable zone of human comfort on one side from the constantly fluctuating conditions of the outdoors on the other; it achieves its goals most efficiently when it is able to adapt with the current conditions. Adaptronics would be a new method for adaptive façades. In conventional adaptive facades, the adaptiveness is generally achieved with a set of electrical components that animate the façade elements, like a puppet. In adaptronics, the adaptiveness goes one level deeper, into the materials themselves.

Empowering the designer with Shape Memory Technology

Shape Memory Alloys have not yet been widely used in architecture, yet it has great potential for a range of applications besides using it as an actuator. For example, it can be a very effective connector, solid sealant, dampener and structural healing device. The complexity of its behaviour is one of the major barriers to its design, as virtually all past projects required a deep understanding and modelling of its dynamic phenomena. Throughout the thesis, a constant effort was made to remove that barrier and find methods to incorporate SMAs into the design process of a non-specialist as well as adapting the material to the physical capabilities of the construction industry, which tends to favour conservative approaches. The script produced is able to model the material as it changes with temperature, without needing specialist knowledge. The tool will empower designers to incorporate the shape memory technology into their own projects, and for climate engineers, it makes it possible to track the changing opening sizes with changes in weather, and thereby evaluate the resulting energy and comfort parameters of the indoor condition.

2. Reference Projects

Innovative Atria

Bengt Sjostrom Starlight Theatre

Theatre in Illinois, United States, by Studio Gang (2003)

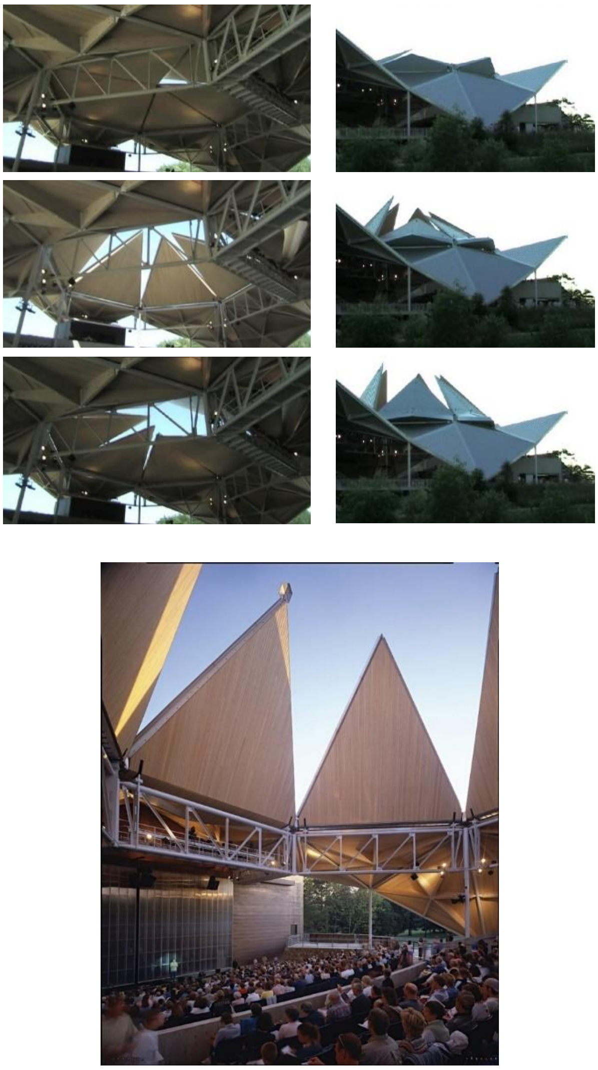

Figure 24: a) Sequence images of roof opening, b) view from inside (Studio Gang)

Situated in a hot climate, this project features a striking 6-piece roof that uses hydraulics to open up and thereby increase the flexibility and comfort of the space. The clients are able to extend their season of performances, as well as present a very special experience. Data regarding the energy savings or comfort levels due to the cooling nature of the open roof are not available, but the project illustrates the possibilities of a dynamic roof.

Q1 building

Office building with central atrium in Essen, Germany, by JSWD Architecten and Chain&Morel et Assoils, 2010

Figure 25: Q1 building on the campus of ThyssenKrupp AG in Essen, Germany[6]

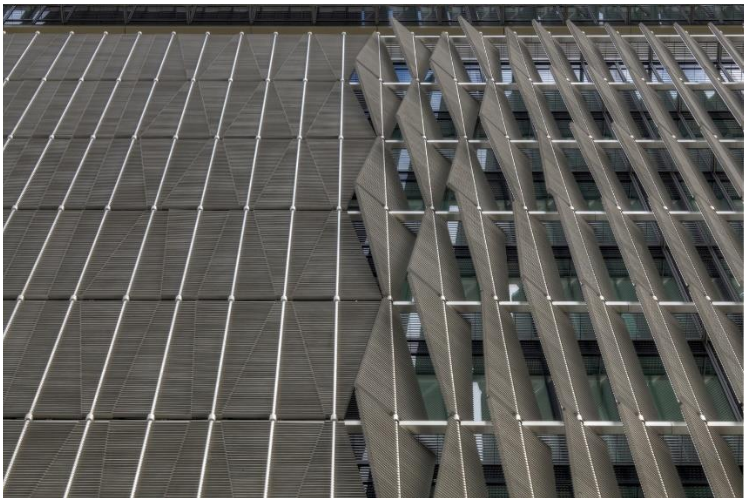

Figure 26: stainless steel lamellas, which track the sun and rotate automatically throughout the day[7]

ThyssenKrupp AG's main building at the Essen campus features a ten-story atrium which facilitates natural ventilation and is neither heated nor cooled. At the façade of the offices is an intelligent system which involves a dynamic stainless steel mesh that traces the Sun's movement throughout the day. Overall, the primary energy consumption of the new buildings in the innovative complex is estimated to be 20 to 30% lower than statutory requirements, which in its time only very few buildings in Germany had achieved (Sayigh, 2014).

---

[6] Image credit https://www.archdaily.com/326747/q1-thyssenkrupp-quarter-essen-jswd-architekten-chaix-morel-et-associes/

[7] Image credit https://www.archdaily.com/326747/q1-thyssenkrupp-quarter-essen-jswd-architekten-chaix-morel-et-associes/

Academy Mont-Cenis Herne

Training academy in Herne, Germany, by Jourda et Perraudin, Hegger Hegger Schleiff, 1999

A cluster of buildings is effectively enclosed under a 180m long giant glass box that creates its own microclimate of 16 000 m^2. PV panels on the box provide shading and there are openable glass panels to control ventilation and thereby deliver year-round temperatures that are milder than the external condition. The energy requirements of the buildings under the glass skin are lower because in the Winter, the microclimate is warmer than external conditions. With optimal control of the systems, the energy consumption is 32 kWh/m^2 (Hegger, 2008, p. 228). This can be compared to the average school anticipated energy consumption of 230 W kWh/m^2 in Europe (Energy Performance of Buildings, 2015). It should be noted that the construction value was 2896 Euros/m^2 if counting just the internal heated buildings as the useful floor area, whilst the other innovative low-energy projects of similar size in the same literature tend to be around 1000 Euros/m^2.

Figure 27: a) The 'glass box' of the academy, b) View of openable vents in the atrium facade

Adaptronics and Architecture

The following reference projects represent the intersection between adaptronics and architecture. They involve mechanisms that sense the environment and respond without the use of electrical controllers, by utilizing the innate properties of materials and special geometries. They all have either a sustainable drive to save energy or to regulate the indoor comfort. To start off with, an adaptronic SMA project has already been envisioned.

Shape Memory Alloy

Figure 28: Adaptronic shading in façade

Fraunhofer Institute for Machine Tools and Forming Technology IWU (part of the Fraunhofer Adaptronics Alliace) and the Department of Textile and Surface of the Berlin Weissensee School of Art collaborated to work on the idea of a design student, Bara Finnsdottir for this project. It is a façade element capable of two settings in hot and cold states. Exposure to sunlight causes the element to activate and open up, providing autonomous shade that retracts once the sunlight is gone (Fraunhofer Adaptronics Alliance). A demonstrator has been built, but additional information is not available.

Bilayer strips

This type of composite material is made by bonding materials together so that their structures interact; each material has its own coefficient of expansion for a given stimulus, for example in response to temperature.

Figure 29: Bloom, a temporary installation that demonstrates the adaptronic qualities of bimetal strips (Sung, 2012)

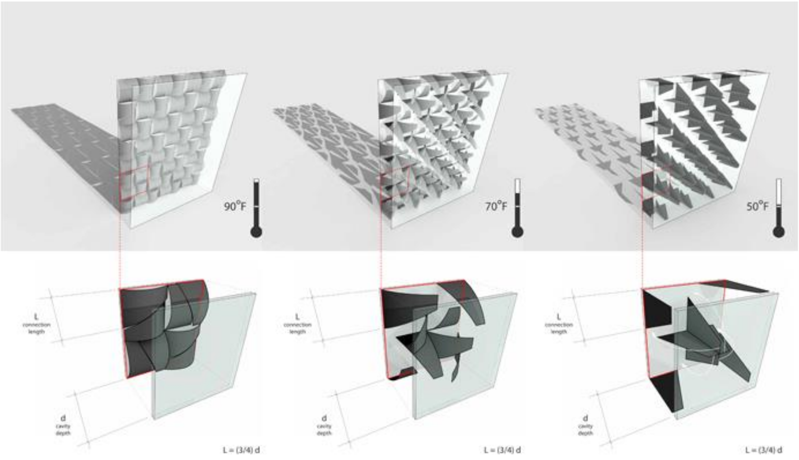

Figure 30: Glass panel and solar-responsive SMA shutter system by Sung. Concept design for an adaptronic façade (Sung)

Bimetal strip is a simple and the most common example of this type, where two metals with a different coefficient of thermal expansion are able to curve or straighten itself based on the environment temperature. Showing potential as the active ingredient in adaptronics, it has been used in standard thermostats for household temperature control. Doris Kim Sung explores this composite in architectural constructions, for instance metal skins with flaps that are closed in normal conditions, but open up when exposed to sunlight as shown in Figure 29. The idea is to build a self-controlled façade which dynamically shades and ventilates based on the external conditions; a true adaptronic façade. A concept modular design is shown in Figure 30.

Figure 31: A design for an an adaptronic façade actuated using bimetal beams

Adriaenssens et al. studied the form finding and structural aspects of a facade design which utilized an adaptronic shading system actuated using bimetallic structure, seen in Figure 31. Calculations in this report showed that a 1m bimetal beam made of ASTM TM2 of section size 15 x 0.36 mm can cause a 4mm displacement in the middle of the beam when subjected to a temperature change of 10°C (Adriaenssens et al., 2014). The element could cause an attached shade structure to deform, thereby delivering the adaptronic response. It should be noted that the effect of wind forces were not accounted for in this design, which would be significant on such a thin profile.

Despite its potential, bimetals have not been seriously pursued elsewhere in the architecture profession. One major disadvantage is that strips necessarily need to be very thin (compared to their length) in order to have substantial bending effects, which limits their structural capabilities unless full shielded. In the example above, the bimetal beams were only 0.36 mm thick, resulting in a span/thickness ratio of 2778. The actuation forces from such devices are therefore very small and in practice will not function outside.

Responsive Polymers

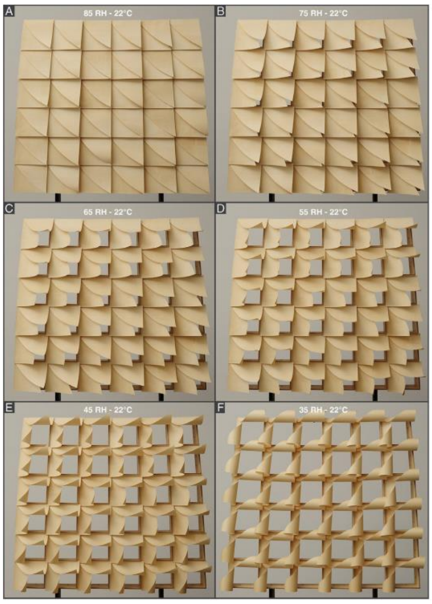

Figure 32: Veneer-composite material that opens at low relative humidity and closes at high humidity. Image from (Reichert, Menges, & Correa, 2015)

The 2015 study of Correa et al. focuses on programmed 3D-printed wood-like materials made of cellulose fibres and polymer, taking inspiration from the properties of Conifer pine cones and the ability of wood to expand based on humidity (Correa et al., 2015). Possible options for activation include water submersion, water vapour and thermal radiation. An organic-looking façade vent prototype is seen above.

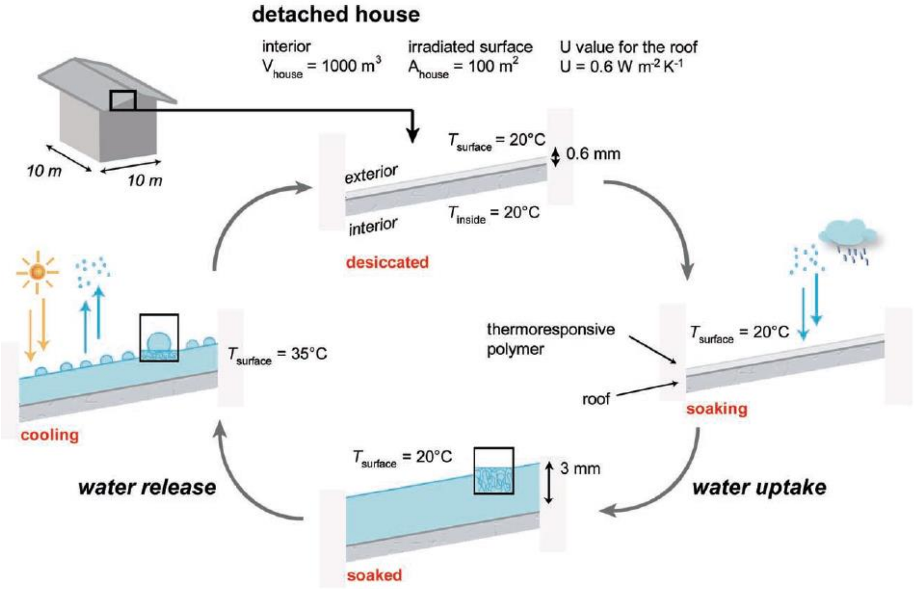

Figure 33: Mechanism for the use of PNIPAM as a method of solar-responsive evaporative cooling. Image from (Rotzetter et al., 2012)

(Rotzetter et al., 2012) demonstrate the effectiveness of a special polymer at providing evaporative cooling, inspired by the sweat response of mammals. The material, an easily mass-produced hydrogel named PNIPAM, is placed on the surface of a building and is designed to absorb rain water. Upon a set temperature of 32°C, the water is 'sweat' out of the material, thereby cooling the building in times of solar radiation. This method reportedly saved 60% of cooling energy.

Figure 34: a thermotropic resin used as a window, to provide adaptronic glare and overheating reduction. This example, from (Nitz & Hartwig, 2005), takes 15-60 minutes to activate. Using it on all the windows of a room was not recommended, due to obstruction of views

(Nitz & Hartwig, 2005) Investigated the potential of a thermotropic cast resin layer being used as glazing. In addition to moderating the indoor temperature fluctuations, when the material heated up to a certain temperature, the glazing becomes translucent and reduces glare and overheating. In the winter, the low ambient temperatures prevent the material from activating, so beneficial solar gain is maintained in that season. A variety of materials can perform the behaviour, including hydrogels, polymer blends and PCM.

Paraffin wax actuators

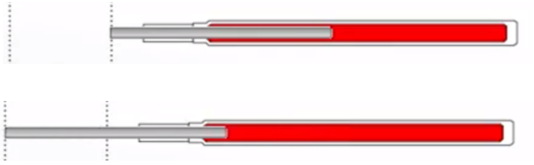

Figure 35: The expansion of paraffin wax when melted can drive a temperature-dependent actuator with considerable force.[8]

An interesting emerging technology exploits the 10-20% volume change when paraffin wax changes states between solid and liquid. The material can be placed within a telescopic chamber which essentially becomes a heat-responsive actuator that requires no other power input, as seen in Figure 75.

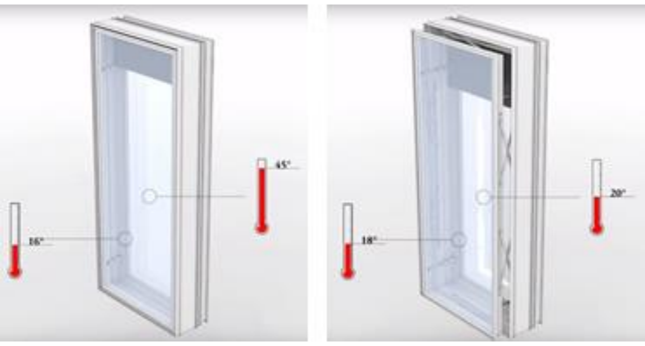

Figure 36:When the temperature in the cavity exceeds 23ºC, the paraffin wax actuators push the outer pane out by 5cm. The window self-closes when temperature cools back down.[9]

Flexcover is a collaborative research project of the TUM (Technical University of Munich) Department of Architecture and Frener & Reifer Fassaden. It had recently developed an adaptronic double skin façade system with paraffin thermoreactive actuators. Some variations of the concept do different jobs, for example ventilate the cavity of the façade which is prone to overheating when shades are placed within it, regulate humidity of the cavity and to control direct solar radiation whilst allowing natural diffuse light through. Their simulations claim a 50% reduction in energy consumption for heating and cooling of the internal spaces, with the majority of the savings being cooling-related.[10]

---

[8] Image credit: Technical University of Munich https://www.tum.de/en/about-tum/news/press-releases/detail/article/34337/

[9] Image credit: Technical University of Munich https://www.tum.de/en/about-tum/news/press-releases/detail/article/34337/

[10] Image credit: Technical University of Munich https://www.tum.de/en/about-tum/news/press-releases/detail/article/34337/

Figure 37: adaptronic temperature-sensitive panels that use paraffin-based thermal passive actuators. A stroke angle of 66 degrees is achieved using a temperature difference from 16.5°C to 35.6°C

(Leung, 2014) studied the use of these type of actuators in an adaptronic façade module, for passive indoor environmental control and found many benefits due to its selectable temperature range of expansion, the robustness and the high load capacity. One of the disadvantages was the low actuation speed due to the time taken for the material to heat through. The project successfully built adaptronic panels which were temperature sensitive and powered by the 'passive actuators'.

An in-depth study was done to quantify the behaviour of the actuator against the weather, and to influence it by designing a heat chamber for the paraffin wax actuator that had its own environment. The temperature within the heat chamber depended on weather conditions such as sun intensity, angle, ambient air temperature. The physics was modelled to predict and influence the temporal patterns of window opening, and so the reference project pursued similar themes and challenges to this thesis. It will be elaborated in Chapter 5.

3. Material Study

Introduction to Material Behaviour

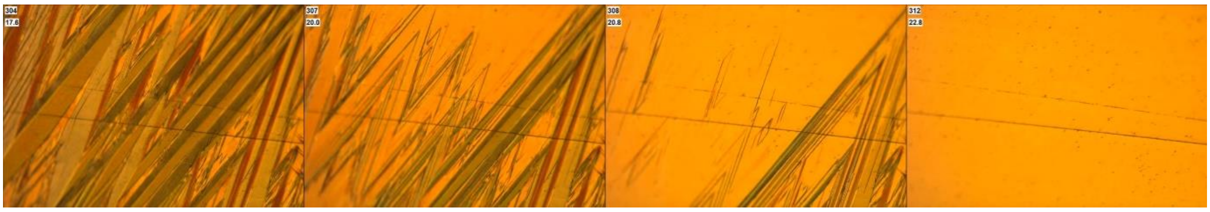

Figure 38: Optical microscopic snapshots of the surface of a CuAlNi Based SMA, undergoing transformation from Martensite to Austenite[11]

The term Shape Memory Alloys, or SMA for short, refers to alloys which exhibit two special phenomena: the Shape Memory Effect and superelasticity, also known as pseudoelasticity. Both of these phenomena are the result of a phase change in the material from one solid state to another solid state. The rearrangement of the atoms in the crystalline structure during the phase change results in the perceived macroscopic changes.

By far the most common type is the Nickel-Titanium alloy, also known as Nitinol, which is around equal parts nickel and titanium by atomic percentage, and has found successful commercial use in the medical and aerospace industries.

The Shape Memory Effect

The Shape Memory Effect happens when an SMA is heated through a certain temperature range which causes it to gradually transition from one state to another. The martensite state is stable at colder temperatures, whilst the austenite state is stable in warmer temperatures. When SMA material is deformed at the martensite state, it is able to thereafter repair its “permanent” deformations upon being warmed through its transition temperatures into the Austenite state. It therefore returns to a “remembered” shape by transitioning from Martensite to Austenite. Limitations do apply: the material is only able to a certain percentage of deformation strain. In the case of Nitinol, this maximum strain recovery is typically about 8% (Lecce & Concilio, 2014, p. 38).

---

[11] Image credits: University of Miskolc https://www.youtube.com/watch?v=8g0pxYClDaM

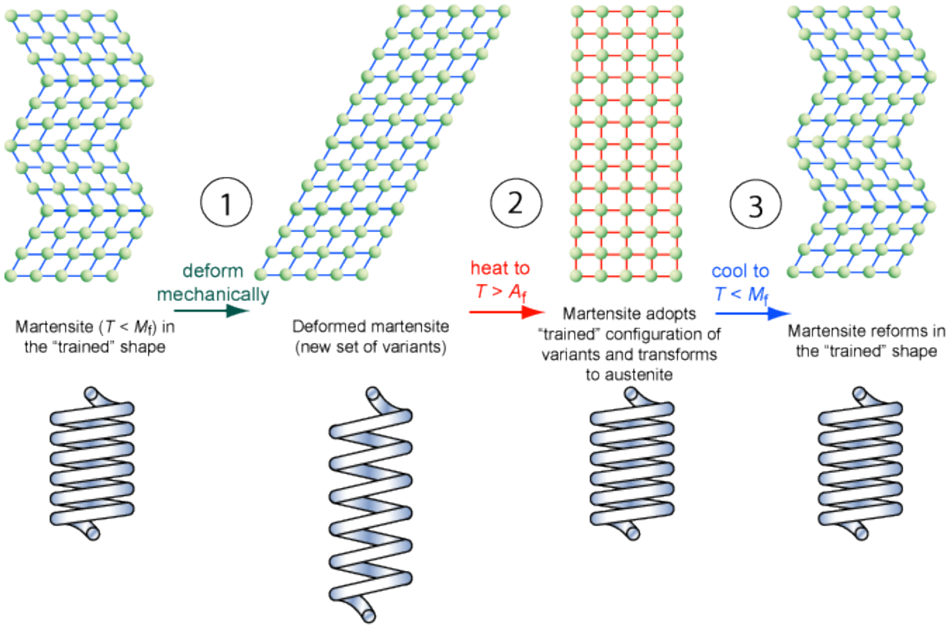

Figure 39: An SMA being deformed and recovering its former geometry through SME, along with its crystalline arrangement[12]

Standard one-way SME action is illustrated above. The SMA spring starts out in the martensite phase at room temperature and in step 1 is deformed permanently by a load. The load is then removed, resulting in the longer spring. In step 2, heat is applied to the spring, which causes a gradual transition of the material from 100% martensite to 100% austenite. As it becomes austenite, the shape of the spring that was previously deformed is now recovered, resulting in the starting length. In step 3, the material cools down again, and again passes through a temperature transition zone that changes it gradually from 100% austenite to 100% martensite. It has now returned to the starting condition. The microscopic crystalline situation is seen in parallel to show how the macroscopic effects are the result of the atoms rearranging themselves depending on the condition. Note that the martensite state can be further divided into the twinned martensite state, which is a 'fresh' state with no deformation compared to the austenite shape, and the detwinned martensite state, which the a deformed state.

Possibility of Two-way Shape Memory Effect

This effect of a material "remembering" its former shape is usually a one-way effect; in conventional scenarios, cooling the material back down from a recovered Austenite form to the Martensite phase will not cause the deformation to return. However, it is possible to make this happen by special treatments that result in the Two-way Shape Memory Effect (TWSME). There are various methods to do this to different degrees of success, and they generally involve repeated cycles of restrained heating and cooling in a specific fashion (Luo & Abel, 2007a). In all cases, the shape recovery ability is not as strong, typically only able to recover about 2% strain (Perkins & Hodgson, 1990, pp. 195-206).

Achieving two-way actuation with the One-way Shape Memory Effect

Due to performance limitations of TWSME, many any adaptronic designs have favoured other methods to achieve two-way actuation using the one-way SME. One method is to have two separate pieces of SMA that work antagonistically and are activated one at a time to move the actuator forwards and backwards. The other method is to apply a permanent opposing force against the SMA element so that it is always trying to deform the SMA. In this way, the SMA is instantly deformed into a certain shape as soon as it cools into the

---

[12] Image Credit: University of Cambridge
https://www.doitpoms.ac.uk/tlplib/superelasticity/images/fig3_SME_schem_cs.gif

martensite phase, with the help of a spring, counterweight or other force provider. The effect of heat causes the SMA to remember its original shape and do work against the bias force object, thus returning to its old position. The SMA element, and rest of the attached structure, therefore assumes a hot position and a cold position.

Transition temperatures

For any given SMA, the martensite-to-austenite phase transition does not happen over the exact same temperature range as the austenite-to-martensite. This is best illustrated by plotting a graph of a spring's length as the temperature changes, whilst it is subjected to a constant load as shown below.

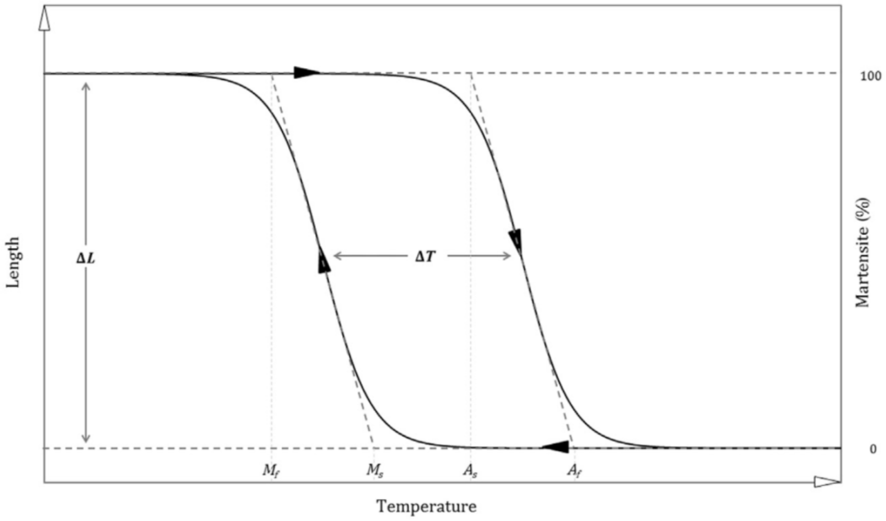

Figure 40: The effect of changing the temperature on the length of an SMA spring or rod (both exhibit the same shape curves). Here it is shown being heated up and cooled down again, whilst under a constant load. Notice the hysteresis, denoted by the lambda T (Lecce & Concilio, 2014, p. 36)

Starting at the top left point of the line, the spring is heated until it reaches its austenite start temperature, A_s. The transition to fully austenite causes a reduction of spring length as it recovers its remembered shape in opposition to the effect of the constant load. It completes at the austenite finish temperature A_f, and thereafter the spring has a constant length because phase changing actions have completed. As the rod is cooled down, another set of temperatures happen for the transition to martensite, martensite start, M_s, and austenite finish, M_f. The four values of transition temperatures are key properties of the material and are determined by the metallic composition of the alloy.

The difference between the austenite transition temperatures and the martensite transition temperatures effectively represents a 'lag' in the response of the SMA, and this can be problematic for actuators, as it means there is more than one possible length for an SMA element if it is at a given temperature, and it depends on the history of the element. The difference, denoted on the graph as lambda T, is known as hysteresis. The curves which exhibit this concept of a lag are sometimes referred to a hysteresis loop, and they are a common theme in the phenomenology of SMAs. This effect is important for modelling the true behaviour of adaptronic structures, and complicates dynamic computational models.

The Superelastic Effect

The second phenomena of SMAs can be seen whilst it is in a temperature above A_f. An applied stress can induce a phase change to martensite, causing it to undergo a non-uniform stress-strain curve as it deforms. This can be seen in Figure 41.

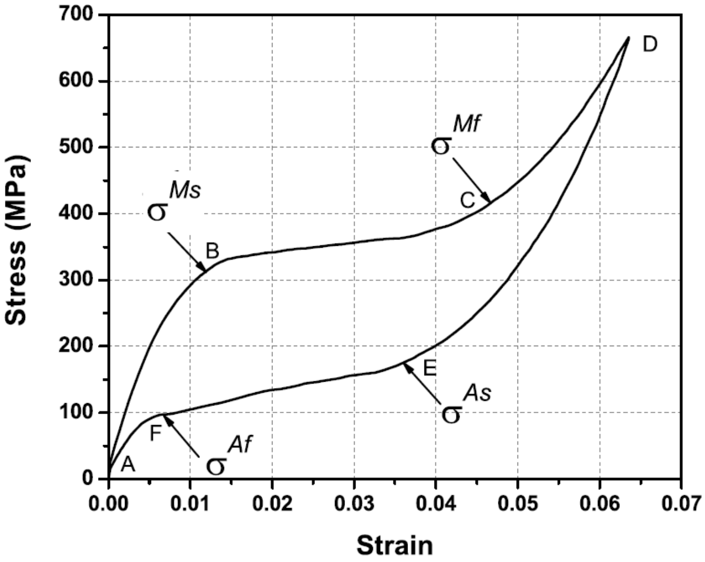

Figure 41: The stress-strain curve for an SMA spring in its austenite phase being loaded and then unloaded, causing the superelastic effect (Lagoudas, 2008, p. 14)

The SMA spring starts in the bottom left of the graph, and the gradual load is applied. It initially causes the classic straight-line deformation on the stress-strain curve until it reaches point B, at stress M_s. Here, the material begins to change phase to martensite. It undergoes a further lengthening without much change in force exerted by the spring, whilst the material reaches full martensite at stress M_f. Classic straight-line stress-strain resumes within the fully martensite material until point D. The load is gradually removed and the reverse effects happen at points E and F, until the material returns to the start point. Again, the material does not take the same curve in the graph when it returns to its original length.

Interdependency of the Temperature and Stress-induced transitions

The graphs shown so far demonstrate the changing of one variable, either stress or temperature, whilst the other remains constant. An additional level of complexity underlies the behaviour: at different levels of stress, the sets of transition temperatures will be different, as shown in Figure 42. For a material that effectively has an extra dimension of property compared to conventional materials, a 3D field can be a very effective way, compared to a two-dimensional graph, to visualise the added complexity of the mechanics. The axis denoted by the symbol ξ indicates the progress of the material in the transition to the full martensite phase, as a number between 0 and 1, with 0 representing full austenite.

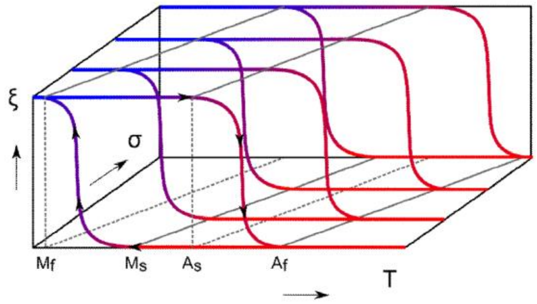

Figure 42: The transition temperatures of an SMA sample will change based on its stress level (Cianchetti, 2013)

The graph below shows how the strains and the temperature transition points change with each cycle of increasing stress.

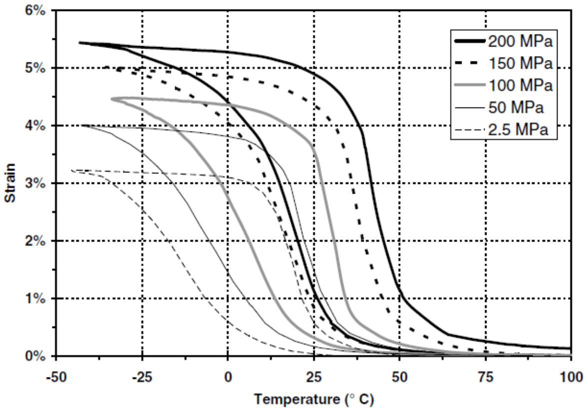

Figure 43: Thermal cycles of a Nitinol sample under different levels of stress (Lagoudas, 2008, p. 79)

In Figure 44, the behaviour of a piece of SMA is mapped onto a 3D strain-stress-temperature graph. Starting at 0, the SMA is in its martensite state and it is loaded to point 1, which is at 8% strain, the limit for a typical Nitinol piece. The curve exhibits a plateau similar to those in Figure 41, which shows the two states and transition between twinned and detwinned martensite. The load is removed completely, taking the curve to point 2; there is partial shape recovery, but a large residual stress remains. The SMA piece is heated and undergoes shape recovery and transition to austenite through points 3, 4 and 5, the same movement as the bottom portion of the curve in Figure 40. The austenite-state piece is then loaded until stress-induced transition to martensite starts to happen at point 6, which is analogous to point B in Figure 41. The loading continues to increase until point 7, where it is removed, causing it to undergo transition back to martensite at between points 8 and 9, and recovering the austenite pre-load shape at point 10. Note that points 2 to 5 represent the thermally induced shape memory effect, whilst points 5 to 10 represents the superelestic effect.

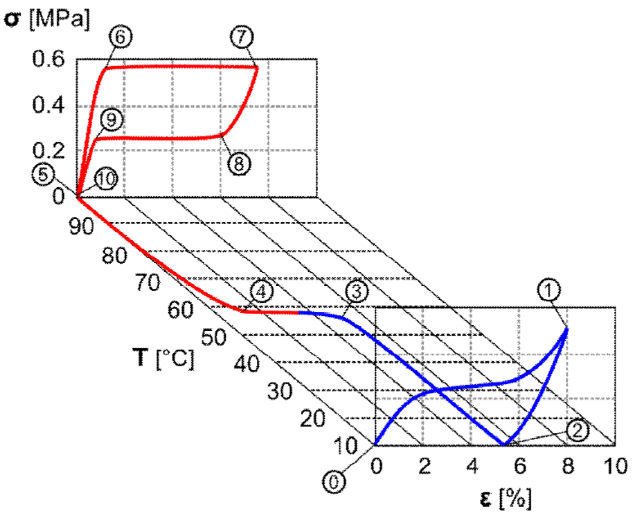

Figure 44: An SMA subjected to loading and thermal effects (Cianchetti, 2013)

These 3-dimensional graphs show the complexity of the material which is both non-linear and interdependent. A pattern for the behaviour can be seen, and the path of the curve through the strain-stress-temperature graph can be predicted given enough knowledge of the material and by testing the macroscopic behaviour of a sample, instead of the microscopic detail.

The R-Phase

Another phase sometimes occurs in between austenite and martensite, known as the R-phase, which stands for Rhombohedral. It comes with its own Shape Memory Effect, but on a much smaller level of strain recovery at about 1% (Lecce & Concilio, 2014, p. 37). The existence of this in-between phase depends on specific processing conditions and, in the case of nitinol, adding certain extra elements to the atomic composition (Gautier & Patoor, 1997). It has been noted for its low hysteresis and great repeatable reliability compared to the austenite-martensite SME. This has lead some researchers to pursue the transition as the driver of actuation, but for this thesis the R-phase will not be studied in detail. It is not likely to occur during experiments, and if it does the effect is so small as to be unnoticeable.

Shape-setting

The determination of the remembered shape in the austenite phase can be programmed into an SMA piece by restraining it into a shape with a jig or clamping device and then heating it up past a certain temperature for a set amount of time before quenching in water. The particular details and amount of time and heat involved in the process have a great effect on the functional properties and qualities of the SMA phenomena. The intricate science of the procedure have lead to patents and the protocols are not widely disclosed by manufacturers. Parameters such as transition temperatures, recoverable strain limit and recovery stress can be influenced, so in many instances it is tailored to a certain application. The heating is generally done in the range of 300-600°C and between a few minutes to an hour. The very upper end of the temperature range is associated with rapid and accurate SME but poor mechanical properties (Lecce & Concilio, 2014, p. 90), (Zanaboni, 2008).

Effects of Cycling and Training

Upon first use of an SMA element, initial cycles of mechanical and thermal loading will have lower strains. After a certain number of repeated cycles, the stress-strain path will stabilise; it is therefore advantageous to do this to SMAs before using them for an actuator device, and this process is called training. For thermal cycling at constant stress, this process can be seen in Figure 45 and Figure 46. The latter takes many more cycles to stabilise, potentially due to the higher constant stress and a slightly different alloy composition. To bring an SMA actuator to functional standards, it is recommended to train it (via thermal cycling) under either a constant stress that exceeds the expected stresses of its application, or under a stress pattern that mimics the actuator usage, for example with the same antagonistic spring (Lecce 2015, p71).

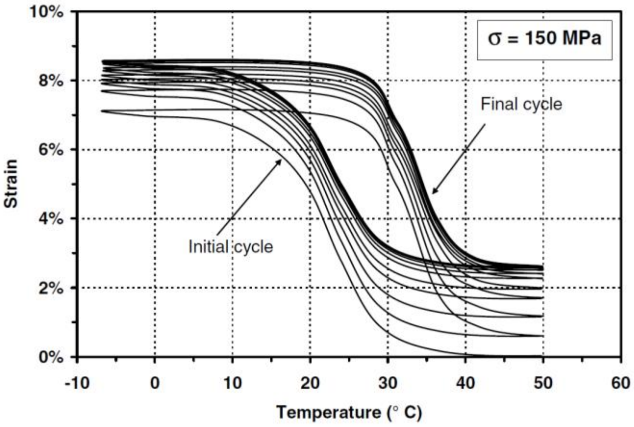

Figure 45: 50 cycles of thermal activation with a constant stress of 150 MPa, for a Nitinol element. As shown, the element is effectively stable after 5 cycles (Lagoudas, 2008, p. 16)

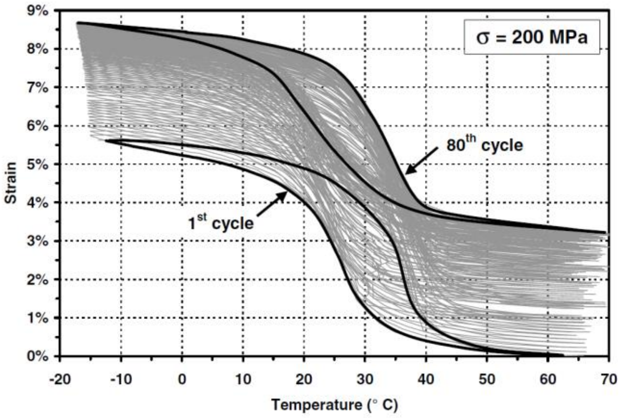

Figure 46: 80 cycles of another Nitinol sample at 200 MPa. This one takes many more cycles to stabilise (Lagoudas, 2008, p. 78)

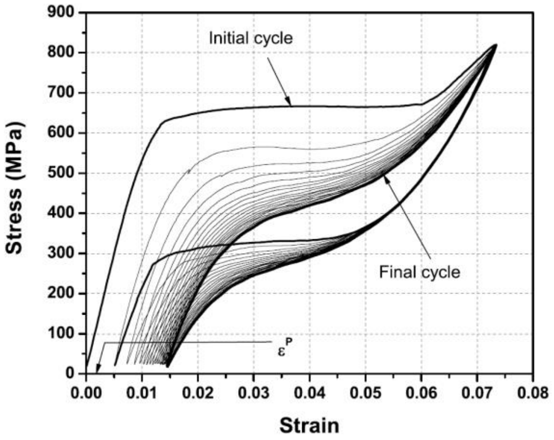

Figure 47: 20 mechanical loading cycles of Nitinol with austenite finish temperature of 65^{0}C , experiment done at T = 70^{0}C (Lagoudas, 2008, p. 16).

Variations of SMA

Within the Same Base Alloy

For any SMA, metallic composition has profound effects on the macroscopic behaviour. Not only do different base-alloys have vastly different values of maximum strain recovery, hysteresis etc, but even small differences within a base alloy need to be appreciated. For example, even a 1% shift in the amount of nickel or titanium in Nitinol will result in 100°C change in transformation temperature (Wu, 2002). In medical applications, the transformation temperatures need to be controlled within 5°C, which means that the composition needs to be accurate to 0.05%. This potentially makes the production of SMA actuators a very precise and expensive business. Overall, the composition of an alloy will affect its hysteresis, maximum strain recovery, the four transformation temperatures, Youngs Moduli of the two phases, transition stresses and maximum residual strain. All these factors affect its performance when utilizing SME or superelasticity. Below is a brief overview of the base-alloy types of SMAs and their properties.

Different Base Alloys

Besides the variation within one base alloy, there are also vast differences with other base alloys of SMA. Their selection for an actuator depends on the suitability of their transition temperatures, hysteresis and the Young's Modulus of the two states. Some notable examples are Fe-Mn-Si, which has an austenite Young's Modulus that is around double that of typical nitinol (Lecce 2015, p23), In-ti, which has a hysteresis of just 4°C compared to the 30°C of nitinol and Ag-Cd, which has its transition temperatures between -190 and -50°C.

Of all the base alloy types, Nitinol generally has the greatest strain recovery and has excellent corrosion resistance. It also has a very high recovery stress, at up to 800 Mpa. It is by far the most widely used in commercial and academic pursuits. Typical values for nitinol properties are given below. It must be stated that some parameters can vary by a great degree, so should only be used as a rough guide for what to expect.

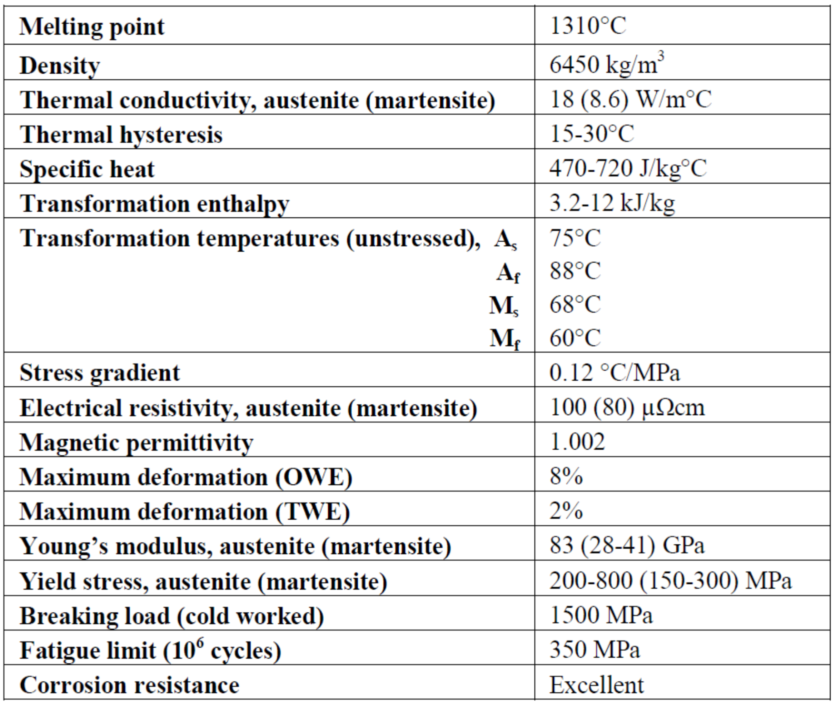

Melting point	1310°C
Density	6450 kg/m^3
Thermal conductivity, austenite (martensite)	18 (8.6) W/m°C
Thermal hysteresis	15-30°C
Specific heat	470-720 J/kg°C
Transformation enthalpy	3.2-12 kJ/kg
Transformation temperatures (unstressed), A_s	75°C
A_f	88°C
M_s	68°C
M_f	60°C
Stress gradient	0.12 °C/MPa
Electrical resistivity, austenite (martensite)	100 (80) μΩcm
Magnetic permittivity	1.002
Maximum deformation (OWE)	8%
Maximum deformation (TWE)	2%
Young's modulus, austenite (martensite)	83 (28-41) GPa
Yield stress, austenite (martensite)	200-800 (150-300) MPa
Breaking load (cold worked)	1500 MPa
Fatigue limit (10^6 cycles)	350 MPa
Corrosion resistance	Excellent

Figure 48: typical nitinol properties from (Cianchetti 2013)

Applications

Commercially Successful

The SME and superelastic abilities of SMAs allow them to be applied in different ways. By having it recover its shape so that it bears a clamping force on two other parts, it can be used as a permanent connection device. This means its SME is activated just once in the life of the product. Its superelastic effect makes it a good dampener, which finds use in large static structures subjected to vibrations.

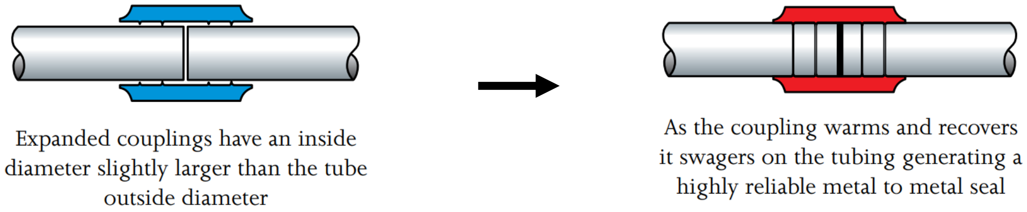

Figure 49: SMA cylinder being used as a pipe coupling, martensite and austenite in blue and red respectively

The gold-based SMA, Au-Cd, was the first to be discovered and it is used for jewellery and dental applications. Copper-based alloys are cheap, due to their inexpensive constituent metals, and used for seismic attenuation devices, dampeners in civil structures, reinforcement, connectors, thermal actuators, sensing systems and safety valves. Nitinol, Ni-Ti, has the highest recoverable strain of them all, which along with its biocompatibility and excellent corrosion resistance makes it a great material for medical applications such as stents and orthodontics wires placed into the mouth. In the medical industry, cost is less of a limiting factor due to the very small amounts of material required.

Nitinol is also used as pipe couplings, electrical connectors and micro-actuators to a lesser extent. The pipe coupling found great success in the F-14 Tomcat fighter jet of the US Navy and is now commonplace in aerospace connections as *Cryofit*. An estimated 300,000 couplings have been installed with virtually zero failure rate (Intrinsic Devices Incorporated). Iron-based SMAs are normally used as a one-time SME connection and the transition temperatures often starts at 50°C and ends at variable temperatures of hundreds of degrees Celsius higher, making it impractical for fast-acting actuators. They are however particularly useful as a one-time SME connector help negate inaccuracies of the construction (reducing gaps between elements), and for the superelastic effect ensure a connection resistant to gradual migrations due to vibration. In this regard, it can be useful for fishplates for train tracks and for the tracks of large overhead cranes in factories (Tsujimoto et al., 2017). The iron-based alloy is suitable due to two properties: structural performances similar to steel and low cost (Lecce & Concilio, 2014).

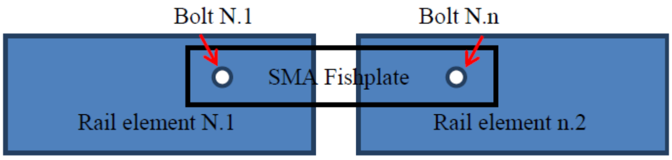

Figure 50:Diagram of SMA fishplate for rail elements, a large-scale use of the iron-based alloy type (Lecce & Concilio, 2014, p. 17)

In Architecture and Civil Engineering

Besides the SMA projects mentioned in the adaptronic Reference projects, some SMA architectural designs have been explored before. In *Pixelskin02*, electrically heated SMA wires are used to animate small tiles for a façade, which are computer-controlled and can behave like pixels to depict an image on a façade (Anshuman, 2009).

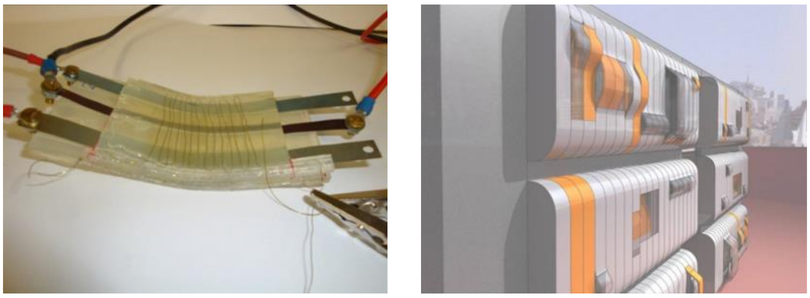

Figure 51: SMA-SMP smart composite, able to move when electrically heated and return back when cooled (Lelieveld & Jansen, 2014)

(Lelieveld & Jansen, 2014) studied the dynamic performance of a composite furniture and façade material, made of SMA strips embedded along with heating wires within a Shape Memory Polymer matrix. In its cold state, it appeared as a flat polymer panel, and when heated two things would happen: the martensite would transition to austenite and remember its non-flat shape, and the polymer would soften and lose its rigidity, thereby allowing the composite structure to assume a new position. The polymer returns the element back to its original shape when cooled.

SMA was first used as post-tensioning for a cracked concrete structure for shear-failing highway bridge in Michigan, USA. Several SMA rods of 10.4mm diameter were attached to span the crack across the webs and then electrically heated to 300ºC to activate it, thereby reducing the crack width by 40% (Soroushian, Ostowari, Nossoni, & Chowdhury, 2001). Similar projects have been implemented in historical buildings to either repair or increase the strength of the construction fabric, especially against seismic threat (Indirli & Castellano, 2008), (Indirli, Castellano, Clemente, & Martelli, 2001).

SMAs can be used to effectively counter vibrations and earthquakes in two ways: firstly as a dampener due the superelasticity in the austenitic phase, secondly as a martensite connection able to self-heal via SME. The detail of Figure 52 incorporates SMA tendons that are in their martensitic phase. The connection exhibits large energy dissipation and ductility capacity. It can also be heated and thereby self-healed after deformations and can undergo repeated performance (Ocel et al., 2004).

In (Sawaguchi et al., 2005), SME is compared with steel when used as reinforcement bar in mortar beams, to assess bending strength in very high temperatures. It showed about 33% improvement, showing great potential for fire performance as seen in Figure 53.

In (Perreux & Lexcellent, 1999), a smart beam of variable bending stiffness is developed by using a special cross-section with a horizontal SMA member incorporated. When activated, it causes the stiff members to pull together and achieve a greater beam height.

Various authors have studied the use of SMA as the actuator within a dynamic linear structure to move like an octopus arm, for instance a smart truss (Lecce 2015, p115), (Sofla, Elzey, & Wadley, 2008), (Elzey, Sofla, & Wadley, 2005).

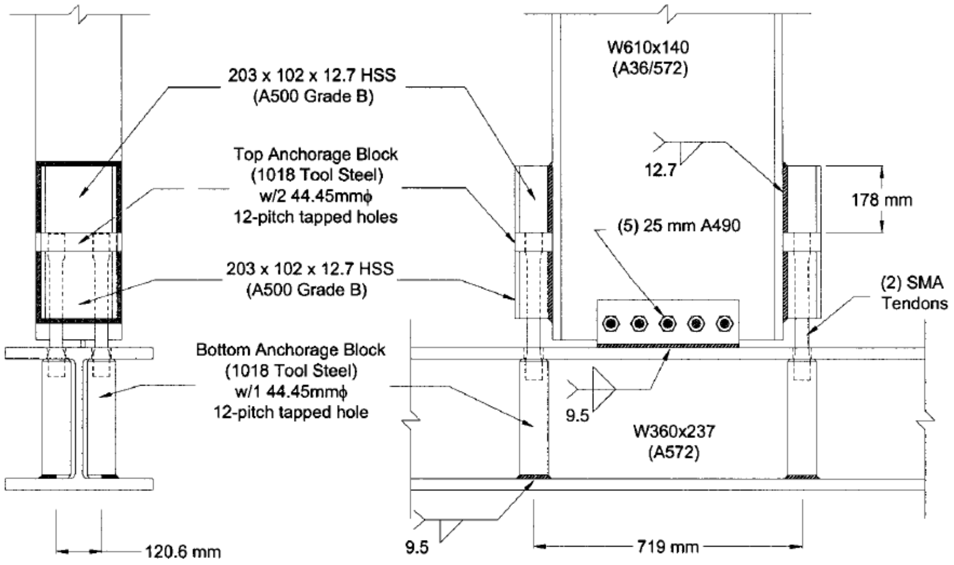

Figure 52: Detail of a column-on-beam connection with martensite SMA tendons, able to self-heal. Image from (Ocel, 2014)

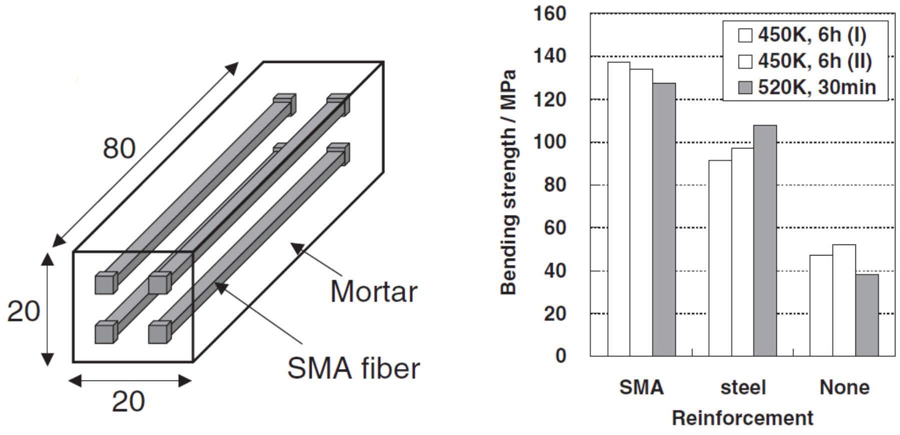

Figure 53: bending strengths of mortar specimens reinforced with special Fe-Mn-Si-based SMAs outperform that of steel-reinforced mortar at high temperatures (Sawaguchi et al., 2005)

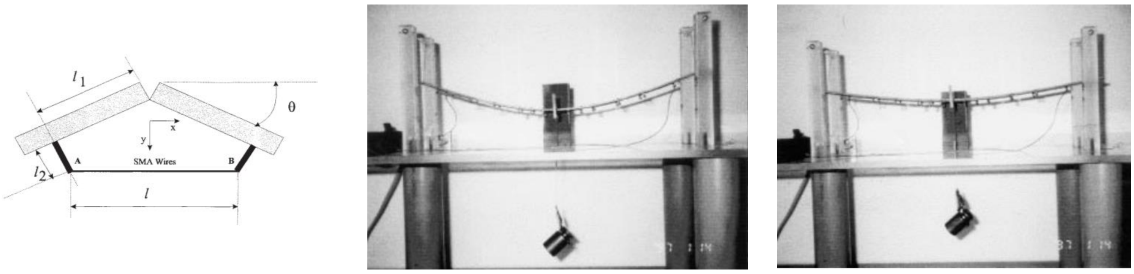

Figure 54:an adaptive beam is able to have variable bending stiffness based on the cross section design (Perreux & Lexcellent, 1999)

Other Applications

Besides the examples already mentioned in the adaptronics references, here are some selected applications to show the range of potentials of the material. There has been much interest for use as SMAs to design micro-actuators in the robotics, aerospace and general vehicular industries. Many studies concern the building of an aerofoil, hydrofoil or a flexible controllable wing, which will be mentioned in the Introduction of Chapter 4. SMA actuators, which may be as simple as a linear element, bias spring and three points of connection, are favourable compared to the heavy, space-intensive and complex hardware of electronic linear actuators.

The seventh-generation Chevrolett Corvette of 2014 featured a shape memory alloy-actuated vent which opened and closed to relieve air pressure and allow the trunk to be opened and closed more easily. The wire actuator was 0.5 kilograms lighter than the conventional motorized alternative. It was planned to be the first of many SMA technologies to be implemented by the manufacturer GM, after investing in 247 patents on smart materials (GM, 2013).

Figure 55: A wheel made of SMA, designed to be used in the austenite phase to traverse a range of alien terrains (NASA)

The material finds much interest along the cutting edge of innovation. NASA has developed a wheel made of SMA 'chainmail', which is able to absorb deformations on harsh bumpy terrains via the superelastic effect in the austenite phase (ASM International, 2017). The product is lightweight, chemically durable and likely has the ability to greatly compact itself for efficient storage.

In a different project, NASA also developed an SMA-based tool for rock-splitting in excavation. It is used by placing a large martensite SMA element into a predrilled hole and heating it into austenite to change the shape and exert enormous stresses exceeding 1.5GPa into the surrounding material (NASA, 2015).

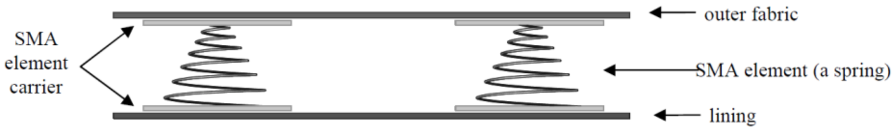

Figure 56:Firefighting protective clothing. Two layers of fabric separate in high temperatures

(Bartkowiak & Dąbrowska, 2016) developed adaptive clothing for firefighting protection. SMA springs are placed between two layers of fabric which are flat when the clothing is inactive. When activated by heat, the SMAs push the meta-aramide fabric layers apart to form a cavity of up to 24mm, thereby increasing insulation and fire protection.

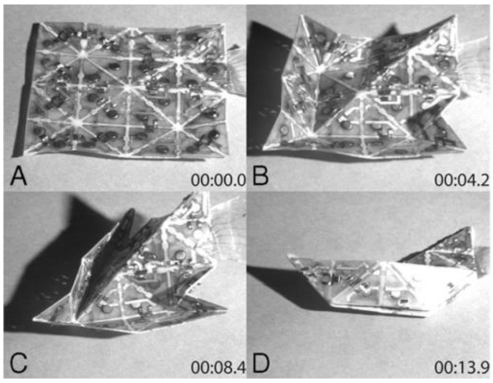

Figure 57: Using SMA smart hinges to programme a shape into a flat object (Hawkes et al., 2010)

(Hawkes et al., 2010) investigated the use of SMA smart hinges to programme a remembered shape into a flat origami-like construction. Each hinge is designed and positioned along predetermined fold-lines of the structure so that heating them would result in the entre structure assuming a desired shape.

Practical Considerations

Manufacture

A wide range manufacturing processing and consequences can govern the choice of SMA: cold and hot forming abilities, machinability, material cost, the range of the 4 transformation temperatures, phase at room temperature, hysteresis, corrosion resistance, recoverable strain, stress at recoverable strain, maximum loading cycles and required training to stabilise properties. The manufacturing for this section will focus on nitinol production.

Vacuum induction melting (VIM) and Vacuum Consumable Arc Melting (VAR) are the primary methods of manufacture for Nitinol. The vacuum is necessary because of the tendency of oxygen to contaminate the mixture of nickel and titanium. The alloy has a melting point of 1280-1330°C. As mentioned earlier, small differences in atomic composition have a profound effect on the transition temperatures. If the mixture is kept below 1450°C when using a graphite crucible, carbon contamination can be avoided and the transition temperatures controlled to within 5^{0}C. The nitinol can be hot worked at an optimum of 800°C, but higher temperatures can result in oxidation. (Wu, 2002)

The process of shaping the nitinol thereafter is a complex one, involving oxide layer removal, cycles of coldworking to around 40% and heat treatments and finally the shape setting procedure followed by surface preparation (Lecce & Concilio, 2014, p. 82). The exact details of the complex process will not be elaborated in this thesis, but for now it is sufficient to state the possibilities: the material can be shaped into bars, wires, tubes and strips. It can be mechanically cut at the cost of significant tool wear with conventional drilling, sawing and other subtractive measures. For the finer products requiring intense precision for example stents and filters, it can be laser or electro-discharge machined or photochemically etched (Wu, 2002).

Joining of SMA components

Welding of nitinol to other materials is not a good idea due to a brittle intermetallic layer. Nitinol can be welded to itself with lasers, electron beam or TIG. A novel and effective way to join Nitinol is to use its Shape Memory Effect to embrace itself into the connection. Joining with screw threads is rarely used because forming or cutting threads in the material is very difficult. Nitinol bars can be connected by bar couplers and mechanical anchors (Alam, Youssef, & Nehdi, 2010a).

For Nitinol wires, connection to an electrical wire (for applying heat) as well as a structural connection may be necessary. For this reason, various crimping techniques have been advised in (Gilbertson, 2005, pp. 2-10). Mechanical clamping, for instance with screws and bolts are also a reliable option.

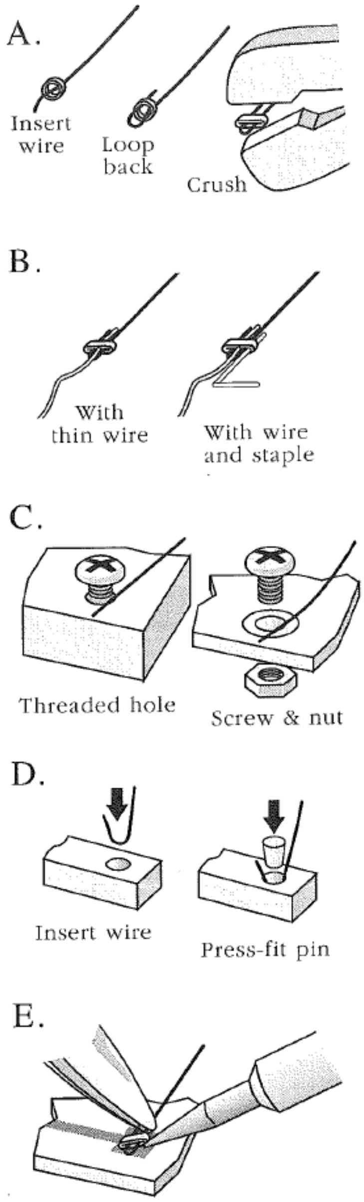

Figure 58: Various methods for connecting a nitinol wire reliably. Images from (Gilbertson, 2005, pp. 2-10)

Cost

Cost is the primary restraining factor for incorporating SMA as a structural material. However, the price of nitinol has been continuously decreasing for the last decade, at a factor of 10, to 100 USD per kg in 2010 (Alam, Youssef, & Nehdi, 2010b). Other base alloys are more promising, as iron-based SMAs are made up of cheaper element metals and can be processed without a vacuum, in normal conditions. In the future, the price is expected to rival high-alloy stainless steels, at about 8-10 EUR per kg (Czaderski et al., 2015).

Fatigue of Nitinol SMA elements

It is well known that the fatigue of SMAs are related to the strains at which they are subjected to in each cycle. At large strains, microcracks form on the surface of the material which get bigger with each cycle. According to (Gilbertson, 2005, p2-11), at the maximum strains of 8%, the material will last a few dozen cycles, but at 3-5% strain can last millions and the SMA may outlast the rest of the mechanism. This is provided the element is not over stressed or overheated. Below, (Lecce 2015) gives a rough indication of life cycle given the strain rate.

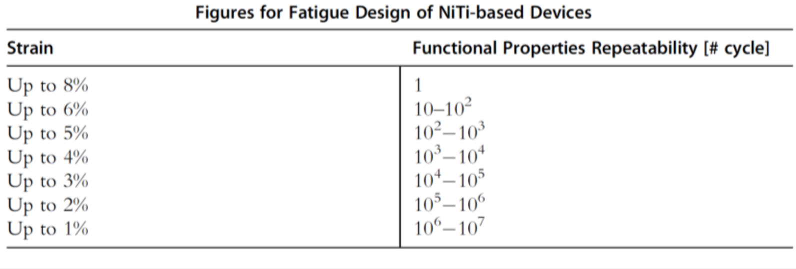

Figures for Fatigue Design of NiTi-based Devices

Strain	Functional Properties Repeatability [# cycle]
Up to 8%	1
Up to 6%	$10–10^2$
Up to 5%	$10^2–10^3$
Up to 4%	$10^3–10^4$
Up to 3%	$10^4–10^5$
Up to 2%	$10^5–10^6$
Up to 1%	$10^6–10^7$

Figure 59:Functional fatigue, which is the number of cycles before SME or the SE has functionally deteriorated (Lecce & Concilio, 2014, p. 228)

The study of (Fumagalli, Butera, & Coda, 2009) tested the fatigue of SmartFlex Nitinol (49-51% atomic) wires for different stress and strain cycles, finding that an increase to either would reduce the cycle life.

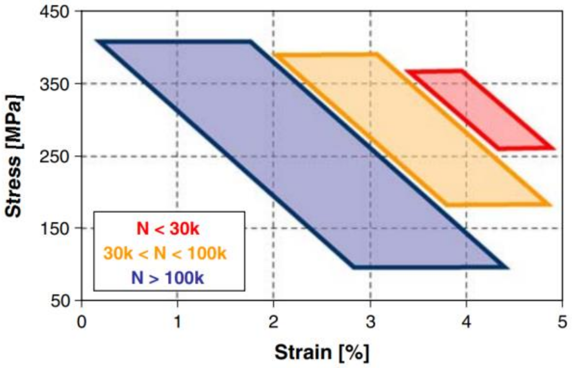

Figure 60: Fatigue life testing results for SmartFlex wires by (Fumagalli et al., 2009)

A more in-depth study is done by (Mammano & Dragoni, 2013) to assess the fatigue at different conditions, including conditions of an SMA actuator where stress is variable against displacement and also restrained below a certain percentage. This was done for a nitinol type with 54% nickel by weight. For a piece of SMA under constant stress of 200 MPa and prevented from ever exceeding 4% strain, it can be seen in the figure below that it would last over 10 000 cycles before failure by fracture.

Interestingly, the same study found that constant strain is worse for fatigue life than constant stress. In a case where an SMA rod is not allowed to contract below 4% elongation, the sample exhibited decreasing maximum stress levels for each successive cycle. The stress levels decreased by around 37% from the first cycle to the thousandth, indicating poor functional fatigue.

As always, it must be stated that different nitinol materials will have various behaviours, and lifetimes.

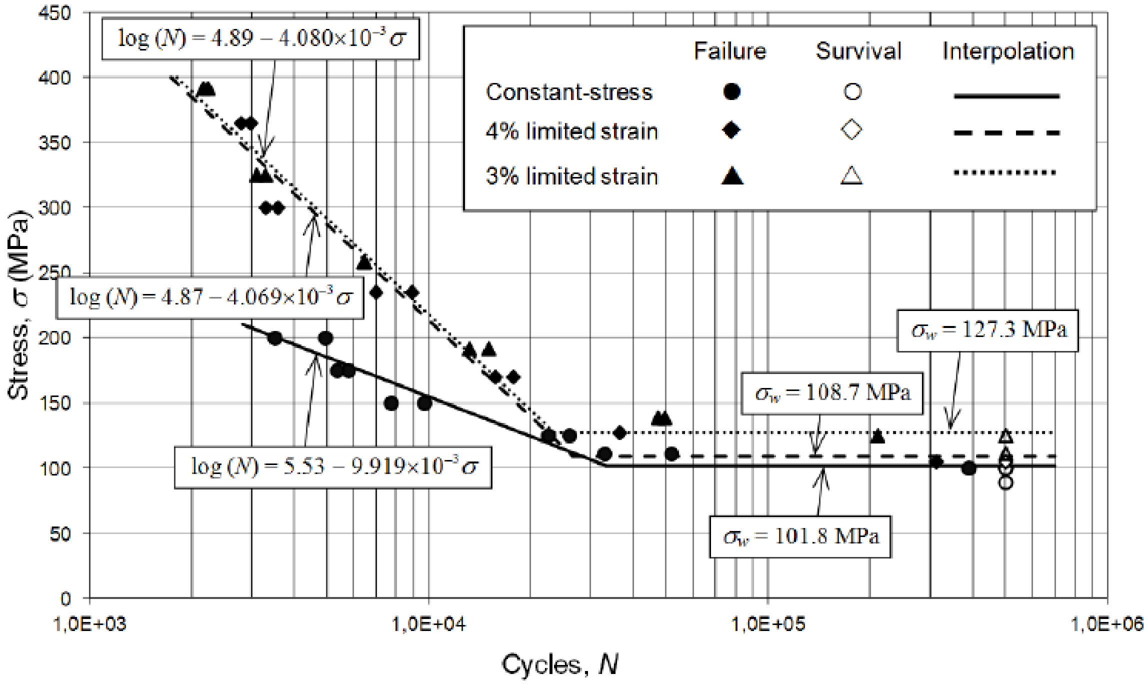

Figure 61: A graph showing how altering the constant stress will affect the fatigue. Three sets of variables: first, no limit to the strain, second with a 4% limit to the strain and third with a 3% limit to the strain. Strain was restricted by use of a mechanical stopper. Graph from (Mammano & Dragoni, 2013)

Potential as Actuators

Besides the attractive possibility of having innate adaptronic abilities of sensing and responding in the material itself, shape memory alloys are noted for their great space efficiency. The activation force can be efficiently provided through the entire cross section of a metal part with very high Young's Modulus, instead of via fluid, polymer or electromagnetics. The comparative simplicity of the constructions is also an advantage, as some designs can be as minimal as a metal piece stressed by a spring and heated by electrical wires attached at both ends. The reduction of parts and elimination of frictional sliding elements therefore make SMA actuators a potentially reliable alternative to the standard electrical variety used in applications such as motorized facades.

The logarithmic graph of (Huber, Fleck, & Ashby, 1997) shows that Shape Memory Alloys can exert great stress and strains compared to other materials and methods when employed as actuators. The only other type of actuator with comparable stress-strain performance is hydraulic, which requires space-intensive equipment and the use of moving fluids.

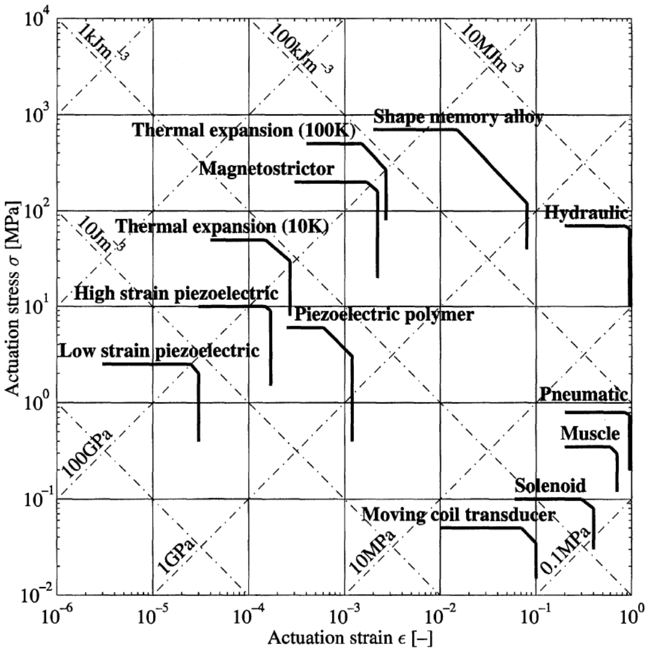

Figure 62: The limits of performance for various types of actuators, with regards stress and strain. Graph from (Huber et al., 1997)

The energy efficiency of a shape memory alloy actuator was investigated in (McCormick, 1987), which found that it was between 1.95 and 3.23% depending on heat recovery. The low number is due to the constant heat loss to the environment when the SMA is heated. This is in contrast to electric motors, which are typically above 75% and can be close to 100% in the right conditions (U.S. Department of Energy). Another limitation to SMAs actuators is the time taken to achieve a change; since it relies on heating and cooling of a solid object, the response time would be proportional to the volume of the material. Robotic actuators with large force requirements therefore design bundles of thin SMA wires in order to minimise the heating and cooling times of the element as a whole.

Summary

The macroscopic behaviour of SMA is very peculiar compared to standard materials. They have two main states which have their own set of properties and are highly configurable with atomic composition and processing technique.

Commercially successful SMAs are used largely as a connecting piece, which utilize the SME once in the life of the product, to achieve a tight fit with other components. They also show great potential as a 'static' damping device in structures because their superelastic properties can absorb vibrations. They are able to offer other forms of protection, such as a beam fitted with SMA material which gets activated in extremely hot temperatures, resulting in beams that last longer in fires. Valves can be used in the nozzles of temperature-regulating devices such as air conditioning, and adaptive clothing has also been produced.

Dynamic systems with structurally utilized SMA are already being designed in the Aerospace industry, which has a demand for shape-changing aerofoils and chevrons without excessive complex or expensive hardware. Many adaptronic devices utilize an antagonistic structure (for example a bias spring) to bring the SMA back into its cold position, which is preferable to Two-way SMA devices, which exhibit reduced strain recovery and forces.

There are not many examples of SMAs being used structurally in architecture, especially not for actuating the exterior skin; most of the work is still in the research stage, and the few built examples tend to be non-structural shading devices and installations. Compared to electronic actuators, SMAs have a very great force-to-weight ratio, low power efficiency and short stroke length. All these parameters can be tweaked or compensated to an extent by modifying the material or design. For an adaptronic device, the power efficiency does not need to be considered because it is powered by the environment.

To design an adaptronic structure would require great understanding of its precise behaviour, as it will interact greatly with the surrounding structure of the device. The strain-stress-temperature field of Figure 44 is a 3D representation of the properties of the material, and is a useful way to visualise the concept of the movements. To start off the design process, some key numerical data from literature can be used to build an animated facade model. In the later stages some first-hand experimentation will be necessary to characterise the physical movements of the SMA.

Nitinol seems to be the most viable type of SMA to use for adaptronics due to its high stress recovery percentage, large number of loading cycles without failure, availability as martensite at room temperature, excellent corrosion resistance and its convenient transformation temperatures that are in the region of ambient air temperatures. They can potentially actuate with a life cycle of millions, if it is not overstrained, overstressed or overheated. Some disadvantages however are its cost of material and its difficult workability in terms of machining and traditional forming. These disadvantages can be overcome, as the price of all SMAs have been rapidly falling for the past two decades due to innovation and increased production volumes. The shape of the SMA element does not need to be complex for the device, and even if it does, it is possible to deform and train it into the desired shape. Notably, SMAs have low power-efficiency and take more time to activate, but these will not be an issue because the adaptronic device will be powered by the environment and it does not need a rapid response to the gradual environmental changes.

It is clear that SMAs require high quality control to ensure a useful set of transformation temperatures. It would be necessary to test the material if it arrives from an external manufacturer, as small changes to the composition of half a percent can change the transition temperatures by a hundred degrees Celsius. Training is necessary to stabilise the hysteresis loops in the stress-temperature behaviour before testing is done. The key variables to find out are the 4 transition temperatures of the M_s, M_f, A_s and A_f, but there are likely some more depending on the ideal modelling technique, as will be seen in Chapter4.

4. Modelling the mechanical behaviour of SMAs

Introduction

The most commercially successful SMA applications tend not to utilize the full potential of their actuator abilities. Those that have been developed until now are either binary (on-off) actuators or are intended to be actuated just once in their lifetime. For example, the pipe coupler connector and medical stent is activated just once at the start of its life, and an orthodontics wire can be activated when positioned into the mouth and cooled down for removal (Lecce & Concilio, 2014, p. 20). None of these applications require precise control of temperature mechanics of the material, and so they do not exploit the potentials for a responsive device.

On the other hand, the world of SMA does not lack ideas: there have been over 10 000 patents for SMA products in the United States, but there is a serious problem in getting products to market for the vast majority of them (Mohd Jani, Leary, Subic, & Gibson, 2014). This has been attributed to a strong focus on metallurgical properties and not so much on the design perspective; a closer collaboration between material scientists and the designers is needed, given the difficulty for designers to grasp the complexity of the material behaviour. (Mohd Jani, 2016) identifies the lack of ‘method’ as one of three categories of limitation towards SMA commercialisation: there are a lack of models that are compatible with computer-based design and analysis methods, which are essential to the SMA design process. This introduction will briefly review the past actuator projects and some computational strategies in literature.

Besides a notable exception of (Hartl, Lagoudas, Calkins, & Mabe, 2010), which places its SMA at the exhaust of a jet engine and therefore can be heated by the ‘environment’, virtually all projects use electrical resistive heating to activate the SMA. Since the first attempts at SMA actuators, control of the position has been done via a feedback loop which measures the displacement and adjusts the electrical current through the SMA accordingly (Honma, Miwa, & Iguchi, 1984), (W. Huang, 1998), (Drossel et al., 2015).

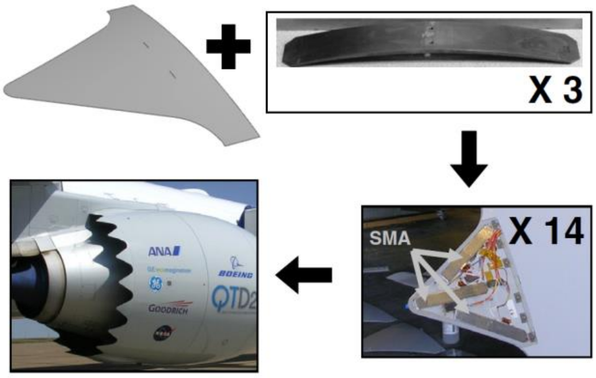

Figure 63: The triangular flaps are active jet engine chevrons, designed to reduce noise during take-off and maintain efficiency during cruising (Hartl et al., 2010)

It should be noted that in most designs, the goal is generally to produce an actuator capable of human control. A convenient way to do this with SMAs is to to make the actuator binary, as it will certainly be in either one of two positions, each position achieved by making the SMA either fully austenite or fully martensite; anything in between is not an intended setting for the purposes of the actuator. The design questions for such projects are therefore partially focused on electrical efficiency (the minimum current needed to fully activate), time-sensitive thermodynamics (the time taken to activate) and geometric optimization. Examples seen in (Garner, Wilson, Lagoudas, & Rediniotis, 2000), (Hartl et al., 2010), (Spaggiari, Scirè Mammano, & Dragoni, 2012). Figure 64 shows the remarkable design for a hydrofoil of (Rediniotis, Wilson, Lagoudas, & Khan, 2002), which is made up of SMA actuator ribs attached in series, each with its own independent electrical signal.

This gives the whole structure the ability to make wavy motions like the body of a fish, as well as to perform other functional manoeuvres using individually binaray actuators. The strategy of binary movement is however not compatible with the requirements of an adaptronic device, which is fundamentally out of human control, as it is governed by environmental stimuli. Adaptronic devices therefore demand an accurate mapping between environmental variable and response; in this case it is between temperature and strain, and the history of the temperature is necessary for a correct mapping.

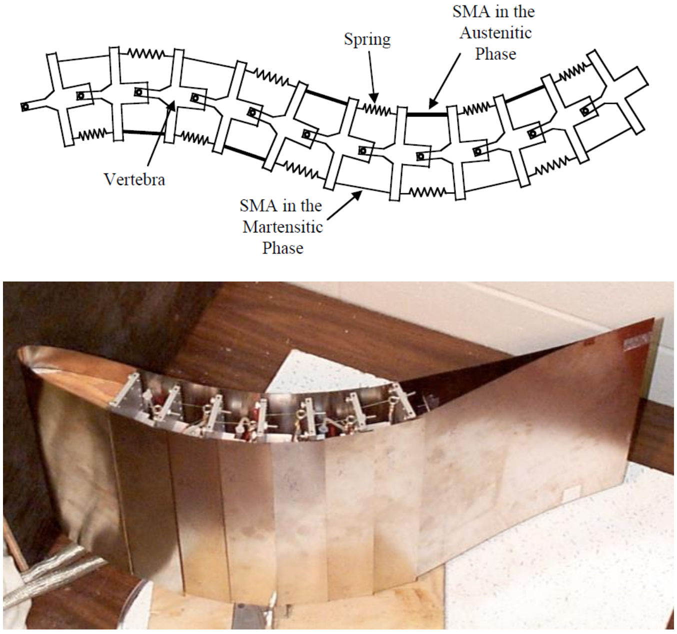

Figure 64: A hydrofoil with independently-activated SMA-based ribs (Rediniotis et al., 2002)

The numerical implementation of the constitutive SMA models plus the overall FEM of the holistic structure tend to be done on specialised engineering tools, sometimes requiring an external input to express the duality and fluctuating properties of the SMA. In many cases, SMA is not available as a material in the native inventory of the software. (Lecce & Concilio, 2014, p. 193) gives an overview of some commercial programs, such as COMSOL Multiphysics, ANSYS and Abaqus, which all have highly useful integrated tools for calculating electrical and thermodynamic aspects, but generally only the superelastic behaviour is implemented. MSC.Marc is a module for MSC.Nastran, the most popular aerospace tool for FEM; the former is useful for applying advanced non-linear simulations, and has implemented the shape memory effect within the latter. Individual authors have used MATLAB (Basaeri, Yousefi-Koma, Zakerzadeh, & Mohtasebi, 2014), Wolfram Mathematica (Drossel et al., 2015) and a combination of MATLAB feeding the material parameter data into COMSOL Multiphysics (Barbarino, Ameduri, Lecce, & Concilio, 2008).

Overall, there is a significant barrier to design for any adaptronic project, as the literature suggests that tracking the dynamics of SMA vs temperature will be a daunting task requiring great theoretical focus and deep understanding of material science. The computational model and design tool to be produced for this thesis therefore fills a void, as it is intended as a user-friendly toolbox for designers without specialist engineering knowledge, thereby removing a major bottleneck when delivering structurally, dynamically stable adaptronic systems. It will describe the dynamics of an SMA structure based on temperature as a variable input, taking history of the temperature into account to model the hysteresis. The scripting software will be Grasshopper, a plug-in of Rhino 3D, which will make it accessible to many designers who do not have an in-depth engineering background. It is a popular software for architects and product designers. With adequate weather data, it would be possible to get an idea of the status of the openable window, and thereby adjust the design accordingly for sustainable benefit.

Uniaxial SMA behavioural models

The complexities of hysteresis, inter-dependent and stimuli-based parameters, nonlinear behaviour, the time-dependency of the dynamics, inconsistencies in cyclic loading and the fact that material properties are profoundly different for small changes of atomic composition, make for a formidable challenge when it comes to the mathematical modelling of SMA. For many decades, various authors have produced constitutive models to describe and predict a type of material which evades the classical stress-strain relationship that underpins conventional structural design.

Recent overviews of SMA modelling methods can be seen in (Paiva, Savi, Braga, & Pacheco, 2005), (Khandelwal & Buravalla, 2010) and (Lobo, Almeida, & Guerreiro, 2015). Ultimately, the foundations of most models are theories and observations at the micro-level, where atoms and crystal structures shift and slide against each other. Under new temperature-stress-energy conditions, the alloy matrix rearranges itself into whatever is the most stable configuration. The hysteresis can be explained by the temperature-dependent Gibbs free energy of the two phases, which near the transition temperatures is a similar value, but they deviate sufficiently at temperatures below M_f or above A_s so that one phase becomes far more stable than the (Daghia, 2008).

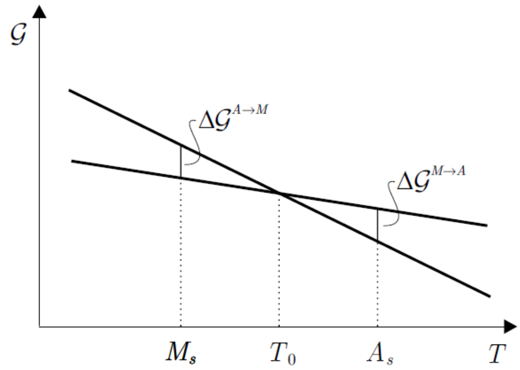

Figure 65: The Gibbs free energy of austenite and martensite as the temperature changes. Graph from (Daghia, 2008)

Different models therefore deal with a variety of parameters and sciences whilst drawing its theory from a range of scales: thermodynamics, crystallographic conditions and atomic structures, free energy and energy dissipation formulations, phase boundary motion and finally macroscopic phenomenological behaviour. The last category are the most favoured by engineers in practice, as they do not involve parameters which are unseen or difficult to measure. The most important parameters here are stress, temperature and martensite fraction, with the latter often being a function of the first two. Overall, these variables are quite convenient for actuator design, as it is easy to translate them into the useful answers of strain and force.

The majority of simulations done in literature concern uniaxial rod and bar SMA elements, which can involve much simpler one-dimensional models rather than three-dimensional (Lobo et al., 2015). The 1-D models available have been well developed to adequately describe all the special phenomena of SMAs, particularly the three that are important for this study: the pseudoelastic effect, shape memory effect and hysteresis.[13]

---

[13] Note that the models generally do not cover the Two-Way Shape Memory Effect, which is not favoured in most actuator designs for a number of reasons, despite the benefit of not having to provide a bias force in the adaptronic device. Although many models exist for the TWSME, they are more complex; they also require a training procedure to 'teach' the SMA the cold shape, and this procedure is itself an area of study; on a practical aspect, the recoverable strain is lower, in the region of 2%, the transformation forces upon cooling are much weaker, causing asymmetry in the push and pull forces of the actuator, the number of cycles before functional failure are much lower and more care needs to be taken to prevent over-heating which will damage the TWSME (Zanaboni, 2008), (Luo & Abel, 2007b).

For this reason, a simple linear SMA element has been chosen as the 'engine' of the actuator and will be the focus of the study.

We will now have a brief summary of the evolution of a commonly used 1D model which is built upon the work of various successive authors. (Tanaka & Nagaki, 1982) introduced the concept of martensite fraction, an internal state variable to describe how much of the shape memory alloy is in the martensite phase: a fully austenite SMA would have a value of 0, a fully martensite 1, and all numbers in between denote a combination of the two. With this, a schematic for determining the martensite fraction based on temperature and stress is drawn up within the *phase transformation kinetics framework*, illustrated in Figure 66.

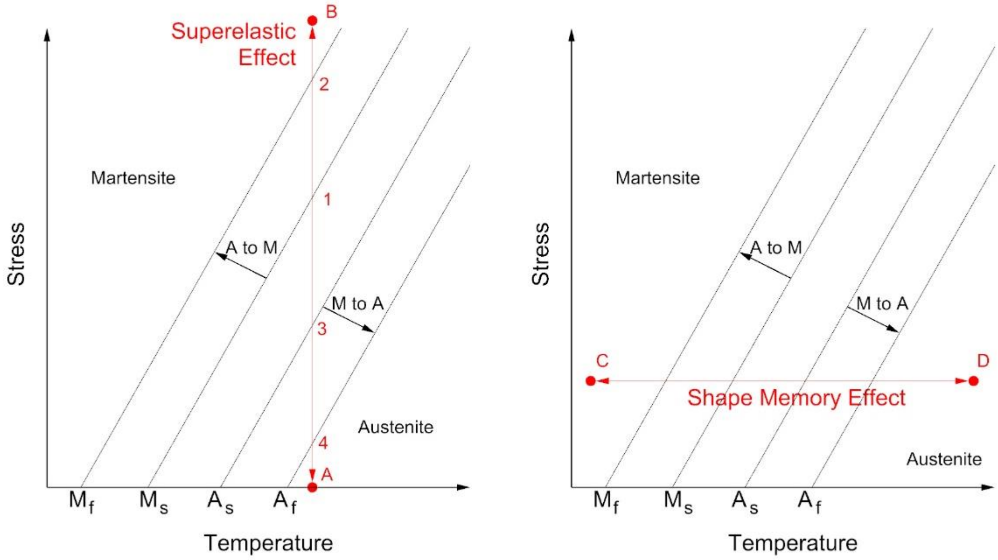

Figure 66: Phase diagrams. a) the Superelastic Effect: an SMA piece starts off at a temperature above Af and is mechanically loaded until it becomes martensitic. B) the Shape Memory Effect, showing the SMA under constant stress being heated to austenite.

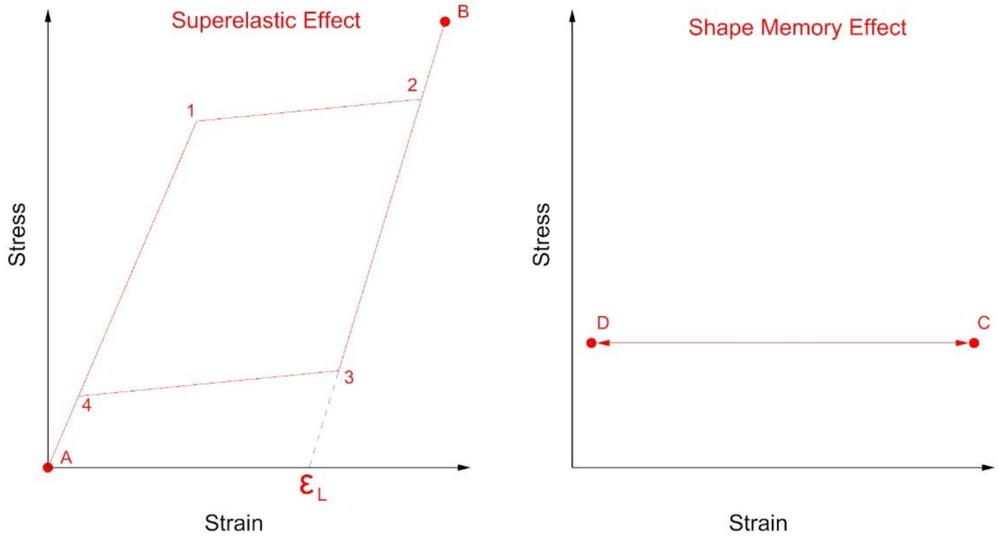

Figure 67: The corresponding stress-strain graphs that result from Figure 66. Notice the points 1, 2, 3 and 4 in the left graphs

Regions of the phase diagram in Figure 66 are bounded by four lines. All temperature-stress points in the far left region denote the conditions where only the martensite phase is stable, whilst the region at the far right is where only austenite is stable. All regions in between may be a pure phase or a combination of the two, depending on temperature history. Note that different SMAs, and different atomic compositions of the same type of SMA, will have very different values of M_f, M_s, A_s and A_f, which are the familiar transition temperatures mentioned in the previous chapter. The two main phenomena of superelasticity/pseudoelasticity and Shape memory Effect is shown.

Regarding superelasticity in Figure 66a and Figure 67a, the material is kept at constant temperature above A_f. Starting at point A, the SMA is mechanically loaded, and so rises up in the graph, remaining fully austenite, until it hits the M_s curve at point 1. It then gradually transitions to martensite as it traverses the zone from point 1 to the M_f line at point 2. At point 2, the material has reached 100% martensite and is loaded further with no change to the fraction, until it reaches point B. On the way back from B to A, the material remains fully martensite until it touches the A_s curve at point 3 and the reverse transition happens between the A_s and A_f curve, becoming fully austenite again at point 4.

The Shape Memory Effect is shown in the graphs on the right, which exhibits a similar behaviour. It can therefore be seen that the interesting phenomena of SMAs are due to these special transition zones. It is only during the transitions that the martensite fraction changes, where the material ceases to behave as a classical material, exhibiting very shallow gradients on the stress-strain curve for a portion of the loading.

The phase diagram explains the phenomena of different temperature transitions when stress-loading, as well as different stress transitions when temperature-loading; moving the vertical line in Figure 66a or the horizontal line in Figure 66b changes the critical points of transition. The gradients of the four curves are the key factors for these phenomena, and so two additional parameters enter the model: C_a and C_m, known as the *stress influence coefficients*. Bear in mind that like all materials, very high values of stress will cause permanent plastic deformation of the material which can't be recovered. This includes the austenite state, which would normally enter martensite recoverable strain phase before reaching a stress yield limit. This stress limit decreases with increasing temperature, and a high enough temperature will mean that the austenite will plastically deform upon mechanical loading first, instead of transition. The exact relationship between temperature and non-recoverable plastic yield is not widely published, but (Ford & White, 1996) suggests that even a 20°C increase from the Austenite finish temperature can effectively close the gap between martensite transition and plastic yield.[14] SMA devices tend to keep the material stresses to the minimum functional level, and to find the least power to activate the SME, so tend not to focus on this upper bound. However, it is something to be aware of.

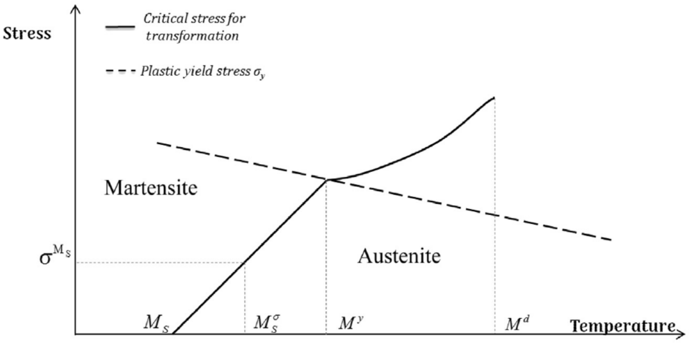

Figure 68: The non-recoverable yield stress of nitinol as a function of temperature as shown in the dashed line. The M_s curve is shown as comparison, to show how an SMA being cooled will increase its plastic yield stress (Aeby-Gautier & Patoor, 1997). Graph from (Lecce & Concilio, 2014, p. 37)

---

[14] For Nitinol of 55% nickel and 45% titanium, 55Ni45Ti, supplied by U.S. Nitonol. A_s at 27°C and A_f at °C

Elaboration of The Phase Diagram

There are some complexities which are not resolved by the version of the phase diagram in Figure 67. (Liang & Rogers, 1990) made a valuable contribution to the constitutive modelling by applying a cosine function to the transition rates; the journeys from points 1 to 2 and 3 to 4 in Figure 67 are in fact nonlinear.

Recall the classic SME demonstration of an SMA element being deformed and then heated at zero stress to recover the deformation, as in Figure 69 with the three successive steps. Its starting condition is zero stress, temperature below M_f, which in the phase diagram of Figure 66a would be a point on the temperature axis between the origin and Mf. The point would rise and then fall as the stress is temporarily applied to achieve the deformation as shown in step 1. According to the phase diagram discussed, there should be no change to the material state, yet it can be seen that the SMA before and after step 1 in Figure 69 has undergone some kind of stress-induced rearrangement on the atomic or crystal level, because both are at zero stress and the same temperature, and they have a different length. A close look under the Transmission Electron Microscope reveals that some change does indeed occur which is not reversed upon removal of the load, as shown in Figure 70. This is the transition from the twinned martensite state and the detwinned martensite state; this makes three phases in total. Differentiating the two sub-phases is necessary to describe the first step of the SME in Figure 69, and so some models have two separate values to quantify the amount of detwinned martensite and twinned martensite.

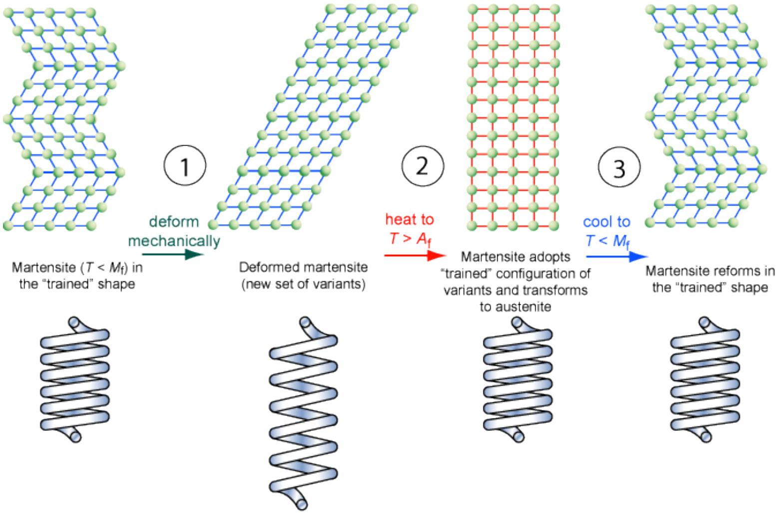

Figure 69: the classic Shape Memory Effect demonstration

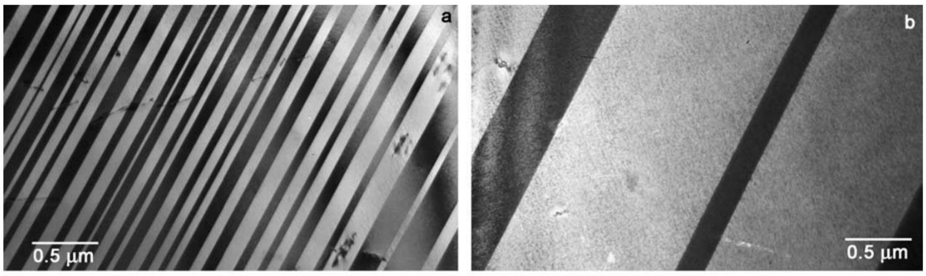

Figure 70: The surface microstructure of martensite before and after a 4% strain (Chernenko, Pons, Cesari, & Zasimchuk, 2004)

In the landmark paper of (Brinson, 1993), two variables of Temperature-induced martensite (twinned) and Stress-induced (detwinned) martensite were presented, along with two more values of start and finish critical stresses, σ_s and σ_f, to denote the transition zone from twinned martensite to detwinned. With this modification, the Shape Memory Effect can be mathematically described even at low temperatures; the new phase diagram is shown below. Also note the nature of thermal martensite production at low stress.

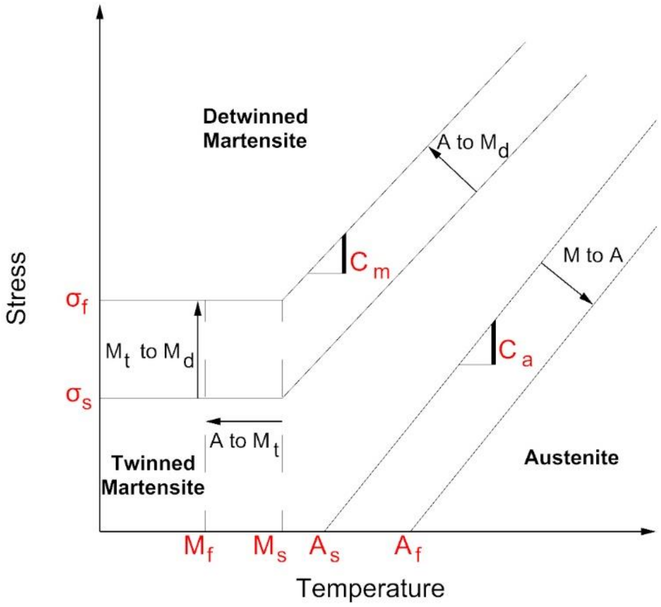

Figure 71: The phase diagram introduced by (Brinson, 1993), which incorporates the concept of two martensite phases.

In all phase diagrams, it is important to remember that the four possible transition zones shown above are all 'one-way streets'. For example, an SMA being cooled (instead of heated) through the A_f-A_s zone or being unloaded (instead of loaded) through the σ_f-σ_s will not undergo any phase change. Furthermore, a partial transition followed by a reversal of loading will mean that the martensite fraction will hit a peak/dip and then plateau as it reverses direction. For example, a fully detwinned martensite SMA being heated at constant stress so that it is halfway through the austenite transition, before being cooled down again, will have its martensite fraction decrease gradually from 1 until 0.5 after it crosses the A_s curve, and then it will remain at 0.5 as the temperature change reverses direction. If the material is cooled sufficiently so that it hits the zone of martensite transformation, it will then start to transition to martensite, but instead of going from 0 to 1 as in a complete cycle, it will go from 0.5 to 1. In this scenario, it can be seen that the 'switch point' of the temperature is a crucial parameter in the scripting of such a model: it is important for the software to 'remember' the martensite fraction at the most recent temperature switch point in order to map the future progression of martensite fraction as the temperature change continues in the same direction. Note that Brinson's model uses cosine functions for the transitions for the changes to the martensite fraction variables, as does (Liang & Rogers, 1990).

Before continuing, some limitations of Brinson's model should be mentioned. The two lines of critical stress are shown as perfectly horizontal; in practice, they actually have a slight negative gradient. The gradient is probably not linear either. The temperature transition curves are also not perfectly linear in experimental observation. Furthermore, a breakdown of the model occurs in the rectangular region of the phase diagram that has stress levels between σ_s and σ_f and temperature between M_f and M_s, when a piece of SMA at the bottom right corner of that region is being simultaneously cooled and stressed until reaching the opposite corner. Starting off at fully austenite, the model dictates that the SMA simultaneously increases both the detwinned martensite fraction as well as the twinned martensite fraction until both reach a value of 1, resulting in a total martensite fraction of 2. This is obviously not possible in reality; (Jong-Ha, Jin-Seok, & Jung-Ju, 2007) provides a set of modified equations to logically moderate the martensite fraction levels, resulting in positive experimental agreement. Another major problem is the assumption that no austenite/martensite is produced until the temperature-stress point crosses into the respective transition region. In practice, this is not true for partial cyclic loops, it would appear that the higher the presence of one phase, the earlier it would transition back in the temperature line, as seen in the experimental observations of (Müller & Seelecke, 2001), which carry out cycles of partial unloading.

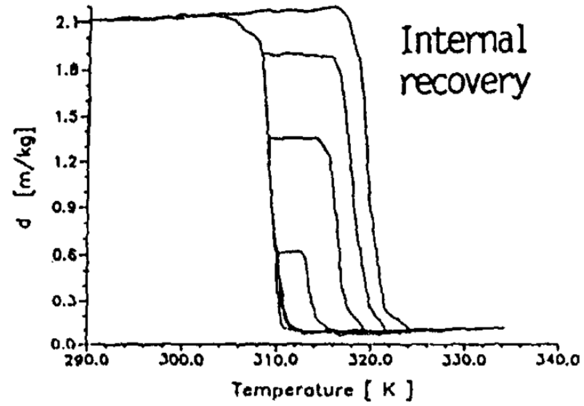

Figure 72: stress-temperature diagrams for an SMA piece under constant tensile load (Müller & Seelecke, 2001)

Despite the minor and major shortcomings, the Brinson model is able to accurately predict the behaviour of SMA, as seen below. (Sayyaadi, Zakerzadeh, & Salehi, 2012) reviews it against the Liang-Roger and Tanaka models, finding that the Brinson model has some marked advantages over the other two models, and concludes that it should be used for SMA wires, whilst (Basaeri et al., 2014) presents the Brinson as the standard model for tensile SMA wires. The model is good enough for most applications has become the backbone of many projects and papers to this day; the next chapter will implement the Brinson model in Rhino and Grasshopper.

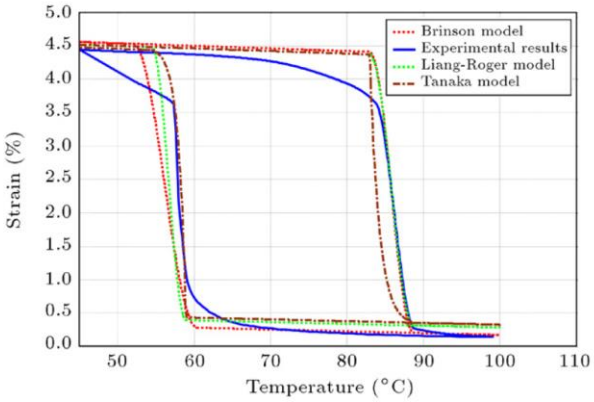

Figure 73: A comparison of the three widely-used 1D SMA models against experimental data, for an isostress test at 100 MPa, $\sigma > \sigma_f$ from (Sayyaadi et al., 2012)

Mechanics of the Brinson Model

In this subchapter, the variables and equations that govern the (Brinson, 1993) model that are relevant to an adaptronic SMA design are explained. It can be assumed that a portion of the phase diagram at low-stress will not be used, as the rest of the adaptronic device structure will provide an antagonistic force to keep the SMA stressed above the σ_f. As a result, the hatched part of the phase diagram in Figure 74 can be omitted from the model. Conveniently, this portion includes the flawed part of the model, in the rectangular region where stress is between σ_s and σ_f and temperature is between M_f and M_s. Furthermore, this removes any scenario of temperature-induced (twinned) martensite being present in the SMA, which simplifies the equations as only one variable of martensite fraction is used instead of two.

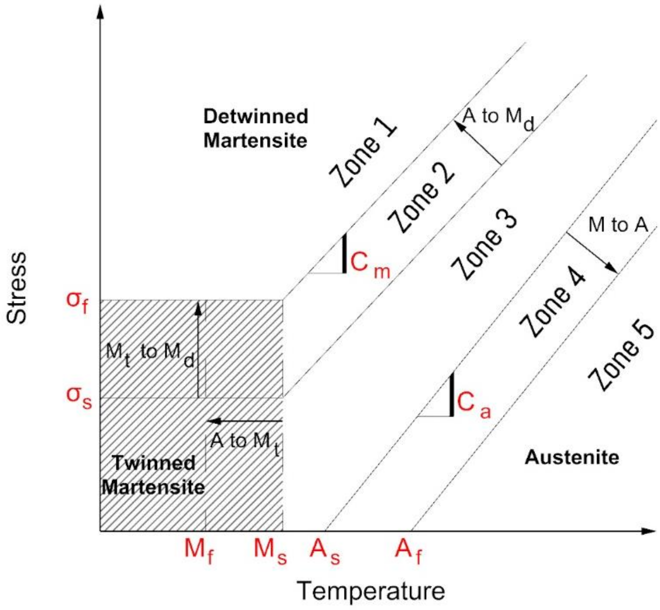

Figure 74: The hatched part of the phase diagram will not be used for this model

Since the intention is to have the SMA perform outdoors, it should be noted that negative temperatures are to be expected, and that they are compatible with the model. The σ_s and σ_f curves can be extrapolated to the left of the graph in that case.

The variables:

- SMA material properties. In practice, some of these are design variables (for example the transition temperatures) can be adjusted by changing the atomic composition of the material. If receiving the material from external manufacturers, the values should be physically tested to ensure the future predictions are matched to the particular SMA as best as possible. In total, there are 11 material properties
  - The four transition temperatures, $\boldsymbol{M_f}$, $\boldsymbol{M_s}$, $\boldsymbol{A_s}$, $\boldsymbol{A_f}$ [°C],
  - The critical stresses at which twinned martensite transitions to detwinned martensite, $\boldsymbol{\sigma_s}$ and $\boldsymbol{\sigma_f}$ [MPa]
  - The gradients of the four transition temperature lines, also known as the stress influence coefficients, $\boldsymbol{C_M}$ and $\boldsymbol{C_A}$ [MPa/°C]
  - The Austenite Young's Modulus, $\boldsymbol{D_A}$ [MPa]
  - The Martensite Young's Modulus, $\boldsymbol{D_M}$ [MPa]

    - The detwinned Martensite residual strain, which is a value to express the rest length of detwinned martensite as a proportional increase of the austenite rest length, $\boldsymbol{\varepsilon_L}$
- SMA conditions, which are the inputs that animate the model:
    - Temperature, $\boldsymbol{T}$ [°C]
    - Axial stress, $\boldsymbol{\sigma}$ [MPa]
- Variables from the model:
    - Detwinned Martensite Fraction, $\boldsymbol{\xi}$, hereafter simply referred to as martensite fraction
    - Martensite Fraction at the most recent temperature switch, $\boldsymbol{\xi_0}$
    - $\boldsymbol{a_M}$ and $\boldsymbol{a_A}$ [$^{o}C^{-1}$], which are useful terms derived from formulas (1) and (2). They will be used in some equations for convenience
    - The effective Young's Modulus of the SMA, $\boldsymbol{D(\xi)}$ [MPa], which is a function of the martensite fraction
    - The SMA strain, the main output of the model, $\boldsymbol{\varepsilon}$**.** Note that the conventional definition of strain is Δ L / L; in SMA literature, strain is Δ L divided by the length of the element at austenite phase, at zero stress, due to both mechanical and SMA phenomena. Temperature strain is generally not accounted for, as it is negligible compared to the other two components.

$$a_M = \frac{\pi}{M_s - M_f} \tag{1}$$

$$a_A = \frac{\pi}{A_f - A_s} \tag{2}$$

For the example calculations in this chapter, the following material properties will be used (Liang, 1990). In practice, these values will be found by testing the specific SMA to be used in the actuator.

$$M_f = 10, \quad M_s = 30, \quad A_s = 60, \quad A_f = 80 \quad [^{o}C]$$

$$\sigma_s = 100, \quad \sigma_f = 170 \quad [MPa] \quad C_M = 8, \quad C_A = 13.8 \quad [MPa/^{o}C]$$

$$D_A = 67\,000, \quad D_M = 26\,300 \quad [MPa]$$

$$\varepsilon_L = 0.08$$

The Equations

Martensite fraction for conversion from austenite to detwinned martensite (A to M), which is used when temperature is decreasing and the stress-temperature point is in Zone 2 as seen in Figure 74:

For $C_M(T - M_S) < \sigma < \sigma_f + C_M(T - M_S)$:

$$\xi = \frac{1 - \xi_0}{2} cos\left\{\frac{\pi}{\sigma_s - \sigma_f} \times \left[\sigma - \sigma_f - C_M(T - M_S)\right]\right\} + \frac{1 + \xi_0}{2} \tag{3}$$

Martensite fraction for conversion from detwinned martensite to austenite (M to A), which is used when temperature is increasing and the stress-temperature point is Zone 4:

For $C_A(T - A_F) < \sigma < C_A(T - A_S)$:

$$\xi = \frac{\xi_0}{2}\left\{\cos\left[a_A\left(T - A_s - \frac{\sigma}{C_A}\right)\right] + 1\right\} \tag{4}$$

With these equations in place, the effective Young's Modulus and effective rest length of the SMA can be derived via linear interpolation between the values from the two phases. It is then possible to derive the stain and current length of the SMA using standard elastic mechanical equations.

Effective Young's Modulus:

$$D(\xi) = D_A + \xi\,(D_M - D_A) \tag{5}$$

Effective rest length:

$$L(\xi) = \xi \times \varepsilon_L \tag{6}$$

Strain, which is made up of two components, that due to SME and due to elastic deformation:

$$\varepsilon = L(\xi) + \frac{\sigma}{D(\xi)} \tag{7}$$

Visualising the Progression of Martensite Fraction

As a visual example, the graphs below illustrate an SMA wire starting the scenario at ξ_0 = 0.5, occupying a point in the martensite transition zone. It likely got to this situation by being cooled down from full austenite earlier, so the scenario therefore starts at a switch point. The scenario is the SMA wire being heated through the austenite transition zone, to achieve complete austenite phase. The ξ − T curve in the middle graph shows how the martensite fraction is constant at the parts outside the transition zone. Note that the inequalities above equations (3) and (4), which are numerical formulations of Zones 2 and 4 in the phase diagram, indicate the domains in which the equation applies; outside the domain, no martensite transition occurs. The graph at the bottom shows how the strain varies with the temperature.

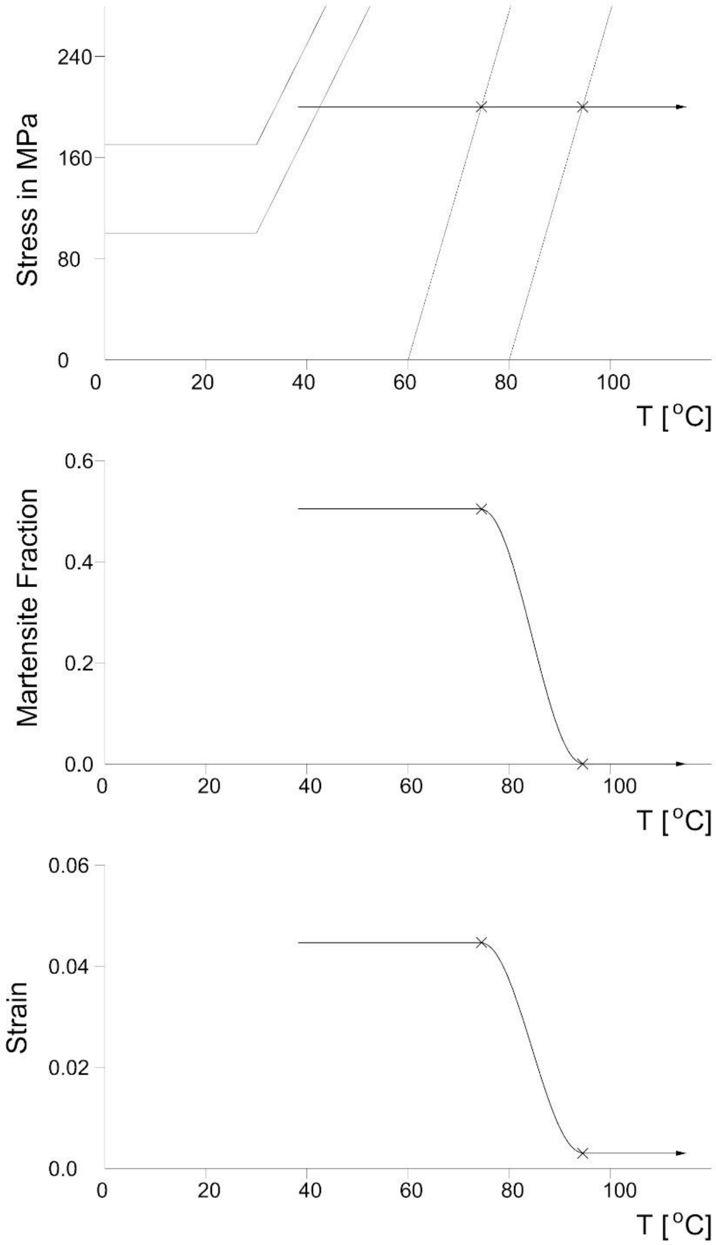

Figure 75: Example of a temperature-induced change in martensite fraction, using the Brinson equations at constant stress, $\xi_0 = 0.5$

Constructing the Solver

Goal

It is important to state the goal of the solver first:

- To take as the constant input: the description of an SMA element, as well as a description of the bias forces caused by the rest of the device structure
- To take variable input: the temperature of the environment/SMA.
- To output: the strain or change in length of the SMA at the prescribed temperature
- Additional output information would be helpful, to describe the current parameters of the SMA and status of the actuator, as well as the 3D graph to show the progression of transformation

Strategy for solver

A common approach to find the position of an SMA actuator is to use a force-strain graph to compare the two curves of the martensite and austenite-phased SMA to the curve of a bias force, normally provided by a spring, constant force or even another SMA. These three options have their various advantages and design implications, which will be discussed in Chapter 6; for now, a spring is assumed as it is the most commonly used bias element. By comparing the force-strain curves of SMA vs spring, one can deduce the displacement at which the force of the SMA equalises the force of the spring, thereby giving an answer for the actuator position as seen in Figure 76.

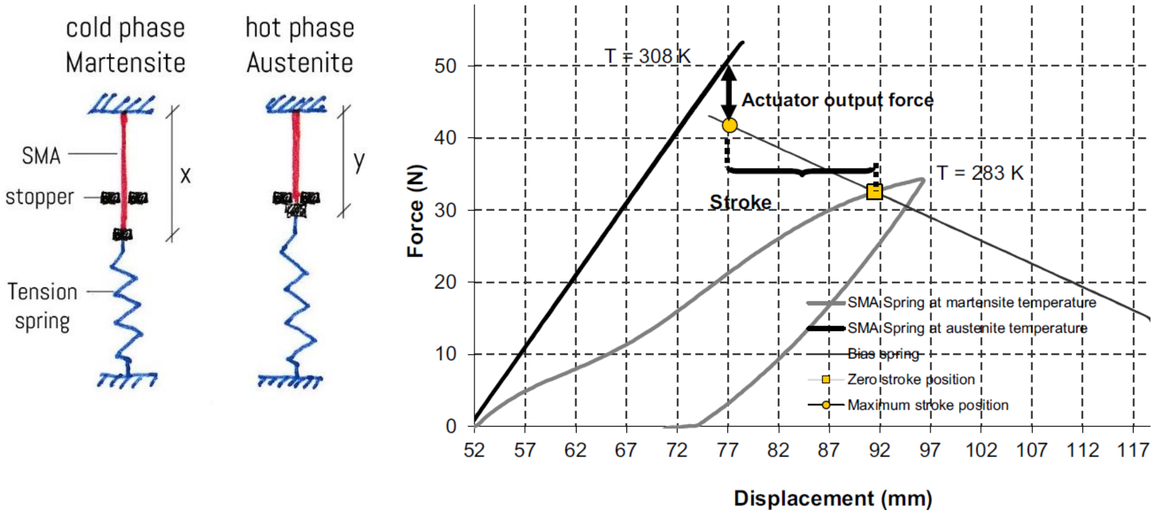

Figure 76: A demonstration of the graphical force-strain method for displacement calculation for an SMA vs spring. In this case, the x length of the sketch on the left is a 91mm displacement as seen on the graph, whilst the y is 77mm. Graph from (Lecce & Concilio, 2014, p. 222)

The example above is for two positions, for temperatures below M_f and above A_f, where the material is certain to be in either martensite or austenite respectively. Note the use of a stopper, which has a few functions. First, it means that there is some useful output force at the end of the stroke activation. Secondly, it provides a certain end position that can be virtually guaranteed upon actuation, whereas the absence of a stopper would mean that the repeated use and gradual fatigue of an actuator would lead to a drift in the end position and stroke length. Finally, the maximum strain of the SMA that it will experience is a fraction of the maximum recoverable strain, so the functional cycle fatigue of the SMA is much higher. Conventional designs allow for 4% strain and nitinol is capable of 10% strain recovery.

The model to be made in this study will produce a dynamic curve for the SMA, instead of just two, that is based on the previous switch point, and is reconstructed every time the temperature switches. By doing this, the hysteresis is accounted for.

By finding the intersection between the dynamic force-strain curve generated by the script and the force-strain curve of the bias spring, the script will in theory output the new length of the SMA, which corresponds to the displacement of the actuator tip.

However, implementing the graphical method with partial martensite fractions using the Brinson formulas will be a little more complex. If an SMA starts out at full austenite and is cooled into the transition zone, one would have to plot many SMA points using equation (3), with the known temperature T and with trial and error of the stress input until both the SMA strain and force matches with that of the spring. The martensite fraction must be known for the next change of temperature, for it may have an influence on the $\boldsymbol{\xi_0}$ value.

To manage the many variables and have a grasp of their fluctuating natures, a technique involving topology surfaces in 3D graphs has been developed and scripted. The principle is as follows: a single curve that relates martensite fraction to temperature can be produced for one value of stress using equation (3) or (4); by calculating all the $\xi - T$ curves for all the values of stress, a 3D topology surface is generated, as shown in Figure 77. The red curve shows the progress of the three coordinate values in a similar manner to that shown in Figure 75.

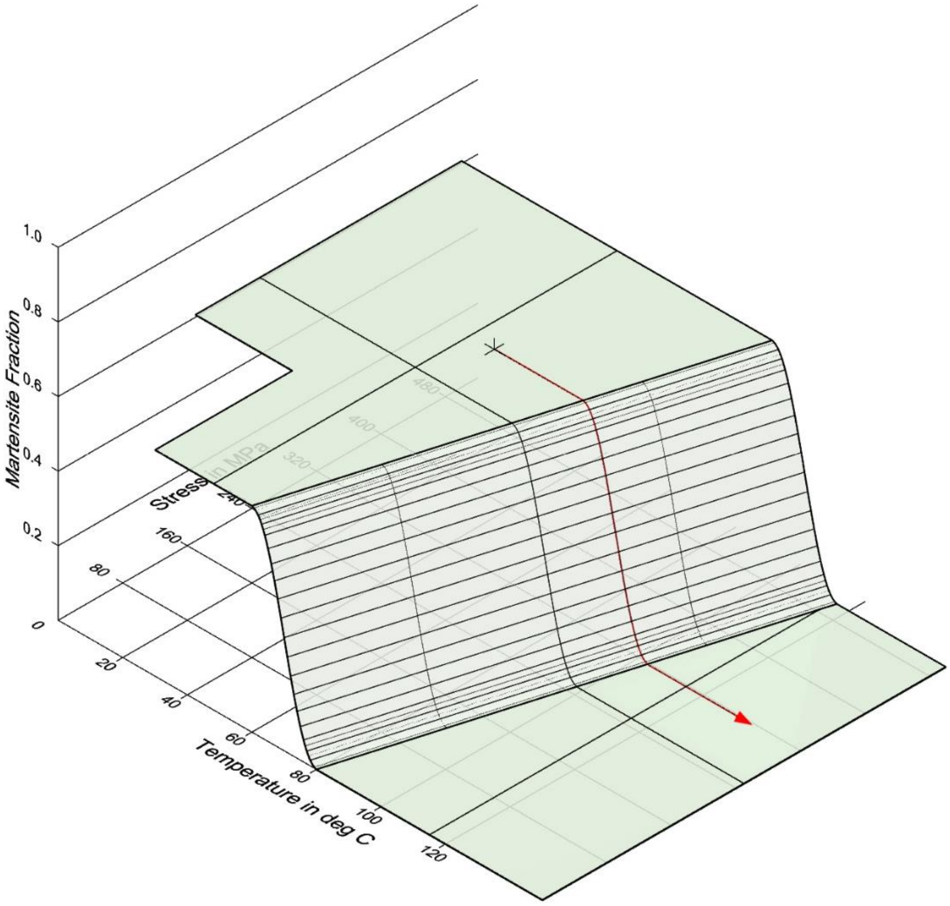

Figure 77: 3D graph containing the surface topology to describe the $T - \sigma - \xi$ relationship of a piece of nitinol being heated from from a partial martensite start point, as formulated in the Brinson model

Recall that with knowledge of the martensite fraction and stress, the strain can be calculated from equation (7). A second topology graph is thereby generated from the first by calculating the strain for every single point on the first topology, resulting in the topology shown in Figure 78. The strain in this case is expressed in meters and requires as an input the original length of the SMA piece. Force is used as a Y axis in the second graph, which is a useful variable that is linearly proportional to stress. Note that the cross-sectional area of the SMA wire is required as an input in order to derive the Force axis scale. Notice how the strain increases (slopes upwards towards the back right of the graph) as the force increases.

From now onwards, the bottom graph will be referred to as G1 and the top graph shall be referred to as G2.

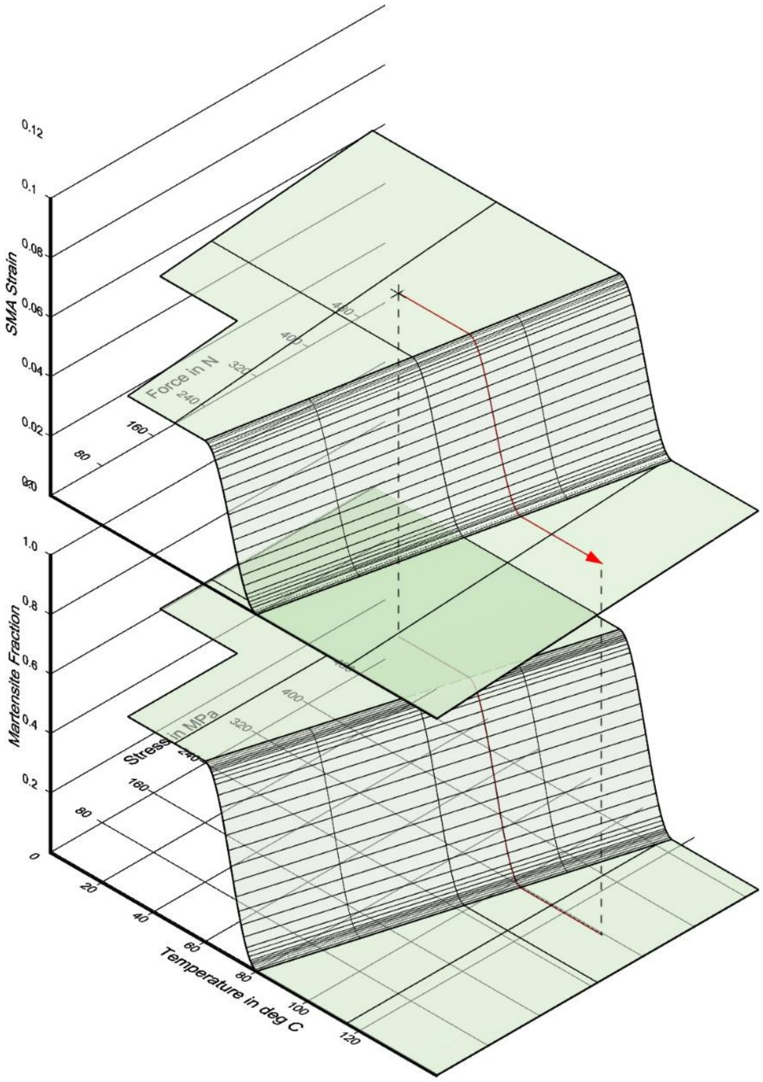

Figure 78: The upper $T - \varepsilon - F$ graph is generated from the data points on the $T - \sigma - \xi$ to procure a topology. The same temperature progression as Figure 77 is shown, to illustrate how the strain evolves

It is on this topology that the graphical method of Figure 76 can operate, by overlaying it with the temperature-force-strain topology of the bias spring and seeing where it intersects, to produce a force-strain curve, as seen in Figure 79. Along this curve is a point at which temperature = T, an input of the model, and the coordinates of this point contains the information for strain and force. By following the point back down to the first 3D graph, the martensite fraction and stress can be found.

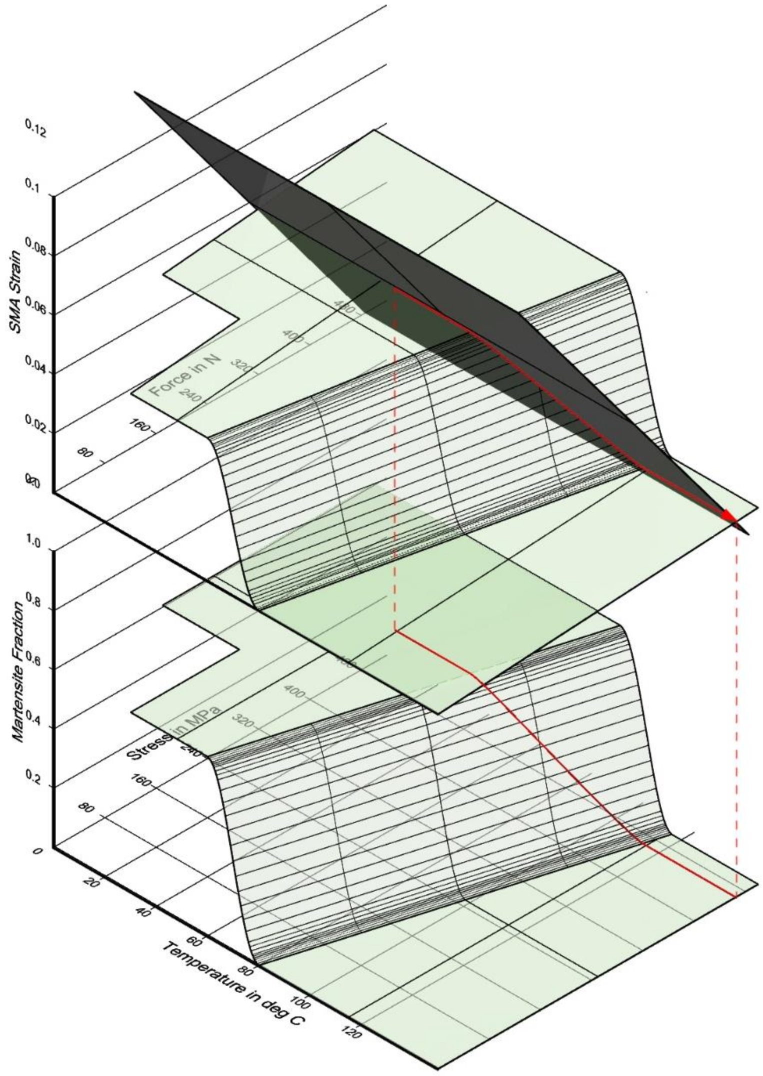

Figure 79: an SMA stressed by a bias spring being heated through to full austenite, starting in partial martensite phase

In summary, the script has a few complexities built into it. Starting at fully martensite and being heated, the script effectively generates a 'future' set of scenarios for the SMA at all possible stresses and the higher temperatures, using $\xi_0 = 0$, and then generates the corresponding force-strains for all these scenarios. This information is expressed as 3D topologies in G1 and G2.

For execution of the graphical method, the G2 topology that describes the bias spring is overlaid (in this case, the spring displacement is mapped onto G2, but alternatively the Z axis of G2 can be 'relative displacement' instead of strain for the same strategy), and the intersection curve between this and the corresponding SMA topology gives a relationship of the strain to expect as temperature rises. The point on the curve that has the coordinate where T = the new temperature will give the answer for strain and stress. This 3D point can be vertically traced back down to G1 to find the corresponding values of stress and martensite fraction at that value.

In the event that the direction of temperature change switches from positive to negative or vice-versa, the value of ξ_0 is changed to ξ at the switch point and a new pair of SMA topologies are generated, this time progressing in the opposite temperature direction. This check should be done, for every time T is changed. As an example, Figure 80 shows what would happen if the SMA was cooled back down to full martensite after the heating session of Figure 79. Notice the lower temperature position of the transition slope, which illustrates the model's capability to account for hysteresis. To compare the change in strains, a side view of Figure 80 can be seen in Figure 81.

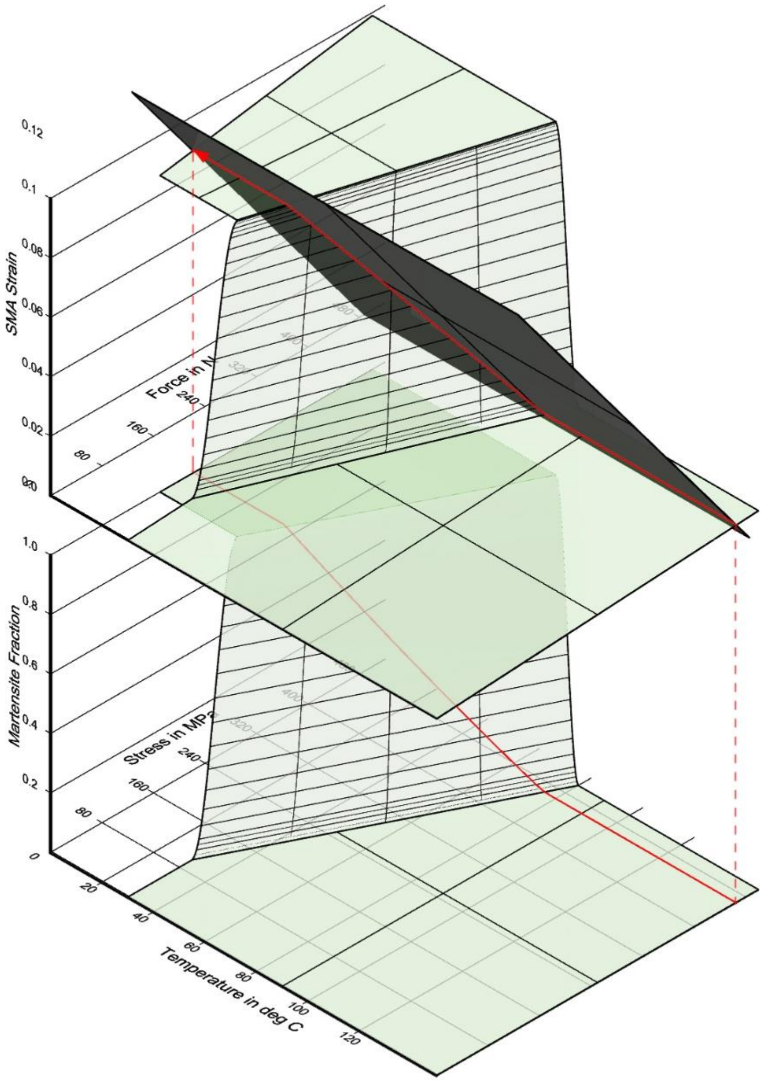

Figure 80: an SMA stressed by a bias spring being cooled from full martensite to full austenite

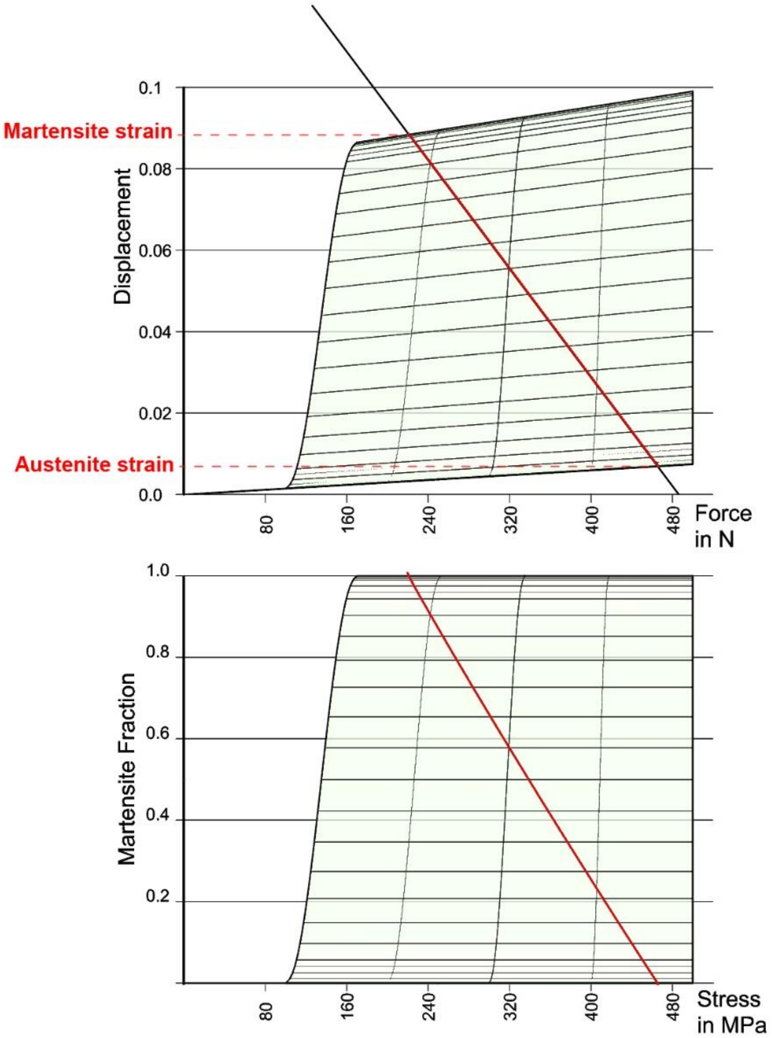

Figure 81: a side view of the topology graphs for SMA being cooled from full austenite to full martensite, subjected to a bias spring.

Using this strategy, the mission of the solver can be achieved. A designer can then derive and use the temperature-dependent value of SMA length as a variable input in a geometric 3D model to determine the position of a movable object, such as a façade window.

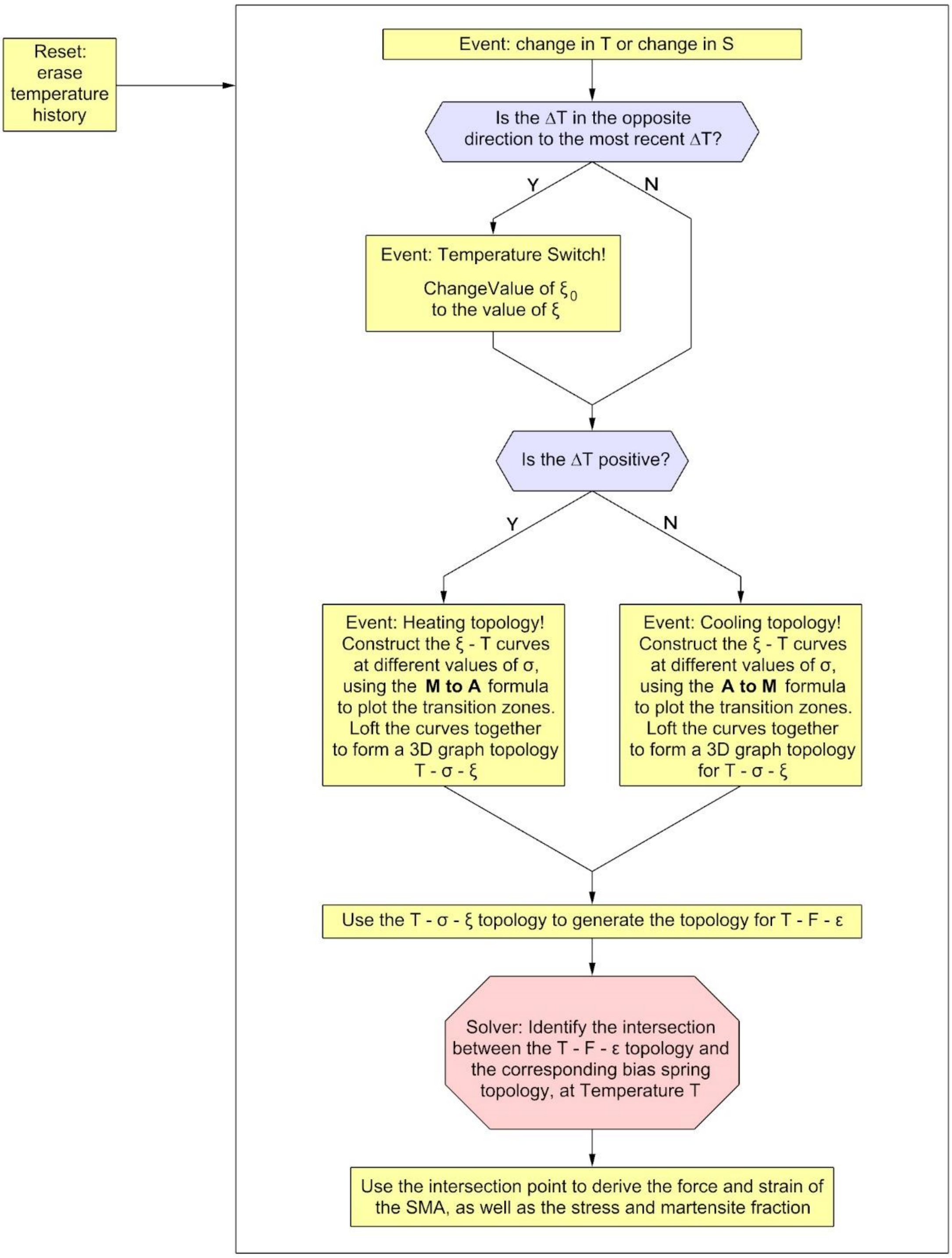

Figure 82: The Framework of the SMA script

Crafting the Computational Tool

The next step involved transferring the solver into a user-friendly script in Grasshopper, the result of which can be seen below. On the far left are the inputs at Box 1. The information is fed into Box 3, which contains a custom-built Python module that does the computational solving as described in this chapter. The outputs are the 3D graphs that are contained in Box 4 and the key information that is the goal of the script, particularly the new SMA length, is shown in Box 5. These will now be elaborated with an example. Note that Box 2 is purely for constructing the axes and labels of the graph, some of which are referenced from the Rhino modelspace within hidden layers.

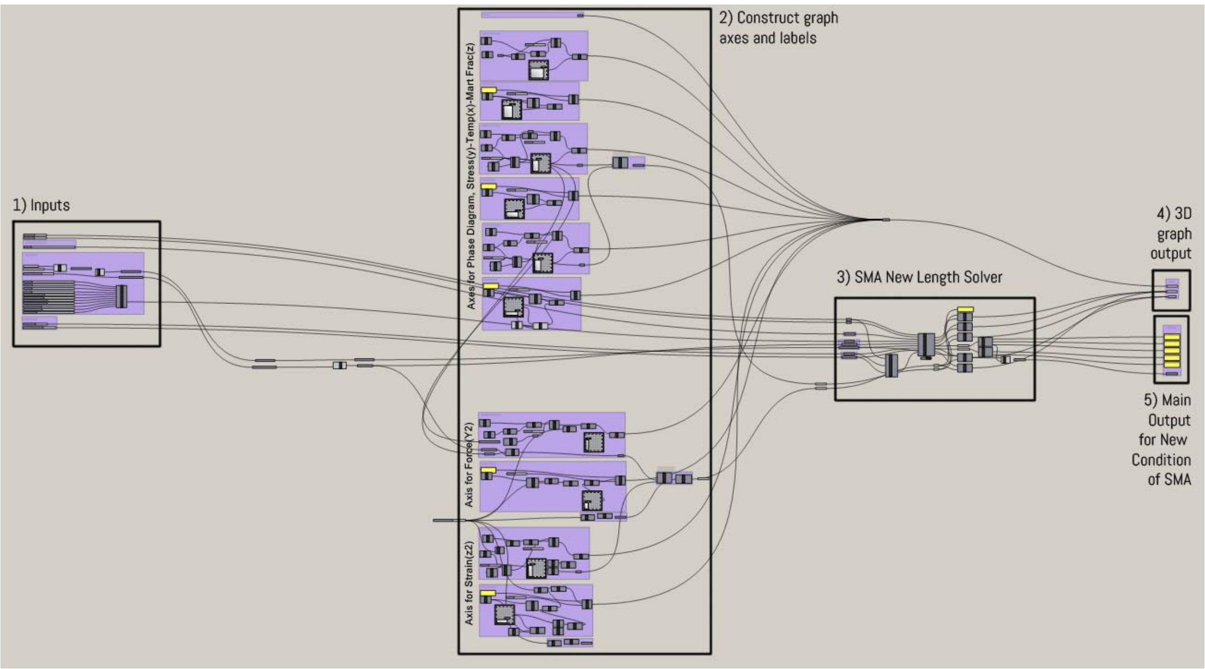

Figure 83: The grasshopper solver with the inputs on the left and outputs on the right

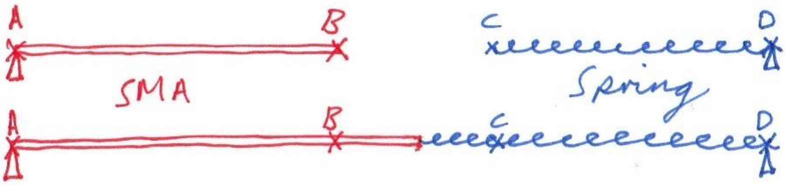

Figure 84: The situation being modelled as an example

A simple scenario of an SMA vs antagonistic spring will be used as an example for implementing the tool. The first step for the user is to draw the two end points of the SMA in its unstressed state, one point being a fixed location on the structure and the other being attached to the bias object such as the spring. Respectively, they are points A and B in Figure 84. These points are to be referenced into the inputs of the software tool. The rest of the inputs are entirely numerical in the version that has been produced for the thesis, but it is possible to upgrade it and model other situations if needed.

Figure 85: In the modelspace, the user only needs to reference two points into the Grasshopper script. These are the endpoints of the unstressed SMA, one fixed and one to attach the bias object. The other inputs are all numerical.

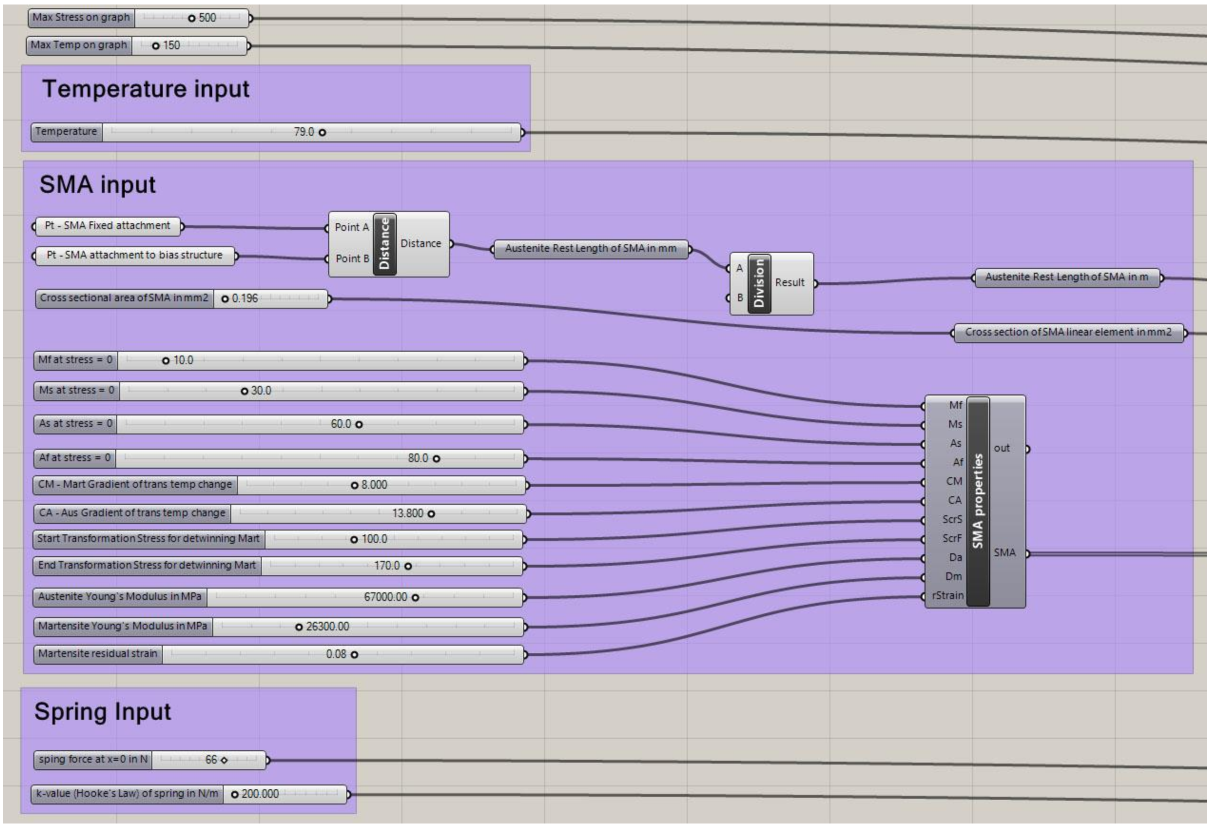

Max Stress on graph 500
Max Temp on graph 150
Temperature 79.0
Cross sectional area of SMA in mm2 0.196
Mf at stress = 0 10.0
Ms at stress = 0 30.0
As at stress = 0 60.0
Af at stress = 0 80.0
CM - Mart Gradient of trans temp change 8.000
CA - Aus Gradient of trans temp change 13.800
Start Transformation Stress for detwinning Mart 100.0
End Transformation Stress for detwinning Mart 170.0
Austenite Young's Modulus in MPa 67000.00
Martensite Young's Modulus in MPa 26300.00
Martensite residual strain 0.08
sping force at x=0 in N 66
k-value (Hooke's Law) of spring in N/m 200.000

Figure 86: Box 1, the inputs of the software tool

The inputs can be seen above. At the top, the maximum stress and maximum temperature are variables to select how much of the 3D surface topologies to generate, in terms of the temperature and stress axes of Figure 80. The temperature input is the variable one that will eventually animate the change of the SMA length. In the SMA Inputs group, the two points are referenced, along with the cross-sectional area of the element. These are enough to describe the SMA shape. 11 more inputs are used to describe the material properties of the SMA. In an ideal situation, these property inputs need to be tested only once for a given material and all future design for that material can then be done efficiently. The 11 parameters are fed into a component, which organises the data to become conveniently readable by the solver.

Finally, the spring input group describes the bias force. Choosing the most user-friendly input for this part was carefully considered, as providing too many options and variables would complicate the matter. In an earlier version, the user could specify the attachment points C and D of the spring as seen in Figure 84, along with the Hooke's Law stiffness. In practice, the thesis found this method to be inaccurate, as Hooke's law did not follow for low values of spring displacement during testing. A much more reliable method was to specify the spring force when the spring is stretched to point B, and to specify the stiffness, which is a value of Newtons per meter of displacement. These two figures were sufficient to completely describe spring behaviour. A constant gravity load can also be modelled by setting the stiffness to zero.

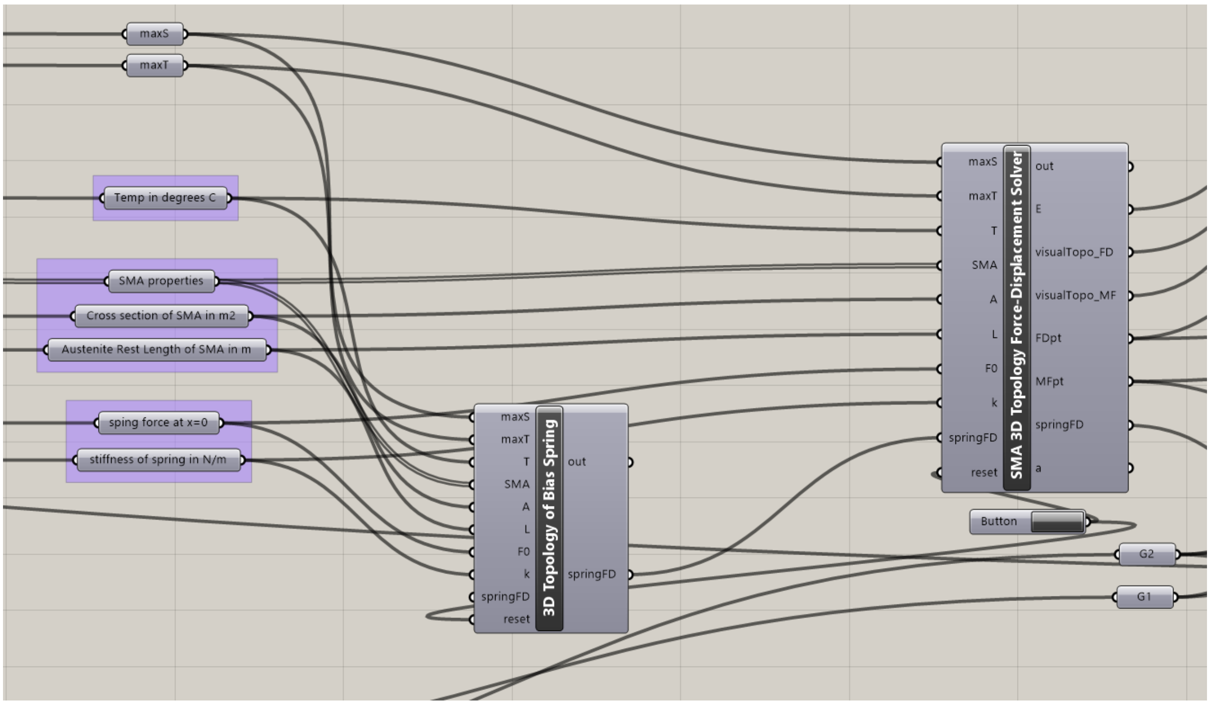

Figure 87: Box 3. The SMA displacement solver is shown on the right

The solver is shown above, which takes all the inputs and executes accordingly to generate the 3D graphs and the key outputs. Note that a separate custom component is used to generate the 3D topology graph for the spring Temperature-Force-Displacement. This keeps the option open for others to input a different topology for a more complex bias object which may not be linear, for example an opposing SMA wire. A new topology BREP is created by mapping the bias object profile of force [N] and displacement [m] onto the world Y and Z axis respectively, and then extruding it along X.

A reset button is incorporated into the solver, which resets the variables and erases temperature history. It must be clicked to start the solver.

On the right, the outputs are *E* for martensite fraction, followed by the BREPs *visualTopo_FD* and *visualTopo_MF* to represent the G2 and G1 topologies of the SMA respectively. The points *FDpt and MFpt* are the active points in G2 and G1 respectively, representing the status of the SMA. By deconstructing these points into their x-y-x components, the values of Temperature-Force-Displacement and Temperature-Stress-Martensite fraction can be extracted.

Both components have been custom-written in python code. The code for the SMA solver can be seen on the next page. The individual custom-built functions that generate the topologies are *austwardTopo_D austwardTopo_MF, martwardTopo_FD*and *martwardTopo_MF*. FD (force-displacement) denotes the G2 graph and MF the G1. For an elaboration of the entire code with all the custom-written functions, see the appendix. Note that due to an internal glitch with grasshopper, the temperature slider works best if changing the numbers by typing them in, as opposed to sliding the component left and right. The latter method produces new values of E0 when it is not needed when the mouse is released after a temperature decrease. Manual typing of the number works as intended.

Note that the solver does not work in low temperatures when the stress is below the critical finishing stress for detwinning, as that portion of the topologies have not been scripted. To ensure the shape memory effect is fully utilized in the design, and that the script functions at all temperatures, the stress should be maintained above the critical finish stress.

```
origDir = (pT >= T0)
newDir = (T >= pT)

if origDir != newDir:   #REVERSAL of the direction of temperature change
    T0 = pT
    pT = T
    E0 = pE
else:                   #NO REVERSAL of the direction of temperature change
    pT = T

if T > T0:
    topo_FD = austwardTopo_FD(E0)
    topo_MF = austwardTopo_MF(E0)
else:
    topo_FD = martwardTopo_FD(E0)
    topo_MF = martwardTopo_MF(E0)

tPlanePt1 = [T, 0, 0]
tPlanePt2 = [T, maxS * 1000000 * A, 0]
tPlanePt3 = [T, maxS * 1000000 * A, 1]
tPlanePt4 = [T, 0, 1]
tPlane = rs.AddSrfPt([tPlanePt1, tPlanePt2, tPlanePt3, tPlanePt4])

springFDcrv = rs.IntersectBreps(tPlane, springFD)
FDpt = rs.CurveBrepIntersect(springFDcrv, topo_FD)[1][0]
force = rs.PointCoordinates(FDpt)[1]
disp = rs.PointCoordinates(FDpt)[2]
S = force / A / 1000000
stressTempCrv = rs.AddLine([T, S, 0], [T, S, 1])
MFpt = rs.CurveBrepIntersect(stressTempCrv, topo_MF)[1][0]
E = rs.PointCoordinates(MFpt)[2]
pE = E

visualTopo_FD = topo_FD
visualTopo_MF = topo_MF
```

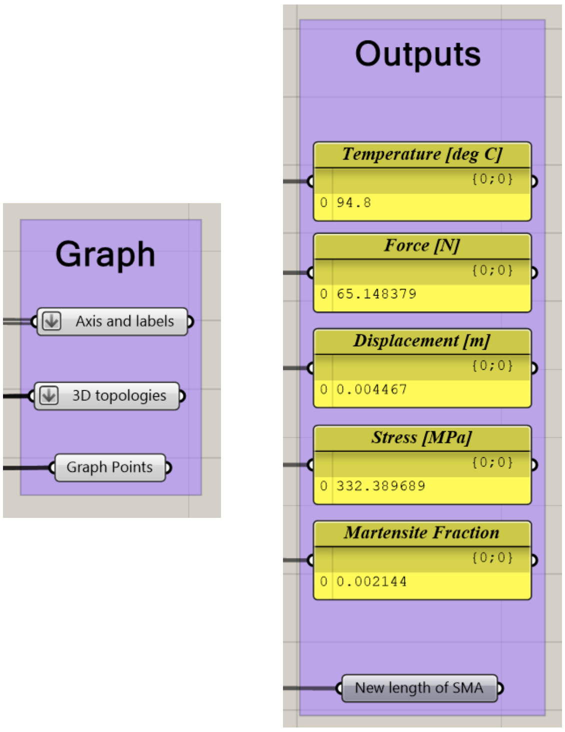

Temperature [deg C] {0;0}
0 94.8

Force [N] {0;0}
0 65.148379

Displacement [m] {0;0}
0 0.004467

Stress [MPa] {0;0}
0 332.389689

Martensite Fraction {0;0}
0 0.002144

Figure 88: The Grasshopper outputs of the tool

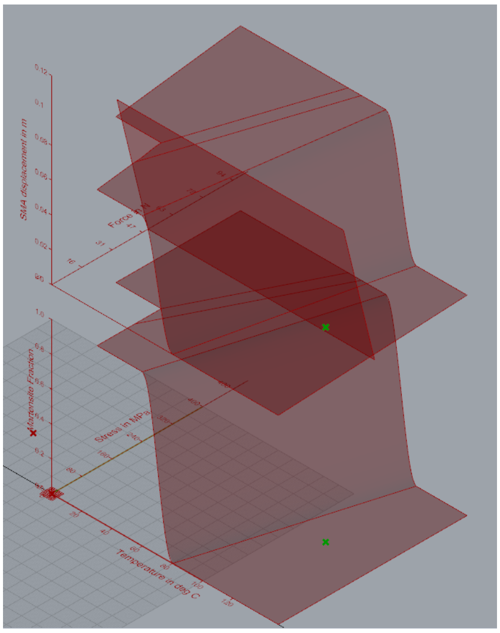

Figure 89: The rhino modelspace output for the 3D graphs

The outputs are seen above. The tool itself has no modelspace output to show the new position of the SMA, as the user should be able to construct their own animated model using the new length of SMA. This gives more freedom for special designs. The example on the next page shows the 'New length' output being put to use in a model.

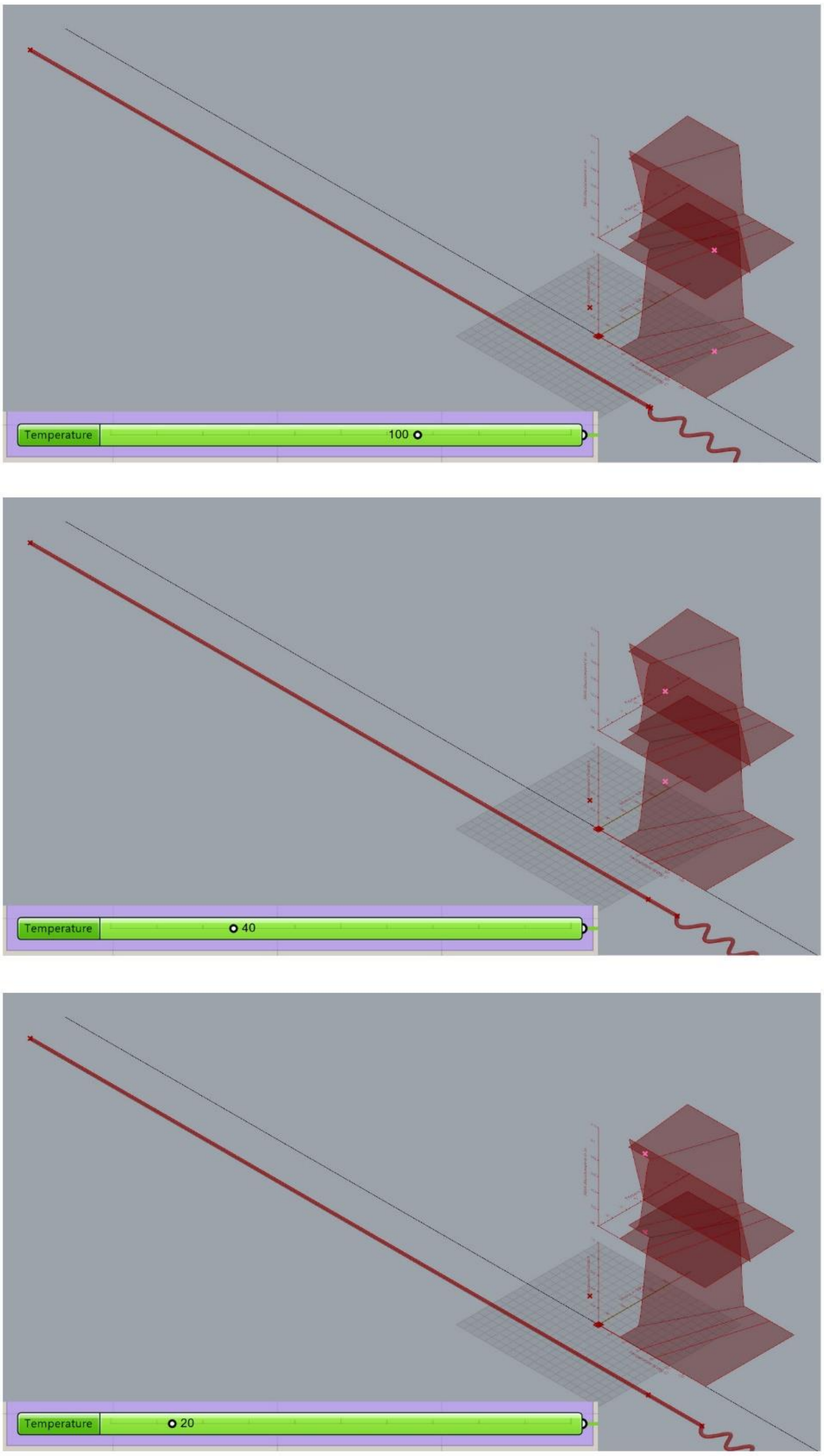

Figure 90: The output being put to use to animate an SMA wire vs a spring

The script has been made available in the Google Drive link below. It is licensed under the Creative Commons Attribution 4.0 International License which is the most free, so the software can be shared and commercially used.

https://goo.gl/hiN6JN

The files are in the format Rhino 5 and Grasshopper 0.9.0076. It will be necessary to download Python and GhPython to run the solver. Elefront for Rhino 5 has also been used for the graph axis labels.

In the examples folder, the files for the SMA vs linear spring scenario of Figure 90 can be found.

Recommendations for Improving the tool

The most noticeable missing part to the script is the portion of the topologies at both low stress and low temperature, which are the conditions that contain twinned martensite. This part is not necessary for the thesis, but modelling it will be useful for other applications to predict how the SMA behaves in all situations.

Additional features can be added to increase the utility for a designer, for example a pre-strain option for the SMA, as well as an option to place a maximum cap on the strain. Both are often done in practice to influence the short and long term performance of the SMA element. The incorporation of external forces into the model is also a feature that could be added. In the case of an adaptronic window panel, wind forces could be added to the bias force before it is applied to the SMA.

A complex phenomena that has been cited in various literature is the changing Young's Modulus of an SMA as it transitions. The pattern is much stranger than the standard linear one used in Brinson's model, exhibiting a V-shape where it falls and then rises again as it transitions from martensite to austenite (W. H. Huang, Wu, Lim, & Vahhi, 2005), (Mizar, 2005). This also implies that residual stress is not linear either, as Brinson's model makes it a function of the modulus. Modelling this into the software would no doubt be a complex procedure; different SMAs may have different shape profiles, and they can't be easily expressed in a few numbers.

Finally, in the longer term there can be extended or new software tools to model the behaviour of SMAs in bending, as a spring and as shell elements. It is possible to transfer the principles of 1D models to the first two applications.

Summary of Contribution

In this chapter, a script was developed that allows three design inputs to dynamically model the behaviour of an SMA element within an adaptronic device as the temperature of the environment changes, using the equations of (Brinson, 1993). The inputs are as follows: 1) information to describe the shape and material properties of a linear SMA element 2) description of a bias force (such as that from a spring) as it changes with strain or displacement and 3) temperature. By changing the last input while keeping the first two constant, it is possible to generate the SMA displacement that respects the complexity of hysteresis. Since most of the project literature only focuses on SMA as being in on-off positions, this is a novel feature.

With this model, it is possible to predict the behaviour of the rest of the adaptronic device with conventional mechanical formulas. Since it takes just three inputs, the complex task of adaptronic modelling is made simpler. Additionally, the script has been made in Grasshopper, a plug-in of Rhino 3D, which is much more accessible and designer-friendly to those in the building industry that have no engineering background.

5. Concept and Explorations

Design Criteria

Compared to the medical and aerospace fields where Shape Memory Alloys have found by far the most success, the building industry is rather conservative and lacking in high-tech precision equipment, especially in the final stage of construction at site. Researchers of innovative SMA projects often employ very specialised equipment such as a Differential Scanning Calorimeter (DSC) to accurately measure the temperature transitions at zero stress, and recommend systematic testing for new samples. Such things can be done and incorporated into a prefabricated product, but actually installing SMA elements at site is not recommended due to the high level of precision required. At the building site, inaccuracies are generally minimized but accepted as a fact of the construction process and are accounted for instead of eliminated. This is a reality which had to be addressed when approaching building technology with an SMA solution.

Even within the factory, there may need to be ways to account for inaccuracies or unexpected behaviour of SMA wires after attachment. These were the findings of the prototyping activities, which have indicated a need for adjustment devices to allow for tweaking after installation and after the first few activations. The design of the final product therefore reflect the limitations at the building site, the expected abilities of contractors and realistic manufacturing and assembly processes for construction products.

The final design will keep the mechanisms simple for the time being, with the sole purpose of creating a façade module capable of environmentally passive activation. A set of design criteria has been drawn up from the findings of the earlier studies to deliver a product that can achieve the adaptronic module.

Design Criteria for the Façade Module

The module must be:

- Rectangular and modular
- Made of standard aluminium profiles
- A prefabricated unit
- Possible to be supported on standard steel structural elements
- As transparent as possible
- Able to meet standard requirements of a conventional façade, for eample keep out the rain, insulate and resist wind loads

Design Criteria for the Adaptronic Mechanism

For the criteria concerning the adaptronic mechanism itself, all the aspects have been simplified compared to the expected criteria of a final commercial product, as it would be wise to start in small steps and set achievable goals. The final design of this thesis will therefore conform to the simplified set; many aspects will require much more development in order to optimize it for good function and its eventual use as an energy-saving device for HVAC reduction.

Design Criteria for market-ready product	Goal for the Design of the Thesis
• Self-actuate so it is closed in cold weather conditions and open in hot weather conditions	• Achieve a 90 degree actuator stroke, by utilizing the Shape Memory Effect with an elongation of no more than 4%
• Be able to assume a closed position and locked at will with some form of override mechanism, for security reasons or in times of inclement weather	• Feature a water-based cooling system to bring the SMA back to martensite and close the panels; the lock is outside of the scope
• Last at least 20 years, with an adequate fatigue life of SMA cycles given the intended frequency of use	• Analyse the number of expected activations per year due to the environment, and ensure it is below the design fatigue
• Have a body to hold the moving parts in place that is magnitudes stiffer than the SMA wire and spring system	• Use a steel body of reasonable cross-section to ensure stiffness
• Feature a heat mediator between the environment and the SMA element	• Enclose the SMA in a solar absorbing chamber in order to magnify the temperature range from the weather

Concept Module

First Concept Designs

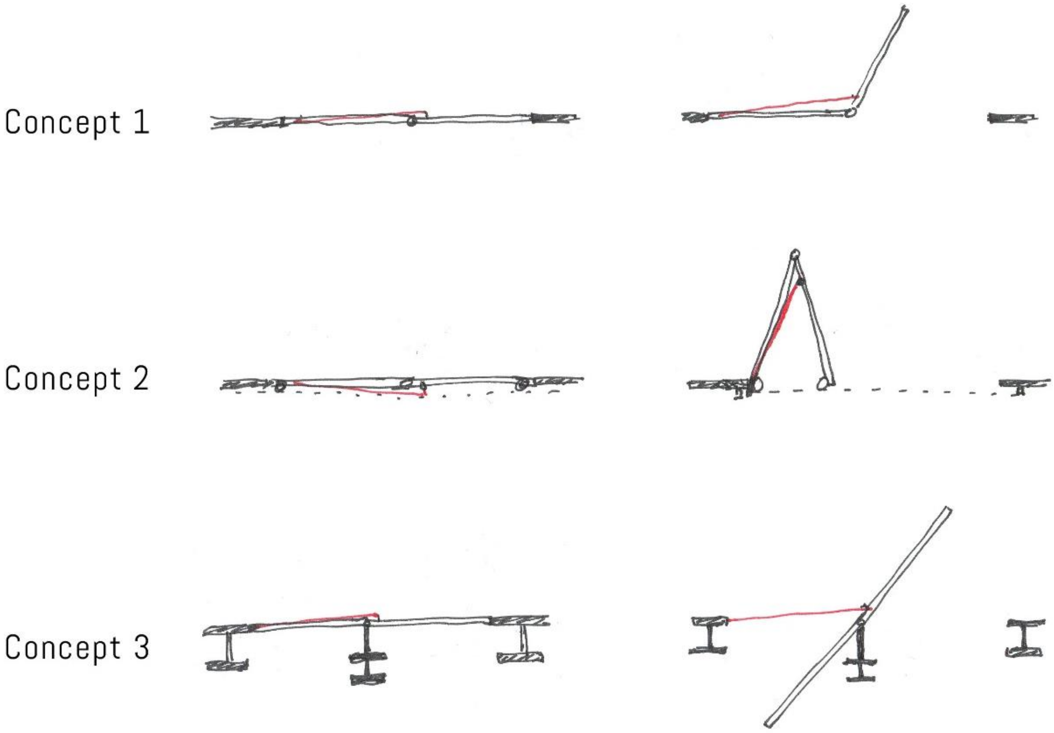

Figure 91: Concept designs for adaptronic roof panel. SMA in red, which gets shorter upon activation. Concept 3 was chosen to proceed the design

Shown above were the first concept designs for an adaptronic roof module, shown in section. Concept 1 was inspired by the mechanics of the human arm. A biological analogue was chosen due to the similarities of the actuator in question; human muscle and SMAs both exert a great force over a small stroke length, which is a highly favoured actuator in nature, as opposed to a weak force over a large stroke length. Such a design leads to limbs which take less space (biceps would be cumbersome if they had to span between shoulder and wrist).

The general idea is to fix one end point of the SMA at static part of the structure, and place the other one on a part of the moving frame that is very close to the hinge. The rotation of the moving frame would mean that there is a slight change in distance between the two attachment points when opening and closing; the SMA can therefore use its Shape Memory Effect to facilitate this change of distance between the two states. The change in length should be very much smaller in proportion to the total length, in order to ensure there is enough SMA stroke to reach the whole 90° movement.

The main problem with Concept 1 was that half the module would be static, unless they were made to overlap (which may have been more complicated). The second concept ensures both halves of the module to move, but each time it activates, the structure is rising up and therefore fighting against gravity. The third concept solves this by ensuring the centre of gravity of the moving part remains in the same place; it would take very little energy for anything to move the panel, and in an ideal condition only the friction in the hinge needs to be overcome. The third concept was chosen to progress further.

Heat Provision

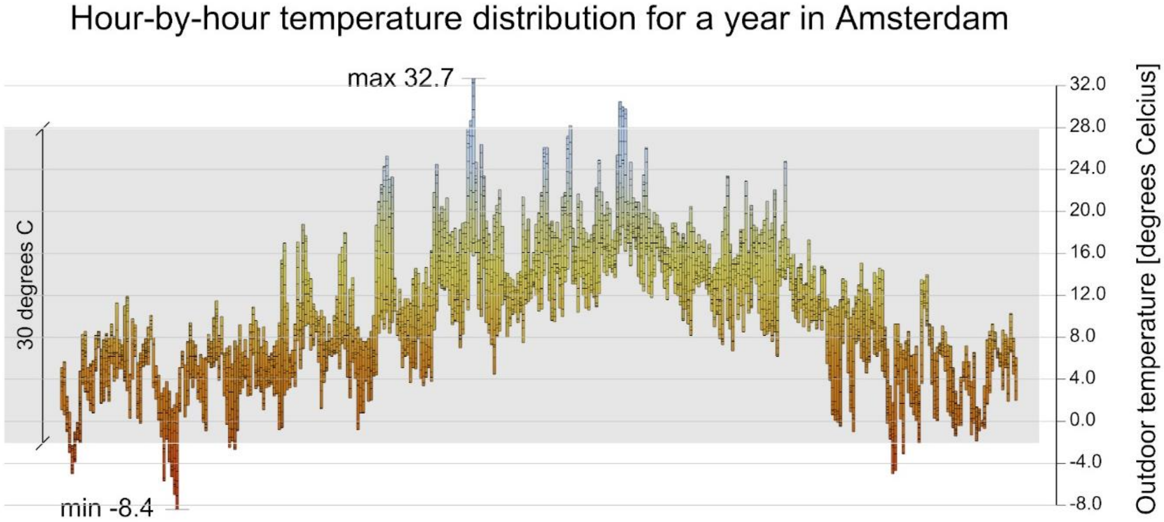

Figure 92:A temperature distribution chart showing the outdoor temperature of every single hour for a whole year in Amsterdam. Each of the 365 vertical strips represent a single day, and each cell an hour.[15] Graph produced with the help of Ladybug, plug-in for Rhino Grasshopper.

An early realisation concerned the provision of a temperature at the right level and at the right times to the nitinol within the module, in order to animate it meaningfully for HVAC savings. Recall that the transition temperatures of nitinol can be adjusted upwards or downwards by changing the percentages of the atomic composition, but the hysteresis is a problem when it comes to the function of an actuator. Typical nitinol has a hysteresis of around 30ºC (Lecce & Concilio, 2014, p. 48). This is a problem when it comes to using the ambient temperature as the stimulant for opening and closing the module, as it means there will be a large 30 degree range of temperature in which the module may be open or closed, depending on the history of the temperature. 30 degrees would cover a majority of the outdoor temperature range, as shown in Figure 92; it can be seen that the temperature range isn't great enough to result in much responsiveness.

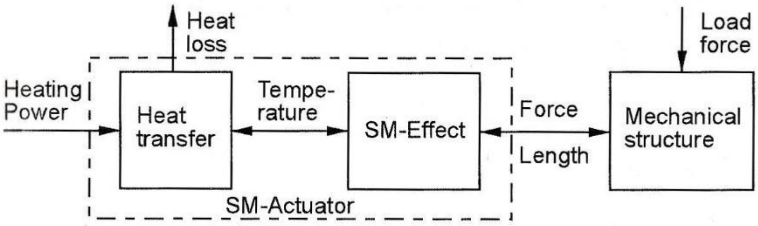

Figure 93: Framework for design of an SMA adaptronic actuator device, to show energy and force inputs and outputs (Janocha, 1999, p. 153)

This is where an intermediate element between the environment and an SMA can play a role. In the framework above for an adaptronic SMA device, a heat transfer mediator has the function to modify the incoming environmental heat energy in some way before passing it on to the SMA. In this case, the temperatures need to span a much greater range in order to facilitate meaningful movement of the panels. It was therefore decided that the SMA should be housed in a solar absorbing device, to greatly elevate the temperature when exposed to solar radiation.

---

[15] Original Source Data (c) 2001 American Society of Heating, Refrigerating and Air-Conditioning Engineers (ASHRAE), Inc., Atlanta, GA, USA. www.ashrae.org

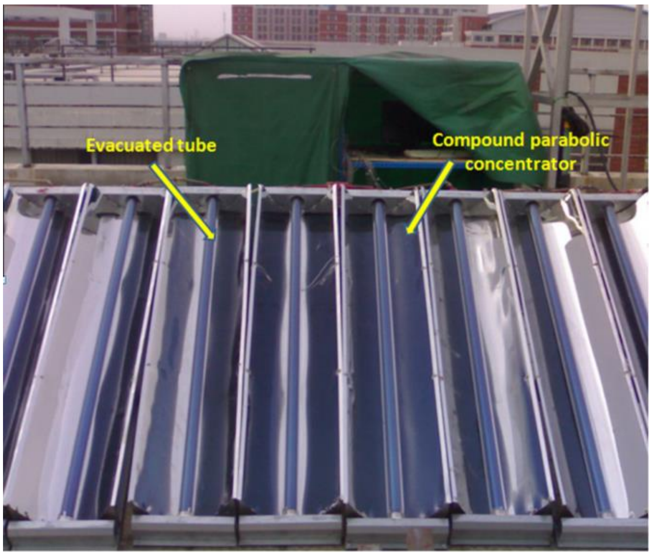

Figure 94:Innovate solar collector with U-shaped tubes to achieve high temperatures of 200oC even in the Winter, developed in (Wang et al., 2014)

Some solar thermal collectors exist which achieve high temperatures even when they are not exposed to direct sunlight, and they do not require any smart materials or electricity to work. Task 49, which is a group associated with the International Energy Agency, defines a medium temperature solar thermal collector as one that is able to output 300 W/m at operating temperatures above 100°C, among other criteria.[16] In (Wang et al., 2014), an innovative solar collector utilizing a compound parabolic concentrator as a U-shaped tube is able to focus the sunlight and achieve 200°C. However, it must be remembered that simply having a solar collector that is hot all year round is not the goal.

The goal is to achieve a wide range of temperatures so that the summer one is much hotter than the winter one, by a difference of at least 30 degrees, so as to provide distinct and useful times of open and close. This can be done by selectively absorbing the summer solar gain and avoiding the winter.

The reference project of (Leung, 2014) incorporates such a device for heating of its paraffin wax-based adaptronic actuator for an attempted seasonal opening pattern. It looked at the different levels of solar radiation incident on two 'heat engines' with a South-facing vertical plane (A) and a horizontal plane (B), each containing the wax to be actuated. As Figure 98 shows, the horizontal plane of motor B is very effective for selectively absorbing solar gains in the Summer, due to the higher angle of the Sun in that time of year. Accordingly, a detailed temperature model was produced with the ambient air as heat sink, to see the number of hours per day the paraffin wax could in theory be actuated, seen in Figure 97. Heat motor B, which in this case was used to actuate a shading device, was able to be activated for a series of warm months from June until September.

Going forward, it can be assumed that the necessary temperature range for SMA activation can be achieved with the help of a thoughtfully designed solar energy-absorbing device, hereafter referred to as the heat chamber. The SMA can be located within the heat chamber.

---

[16] Frank E, Mauthner F, Fischer S. Overheating prevention and stagnation handling in solar process heat applications. International Energy Agency - Solar Heating and Cooling Task 49. Solar Process Heat for Production and Advanced Applications, 2015

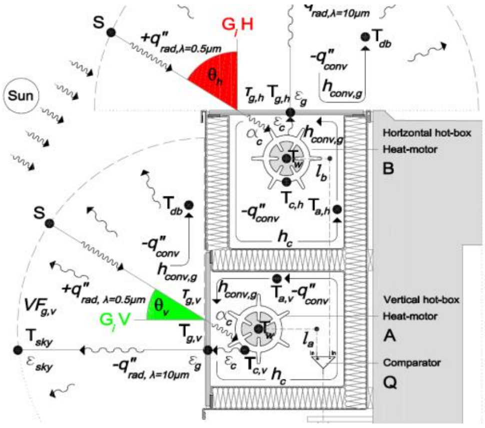

Figure 95: Cross section of 'heat motors' design concept, using different solar absorber surface orientation to selectively control the times of high temperature within the chamber. From (Leung, 2014)

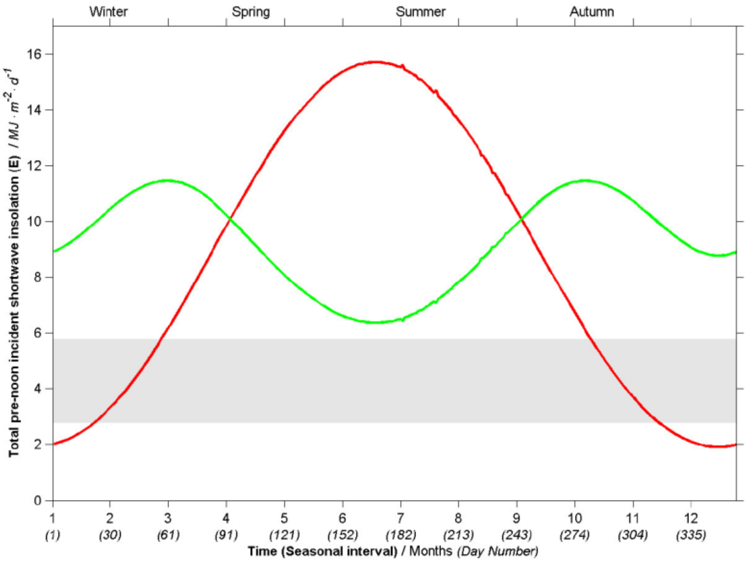

Figure 96: A graph of total solar energy incident on the horizontal plane of B, red curve, and the South-facing vertical plane of A, green curve, throughout the months (and days in parenthesis) of the year. Graph from (Leung, 2014)

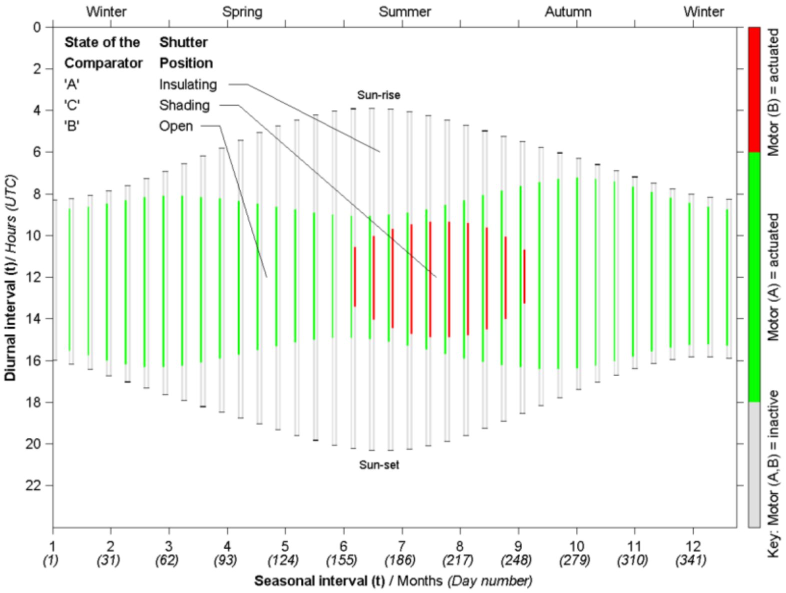

Figure 97: the number of hours in which the respective actuator/motor is able to actuate, for given days of the year. Graph from (Leung, 2014)

3D Analysis for self-shading

As a consequence of utilizing a solar-absorbing heat chamber with the SMA, it became important to ensure that the element would always be accessible to the sunlight. Parametric 3D models were animated in Rhino Grasshopper to see the self-shading consequences, and how the dynamic geometry performs functionally. Concept 3 was tested first, as Option A. The 3D models for both horizontal and vertical facades can be seen on the following page; in every example, The wall is assumed to be South-facing in all cases, so the atrium is positioned to receive maximum sunlight. Each option is reviewed below.

The SMA elements of Options A and B were shaded by the frame in both the horizontal and vertical façades, especially at noon, when they were effectively fully shaded. The main idea of Option B was to halve the number of SMA elements by making neighbouring panels share the same piece.

Option C attempted to fix the self-shading issues of the first two by positioning the hinges to make the panels swing inwards, whilst the SMA remains near the boundary of the building to avoid getting shaded.

Option D took a similar approach to Option B, but in the open states, the SMA element has great clearance to the South direction so it is not fully self-shaded at any time of day.

Option E combined the strategies of B and C, to have pairs of panels sharing one SMA actuator, and having panels swing inwards. However, the inward swing requires a hinge placement that is far from the centre of gravity of the object, so the SMA actuator would have to work against gravity loads when opening or closing the panel. This was decidedly not acceptable, as it could potentially place a great load on the actuator that could otherwise be avoided.

Option D was chosen, as it avoided self-shading quite effectively and had a good hinge placement for easy opening and closing in terms of actuator force requirement.

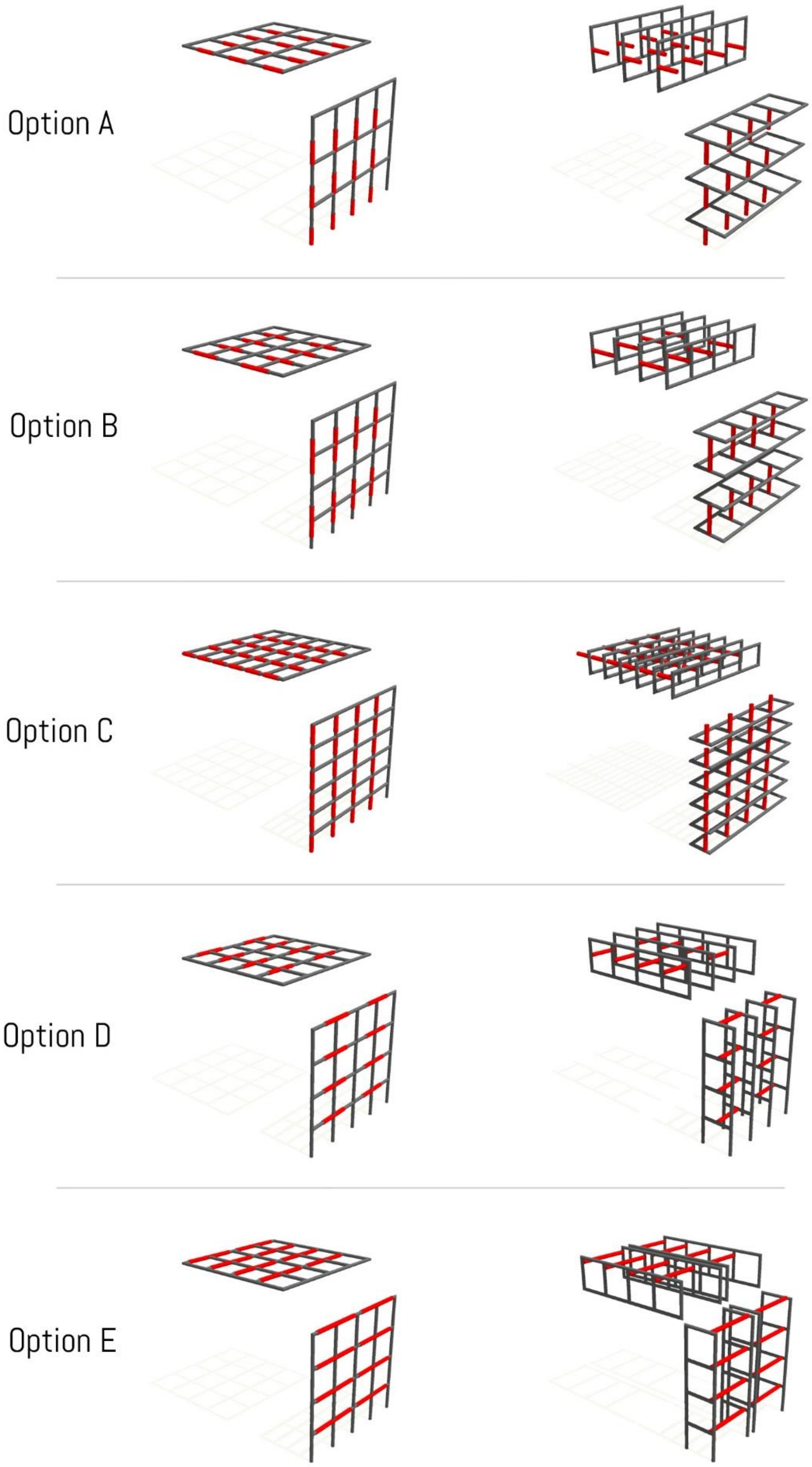

Figure 98: Different design options for the wall and roof adaptronic module, to experiment with SMA and hinge strategy for dynamic and self-shading consequences. The wall is assumed to be South-facing in all cases, so the atrium is positioned to receive maximum sunlight

Concept Module Development

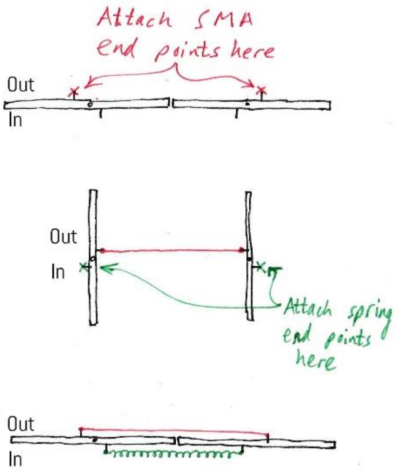

Figure 99: The logic behind the concept module, shown as a sequence of plan sections of a pair of vertical façade panels.

As discussed in the previous chapter, a standard one-way Shape Memory Effect will be employed to activate the SMA, so it will need a bias object to return it back to position in the cold phase. A spring has been chosen as it is a commonly used solution.

The images of Figure 99 shows the logic behind the design, in plan section for a vertical façade module. In the first image are two centre-pivot glazing units. An SMA wire spans between the two points in the correct length so that that the austenite phase would result in the second image, where the left glazing unit is pulled clockwise and the right unit anticlockwise. By placing the spring in between the green points, in the third image results: the bias force is applied at the correct positions so as to return the panels back to a closed setting in the cold martensite phase.

Next, it was decided that the SMA and spring should occupy the same height position in the panels, and that they should be in the middle of the height, to minimize torsion in the panel structures. This causes a problem in the spatial layout, as the spring and panel would spatially overlap upon opening, as shown below.

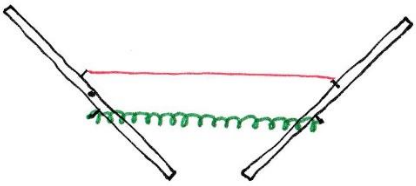

Figure 100: the spring and panels occupy the same space during activation; this would need to be resolved in 3D

The solution was to have specially shaped glazing units with empty parts in the middle so as to not conflict with the spring. This is shown below in the developed concept. The hatched grey structure that runs down the spine of the design in Figure 101a serves as both the body of the adaptronic engine and a sealant for the windows when closed.

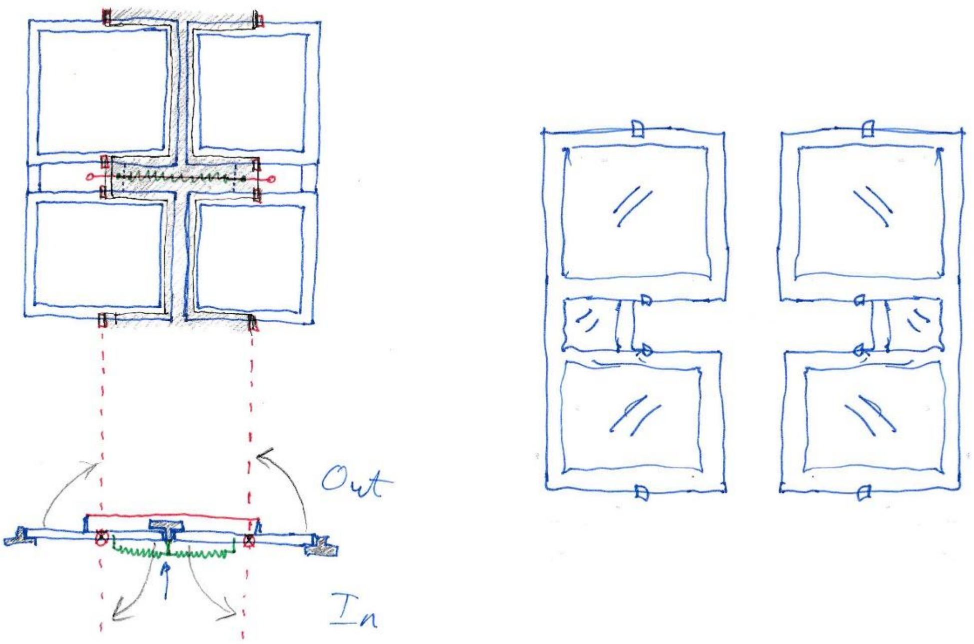

Figure 101: a) Development of the concept in elevation. b) The shape of the glazing units have been designed so as to not conflict with the spring

Concept 1:10 Prototype

A 1:10 prototype with rotating glazing units was built as proof of geometric concept.

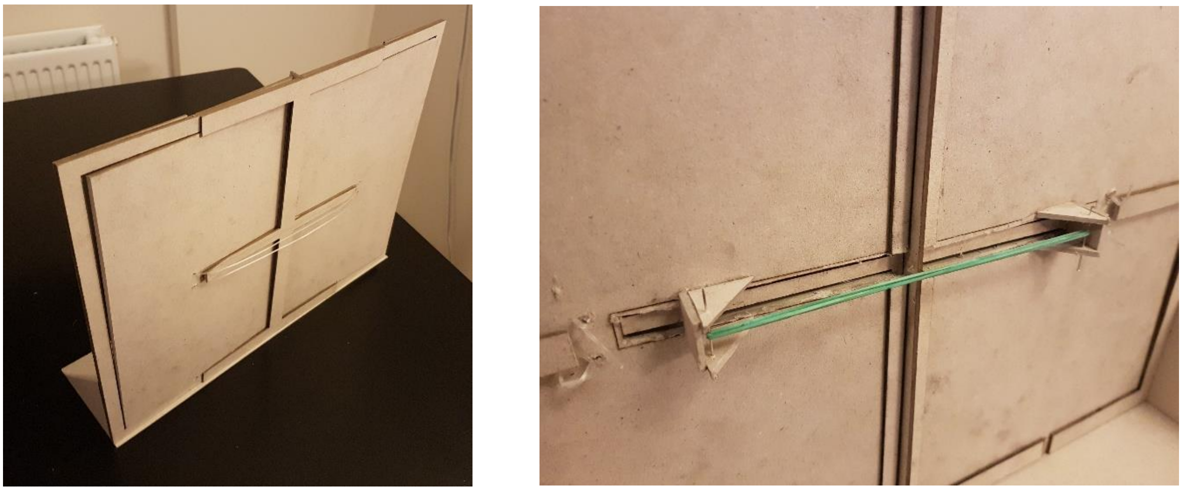

Figure 102: a) 1:10 prototype, showing the exterior side of the façade module. The green elastic band represents the SMA element b) the hardware on the other side, with an elastic band representing the bias force that always applies tension into the SMA wire

Figure 103: testing of the opening motion with the 1:10 prototype

The most important finding from this prototype was the need for very precise placement of the SMA and spring mechanism. The attachment points need to very specifically positioned around the hinges, as shown in the diagram below, which varies the distance between SMA attachment and the pivot point.

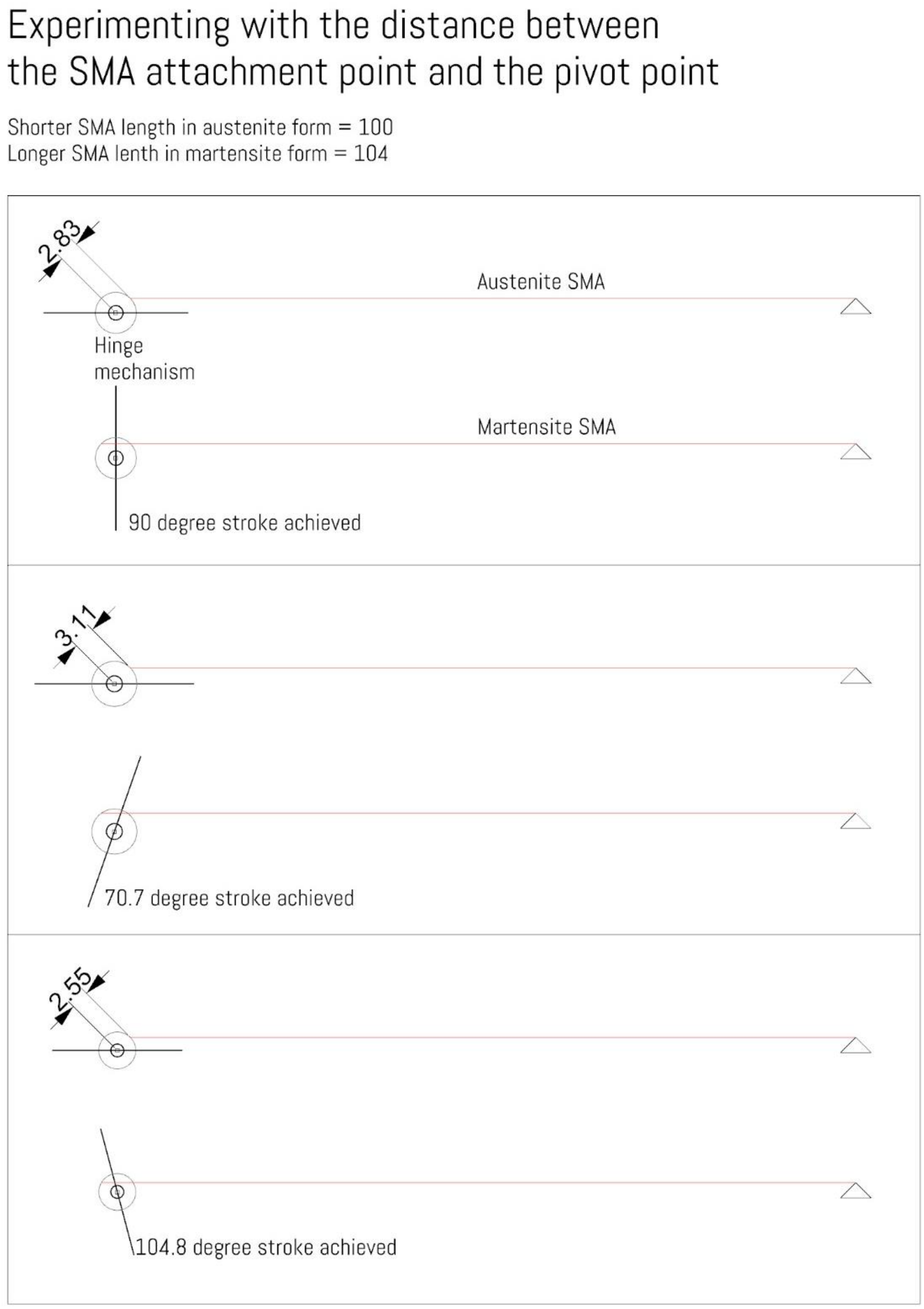

Figure 104: the angular stroke is highly dependent on the distance between the SMA attachment and pivot point. Here, it is increased by 10% in the second example and decreased 10% in the third.

Ideally, a 90 degree stroke should be achieved make the atrium truly open up, but a smaller one may have the same effect climatically. A larger distance between attachment and pivot means less force is needed to apply the same moment to the rotating panel, so there is a trade-off between force needed and angular stroke.

Not only did the prototype highlight the importance of precision in the mechanical placement, it also the showed the importance of stiffness. The original intention was to design the prototype so that the translucent nylon wires representing the SMA in Figure 102a could be pulled and thereby simulate an austenite transition. In practice however, this had the effect of deforming the card structure, instead of rotating the panels and stretching the elastic. Therefore, it is of great importance to ensure the body which holds the bias object and SMA are many magnitudes stiffer them, in order to keep them in the desired positions for all scenarios.

Actuator Engine Prototyping

Strategy

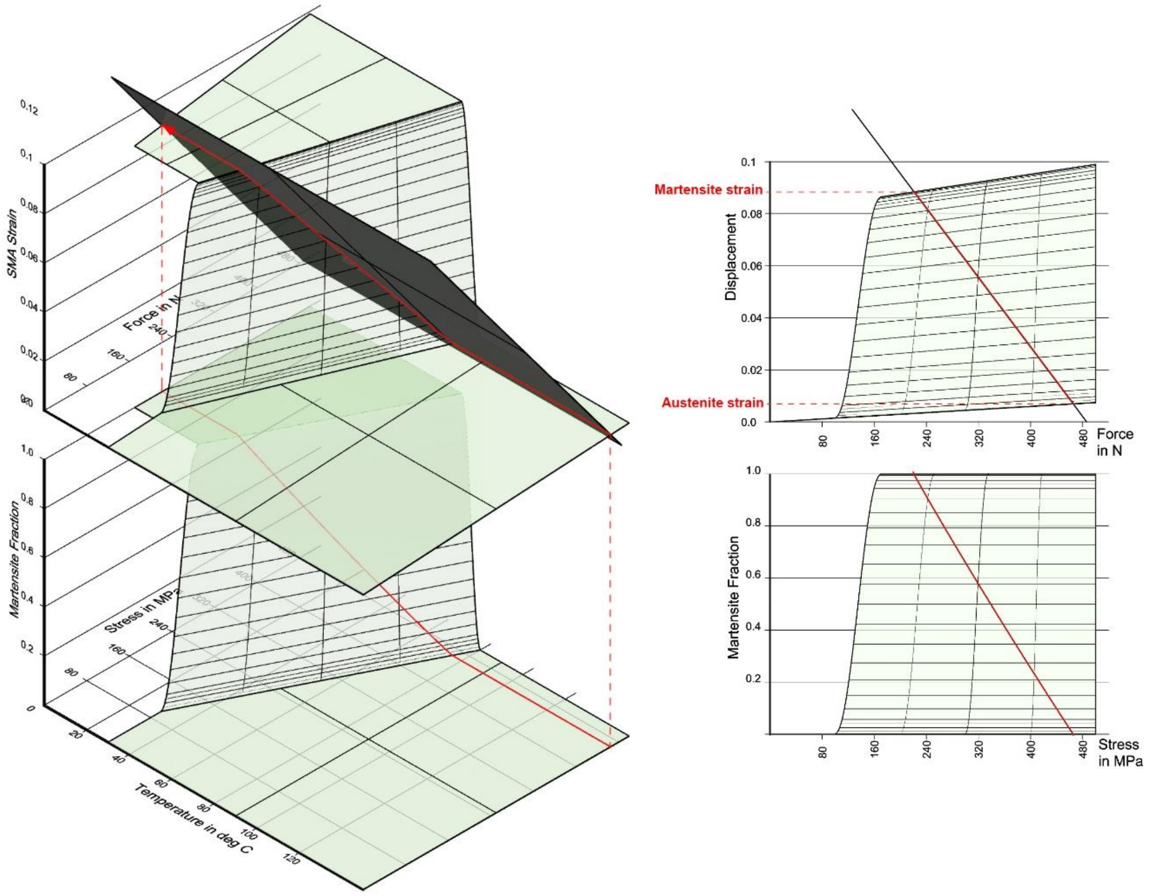

Figure 105: The temperature-stress-strain relationships from Chapter 4, showing an SMA being cooled from full martensite to full austenite whilst subjected to a bias spring. The red curve represents the changing status of the SMA.

Due to the high precision and complex mechanical design that is demanded of the moving parts of the module, it was decided that a separate line of equiry should be done on the 'engine' that animates the module. This sub-chapter describes the investigation, which culminates in a working prototype.

Recall the lessons from Chapter 4 about the stress and strain of the SMA element that is subjected to a bias spring, shown above. If the stress from the spring is not sufficient, the low temperature situation runs the risk of entering the twinned martensite zone of the phase diagram, which has not been modelled, but based on a corrected Brinson model would look like the topography shown below. The new 'hill' that rises up represents the transition from twinned martensite to detwinned martensite when stress is increased. This region has not been built into the parametric tool, but it will not be a problem if the stress from the bias is at a sufficient level to avoid the region. The threshold of stress at the top of the 'hill' is $\boldsymbol{\sigma_f}$. Once this is known via experimental testing, the spring can be designed in order to supply the necessary stress at all positions of the rotation.

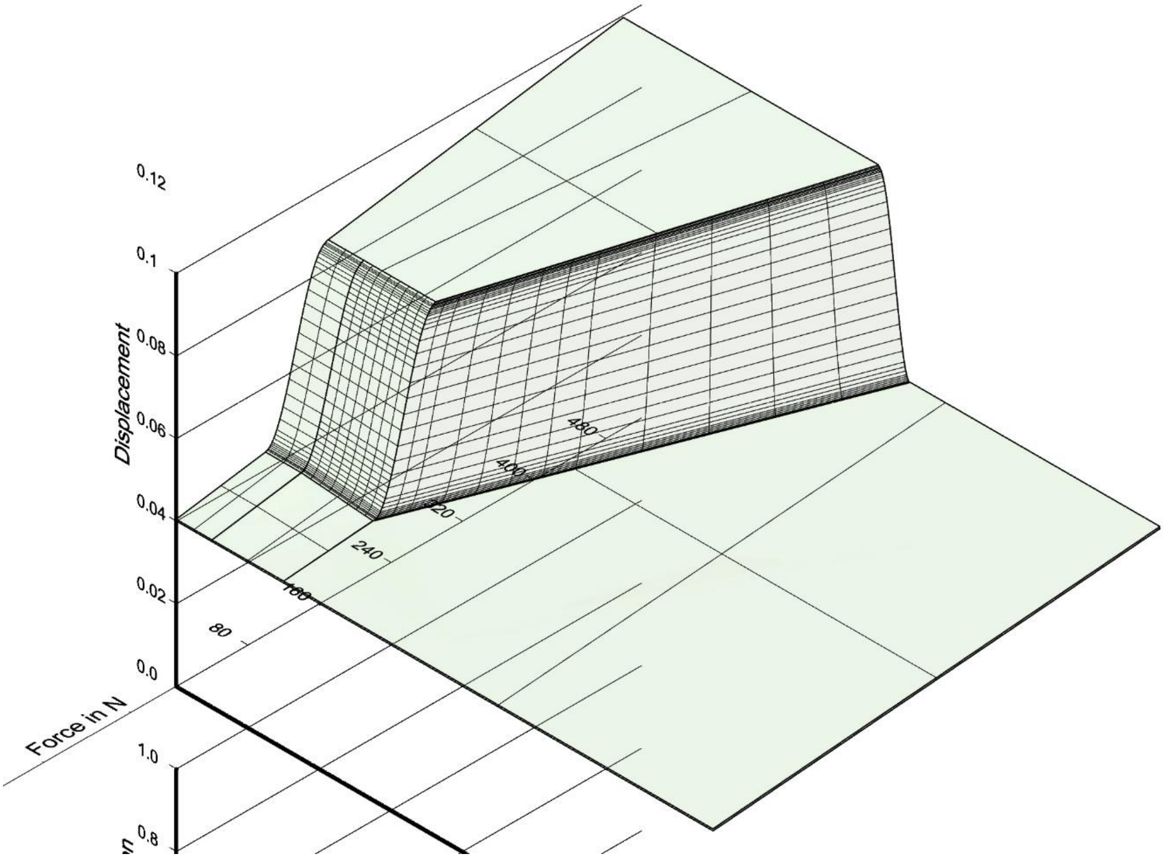

Figure 106: The temperature-Force-Strain topography that includes the twinned martensite region

Material

The SMA to be used in all the physical testing and prototyping for this thesis will be Nitinol, available as *Nitinol (shape memory)* from smartwires.eu.[17] The manufacturer states the product information: diameter: 0.5mm and Activation temperature 45°C ± 5. No other information is given about the material or the four true activation temperatures.

A thin diameter was chosen because a thicker one means much more force is required to achieve the stress, resulting in a much stiffer and heavier prototype body. '45 °C' is currently the lowest available activation temperature for the wire, but an ideal one would be slightly lower, in order to be activated at a temperature at the upper boundary of human comfort.

In the next section, the material will be tested to find out, among other properties, its critical finishing stress for detwinning.

---

[17] https://smartwires.eu/index.php?id_product=13&controller=product&id_lang=1

Mechanical Cycling Experiment to find Critical Stress

Aim and Objective

To do initial tests on the Nitinol material for basic approximate data and most importantly, to find out the approximate finishing critical stress $\boldsymbol{\sigma_f}$. Other useful properties of investigation are the martensite elongation against stress, Young's Moduli and residual strain, and how all of these parameters vary with multiple cycles.

Set Up

Preparation: A nail was secured onto a tape measure at a certain measurement, in this case 40mm as shown in Figure 107a. A nitinol wire was then clamped onto the tape and nail, so that it was secured in position against the tape at exactly 40mm. This contraption was then suspended so that both the tape and wire could hang down as seen in Figure 108a. At about a meter down the wire, some masking tape was applied and a point on it marked in order to set up a measurable distance. Below this, the nitinol wire was wrapped tightly around a wooden cylinder and then clamped as seen in Figure 108b. The clamp was used for attaching a bag that could hold varying amounts of weight in order to stress the nitinol wire in tension. To ensure the test did not start out with detwinned martensite due to accidental stressing, the sample was passed through boiled hot water to ensure it became austenite and then subsequently cool into twinned martensite at its 'natural' length. The first reference distance was then measured by reading off the tape at the marked point and subtracting 40mm. Note that it was measured whilst the wire was being hung, so that the weight of the clamp, wooden cylinder and bag would apply a small stress on the wire. The measured weight of the hardware, 0.75 kg exact, meant that 37.5 MPa was induced while measuring, so there would be a small amount of strain present. This was deemed more accurate than measuring the wire at zero stress, as it tended to curl. The strain from 37.5MPa is assumed to be negligible, as the young's modulus should be around 20 GPa for martensite, and this results in a 0.2% strain, or 2mm elongation per meter. Compared to the eventual results, this would represent 2% of the highest elongation length.

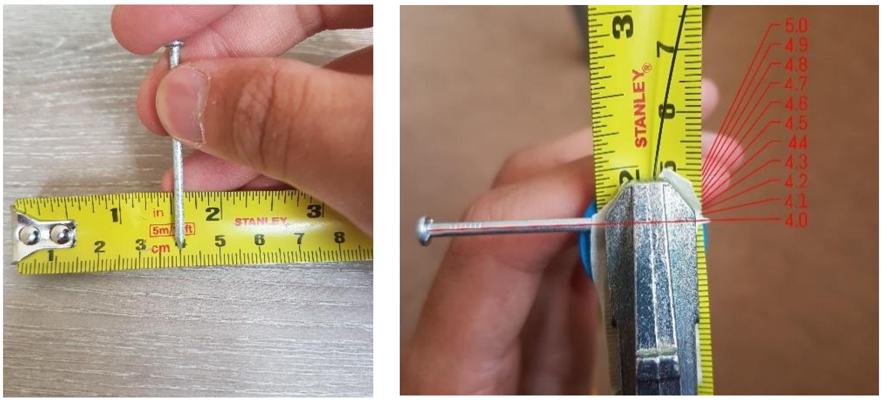

Figure 107: a) the nail is secured onto the tape at 4cm b) the nitinol wire is clamped against the nail, so that it is held in place at the 4cm position of the tape.

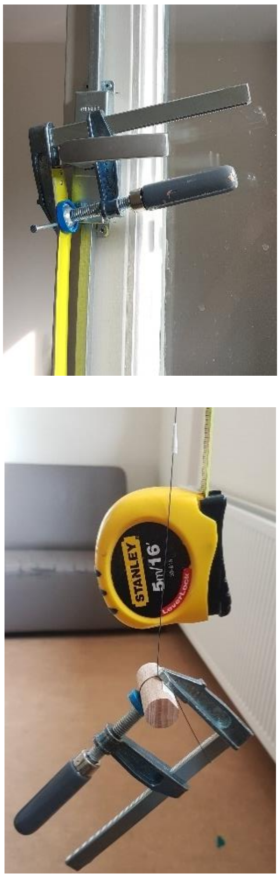

Figure 108: a) the clamp to secure the nitinol wire to the tape at the top. The clamp also allows the contraption to be hung. b) the marked masking tape for taking length measurements, and the clamp and wooden cylinder at the bottom for attaching weights

Test

The suspended wire was incrementally loaded with 0.25kg weights to achieve different wire stresses. A starting weight of 0.7kg was used (taking into account mass of the attachment hardware), and the highest weight was 4kg. An electronic household scale with a precision of 1 gram was used for measuring and verifying all weights in the experiment.

For each added weight, the new length of nitinol wire was measured and thereby the strain of the material could be calculated. In between each new load, the wire was unloaded back to 750g to see how much residual stress had built up. The new length at these unloaded moments were also measured to give an indication of the progress of transformation towards detwinned martensite. This could be inferred by dividing the end residual strain by the residual strain at that moment.

During the experiment, it was found that the wire took considerable time to reach a new length, as it slowly creeped into position. A timer was therefore used to measure the time and to make a reading at a maximum of 2 minutes after loading, even if the wire had not stabilised. The exact time taken for stability could not be measured accurately due to the very slow pace.

Once the final stress of 200MPa was applied and then unloaded and measured, the wire was taken down and reset back to austenite with boiled hot water to recover as much of the strain as possible, and the experiment repeated after allowing time for the wire to cool back down to twinned martensite. This was done 5 times.

Results and Observations

The graph showing the progression of elongation at higher stresses is shown below, for the 5 tested load cycles.

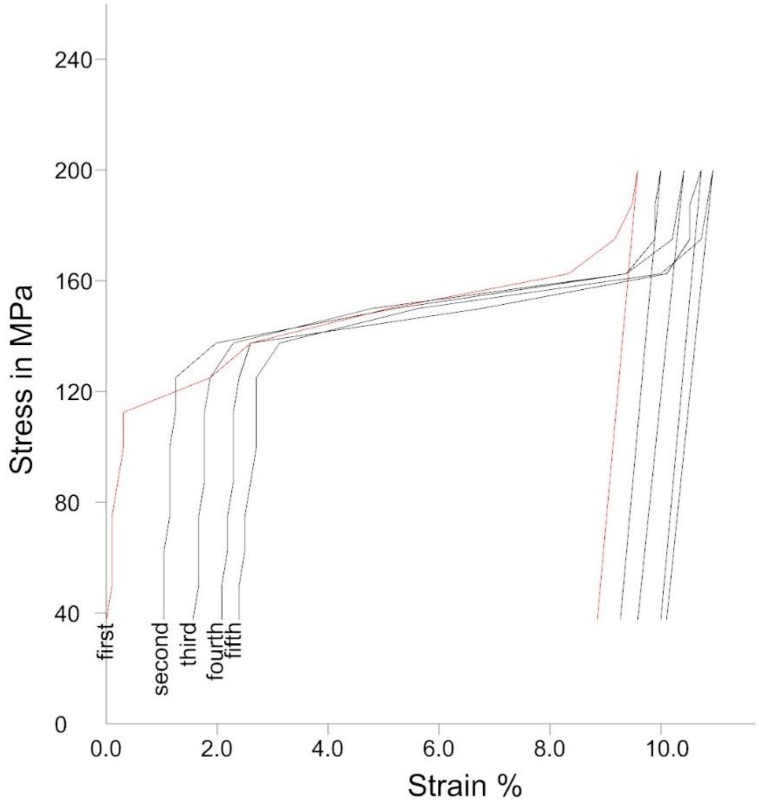

Figure 109: The strain of the nitinol wire against stress, for 5 cycles

For each cycle, some key parameters were measured such as the start and end length. The recovered strain was measured as well as the Young's Modulus of the detwinned martensite phase. The latter was inferred by the values of stress and strain at loads of 4kg and 0.75 kg at the end of the cycle. They are as follows:

1st cycle:

Start SMA length	940 mm
Recovered strain	n/A
End SMA length (unloaded)	1045 mm
Detwinned martensite Young's Modulus	24 253 Mpa

2nd cycle:

Start SMA length	970 mm
Recovered strain	88.2%
End SMA length (unloaded)	1049 mm
Detwinned martensite Young's Modulus	24 346 Mpa

3rd cycle:

Start SMA length	975 mm
Recovered strain	93.7%
End SMA length (unloaded)	1052 mm
Detwinned martensite Young's Modulus	21 363 Mpa

4th cycle:

Start SMA length	980 mm
Recovered strain	96.1%
End SMA length (unloaded)	1056 mm
Detwinned martensite Young's Modulus	24 508 Mpa

5th cycle:

Start SMA length	983 mm
Recovered strain	96.1%
End SMA length (unloaded)	1057
Detwinned martensite Young's Modulus	21 465 Mpa

End:

Final activated SMA length	987 mm
Recovered strain	94.6%

The table below shows additional information for the third cycle, such as the strain as a percentage of the end residual strain, which is a rough indicator of the percent transformation towards detwinned martensite. The full set of results for all loading cycles can be found in the appendix.

	True mass kg	Axial force N	Stress Mpa	Tape measure reading mm	Actual SMA Length mm	Strain compared to start of this session	Strain compared to start of 1st session	strain as % of End Residual Strain
3rd Loading Session	0.75	7.36	37.49	1015	975	0.00%	1.56%	16.30%
	1.00	9.81	49.99	1016	976	0.10%	1.67%	
	0.75	7.36	37.49	1015	975	0.00%	1.56%	16.30%
	1.25	12.26	62.48	1016	976	0.10%	1.67%	
	0.75	7.36	37.49	1015	975	0.00%	1.56%	16.30%
	1.50	14.72	74.98	1016	976	0.10%	1.67%	
	0.75	7.36	37.49	1015	975	0.00%	1.56%	16.30%
	1.75	17.17	87.48	1017	977	0.21%	1.77%	
	0.75	7.36	37.49	1016	976	0.10%	1.67%	17.39%
	2.00	19.62	99.97	1017	977	0.21%	1.77%	
	0.75	7.36	37.49	1016	976	0.10%	1.67%	17.39%
	2.25	22.07	112.47	1017	977	0.21%	1.77%	
	0.75	7.36	37.49	1016	976	0.10%	1.67%	17.39%
	2.50	24.53	124.97	1018	978	0.31%	1.88%	
	0.75	7.36	37.49	1016	976	0.10%	1.67%	17.39%
	2.75	26.98	137.46	1022	982	0.72%	2.29%	
	0.75	7.36	37.49	1019	979	0.41%	1.98%	20.65%
	3.00	29.43	149.96	1046	1006	3.18%	4.79%	
	0.75	7.36	37.49	1043	1003	2.87%	4.48%	46.74%
	3.25	31.88	162.46	1090	1050	7.69%	9.38%	
	0.75	7.36	37.49	1084	1044	7.08%	8.75%	91.30%
	3.50	34.34	174.96	1098	1058	8.51%	10.21%	
	0.75	7.36	37.49	1091	1051	7.79%	9.48%	98.91%
	3.75	36.79	187.45	1099	1059	8.62%	10.31%	
	0.75	7.36	37.49	1092	1052	7.90%	9.58%	100.00%
	4.00	39.24	199.95	1100	1060	8.72%	10.42%	
	0.75	7.36	37.49	1092	1052	7.90%	9.58%	100.00%

Discussion

As expected, in all loading sessions there was a period of elastic deformation at low stress. Past a certain point, the stress-strain curve became drastically shallower as the material transitions at the atomic scale. This always happened between 125 and 175 MPa in all cycles. Interestingly, the loads that caused the greatest transition took considerable time for the wire to stretch out and stabilise to its new length. For example, at 3.25kg loading, the wire very slowly creeped into its new position over a period of about 2 mins 30 seconds. The amount of time taken was about proportional to the magnitude of the transformation in each loading case. This became a good way of realising that the transformation had completed: at the end, the new length was instantly achieved without any movement.

Each loading session caused the austenite/twinned martensite rest length to increase, as only around 90% of the recovery was possible at each activation. The recovery appears to improve over the cycles, but there are not enough tests to confirm this. The Shape Memory Effect was still strong by the final cycle, and the sample had a permanent non-recoverable elongation of 7.0% compared to the starting condition.

200MPa consistently resulted in strains of between 9-11% compared to the length at the start of the first session, but compared to the start of the current session, the strain gets successively smaller each cycle. It would appear that in each cycle, part of the material was losing the ability to become twinned martensite again, and perhaps became an inactive material with reduced shape memory abilities.

The Young’s Modulus of the detwinned martensite phase is very similar for all sessions at between 21 and 25 GPa.

An interesting phenomena that wasn’t expected was a colour change of the SMA from its usual dark grey to a dark yellow. When loaded, some tiny fraction-of-mm lengths of the wire turned yellow, forming a sparse black-and-yellow honeybee pattern. This was a gradual process, and as the wire became more strained, the yellow become denser due to the yellow segments getting longer and new yellow segments appearing. This continued until the entire wire transitioned to a fully yellow colour, thought to be the physical appearance of the martensite. Literature has often observed the microscopic surface texture change, but the macroscopic colour change is not mentioned so much.

Figure 110: Very subtle differences in colour along the length of this partially transitioned SMA

Limitations

Repeat experiments with different wires would be useful to validate the result further. Note that the wire becomes unusable after testing, as the long elongations damage the shape memory effect. It is not known how many cycles it would take before the SMA wire loses its SME, but literature suggests that it would be dozens given the large strain (Gilbertson, 2005, pp. 2-11). Repeat experiments can confirm the consistency of the wire, allowing it to be used in a predictable manner for the engine.

Recommendations for further characterisation

For the prototype, of this thesis, only the critical stress value is needed. However, a complete characterization of the other shape memory parameters, particularly the temperature transitions and the stress influence coefficients, would be necessary in parallel with the design of the solar absorber chamber in order to orchestrate the adaptronic behaviour against the weather.

To build up the temperature transition lines of the phase diagram, there are two alternatives. First, the experiment of this chapter could be repeated at two different temperatures above the austenite finish temperature, and the transition stresses could be inferred. Secondly, the temperature can be loaded slowly at two different constant stresses, to see the temperature transition points. The data from these tests can be used to build the rest of the phase diagram, as shown below.

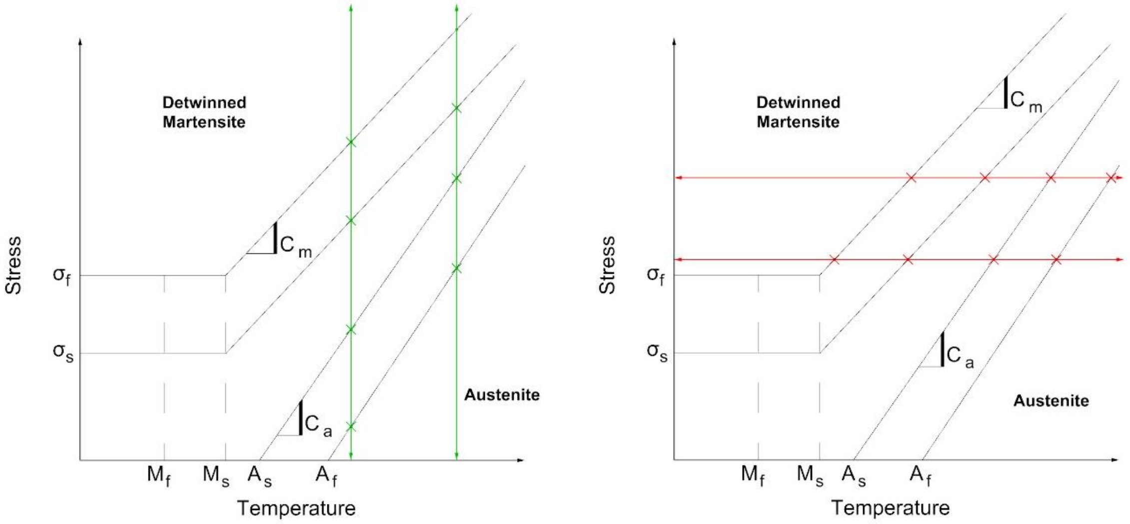

Figure 111: Experiments to characterize the temperature transition paramters of the SMA. In each case, points of the curve are derived and thereby a curve is joined a) stress loading at two different temperatures b) temperature loading at two different stresses

Conclusion

The samples generally agree with findings from the literature. They suffer from accumulative permanent elongation after every cycle. The first session appears to transition at a much later stress point. It is not known what caused this, and whether it is an error. For the rest of the sessions, transition from twinned to detwinned martensite happens between 125 and 175 MPa.

Engine Prototype Construction

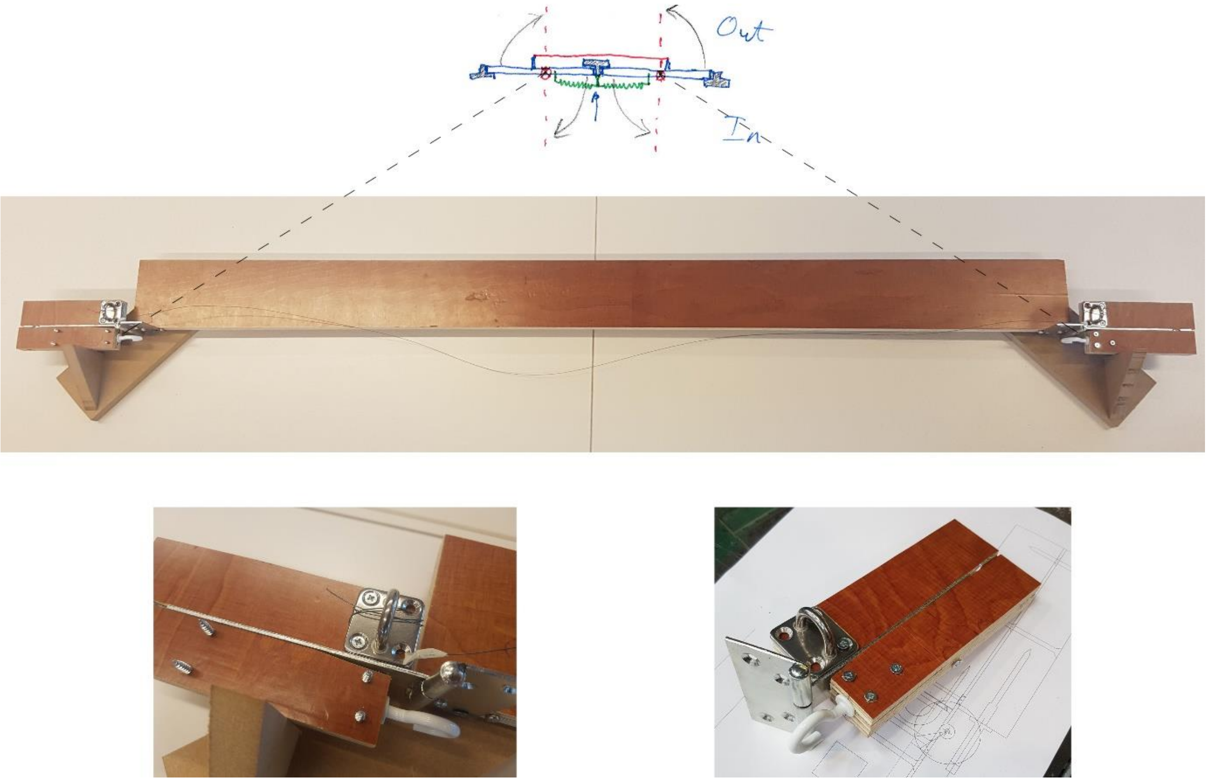

Figure 112: a) Top: the original sketch

b) Middle: The prototype with the corresponding hinge positions shown

c) Bottom left: the rotating arm representing the rotating window panel, with the SMA attached. It is fed through a hole and then clamped to ensure a connection that doesn't move during use. The hook is used for attaching the bias object, such as a spring.

d) Bottom right: the construction of the moving arm, based on a steel hinge.

The goal of the prototype was to actuate two rotating objects using the SMA and a bias force, in such a way that they would move in a similar way to the adaptronic window panels. The prototype is therefore proof of concept and can be adapted to the final design. The prototype is shown above, with the rotating arms in the 'windows closed' position. The 'windows open' position would have the arms pointing upwards in the photo of Figure 105.

As learnt from the earlier adaptronic module prototype, the large timber body needs to be much stiffer than the SMA wire. The rotating arms are made of timber parts with a hook to attach the bias object and a steel plate which can screw-clamp the SMA. Both of these have been positioned precisely so that a wire elongation of 4% can provide the full 90 degree stroke, as in Figure 104. A wooden stop mechanism is placed behind the arm, so that it prevents it from being pulled by the bias spring more than 90 degrees. This is important to ensure it is not over-strained, which would reduce the life of the SMA.

The hinge points are spaced 1245mm apart. A long length has been chosen in order to deliver sufficient change in length of the SMA for animating the arms, as well as to scale up so the construction components can be fitted. The distance from attachment to pivot point in plan view, which is the radius of the applied force, is the same for both SMA and spring, at 17.3mm. They rotate together but are positioned symmetrically around the pivot, so in theory the force from the spring should transfer to the SMA equally.

Joule Heating Test on SMA wire

A reliable and quick heating method was needed to activate the wire. Joule heating is one of the most common methods in SMA projects, so this was tested. The Joule effect is the phenomena of objects heating up when a current is passed through. The wire was electrified with a larger and larger current until full activation occurred.

With a loaded nitinol wire stressed to 200 MPa by a gravity load, 9V batteries were used, and two of them were enough to visibly shorten it, indicating austenite activation.

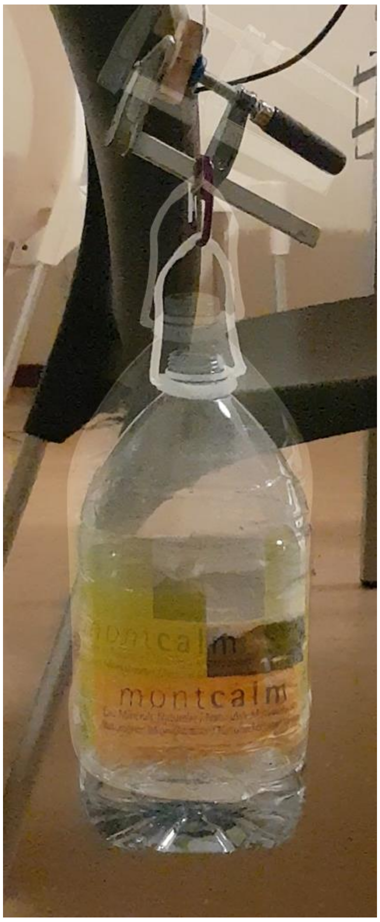

Figure 113: Two overlaid snapshots from a voltage testing video. The 4kg mass being used to stress the nitinol wire to 200MPa. When an 18V current is passed through the wire, it shortens and raises the mass as shown

Prototype Testing with Spring-scales as Bias

Figure 114: the bias spring system fitted onto the engine, which has now been painted black. Notice the turnbuckle in between the 3rd and 4th springs to control the level of applied force

Set-up

A spring system was installed into the engine as a bias force to apply the 175 MPa for detwinning at the martensite phase. It was important to not go far above the needed stress, as it could reduce the fatigue life of the SMA. Recall from Figure 105 that the stress rises in an SMA when it is activated in opposition to a bias spring; as shown by the red curve, this is due to the material shortening as it becomes austenite and pulling the spring further. Springs exert a force proportional to their displacement, so the force and stress in the SMA therefore increases as it displaces the spring. The increase is largely determined by the stiffness of the spring, also known as the K-value, which is a number denoting the Force per distance of displacement. A spring of minimum k-value is therefore preferred to keep stresses in the SMA as low as possible, and it would ideally have a large displacement to compensate and deliver the force necessary to achieve 175 MPa.

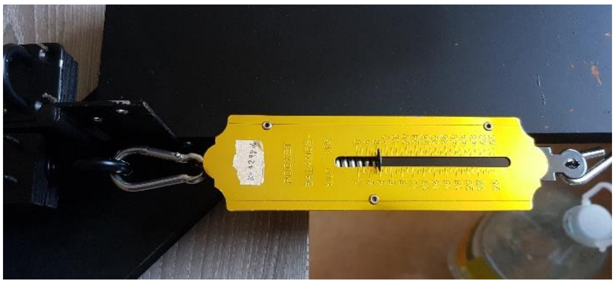

Figure 115: A closeup of a spring-scale device. K-value = 4298 N/m

Five spring-scale devices were placed in series for the spring system. This was done because placing springs in series has the effect of dividing the K-value by the number of springs, for the system as a whole. To ensure that 175 MPa is achieved accurately and not more or less, a turnbuckle is included in the system. This allows a length adjustment, and it is shortened to stretch out the springs and thereby increase the axial force going through them. The k-value for these springs were measured and the hardware modelled in Rhino to ensure accuracy in both theory and practice; the springs have the added advantage of indicating the force going through them, allowing validation of the Rhino model.

In theory, the axial force is transferred via the pivots into the SMA wire. The attachments of both SMA and springs are equally spaced from the pivot and on opposite sides of it, so their axial forces should equalize by consequence of equilibrium of moment forces in a stationary object.

The SMA was fitted into the device at the correct length so that the austenite length would result in an 'open window' state.

Electricity was passed through the SMA device by attaching it at points in the non-stressed portion of the wire beyond the end connections. This was done because it would result in a constant current running along the entire length of the wire, and therefore a more consistent heating. The alternative of attaching it near the end points of the stressed part of the wire itself would have left some millimetres of wire without current, so it would transition to austenite much later than the rest. The rest of the austenite wire could essentially strain the martensite portion in that case, to a point beyond plastic slip.

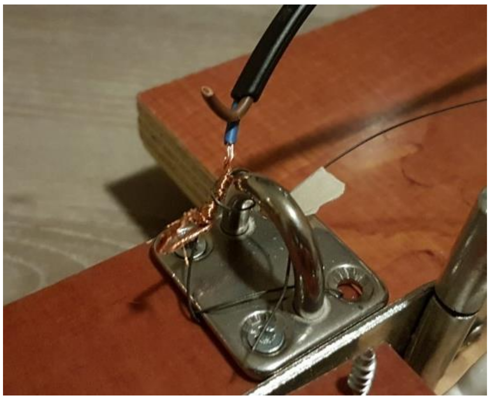

Figure 116: The electrical connection detail, to ensure a consistent current along the stressed portion of the wire. The masking tape is seen in the background, which is used as a marker to attach the SMA with an accurate length.

Observation

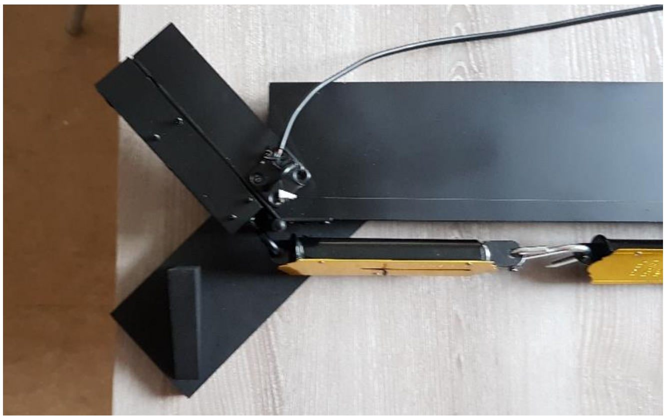

Figure 117: The SMA wire is attached with the spring system in place. The electrical wire connection is shown.

Unfortunately, the force of the spring was only able to pull the wire back partially, as shown above. Even the act of manually forcing the arms all the way back would result in them bouncing back to the approximate 45 degree position. Some mechanical imperfections also meant that the rotating arms were not necessarily rotated symmetrically the whole time. Activation with the Joule effect yielded almost no response.

It became clear that at least a few things were underperforming. It was a possibility that there was friction in the hinges and in the springs. This meant that not much force was being transferred from the actual springs to the SMA. It would also have an effect of adding an additional layer of hysteresis to any response to a change of force or strain from the SMA. The spring friction came from the sliding parts within the mechanism; having an actual spring would in theory result in a frictionless one.

One option would have been to shorten the turnbuckle until the rotating arm were to be pulled back entirely. However, this would be risky because it may apply too much stress and cause permanent plastic slip upon austenite activation. A further problem compounded the setup in that after every thermal cycle, the rest length of the SMA appeared to increase, as was the case in the mechanical loading experiment. This meant that the arm position for the austenite phase would gradually migrate from the open position after each cycle, to something more closed. This would cause the engine to eventually assume a permanent 'open' position, unless the SMA is disconnected, tightened and reconnected. It was not known whether this was caused by an actual lengthening of the wire or a loose connection.

Prototype Testing with Counterweight as Bias

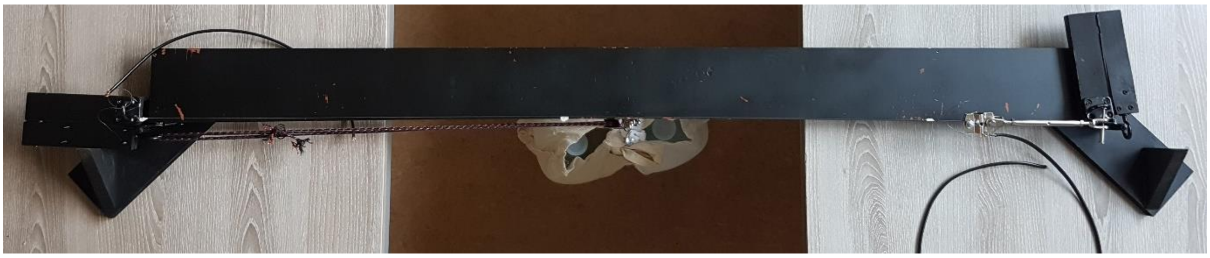

Figure 118: The new set-up, which uses one SMA per rotating arm. The left is active in this photo, whilst the right arm is not

Figure 119: the counterweight and pulley system

Set-up

In the next test, a counterweight was used as the bias force instead of a spring, provided by water bottles suspended from a pulley that fed some ropes to the rotating arm. Multiple ropes were chosen because together they would be less elastic; this would help maintain constant stress when there is movement from the SMA. Another change was to animate just one rotating arm with the SMA instead of both, so that all of its length change was dedicated to just one rotating movement instead of two. The ratio of SMA length to hinge radius was now much greater, leading to a longer stroke length for delivering actuation angle.

Figure 120: The attachment to the left and right SMA ends. The right hand side is now fixed to a stationary point instead of to the other rotating arm, with a turnbuckle to allow adjustment.

The SMA wire spanned across the whole prototype to actuate one arm. According to the Rhino model, a 90 degree angle rotation required a length change between the austenite and martensite states of 2.6%, well within the 8% ability and 4% recommended level for good fatigue life.. A turnbuckle was now applied to the SMA wire to address the problem of it constantly lengthening after each cycle. The intention is that the turnbuckle can be adjusted after each thermal cycle, to compensate for the increased rest length. After a number of cycles, the material should stabilise according to the literature, and the engine can then be used reliably.

The initial counterweight of 4kg (3.5kg is needed within the SMA to achieve 175MPa) was not enough to bring the arm into a fully closed position, so the assumption was that there is friction at the pulley and/or the pulley and hinge. The activation did not yield much of an angular change either.

Test

The test set-up was Joule heated with varying counterweights and eventually with a pre-strain to experimentally find a high angular stroke. In each case, the angle in the cold phase was measured after letting the cold position settle and then a 18V current applied to move the arm. The end angle was measured along with some other related parameters to assess the effectiveness of the set-up. With the help of modelling in Rhino, it was possible to calculate the amount of strain that had brought about the change in angle. Before each test, the turnbuckle was adjusted to remove slack and bring the unloaded position back to the 'open window' position.

In the penultimate test, a pre-strain of a few millimetres is applied to the SMA wire while there is no counterweight attached and the arms are in the open-window position.

In the final test, a pre-strain is applied so that the rotating arm in the martensite position is kept at 90°, and an extra battery is added to the circuit, to bring the number of 9V batteries to 4, for a total nominal voltage of 36V.

The test results can be seen on the next page.

Figure 121: The set-up of the test. The connection of the wire is shown.

Results

Test 1: counterweight of 4.75 kg (46.6 N)

Angle in martensite phase: 67.2°
Angle in austenite phase: 43.5°
Stroke angle: 23.7°
Change in SMA length: 7.07mm
Austenite rest length: 982mm
SME stroke length: .07%

Test 2: counterweight of 5 kg (49.1 N)

Angle in martensite phase: 71.9°
Angle in austenite phase: 47.3°
Stroke angle: 24.6°
Change in SMA length: 7.2mm
Austenite rest length: 992mm
SME stroke length: .75%

Test 3: counterweight of 5.5 kg (54.0 N)

Angle in martensite phase: 67.8°
Angle in austenite phase: 34.6°
Stroke angle: 33.2°
Change in SMA length: 9.9mm
Austenite rest length: 1000mm
SME stroke length: .99%

Test 4: counterweight of 6 kg (58.9 N)

Angle in martensite phase: 90.0°
Angle in austenite phase: 50.0°
Stroke angle: 40.0°
Change in SMA length: 10.83mm
Austenite rest length: 1003mm
SME stroke length: 1.08%

Test 5: counterweight of 6 kg (58.9 N) with prestrain of 4-8mm

Angle in martensite phase: 78.0°
Angle in austenite phase: 28.2°
Stroke angle: 49.8°
Change in SMA length: 14.6mm
Austenite rest length: 1013mm
SME stroke length: 1.44%

Test 5: counterweight of 6 kg (58.9 N) at 36V with prestrain to keep martensite phase angle at 90°

Angle in martensite phase: 90.0°
Angle in austenite phase: 28.7°
Stroke angle: 61.3°
(Change in SMA length, austenite rest length and SMA stroke length not measured)

Observations and discussion

Figure 122: Testing the actuator stroke performance for the 6kg, 4-8mm prestrain, which resulted in a 49.8° angle

When the counterweight was first attached to the arm, it gradually and slowly settled into the new position over about a minute.

The increasing counterweights gradually pulled the arm further and further back, and 6kg was the first counterweight able to pull from an unloaded open window position to a fully closed loaded position in the martensite phase. Overall, an increase to the counterweight consistently resulted in greater actuation angles. The penultimate test with the prestrain further increased the performance, to 49.8°. An increase to the counterweight beyond 6kg was not carried out, as the structural limit of the engine body was not known. The final test with both prestrain and increased voltage resulted in the highest activation of 61.3°.

Throughout the test, the austenite rest length continued to increase by a small amount each time. That particular sample had been through about 40 cycles and gained roughly 8% of permanent non-recoverable strain compared to its factory condition. By the end of the test, the SME was still apparent but the wire felt thinner. It is not known if the rest length would stabilise in the long term before failure. A subsequent inspection of the force on the wire during different angles of the arm was done, by attaching a spring-scale to the wire end and manually pulling the wire against the counterweight whilst reading the force. This revealed that 78.4N were being exerted on the SMA wire during the activation movement, in contrast to the 58.9N counterweight. The excessive force and resulting high stress of the 79.4N may be the reason for the relentless elongation of the wire after every cycle. The high force indicates the presence of friction in either the pulley or the hinge. The pulley could be removed by either rotating the entire prototype 90 degrees so that gravity is already pulling in the correct direction against the arm, or by replacing the counterweight with a frictionless spring. The latter was done for the next test.

Recall that in the mechanical load test of Figure 109, a 4kg gravity load on a suspended wire was enough to strain the wire 9-11%. However, 6kg is needed to stretch or return the wire back to the strained 'closed window' position. This is also likely caused by the same friction just mentioned.

The maximum wire stroke length achieved was 1.44% in the penultimate test (this figure was not measured in the final test). This is in contrast with the 4% recommended from literature, and the 2.6% that would have achieved a complete 90° rotation in this case. There is some slight movement in the connections between the steel hinge and body when it is pulled. Other movements might exist. A potential problem with the hinge mechanism is that the force is not applied at the optimum vector for rotating the arm when the connection is in line with the pivot point. This effect is seen in Figure 123.

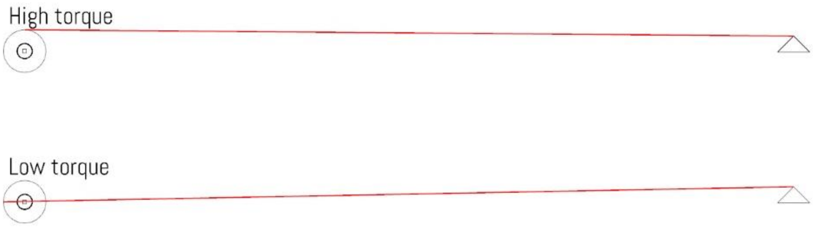

Figure 123: the torque exerted by the tensile SMA piece is high at some angles and almost zero at the farthest/nearest reach of the rotation. Beyond a certain range of angles, the SMA-bias system will not be able to overcome the friction in the hinge

Conclusion

An angular stroke of 61.3° was achieved using a set-up of a 6kg counterweight acting on one rotating arm. This best result was yielded by the final test, which had the highest voltage and a prestrain which allowed for a 90° arm position in the martensite phase. The act of prestraining the SMA also increased the stroke angle. The SMA wire was getting longer each time, which might indicate that the stresses are too high during a portion of the stroke, or perhaps the wire would stabilise at a new austenite rest length after many more cycles.

Prototype Testing with Springs as Bias

Figure 124: A standard spring of low stiffness is used as the bias to actuating one arm

Set-up

In the final arrangement, steel springs of low stiffness were used to deliver the bias force, thereby eliminating the frictional sliding parts of the spring scales from the first set-up as well as the pulley in the second.

The SMA length in the austenite phase was 834mm, so a 3% change in length would achieve the 25mm displacement for the 90 degree rotation. A turnbuckle was placed at the end of the SMA wire to stretch the wire as needed at the end of each cycle, given the fact that it gets permanently slightly longer each time. A 5mm prestrain is also applied, as this was found to greatly improve performance in the previous setup.

Figure 125: testing the force transmission loss between spring and SMA, due to the hinge

It was suspected in the previous experiment that there was some transmission loss of force between the spring and the SMA wire via the hinge. This was quantified to determine how much stronger to make the spring in order to achieve the 175MPa needed in the SMA. An accurate spring-scale with a precision of 0.1kg was used to measure the axial force that the SMA would undergo as the arm is rotated against the spring. The spring-scale was hooked to the end of the SMA whilst the arm had the bias sprint attached, and then the arm was opened and closed slowly by pulling on the spring-scale whilst reading the forces. The forces were much higher in the opening direction than in the closing direction, for example exhibiting 5kg (49N) of force to open, and 2.8kg (27.5N) of force in the closing motion, an increase of 79%. Using the latter number to compare with the actual force in the spring of 42.8N, a transmission loss of 37% was found in the cooling portion of the cycle. The springs were adjusted accordingly to compensate in order to aim for the 175 MPa stress. Note that the hinge used in the prototype may not be representative of hinges in general. Some may exist with much less friction.

The springs used were steel TR1160 from Alcomex. A low stiffness and high displacement limit was chosen. They were tested for their k-value and effective rest length using a tape measure and weights in order to ensure its performance: 0.223 N/mm and effective rest length of 262mm. Two of these were used so that the effective k-value of the system was halved to 0.112 N/mm (compared to the combined value of 0.860 N/mm of the five spring-scales). Once again, a turnbuckle was placed in between to moderate the spring displacement and force. A 25mm change in length of the spring during activation would therefore cause a 5.58N increase in force, which translates to an increased stress in the 0.5mm SMA wire by 28.4 MPa.

Taking all parameters into account, each spring needed to be around 489mm in order to achieve the 175Mpa in the SMA during the cooling movement. This was tested, along with lower spring extension values. It was not possible to test for longer extensions due to size constraint of the prototype. Note that the stress in the heating movement is expected to be 79% greater, so a stress of 313MPa can be expected during activation.

To eliminate the possibility of the battery running out of power during the experiment, a multimeter was used to monitor the voltage and ensure it did not drop far below the starting condition.

Results

Approximate voltage in all tests: 32 Volts

Test 1 [204531.mp4]
Length of each spring in closed state: 489 mm
Bias force in closed state: 50.6 N
Start angle: 0°
End angle: 60.7°
Actuated angle: **60.7 °**

Test 2 [150250.mp4]
Length of each spring in closed state: 472 mm
Bias force in closed state: 46.8 N
Start angle: 0°
End angle: 32.6°
Actuated angle: **32.6°**

Test 3 [193651.mp4]
Length of each spring in closed state: 466 mm
Bias force in closed state: 45.5 N
Start angle: 5.9°
End angle: 48.7°
Actuated angle: **42.8°**

Test 4 [151147.mp4]
Length of each spring in closed state: 459 mm
Bias force in closed state: 43.9 N
Start angle: 0°
End angle: 43.9°
Actuated angle: **43.9°**

Test 5 [152205.mp4]
Length of each spring in closed state: 459 mm
Bias force in closed state: 43.9 N
Start angle: 9.1°
End angle: 57.8°
Actuated angle: **48.7°**

Conclusion

Testing the forces going through the hinge found two phenomena: firstly, that during a cooling motion, there is a transmission loss of force from spring to SMA, of 37%. This is useful to know so that the spring can be extended further and provide a greater force to compensate and ensure SMA detwinning is achieved. Secondly, the force in the SMA during the heating motion will be 79% greater than the force during the cooling motion. This means that there will be a peak stress in this movement. For 175 MPa required in the cooling phase, it will be 313 Mpa.

Not all hinges have equal friction; there may be some available which have almost none. The study however has produced a method to account for it if it exists; it can evidently have an adverse effect on the performance if it is not addressed.

When the spring was first applied to the SMA and arm in test 1, the arm slowly moved for the first portion of the angle, before speeding up in the middle and slowing down again for the last portion. The middle portion is assumed to be a transformation event from twinned to detwinned martensite. This test proved to be most successful actuating an angle of 60.7^o, rivalling the top performance of the counterweight test of 61.3^o. A prestrain of 5mm is effective for ensuring high stroke; this translates to 0.6%, given the 834mm SMA length.

Solar Activation Test

Goal and objective

To find out whether the SMA is able to transition from martensite to austenite via environmental stimulation of the space inside a solar absorbing device

Set-up

To see whether it is possible to activate the engine using just external environmental effects, a solar absorber device was placed around the SMA. Early ideas involved wrapping two small tubes around the SMA, a black inner one of low insulation and a transparent outer one of high insulation. This would cause the greenhouse effect within the tube, as it would receive solar gain and then trap the heat inside.

However, this idea was problematic because the ends of the SMA needed to heat up at the same rate as the rest of it, and the detailing of the solar absorber at these sites would be difficult. The danger of having martensite coexisting with austenite on the stressed wire could result in the martensite being strained and stressed to a much higher amount, and possibly damaged by plasticly slipping. Therefore, instead of putting a solar absorber into the engine, the entire engine was put into a solar absorber, as shown below.

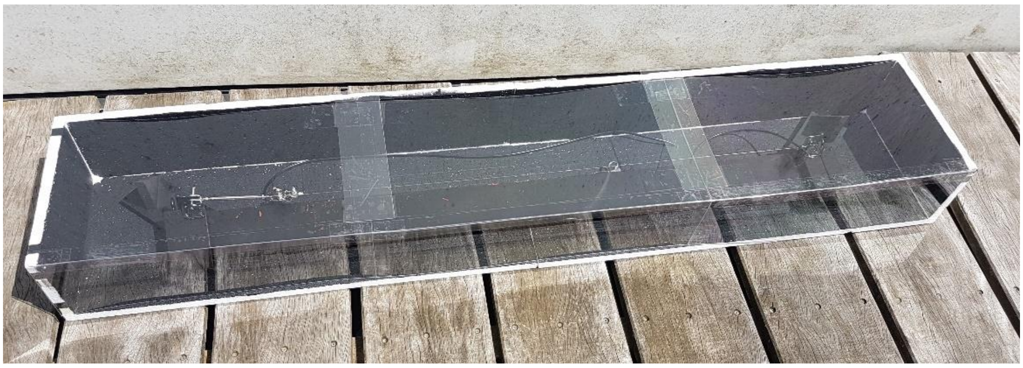

Figure 126: The adaptronic engine placed within a solar absorber

The solar absorber is made of 2cm polystyrene with acrylic black paint paint, with a 1mm plexiglass cover to let in the sunlight. The dimensions are 1640 x 316 x 171 mm.

Test

The engine was placed into the solar absorber box without a counterweight or spring, so there were no bias objects. The SMA wire was attached so that it had a slight tension in the open-window mode. It was stretched manually by pulling the rotating arm back and pulling upwards on the middle of the wire, and then released so that it was slack. The cover was then placed on top to allow the box to heat up. It is therefore a zero-stress activation test.

The test was carried out on 12th May 2018 at 13:30. The weather was sunny and the temperature was reported to be 23 °C (high) and 21°C (low), with wind at 13 km/h.[18] The solar absorber was placed in an enclosed courtyard with direct exposure to the sun.

---

[18] https://www.timeanddate.com/weather/netherlands/delft/historic

Results

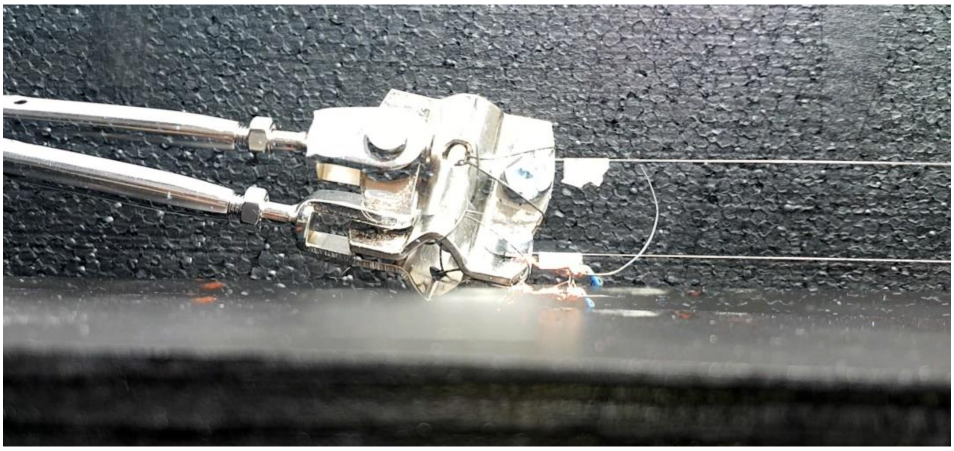

Figure 127: The image is an overlay of two video snapshots with a difference of 80 seconds: The activation of the SMA engine by environmental stimulation, largely solar power.

The SMA successfully activated and started to recover its tension virtually immediately after the transparent cover was placed on top. It took around 80 seconds to fully activate.

Discussion

The result shows great potential for building a heat chamber that facilitates a temperature-sensitive adaptronic engine. It is not known whether the material completely transitioned to austenite in the eventual stabilised position, but it is a solvable problem if not. The solar absorber is quite a simple construction with gaps in the detailing and very low-tech approaches. Constructing a better one with higher temperatures is very much possible.

There remains the question of whether the SMA can be activated by solar power when the bias force is applied. With the exact material being used for this study, it may or may not be possible. However, in practice the manufacturer can tweak the atomic composition of the nitinol so that it results in the ideal set of transition temperatures to suit the range of values in the heat chamber.

Furthermore, the adaptronic façade module should only open up in times when the building is overheating in the hot months that require cooling. The heat chamber needs to therefore differentiate these times as best as possible, as has been attempted by (Leung, 2014).

Conclusion

It is possible to actuate a nitinol wire using the environmental conditions within a solar absorber device such as a black box with a sun-facing transparent cover.

With this knowledge, it is possible to begin the final design of the adaptronic panel and to downscale the large engine into the necessary components at the minimal sizes.

6. Final Design

Module Size and Atrium Structure

In the final design, the four-quadrant window module is composed of four centre-pivot windows made from standard aluminium profiles for simplicity and ease of manufacture. The designed hardware is attached to the outside of these four rotating panels.

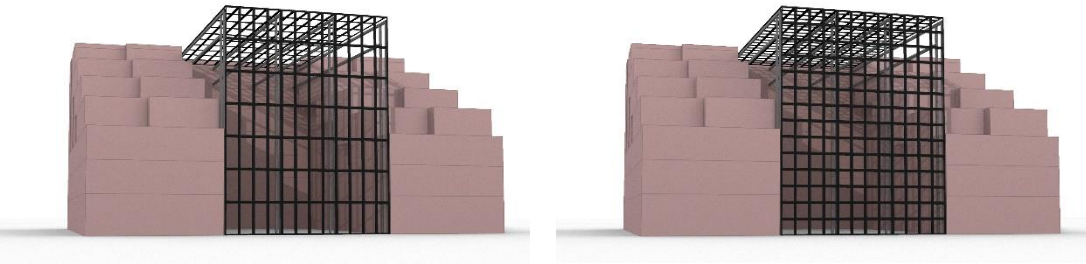

Figure 128: modelling the panel sizes onto the court of the Gerschwin Brothers building. One module is made of 4 panels, 2x2. Two iterations are shown, a) one with double-storey modules and the other with b) single storey modules.

The size of each façade module was the first thing to be decided. It had to suit functional requirements as well as the context, the Gerschwin Brothers building. It was found that a glazing panel height of half a storey would suit the 2x2 module quite well, so a single module would fit into one storey as seen in Figure 128b. The alternative was to have a glazing height of one storey, seen in Figure 128a. These taller glazing units were aesthetically much better, however it was introducing more structural demands which were unnecessary for now: bigger panels are heavier, receive more wind load and place greater demands on the SMA vs bias system. The single storey iteration of Figure 128b was chosen. The module grid sizes chosen to suit the context are shown below.

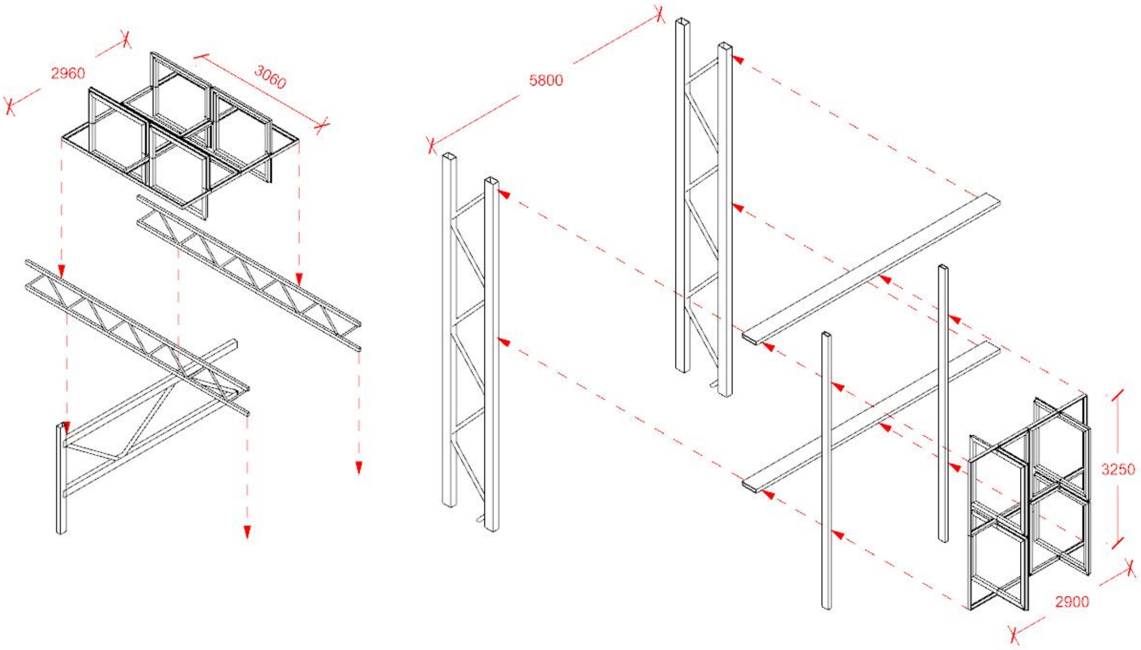

Figure 129: The primary, secondary and tertiary structure of the atrium roof and walls, on which the adaptronic window modules are mounted

Glazing Units

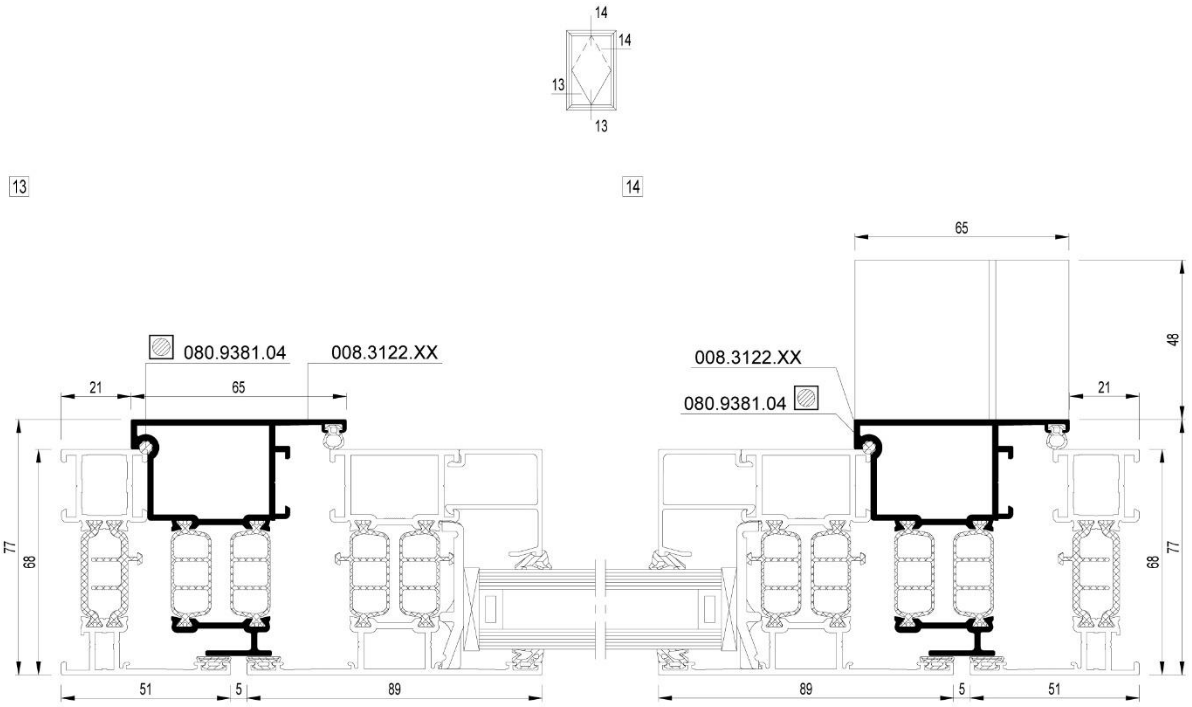

Figure 130: Standard profiles from the Reynaers Aluminium centre pivot window model of CS77-012 will be used for the adaptronic panels. Drawings from online catalogue[19]

The glazing unit is adopted from the *CS77-012* centre pivot window of *Reynaers Aluminium*. These profiles can be used to arrange four panels next to each other. The frames can be attached to the larger structure of the atrium with vertical mullions, which in this case will transfer to horizontals before transferring to the primary truss structure. The hinge mechanism will be custom designed for this thesis, and the engine will act upon the panels via the hinge. The locations on the module where the custom hardware is to be attached are shown in the next page, in the two desired settings of open and close. The intention is to design the hinge and engine system so that these positions can be delivered.

---

[19] Image Credit: Reynaers Aluminium

https://www.reynaers.nl/sites/default/files/public/product/cad/cs%2077%20%28windoo%29%20section%20drawings%20architect%20catalogue%20nl.pdf

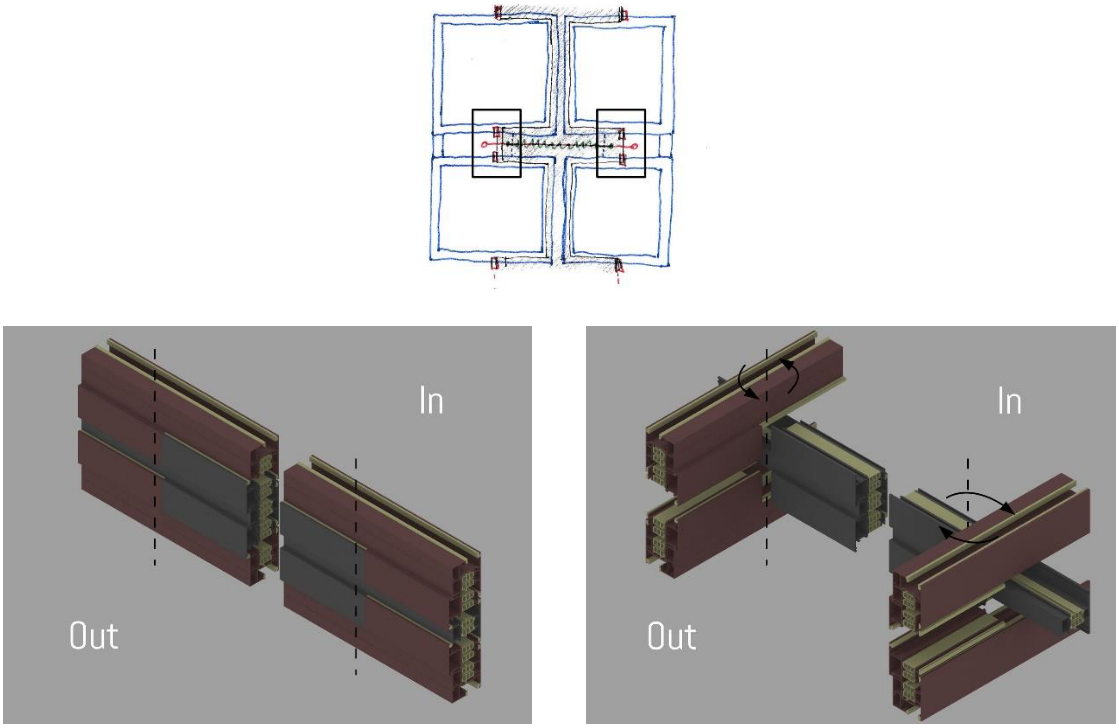

Figure 131: Below left and right: The desired open and closed positions to be achieved with the adaptronic engine, situated in the region of the module as shown in the top image

The general strategy is shown in the sketch of Figure 131. For each of the four window panels, two hinges support and allow for the pivoting motion. One of the two hinges is always located at a point on the engine, and it provides the actuation force.

The hardware to be attached is constrained to the rectangular black areas shown in the visualsations (partially cut away). The large central rectangular region measures 1480 x 159 mm in both the vertical and the horizontal versions of the module.

Adaptronic Engine

The images and drawings of this subchapter will focus on an adaptronic engine for a vertical façade module, shown in Figure 132. Note that due to the identical widths of both the roof and wall panels, a similar engine design can be fitted to both versions, with a rotated hot box in the roof design so that it reacts the same way to solar conditions. The strategy is to have the entire module prefabricated, so that precision attachments can be made without the uncertainties and difficult conditions of the building site.

The engine is essentially made up of two axles at opposite ends of a long steel spine, each one with its own nitinol wire vs spring system which orchestrate the movement in the same way as the spring-based prototype. A spring-based one was chosen in favour of the counterweight option because experiments showed that it could perform equally well. It is also much lighter and requires less space. The custom hardware can all fit into a box of dimensions 1560 x 160 x 67 mm (w x h x d).

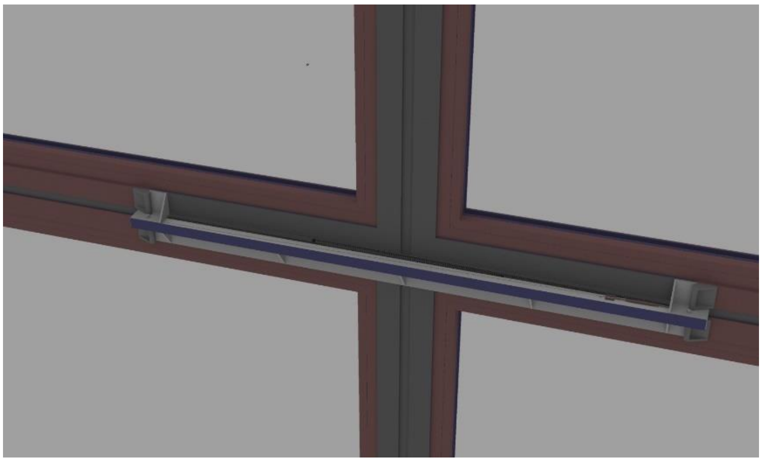

Figure 132: The adaptronic engine applied to the windows, closed position. Viewed from exterior

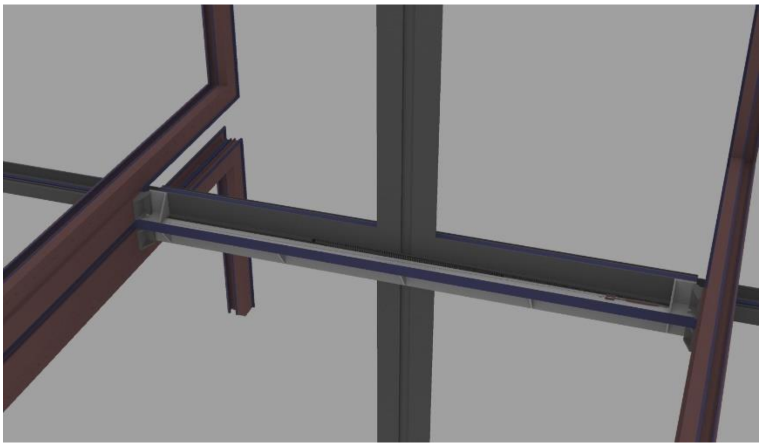

Figure 133: The adaptronic engine applied to the windows, open position. Viewed from exterior

Each SMA-axle-spring system can be effectively treated as a separate mechanical system, but they are subjected to the same temperatures as they are in the same chamber. The nitinol wires shorten when heated, thereby turning the axels which are attached to the window panels. In the next images, the construction sequence is shown to illustrate how the device is composed.

1)

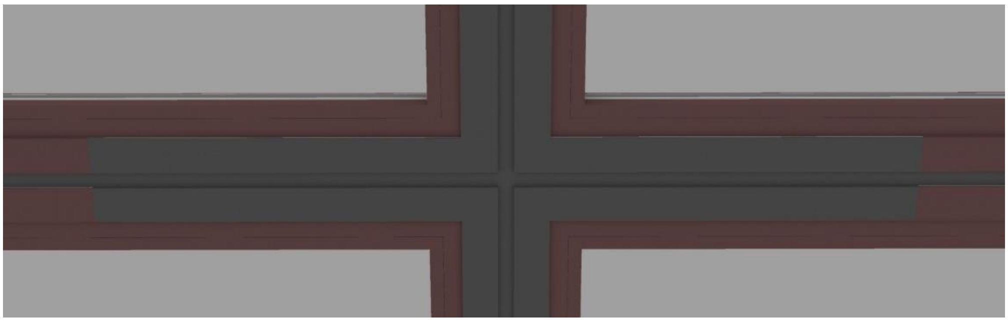

Figure 134: Starting condition: the standard pivot window profiles and window panels, currently not fixed to each other but awaiting a hinge mechanism to hold them in place. The black represents the stationary part of the frame and the red represents the pivoting parts of the profile

2)

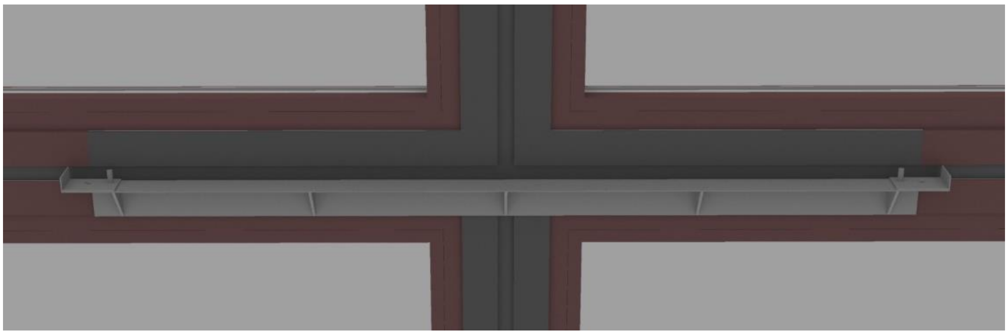

Figure 135: The spine of the engine is screwed onto the stationary part of the frame. It is made of welded steel parts. On the left and right ends are holes drilled into the horizontal surface, in which the axle is inserted for the next step. A nylon film is needed to separate steel from the aluminium profile to prevent increased corrosion.

The rest of the construction sequence zooms into the right side. The construction on the left side is largely symmetrical, except for the placement of spring attachments near the middle of the spine. The process therefore is mirrored at the same time on the left.

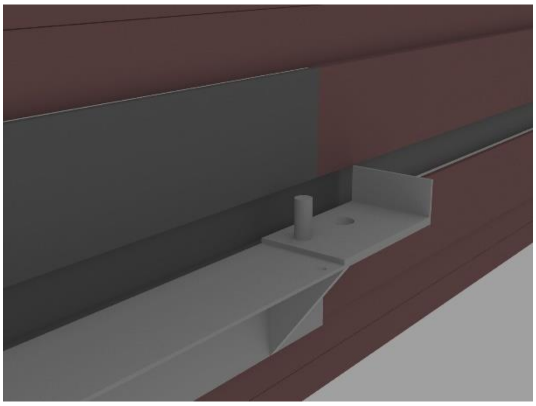

On the left and right ends of the spine are pre-drilled holes, in which the axle is inserted later on.

3)

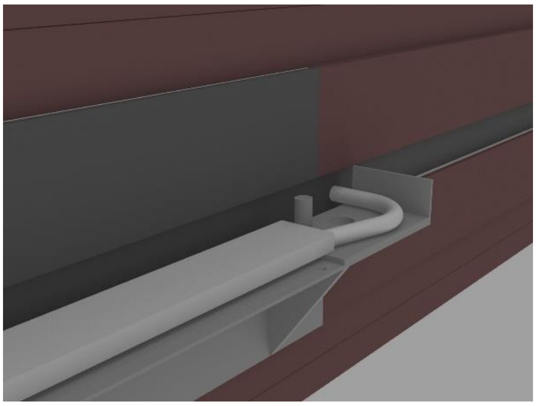

A plastic tube concealed within the aluminium profile is fed through into the chamber. It is connected to a steel rectangular pipe of 35x10mm. This behaves like a cold radiator, passing tap water to cool down the chamber and nitinol in case the windows need to closed by the user. A plastic tube at the other end of the pipe carries water away.

4)

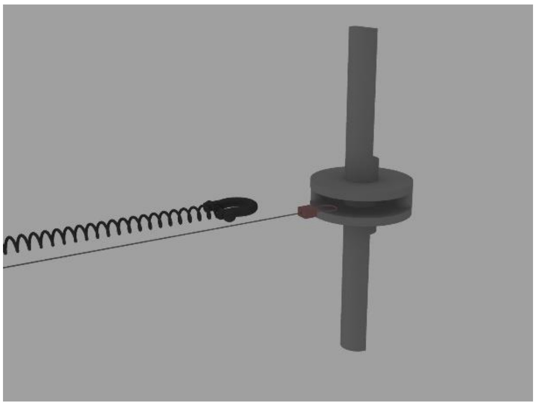

Preparation of the axle mechanism. The axle, which is a single cast piece, is fitted with 0.5mm nitinol wire and a spring. The wire is looped around a column between two discs and then crimped into itself. The spring also attaches to another column between the disks via bow shackle, positioned at the opposite side of the pivot in relation to the nitinol attachment.

5)

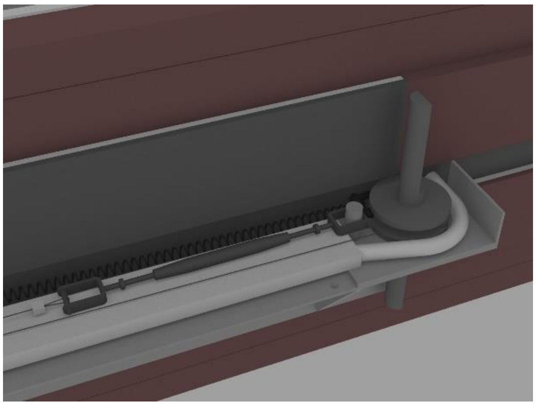

The axle is inserted into the hole with the nitinol and spring attached. The nitinol wire belonging to the other side of the engine can be seen here, attaching to a turnbuckle that is held in place at a protruding feature of the spine. The turnbuckle allows for minor adjustments to finetune the wire length after installation. About 0.6% prestrain is recommended, according the prototyping findings

6)

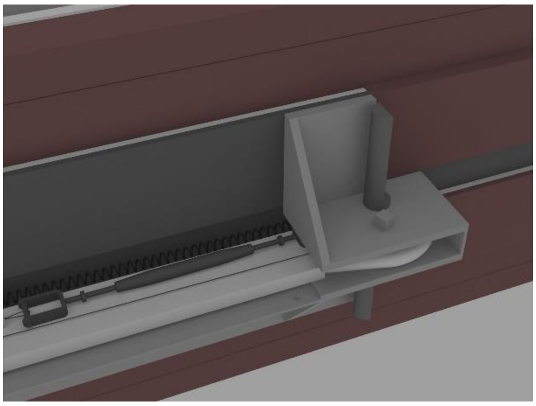

The top axle support is positioned to secure axle. It screws onto the stationary part of the frame. Note the protruding cube feature, which acts like a door-stop to prevent the window panels from rotating more than 90^0

7)

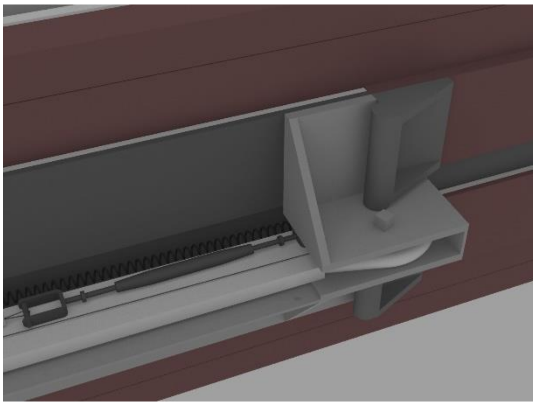

The attachment between axle shaft and the moving part of the frame is applied. There are two of these, one for the upper and one for the lower glazing panel. Each part is a mirrored copy; they are screwed into the frame and bolted to the axle. The window panels are now secure and move with the axle.

8)

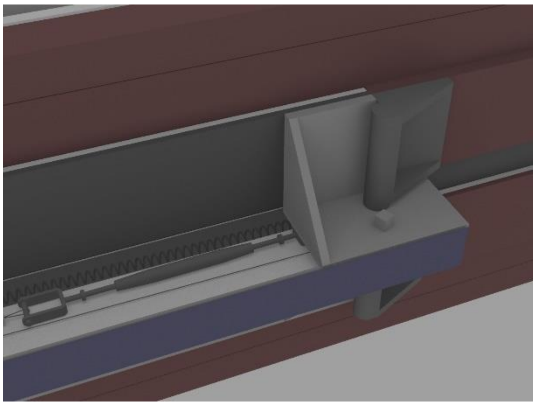

Finally, a transparent polycarbonate cover is slid horizontally into the construction and blind-pop riveted from the bottom. The PC is originally from a rectangular tube and is used as a 'roof' and 'façade' of the heat chamber. Parts of it are cut out in order to make it fit. The vertical face can be spray painted in order to exclude winter solar gain. All the internal hardware within the chamber can also be spray painted black to absorb more sunlight.

The distance between the two pivots is 1480 mm. The spring and nitinol wire attachments are 20.5mm away from the pivot, so that a 29mm length change will turn a 90^o angle. The active length of nitinol wire is 1226mm in the windows-open state with a 0.6% prestrain applied, so the true rest length is 1218mm. The martensite position will increase length by 29mm, thereby taking the material to 3% strain. Since it is working below its full potential, the nitinol will still be able to close if it needs to counteract a small external force.

The springs are TR1160, sourced from Alcomex. The non-moving end is attached to the aluminium frame by hooking onto a bolt and secured with a nut. Their k-value stiffness has been measured at 0.223N/mm with an effective rest length of 262mm. For each system, two of them ares used in series and kept at 486mm in the closed position, effectively halving their stiffness whilst maintaining a force of at least 50N. Based on the prototype, a 37% transmission loss in the hinge is assumed, which means 31.8 N (175 MPa) acts upon the nitinol wire. This is enough to induce detwinning for the shape memory effect. The stress in the heating motion is expected to be 79% higher, at 313MPa. The SMA and spring force vectors are different by less than one degree; for modelling purposes they can be assumed to be parallel.

Detail Drawings

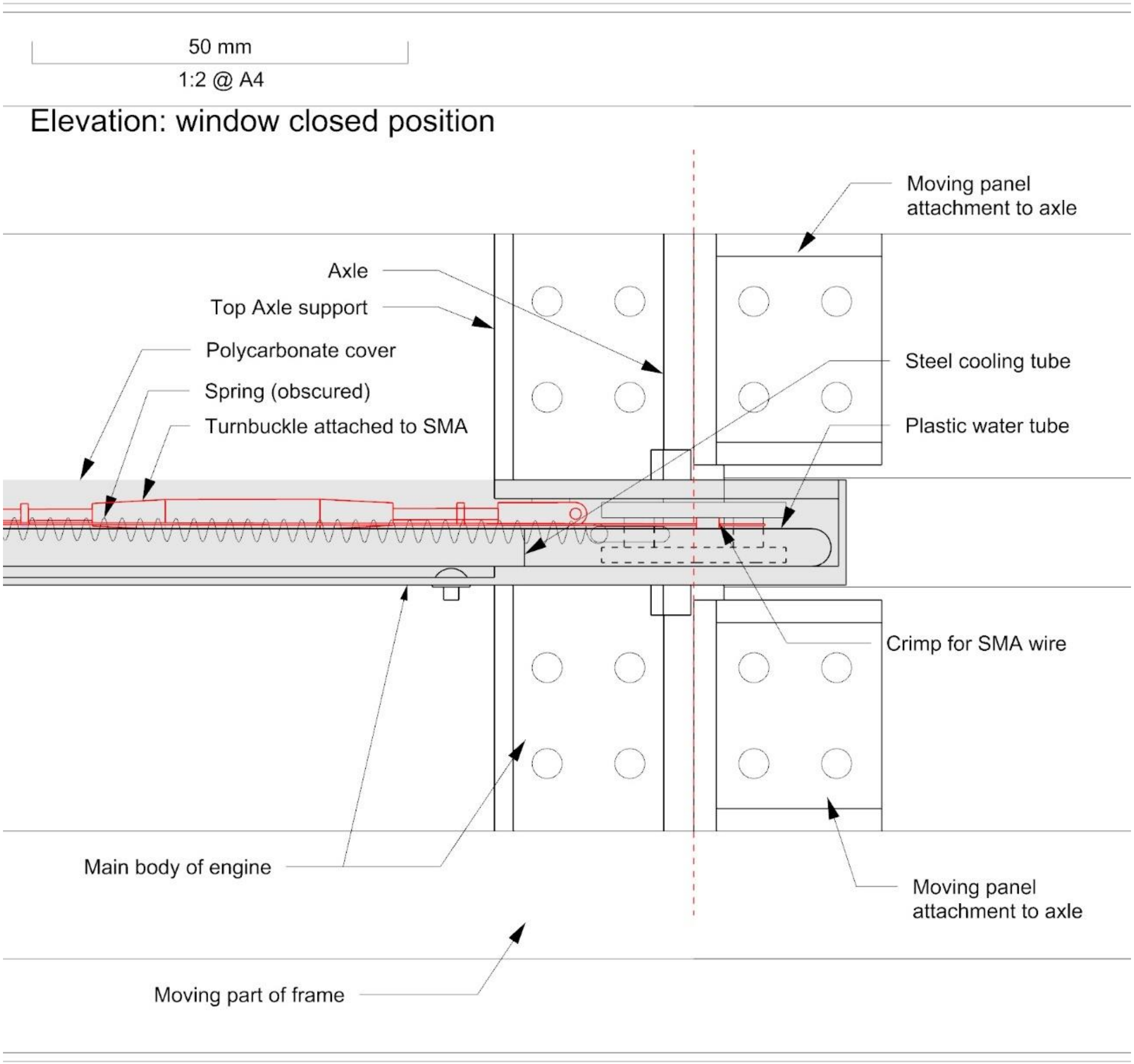

Figure 136: Front Elevation detail drawing of adaptronic engine in the closed position. The SMA wire and related connections, for instance the turnbuckle attached with it, are shown in red.

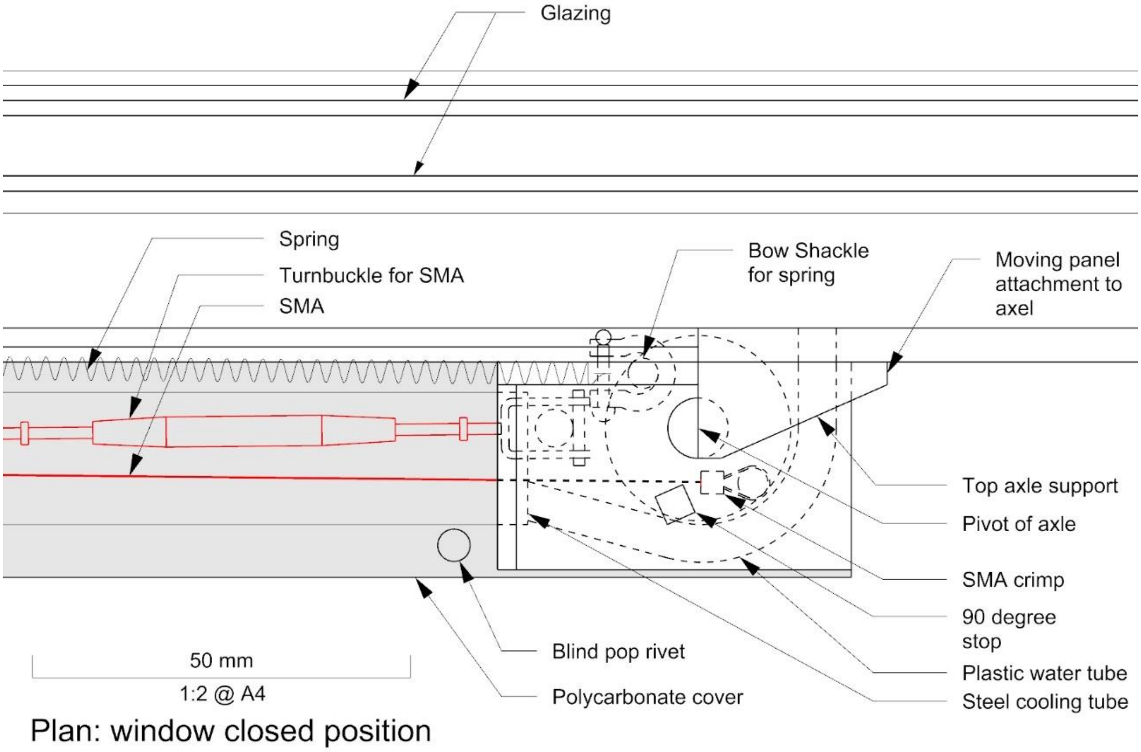

Figure 137: Plan detail of Adaptronic Engine in closed position

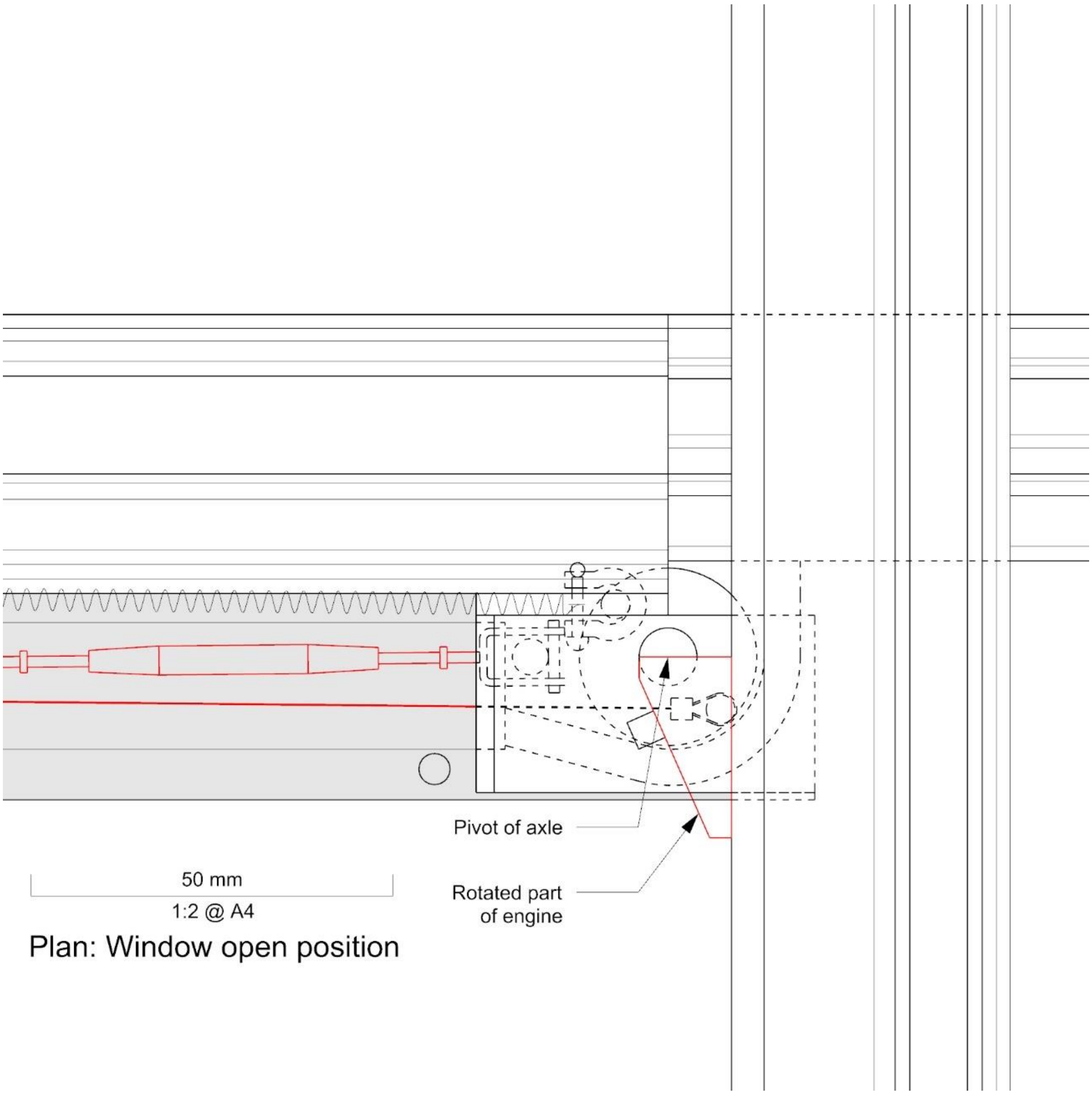

Figure 138: Plan detail of Adaptronic Engine in open position

Visualizations

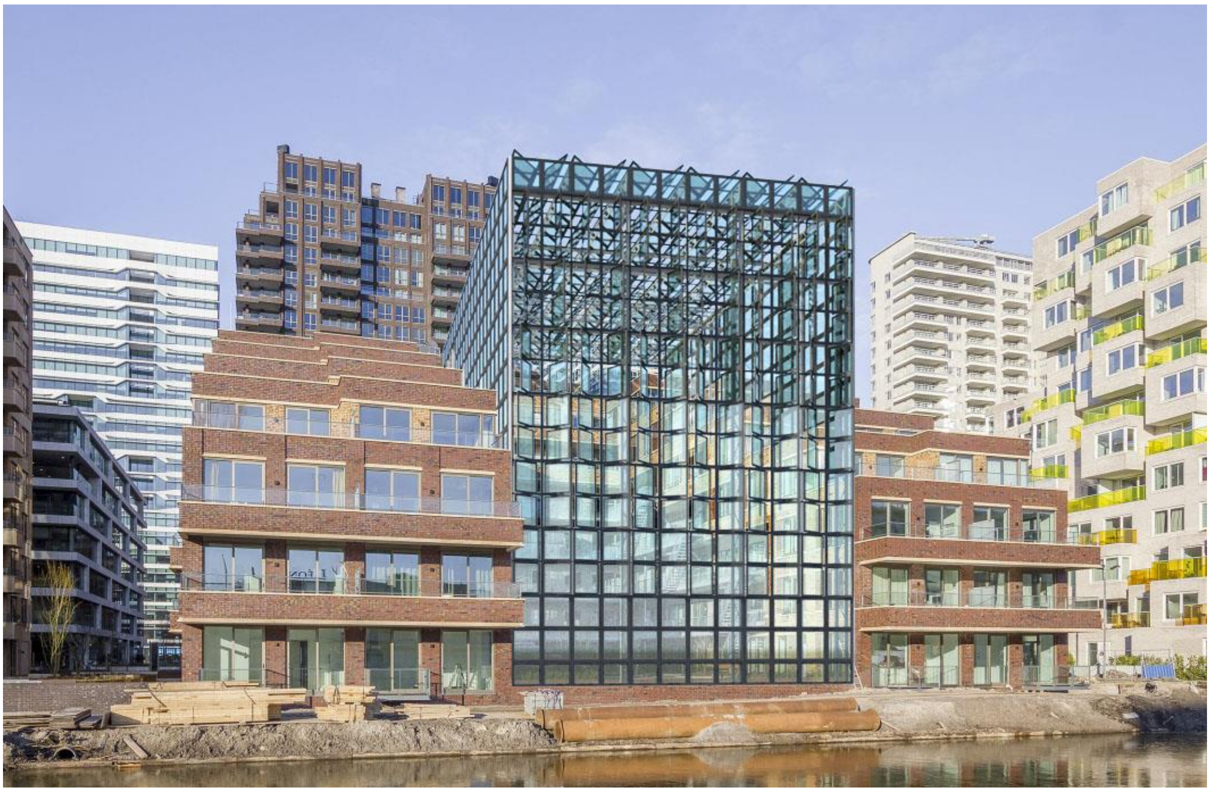

Figure 139: View from across the river, with panels of façade in various conditions of open and closed setting. Such a scenario might happen if there is a height-based temperature difference

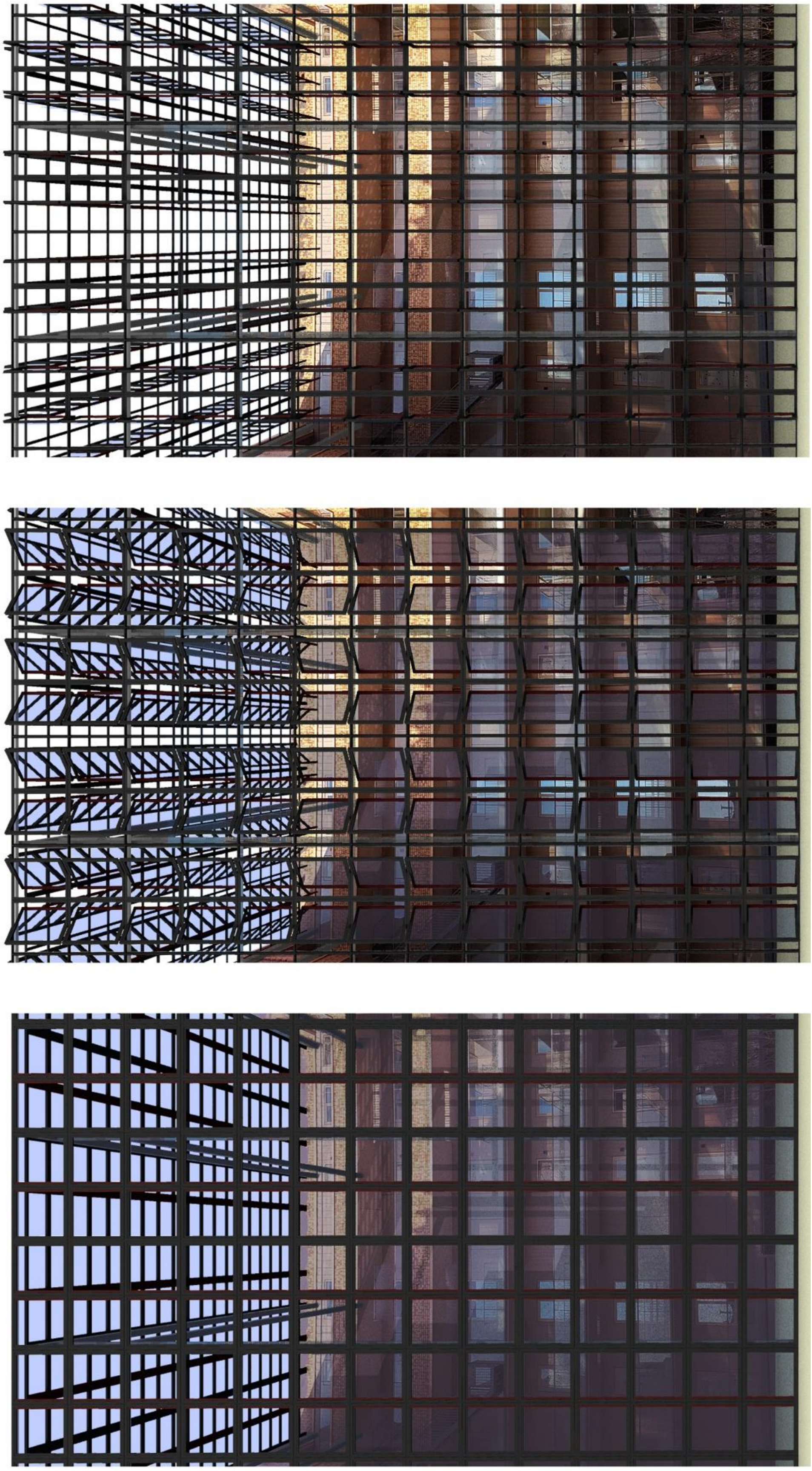

Figure 140: elevation views of the atrium façade in closed, half-open and open conditions

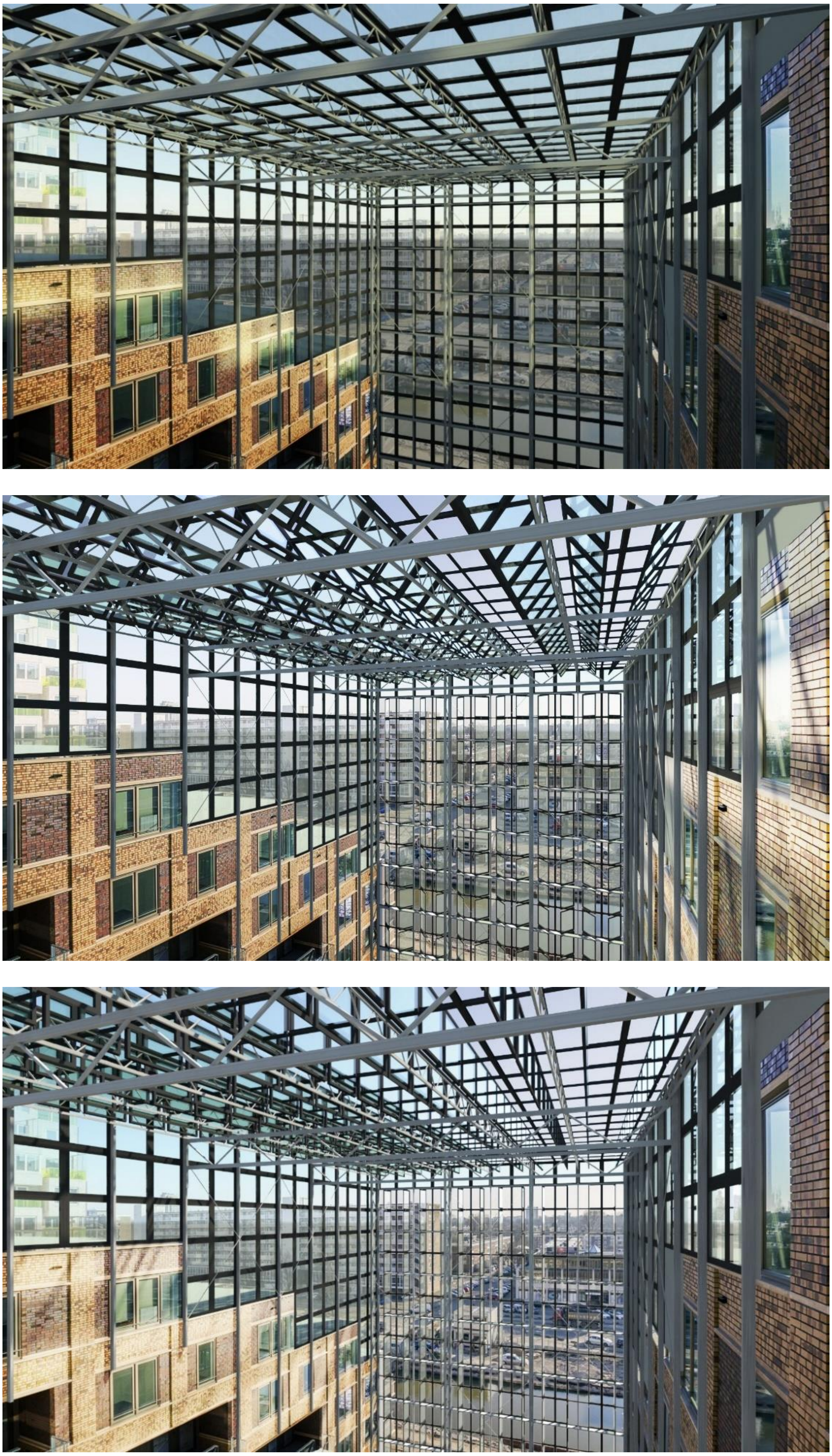

Figure 141: views from inside the atrium, with façade in closed, half-open and open conditions

7. Discussion

Evaluation of Design

Manual Control

In the final design, manual control of the window is partially possible in the event of an emergency. It will be possible to close the window at will, by passing water through the chamber where the nitinol is situated, in order to convert the material back into martensite. A network of tubes in series across the façade can achieve this. It is not possible to force the windows open currently.

Fatigue Life and Long Term Performance

At 3% strain limit and peak stress of 313Mpa is expected in each cycle, so the contraption can expect 4000 cycles if the material in Figure 61 is assumed to have a similar fatigue behaviour (Mammano & Dragoni, 2013). Assuming that the modules are locked shut for half the year, this translates to 1.1 activation cycles per day over 20 years. It is possible to improve the number by reducing the hinge friction and peak stress in the cycle, so that it becomes 175MPa and lasts 10 500 cycles, or 2.9 activations per day for 20 years. However, the effect of over-stressing the wire, for example if the wire is hot enough to begin activating but there is an external force preventing the window from opening, would greatly reduce the fatigue life.

External Forces

The nitinol wire is not expected to be able to counteract a large wind force, due to its proximity to the hinge and the implied large moment force. For this design, it is therefore recommended to close and lock the window in windy weather. A future design can calculate the expected wind loads over the life of the product and size the nitinol accordingly. The question of the stability of SMA wire length remains. Further testing involving dozens of cycles would be needed for this.

The non-South Facing Facades

The question arose whether the East and West facades of the atrium should be adaptronic. They have potential to be actuated by the sun, but not for the whole day. Assuming that the heat transfer mediator will favour solar gains from a high sun angle, Eastern facades can get activated in the late mornings in the Summer, and Western facades in the early afternoon in the Summer. This may not be much of the time, so true adaptronic abilities may be difficult to achieve. In this project, fixed window panels have been used for the side facades, as it has been assumed that an open South façade and open roof will already be sufficient to remove the greenhouse effect in the Summer.

Recommendations

Optimizing for HVAC consumption: Framework

Reduction of HVAC consumption has been the vision driving the project. The parametric and design framework to achieve an optimized reduction is shown in Figure 143. Information packages are represented in blue boxes, whilst scripts are represented in red boxes. The items in grey have been covered in this thesis. As shown, a selection and characterization of an SMA material (in terms of the properties of the Brinson model) is needed to eventually see how it behaves. The effect of weather on the output of heat transfer mediator also needs to be known, so data and a simulator script is required respectively. The simulator script will feed temperature into the Force-Strain Solver, which outputs the displacement and thereby animate the façade opening size. The opening size can be used to make an indoor climate simulation and thereby calculate savings in HVAC load. This number can be used to compare performance between different panel designs, so an iterative process can then be done to optimize the best design.

Implementing the Software Tool to the Design

An example script for "Render new position of adaptronic panel" can be found in the Google Drive link https://goo.gl/hiN6JN. The material properties are based on numbers that can are attainable judging by the values in literature. The basic movement of the device has been programmed, and due to the small percentage of total available stroke being used (3% compared to 8%), the temperature range in which actual motion occurs is small. The following numbers are strictly approximate and only give a rough idea of performance. The windows are able to turn the full 90 degrees in from 59.4 degrees Celsius to 63.5 degrees Celsius, a range of just 4.1 degrees Celsius. However, the parametric model does not currently take into account force transmission loss due to friction at the hinge. Note that the rotation angle, and therefore the elongation, is restricted to 90° using some simple code that processes information out of the main software tool. An upgrade to the tool would eventually be needed to program a maximum strain value along with the correctly displayed resultant SMA stress, and to complete the missing portion of the Force-displacement topography.

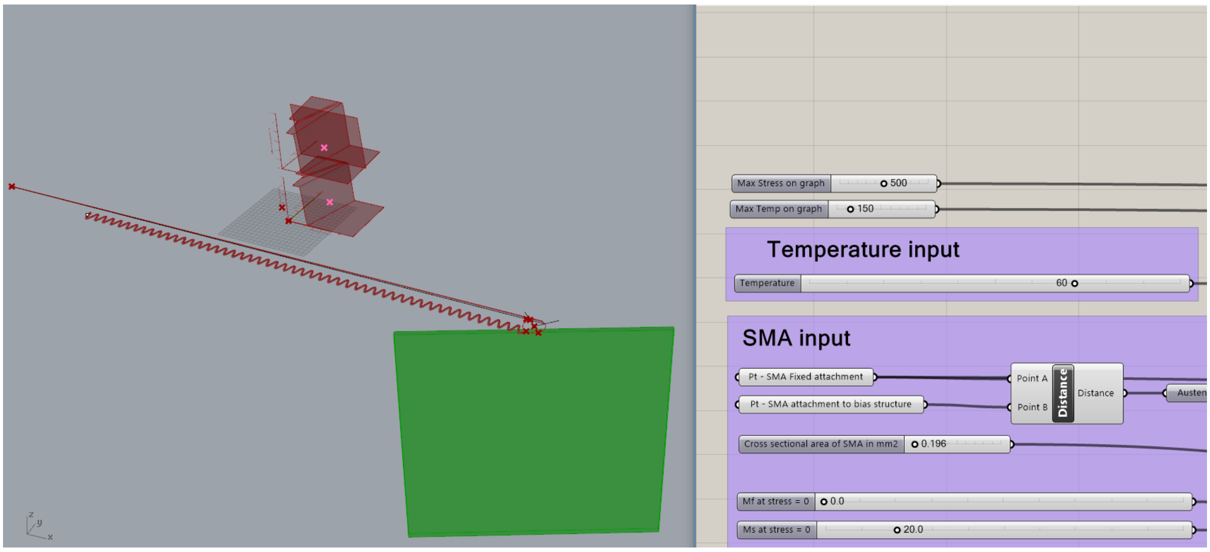

Max Stress on graph 500
Max Temp on graph 150
Temperature 60
Cross sectional area of SMA in mm2 0.196
Mf at stress = 0 0.0
Ms at stress = 0 20.0

Figure 142: First attempt at implementation of the software tool for the final design. Example can be found online

Future Design Possibilities

An alternative design to the module could feature window panels that slide open instead of rotate, so that the effect of wind does not force it to open or close. This would eliminate the threat of wind forces over-stressing the nitinol. A sketch of the idea is shown in Figure 144.

Another possibility is to incorporate electricity into the module instead of using a solar heat chamber. This can be done by fitting a PV cell onto the module and directing current through the nitinol wire so it heats up. The PV would have to be positioned so that the module only opens on a hot summer day. It may be aided by sensors or software that optimizes the behaviour if it does not perform as expected. However, these additional complexities and the use of a central computing source go against the philosophy of an adaptronic façade, which seeks to replace a multitude of components with materials.

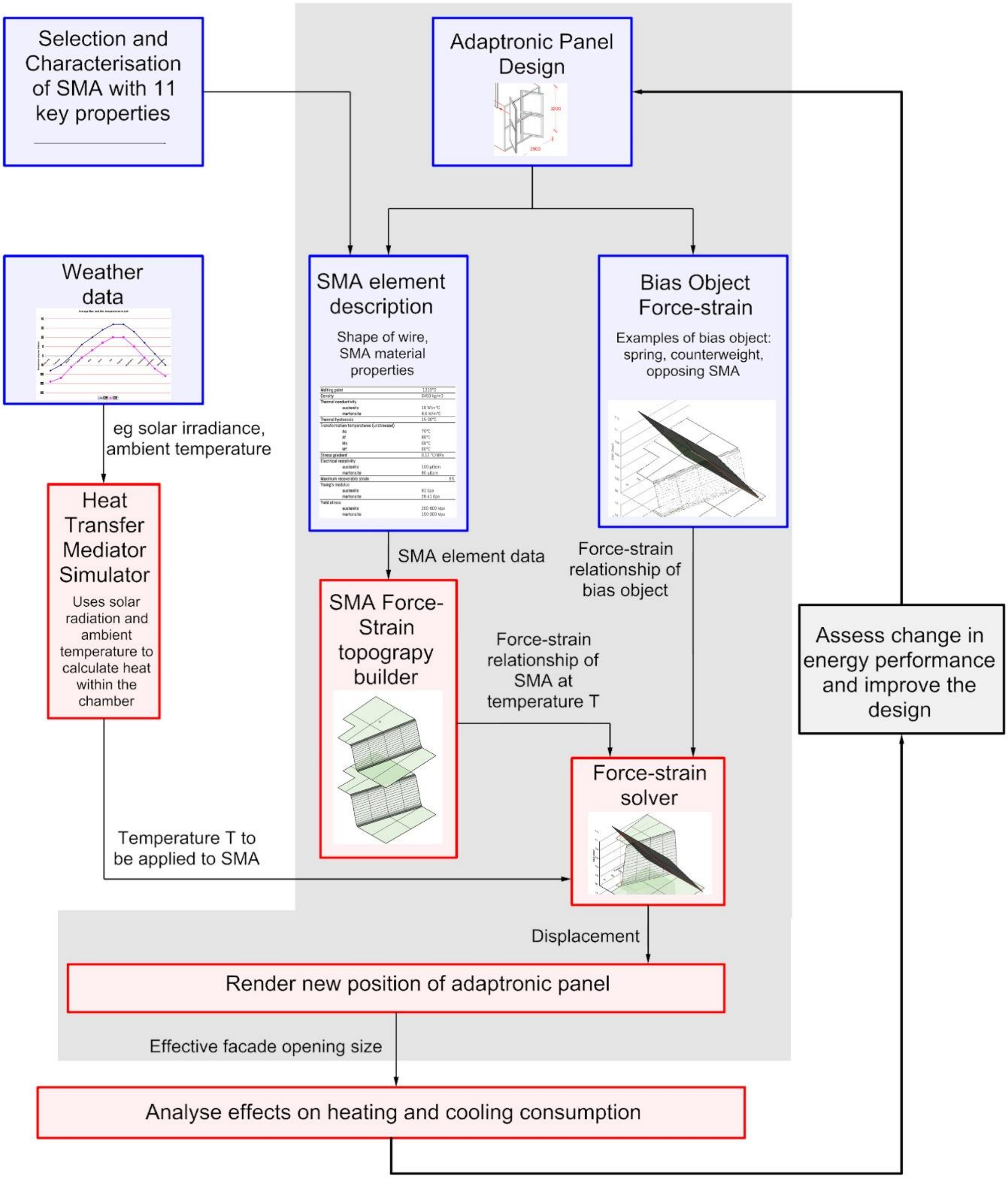

Figure 143: The parametric and design framework to achieve HVAC energy savings with an adaptronic module design. The thesis has covered the items in the grey region

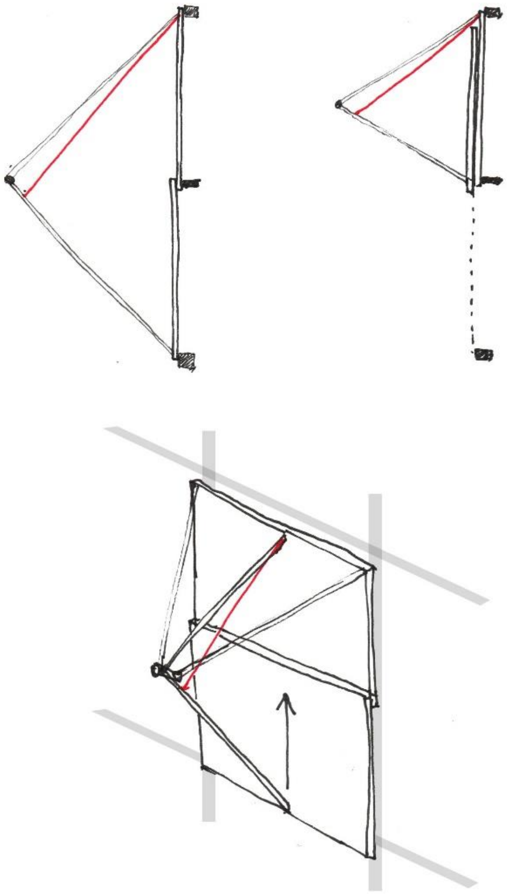

Figure 144: An alternative design for an adaptronic facade module featuring sliding glazed panels, in which the SMA wire does not need to counteract wind forces

8. Conclusions

Evaluation of Research Questions

How can Shape Memory Alloys be used in building technology? What are the conditions and limits when structurally incorporating Shape Memory Alloys as an adaptive component in a façade module?

Currently, SMAs can already be used as a reliable connector of tubes that utilize the Shape Memory Effect once in its lifetime, at the start. They have also been used for closing gaps in damaged civil structures and as a dampener against vibrations due to its pseudoelastic properties. In the design concept chosen for this tesis, an SMA wire can bring adaptive capabilities to a façade module if it is kept in tension and thereby made to have two different strained lengths in its hot and cold state. In the hot phase, the wire is stiff and short, whilst in the cold phase, the wire is weaker and the bias spring stretches the wire to a different position. In this way, it can be made to actuate an element such as a pivoting window panel, so long as it is connected at the right location relative to the hinge. Since only 4% of the wire length can be actuated, there is a stroke limit based on how much straight wire can fit into a single module. A 0.5mm diameter wire is able to deliver forces of up to 58N; the force is proportional to the area, so in theory a large wire can deliver enormous forces. It is limited by cost, the time taken to actuate, as well as the ability to incorporate a bias object strong enough to return the SMA to a strained position in the cold phase. The body of the device would also need to withstand double the force.

How can the behaviour of an SMA element be modelled computationally to predict the movement of the façade module given a stream of temperature data?

The Brinson model for uniaxial SMA behaviour has been adapted into a Grasshopper script, which takes a description of the SMA element, the bias force vs strain description and the SMA temperature as a variable output. The modelling principle is as follows: the state of a tensile SMA, referred to as the martensite fraction, determines an effective Young's Modulus and effective rest length in which to calculate the strain based on classical elastic mechanical formulas. The martensite fraction can be predicted based on its history of temperature and stress. The script produced for this thesis can express the displacement of the SMA vs bias interface as the temperature changes, and the movement of the structure can thereby be animated. The history of the temperature is an important factor in this script, as the most recent temperature switch point determines at what temperature the material will start to transition next.

How can an adaptronic actuator 'engine' be designed to deliver the desired temperature-responsive change of the façade module?

The temperature range needed for an adaptronic device can be delivered by building a heat transfer mediator to influence the temperature that the SMA element is subjected to. This can for example be a solar-absorbing chamber with a transparent horizontal top piece, to selectively get heated by the high sun of the summer days only. The adaptronic device and rest of the building would have to be simulated to ensure it is able to deliver a pattern of open and closed states that has a positive impact on the heating and cooling demands. The SMA element should also not be overheated, as it may decrease the fatigue life.

How can a façade module incorporate the engine that delivers adaptronic abilities, and still function with all the usual requirements of a conventional facade? To what extent can it be done simply, with long-term reliability and with ease of manufacture/assembly?

It is possible to use entirely standard profiles, and to simply bolt on the non-standard hardware for the adaptronic abilities. In such a design, two pairs of center-pivot windows are used, and the pivot points are positioned on the exterior side of the windows. The custom hardware can be compactly fitted onto the standard frame, with weld joints, screws or bolts to attach separate pieces. A pop-rivetted polycarbonate rectangular tube can form the enclosure of the solar chamber. The entire module with its 4 panels and engine can be assembled in factory and transported to site. The long-term reliability of the SMA wire has not yet been verified.

To what extent can an adaptronic system deliver two extreme states of a fully transparent but insulated atrium to a fully open court, in response to a temperature change?

The prototype tested was able to deliver 61.3° of angular stroke using electric Joule heating. It is expected to achieve a higher angle if the friction in the device is heavily reduced. As for replacing the Joule heating with the energy from the environment, it can be done if the solar-absorbing chamber is designed efficiently and the nitinol is produced with the right atomic composition so that the transition temperatures are easier to reach. Activation with solar power was achieved at zero stress with a makeshift heat chamber. The greater challenge will be to design a heat chamber that heats and cools at a pattern to suit the cooling and heating loads of the building; it should not actuate the SMA on a sunny but cold day.

Basic simulations in the software tool showed that hysteresis, which is a temperature difference between activation and deactivation of the module, will exist based on the SMA material properties. It is possible in theory to achieve the full 90° rotation with a temperature change of 4.1 degrees Celcius, and this range can be made smaller by utilizing a smaller fraction of the available recovery 8% stroke that the material is capable of.

Limitations and Recommendations

Regarding the software tool, features can be incorporated to make it more useful, such as a strain limit and prestrain options. Within the solver, the topology generator is currently missing the portion that deals with temperatures below M_f and stresses below $\boldsymbol{\sigma_f}$. This may become useful in some applications. In the longer term, some user feedback would be helpful for guiding further development.

Regarding the prototype and experimental exploration side, an engine with full adaptronic abilities is still yet to be done. A selection of a nitinol sample with around room temperature transitions at stresses of 175 MPa would be ideal; this would then be fully characterized and then implemented. The friction of the hinge was a remaining limiting factor for this thesis. It can be improved or phased out with an alternative solution.

Some structural calculations to fine-tune the structure and find the limit states would be useful. An investigation can be done regarding to what extent the engine can resist wind forces, and therefore how much of the time it is truly able to stay in the position that is desired.

The entire adaptronic design would eventually have to be environmentally simulated with weather data, along with the nitinol, heat chamber and physics of the rest of the building to measure HVAC consumption. In this way, design performance can be measured and a process of optimization can begin.

Conclusion

The thesis aimed to investigate the feasibility and process of constructing an adaptronic Shape Memory Alloy-based façade module able to open itself in hot weather. The idea was to produce an atrium in cold weather and an open court in hot weather, for a seasonal greenhouse effect that could reduce HVAC costs. At the start, literature showed that the potential of such a structure to save 30% of the heating energy for a building. The main question was thus: how can an adaptronic atrium be designed to self-actuate in response to external environmental conditions?

Research was done on the behaviour of SMAs, and a software tool was made to allow users with no specialist knowledge to predict the movement of an SMA wire structure as the temperature changes. The software tool is intended to empower designers to use SMA in projects and is now freely available online at https://goo.gl/hiN6JN.

Nitinol, the most common type of SMA, was used to build a prototype that was able to actuate in a stressed state via electrical Joule heating as well as by solar gain using a heat chamber at zero stress. An rotation of 61.3° was achieved using a counterweight as a bias force and Joule heating. Given that nitinol can be manufactured to adjust its transition temperatures, it can be seen that a weather-powered activation under a stressed state is feasible.

Based on the experimental and prototyping findings, a prefabricated adaptronic façade module for an atrium was designed. It is based on simple parts that can be attached onto the outside of a standard aluminium frame for centre-pivot windows. Its performance as a HVAC consumption-reducing device needs to be verified with a complex holistic simulation, and thereafter the design can be optimized. Furthermore, the fatigue life and performance in windy conditions of the module are not verified.

Going forward, there are many avenues to explore the design and enhance the use of SMAs for non-specialists. These are outlined in the previous subchapter. The future for both adaptronics and SMA-based architectural contraptions is positive; projects are already being developed that have sustainability as a key driver. The new solutions represent a new type of smart-materials based adaptiveness that passively orchestrate the indoor environment. Only time can tell whether these efforts will finally manifest in built projects and, eventually, energy savings.

9. Bibliography

Addington, D. M., & Schodek, D. L. (2005). *Smart Materials and New Technologies: For the Architecture and Design Professions*: Architectural Press.

Adriaenssens, S., Rhode-Barbarigos, L., Kilian, A., Baverel, O., Charpentier, V., Horner, M., & Buzatu, D. (2014). Dialectic Form Finding of Passive and Adaptive Shading Enclosures. *Energies, 7*(8), 5201-5220.

Aeby-Gautier, E., & Patoor, E. (1997). *Experimental Observations for Shape Memory Alloys and Transformation Induced Plasticity Phenomena*.

Alam, M. S., Youssef, M. A., & Nehdi, M. L. (2010a). Exploratory investigation on mechanical anchors for connecting SMA bars to steel or FRP bars. *MATERIALS AND STRUCTURES, 43*(1 SUPP/1), 91-107.

Alam, M. S., Youssef, M. A., & Nehdi, M. L. (2010b). Exploratory investigation on mechanical anchors for connecting SMA bars to steel or FRP bars. *Materials and structures /, 43*(1), 91.

Aldawoud, A., & Clark, R. (2008). Comparative analysis of energy performance between courtyard and atrium in buildings. *Energy & Buildings, 40*(3), 209-214.

Anshuman, S. (2009). PixelSkin02. Retrieved from http://transmaterial.net/pixelskin02/

ASM International. (2017). Nickel-titanium shape memory alloy spring tire designed for Mars rover. Retrieved from https://www.asminternational.org/home/-/journal_content/56/10180/29578482/NEWS

Barbarino, S., Ameduri, S., Lecce, L., & Concilio, A. (2008). Wing Shape Control through an SMA-Based Device. *Journal of Intelligent Material Systems and Structures, 20*(3), 283-296. doi:10.1177/1045389X08093825

Bartkowiak, G. y., & Dąbrowska, A. (2016). Textile Materials with SMA Elements for Active Protection against Heat and Flame. *Advances in Science and Technology, 100*, 11-16.

Basaeri, H., Yousefi-Koma, A., Zakerzadeh, M. R., & Mohtasebi, S. S. (2014). Experimental study of a bio-inspired robotic morphing wing mechanism actuated by shape memory alloy wires. *Mechatronics, 24*(8), 1231-1241. doi:https://doi.org/10.1016/j.mechatronics.2014.10.010

Beesley, P. (2006). *Responsive Architectures: Subtle Technologies 2006*: Riverside Architectural Press.

Brinson, L. C. (1993). One-Dimensional Constitutive Behavior of Shape Memory Alloys: Thermomechanical Derivation with Non-Constant Material Functions and Redefined Martensite Internal Variable. *Journal of Intelligent Material Systems and Structures, 4*(2), 229-242. doi:10.1177/1045389X9300400213

Castex, J. (2008). *Architecture of Italy*: ABC-CLIO.

Chartered Institution of Building Services, E. (2005). *Natural ventilation in non-domestic buildings*. In CIBSE applications manual ; AM10; Applications manual (Chartered Institution of Building Services Engineers) ; 10. Retrieved from Knovel http://app.knovel.com/hotlink/toc/id:kpNVNDBCIA/natural-ventilation-in

University of Alberta Access http://app.knovel.com/hotlink/toc/id:kpNVNDBCIA/natural_ventilation_in_nondomestic_buildings___cibse_applications_manual_am10

http://app.knovel.com/web/toc.v/cid:kpNVNDBCIA/viewerType:toc/root_slug:natural-ventilation-in

https://app.knovel.com/web/toc.v/cid:kpNVNDBCIA/viewerType:toc/root_slug:natural-ventilation-in

https://login.libproxy.uregina.ca:8443/login?url=http://app.knovel.com/hotlink/toc/id:kpNVNDBCIA/natural-ventilation-in

Chernenko, V. A., Pons, J., Cesari, E., & Zasimchuk, I. K. (2004). Transformation behaviour and martensite stabilization in the ferromagnetic Co–Ni–Ga Heusler alloy. *Scripta Materialia, 50*(2), 225-229. doi:https://doi.org/10.1016/j.scriptamat.2003.09.024

Cianchetti. (2013). Fundamentals on the Use of Shape Memory Alloys in Soft Robotics. In *Interdisciplinary Mechatronics*.

Correa, D., Papadopoulou, A., Guberan, C., Jhaveri, N., Reichert, S., Menges, A., & Tibbits, S. (2015). 3D-Printed Wood: Programming Hygroscopic Material Transformations. *3D Printing and Additive Manufacturing, 2*(3), 106-116.

Czaderski, C., Weber, B., Shahverdi, M., Motavalli, M., Leinenbach, C., Lee, W., . . . Michels, J. (2015). *Iron-based shape memory alloys (Fe-SMA) - a new material for prestressing concrete structures*.

Daghia, F. (2008). *Active fibre-reinforced composites with embedded shape memory alloys*.

Danielski, I., Nair, G., Joelsson, A., & Fröling, M. (2016). Heated atrium in multi-storey apartment buildings, a design with potential to enhance energy efficiency and to facilitate social interactions. *Building and Environment, 106*, 352-364. doi:https://doi.org/10.1016/j.buildenv.2016.06.038

Drossel, W. G., Zorn, W., Bucht, A., Kunze, H., Ettrichraetz, M., & Pagel, K. (2015). Development of shape memory alloy actuators with inherent guidance function. *Mechatronics, 30*, 254-258. doi:https://doi.org/10.1016/j.mechatronics.2015.07.011

Elzey, D. M., Sofla, A. Y. N., & Wadley, H. N. G. (2005). A shape memory-based multifunctional structural actuator panel. *International Journal of Solids and Structures, 42*(7), 1943-1955. doi:https://doi.org/10.1016/j.ijsolstr.2004.05.034

Energy Performance of Buildings. (2015). *2016 Implementing the Energy Performance of Buildings Directive*. Retrieved from Lisbon:

European Commission. (2010). *A strategy for competitive, sustainable and secure energy*. Retrieved from Brussels:

European Commission. (2014). *A policy framework for climate and energy in the period from 2020 to 2030*. Retrieved from Brussels:

European Commission. (2016). *Overview of support activities and projects of the European Union on energy efficiency and renewable energy in the heating & cooling sector*. Retrieved from Luxembourg: Publications Office of the European Union:

Ford, D. S., & White, S. R. (1996). Thermomechanical behavior of 55Ni45Ti nitinol. *Acta Materialia, 44*(6), 2295-2307. doi:https://doi.org/10.1016/1359-6454(95)00343-6

Foster and Partners. 30 St Mary Axe, London. Retrieved from https://www.fosterandpartners.com/news/archive/2004/04/30-st-mary-axe-london/

Fraunhofer Adaptronics Alliance. Adaptronics. Retrieved from https://www.adaptronik.fraunhofer.de/en/about/adaptronic/applications.html

Fraunhofer Adaptronics Alliance. Projects. Retrieved from https://www.adaptronik.fraunhofer.de/en/projects/intelliMemoryEffect.html

Fumagalli, L., Butera, F., & Coda, A. (2009). SmartFlex® NiTi Wires for Shape Memory Actuators. *Journal of Materials Engineering and Performance, 18*(5-6), 691-695.

Garner, L. J., Wilson, L. N., Lagoudas, D. C., & Rediniotis, O. K. (2000). Development of a shape memory alloy actuated biomimetic vehicle. *Smart Materials and Structures, 9*(5), 673.

Gautier, E., & Patoor, E. (1997). Experimental Observations for Shape Memory Alloys and Transformation Induced Plasticity Phenomena. In M. Berveiller & F. D. Fischer (Eds.), *Mechanics of Solids with Phase Changes* (pp. 69-103). Vienna: Springer Vienna.

Gilbertson, R. G. (2005). *Muscle Wires Project Book* (3rd ed.). San Rafael: Mondo Tronics.

GM. (2013). Chevrolet Debuts Lightweight 'Smart Material' on Corvette. Retrieved from http://media.gm.com/media/us/en/gm/home.detail.html/content/Pages/news/us/en/2013/Feb/0212-corvette.html

Grado Zero Espace. ORICALCO. Retrieved from http://www.gradozero.eu/gzenew/index.php?pg=oricalco

Hartl, D. J., Lagoudas, D. C., Calkins, F. T., & Mabe, J. H. (2010). Use of a Ni60Ti shape memory alloy for active jet engine chevron application: I. Thermomechanical characterization. *Smart Materials and Structures, 19*(1), 015020.

Hawkes, E., An, B., Benbernou, N. M., Tanaka, H., Kim, S., Demaine, E. D., . . . Wood, R. J. (2010). Programmable matter by folding. *Proceedings of the National Academy of Sciences of the United States of America, 107*(28), 12441-12445.

Heat Roadmap Europe 4. (2017). *Heating & Cooling – facts and figures*. Retrieved from

Hegger, M. (2008). *Energy manual : sustainable architecture*. In Edition Detail. Retrieved from Ebook Library http://public.eblib.com/choice/publicfullrecord.aspx?p=1075583

EBSCOhost http://search.ebscohost.com/login.aspx?direct=true&scope=site&db=nlebk&db=nlabk&AN=641999

ProQuest Ebook Central http://public.ebookcentral.proquest.com/choice/publicfullrecord.aspx?p=1075583

http://www.degruyter.com/doi/book/10.11129/detail.9783034614542

EBSCOhost http://search.ebscohost.com/login.aspx?direct=true&scope=site&db=nlebk&db=nlabk&AN=641999&authtype=uid&lang=de

Volltext http://www.degruyter.com/search?f_0=isbnissn&q_0=9783034614542&searchTitles=true

http://dx.doi.org/10.11129/detail.9783034614542

http://ebookcentral.proquest.com/lib/columbia/detail.action?docID=1075583

https://ebookcentral.proquest.com/lib/ucm/detail.action?docID=1075583

Honma, D., Miwa, Y., & Iguchi, N. (1984). Application of Shape Memory Effect to Digital Control Actuator. *Bulletin of JSME, 27*(230), 1737-1742. doi:10.1299/jsme1958.27.1737

Huang, W. (1998). *Shape Memory Alloys and their Application to Actuators for Deployable Structures.* (PhD), University of Cambridge,

Huang, W. H., Wu, J. A., Lim, B. Y., & Vahhi, I. E. (2005). V-shape in Young's modulus versus strain relationship in shape memory alloys upon mechanical loading. *Journal of Alloys and Compounds, 390*(1), 175-181.

Huber, J. E., Fleck, N. A., & Ashby, M. F. (1997). The Selection of Mechanical Actuators Based on Performance Indices. *Proceedings: Mathematical, Physical and Engineering Sciences, 453*(1965), 2185-2205.

Hung, W., & Chow, W. (2001). A Review on Architectural Aspects of Atrium Buildings. *Architectural science review, 44/3*(3), 285-296.

Indirli, M., & Castellano, M. G. (2008). Shape Memory Alloy Devices for the Structural Improvement of Masonry Heritage Structures. *International Journal of Architectural Heritage, 2*(2), 93-119.

Indirli, M., Castellano, M. G., Clemente, P., & Martelli, A. (2001). *Demo-Application of Shape Memory Alloy Devices: the Rehabilitation of the S. Giorgio Church Bell Tower*.

International Energy Agency. (2013). *Transition to Sustainable Buildings: Strategies and Opportunities to 2050*. Retrieved from

Intrinsic Devices Incorporated. Use of Shape Memory Alloys in High Reliability Fastening Applications

Retrieved from http://www.intrinsicdevices.com/history.html

Janocha, H. (1999). *Adaptronics and smart structures : basics, materials, design, and applications*. Berlin :: Springer.

Jerman, H. (1994). Electrically activated normally closed diaphragm valves. *Journal of Micromechanics and Microengineering, 4*(4), 210-216.

Jong-Ha, C., Jin-Seok, H., & Jung-Ju, L. (2007). Implementation strategy for the dual transformation region in the Brinson SMA constitutive model. *Smart Materials and Structures, 16*(1), N1-N5.

Keylite. (2017). Ketlite ROI Pricelist May 2017. Retrieved from http://staff.keyliteroofwindows.com/files/2017/07/4030_ROI-Pricelist-LR-Spreads.pdf

Khandelwal, A., & Buravalla, V. (2010). *Models for Shape Memory Alloy Behavior: An overview of modeling approaches* (Vol. 1).

Knaack, U., & Bilow, M. (2007). *Façades: Principles of Construction*: SPRINGER VERLAG NY.

Lagoudas, D. C. (2008). *Shape memory alloys : modeling and engineering applications*. In. Retrieved from Ebook Library http://public.eblib.com/choice/publicfullrecord.aspx?p=372732

ebrary http://site.ebrary.com/id/10284712

EBSCOhost http://search.ebscohost.com/login.aspx?direct=true&scope=site&db=nlebk&db=nlabk&AN=254655

MyiLibrary http://www.myilibrary.com?id=149205

OhioLINK http://rave.ohiolink.edu/ebooks/ebc/9780387476858

ProQuest Ebook Central http://public.ebookcentral.proquest.com/choice/publicfullrecord.aspx?p=372732

SpringerLink http://dx.doi.org/10.1007/978-0-387-47685-8

SpringerLink http://www.springerlink.com/openurl.asp?genre=book&isbn=978-0-387-47684-1

SpringerLink https://link.springer.com/openurl?genre=book&isbn=978-0-387-47684-1

MyiLibrary, Table of contents http://www.myilibrary.com?id=149205&ref=toc

Cover http://swbplus.bsz-bw.de/bsz285787705cov.htm

https://ebookcentral.proquest.com/lib/stanford-ebooks/detail.action?docID=372732

University of Alberta Access https://ebookcentral.proquest.com/lib/ualberta/detail.action?docID=372732

University of Alberta Access http://link.springer.com/10.1007/978-0-387-47685-8

Langmead, D., & Garnaut, C. (2001). *Encyclopedia of Architectural and Engineering Feats*: ABC-CLIO.

Lecce, L., & Concilio, A. (2014). *Shape memory alloy engineering : for aerospace, structural and biomedical applications*. In. Retrieved from Ebook Library http://public.eblib.com/choice/publicfullrecord.aspx?p=1798302

EBSCOhost http://search.ebscohost.com/login.aspx?direct=true&scope=site&db=nlebk&db=nlabk&AN=545210

ScienceDirect http://www.sciencedirect.com/science/book/9780080999203

http://0-www.sciencedirect.com.pugwash.lib.warwick.ac.uk/science/book/9780080999203

Lelieveld, C. M. J. L., & Jansen, K. M. B. (2014). Thermal-electric characterization and modelling of a smart composite structure for architectural applications. *Smart Materials and Structures, 23*(6).

Leung, C. (2014). *Passive seasonally responsive thermal actuators for dynamic building envelopes.* (PhD), University College London,

Liang, C. (1990). *The constitutive modeling of shape memory alloys.* Virginia Tech,

Liang, C., & Rogers, C. A. (1990). One-Dimensional Thermomechanical Constitutive Relations for Shape Memory Materials. *Journal of Intelligent Material Systems and Structures, 1*(2), 207-234. doi:10.1177/1045389X9000100205

Lobo, P. S., Almeida, J., & Guerreiro, L. (2015). Shape Memory Alloys Behaviour: A Review. *Procedia Engineering, 114*, 776-783. doi:https://doi.org/10.1016/j.proeng.2015.08.025

Loonen, R. C. G. M. (2015). Bio-inspired Adaptive Building Skins. In F. Pacheco Torgal, J. A. Labrincha, M. V. Diamanti, C. P. Yu, & H. K. Lee (Eds.), *Biotechnologies and Biomimetics for Civil Engineering* (pp. 115-134). Cham: Springer International Publishing.

Luo, H. Y., & Abel, E. W. (2007a). A comparison of methods for the training of NiTi two-way shape memory alloy. *Smart Materials and Structures, 16*(6), 2543-2549.

Luo, H. Y., & Abel, E. W. (2007b). A comparison of methods for the training of NiTi two-way shape memory alloy. *Smart Materials and Structures, 16*(6), 2543.

Mammano, G. S., & Dragoni, E. (2013). Functional fatigue of NiTi Shape Memory wires for a range of end loadings and constraints. *frattura ed integrità strutturale, 7*(23), 25-33. Retrieved from

McCormick, P. G. (1987). On the practical efficiency of shape memory engines. *Scripta Metallurgica, 21*(2), 99-101. doi:https://doi.org/10.1016/0036-9748(87)90416-9

Michael Wigginton, J. H. (2002). *Intelligent Skins*. Oxford: Gray Publishing.

Mizar, S. P. (2005). *Thermomechanical Characterization of NiTiNOL and NiTiNOL Based Structures Using ACES Methodology*.

Mohd Jani, J. (2016). *Design optimisation of shape memory alloy linear actuator applications*.

Mohd Jani, J., Leary, M., Subic, A., & Gibson, M. A. (2014). A review of shape memory alloy research, applications and opportunities. *Materials & Design (1980-2015), 56*, 1078-1113. doi:https://doi.org/10.1016/j.matdes.2013.11.084

Müller, I., & Seelecke, S. (2001). Thermodynamic aspects of shape memory alloys. *Mathematical and Computer Modelling, 34*(12), 1307-1355. doi:https://doi.org/10.1016/S0895-7177(01)00134-0

NASA. Reinventing the Wheel.

NASA. (2015). *Shape Memory Alloy Rock Splitters (SMARS)—A Non-Explosive Method for Fracturing Planetary Rocklike Materials and Minerals*. Retrieved from https://ntrs.nasa.gov/archive/nasa/casi.ntrs.nasa.gov/20150014967.pdf

NASA. (2018). Memory Metals Retrieved from https://ntrs.nasa.gov/archive/nasa/casi.ntrs.nasa.gov/20020086323.pdf

Nitz, P., & Hartwig, H. (2005). Solar control with thermotropic layers. *Solar Energy, 79*(6), 573-582. doi:https://doi.org/10.1016/j.solener.2004.12.009

Ocel, J., DesRoches, R., Leon, R. T., Hess, W. G., Krumme, R., Hayes, J. R., & Sweeney, S. (2004). Steel Beam-Column Connections Using Shape Memory Alloys. *Journal of Structural Engineering, 130*(5), 732-740.

Paiva, A., Savi, M. A., Braga, A. M. B., & Pacheco, P. M. C. L. (2005). A constitutive model for shape memory alloys considering tensile‐compressive asymmetry and plasticity. *International Journal of Solids and Structures, 42*(11), 3439-3457. doi:https://doi.org/10.1016/j.ijsolstr.2004.11.006

Palma Rojas, D. (2014). Atrium building design: key aspects to improve their thermal performance on the Mediterranean climate of Santiago de Chile. *International Journal of Low-Carbon Technologies, 9*(4), 327-330. doi:10.1093/ijlct/ctt009

Perkins, J., & Hodgson, D. (1990). The Two-Way Shape Memory Effect. In T. W. Duerig, K. N. Melton, D. Stöckel, & C. M. Wayman (Eds.), *Engineering Aspects of Shape Memory Alloys* (pp. 195-206): Butterworth-Heinemann.

Perreux, D., & Lexcellent, C. (1999). Theoretical and Experimental Study of a Smart Hinge-Beam Based on Shape Memory Alloy Wire Actuators. *Journal of Intelligent and Robotic Systems, 25*(2), 167-182. doi:10.1023/a:1008025314208

Pollio, V., & Morgan, M. H. (1960). *Los Diez Libros de Arquitectura*: Dover Publications.

Rediniotis, O. K., Wilson, L. N., Lagoudas, D. C., & Khan, M. M. (2002). Development of a Shape-Memory-Alloy Actuated Biomimetic Hydrofoil. *Journal of Intelligent Material Systems and Structures, 13*(1), 35-49. doi:10.1177/1045389X02013001534

Reichert, S., Menges, A., & Correa, D. (2015). Meteorosensitive architecture: Biomimetic building skins based on materially embedded and hygroscopically enabled responsiveness. *Computer-Aided Design, 60*, 50-69. doi:https://doi.org/10.1016/j.cad.2014.02.010

Rojas, D. P. (2014). Atrium building design: Key aspects to improve their thermal performance on the Mediterranean climate of Santiago de Chile. *International Journal of Low-Carbon Technologies, 9*(4), 327-330.

Rotzetter, A. C. C., Schumacher, C. M., Bubenhofer, S. B., Grass, R. N., Gerber, L. C., Zeltner, M., & Stark, W. J. (2012). Thermoresponsive Polymer Induced Sweating Surfaces as an Efficient Way to Passively Cool Buildings. *Advanced Materials, 24*(39), 5352-5356. doi:10.1002/adma.201202574

Sawaguchi, T., Kikuchi, T., Ogawa, K., Kajiwara, S., Ikeo, Y., Kojima, M., & Ogawa, T. (2005). Development of Prestressed Concrete Using Fe-Mn-Si-Based Shape Memory Alloys Containing NbC. *Journal of the Japan Institute of Metals, 69*(8), 659-662.

Sayigh, A. (2014). *Sustainability, energy and architecture : case studies in realizing green buildings*. In. Retrieved from ebrary http://site.ebrary.com/id/10767286

EBSCOhost http://search.ebscohost.com/login.aspx?direct=true&scope=site&db=nlebk&db=nlabk&AN=486050

ScienceDirect http://www.sciencedirect.com/science/book/9780123972699

eBook Academic Collection (EBSCOhost) https://library.aurora.edu/login?url=http://search.ebscohost.com/login.aspx?direct=true&scope=site&db=nlebk&AN=486050

Northern Lakes College Access http://search.ebscohost.com/login.aspx?direct=true&scope=site&db=e000xna&AN=486050

http://www.AUT.eblib.com.au/EBLWeb/patron/?target=patron&extendedid=P_1422444_0

http://0-www.sciencedirect.com.pugwash.lib.warwick.ac.uk/science/book/9780123972699

ScienceDirect http://dproxy.library.dc-uoit.ca/login?url=https://www.sciencedirect.com/science/book/9780123972699

Sayyaadi, H., Zakerzadeh, M. R., & Salehi, H. (2012). A comparative analysis of some one-dimensional shape memory alloy constitutive models based on experimental tests. *Scientia Iranica, 19*(2), 249-257. doi:https://doi.org/10.1016/j.scient.2012.01.005

Sofla, A. Y. N., Elzey, D. M., & Wadley, H. N. G. (2008). Two-way Antagonistic Shape Actuation Based on the One-way Shape Memory Effect. *Journal of Intelligent Material Systems and Structures, 19*(9), 1017-1027. doi:10.1177/1045389X07083026

Soroushian, P., Ostowari, K., Nossoni, A., & Chowdhury, H. (2001). Repair and Strengthening of Concrete Structures Through Application of Corrective Posttensioning Forces with Shape Memory Alloys. *Transportation Research Record: Journal of the Transportation Research Board, 1770*, 20-26. doi:10.3141/1770-03

Spaggiari, A., Scirè Mammano, G., & Dragoni, E. (2012). *Optimum Mechanical Design of Binary Actuators Based on Shape Memory Alloys*.

Studio Gang. Bengt Sjostrom Starlight Theatre. Retrieved from http://studiogang.com/project/bengt-sjostrom-starlight-theatre

Sung, D. K. Smart Window. Retrieved from http://www.dosu-arch.com/smartwindow.html

Sung, D. K. (2012). Metal that Breathes. Retrieved from https://www.ted.com/talks/doris_kim_sung_metal_that_breathes#t-293337

Tabesh, T., & Sertyesilisik, B. *Focus on Atrium Spaces Aspects on the Energy Performance*.

Tabesh, T., & Sertyesilisik, B. (2016). An Investigation into Energy Performance with the Integrated Usage of a Courtyard and Atrium. *Buildings, 6*(2), 21.

Taleghani, M., Tenpierik, M., & van den Dobbelsteen, A. (2014). Energy performance and thermal comfort of courtyard/atrium dwellings in the Netherlands in the light of climate change. *Renewable Energy, 63*, 486-497.

Tanaka, K., & Nagaki, S. (1982). A thermomechanical description of materials with internal variables in the process of phase transitions. *Ingenieur-Archiv, 51*(5), 287-299. doi:10.1007/BF00536655

Tsujimoto, H., Kozaki, S., Okutani, Y., Toyozawa, T., Ando, K., YYorimitsu, S., . . . Ishii, H. (2017). *Lifespan Enhancement of Crane Rails, Runway Girders and Overhead Cranes Using Shape-memory Alloyed Fish-plates*. Retrieved from http://www.nssmc.com/tech/report/nssmc/pdf/115-10.pdf

U.S. Department of Energy. DETERMINING ELECTRIC MOTOR

LOAD AND EFFICIENCY. Retrieved from https://www.energy.gov/sites/prod/files/2014/04/f15/10097517.pdf

U.S. Energy Information Administration. (2009). 2009 RECS Survey Data, Table CE3.1 Household Site End-Use Consumption in the U.S., Totals and Averages. Retrieved 6th Jan 2018 https://www.eia.gov/consumption/residential/data/2009/c&e/ce3.1.xlsx

U.S. Energy Information Administration. (2016). 2012 CBECS Energy Survey Data, Table E1: Major Fuel by End Use. Release date: March 2016. Retrieved 6th Jan 2018 https://www.eia.gov/consumption/commercial/data/2012/c&e/pdf/e1-e11.pdf

U.S. Energy Information Administration. (2017). *International Energy Outlook*. Retrieved from https://www.eia.gov/outlooks/ieo/

Ulrich, R. B., & Quenemoen, C. K. (2013). *A Companion to Roman Architecture*: Wiley.

Vujošević, M., & Krstić-Furundžić, A. (2017). The influence of atrium on energy performance of hotel building. *Energy and Buildings, 156*, 140-150.

Wall, M. (1996). *Climate and Energy Use in Glazed Spaces Building Science.* (PhD), Lund University,

Wang, P.-Y., Guan, H.-Y., Liu, Z.-H., Wang, G.-S., Zhao, F., & Xiao, H.-S. (2014). High temperature collecting performance of a new all-glass evacuated tubular solar air heater with U-shaped tube heat exchanger. *Energy Conversion and Management, 77*, 315-323. doi:https://doi.org/10.1016/j.enconman.2013.08.019

Wu, M. H. (2002). Fabrication of Nitinol Materials and Components. *Materials Science Forum, 394-395*, 285-292. doi:10.4028/www.scientific.net/MSF.394-395.285

Zanaboni, E. (2008). *One Way and Two Way–Shape Memory Effect: Thermo-Mechanical Characterization of Ni-Ti wires.* University of Pavia,

10. Appendices

Reflection

Relationship between research and design

The main question of the thesis was:

> In terms of structure and detailing, how can an adaptronic atrium be designed to self-actuate in response to external environmental conditions, for the purposes of energy consumption reduction, in temperate climate regions?

A literature study was done on Shape Memory Alloys, a type of smart material which is able to change shape if the temperature changes. A deeper mathematical study into the thermal and mechanical behaviours of the material was done and from the findings, the most suitable model for uniaxial behaviour was chosen. A user-friendly software tool was made that allows a user to input the properties and shape of an SMA element along with a description of its antagonistic structure, and see how it behaves when the temperature is changed. This tool gave a convenient method of design for a material that could be complex to understand and would normally require specialist understanding in order design with. The model became instantly useful for realising the implications of using and exploiting the material in certain ways. With findings from both the literature study and the computational model, a concept design was made and some exploration followed. Physical experiments were done to inspect some nitinol for use as a prototype. The prototype engine was thereafter produced, with the capability of actuating a rotating arm by electric heating, and returning to the rest position when cooled. Activation by solar power was done separately. With the experiment and prototypes carried out, a final design was made which incorporated all the learnings and thereby deliver a design for an adaptronic atrium.

The thesis therefore took a journey which dived into cycles of research and design based on what needed to be found out next in order to answer the main question and push the performance of the adaptronics further. To summarise, the journey went through material science literature, reference project literature, computational tool scripting and exploration, concept design, and physical experiments in order to conceive a final design.

Relevance for the Sustainability Studio and Society

An agent against the highly intensive energy costs of HVAC

The thesis fits into the Sustainability Studio, the only studio of the Building Technology Track, as it seeks to tackle a major contributor of carbon emissions and thereby also find societal relevance. Governments and international bodies are increasingly applying pressure on buildings and all other human activities to cut down on energy and fossil fuel consumption, in order to stave off the potentially catastrophic consequences of climate change. The situation places great responsibility on the thoughtful design of energetically sustainable facades, as the heating and cooling of spaces consume 14% of all energy in the EU. Designing against HVAC consumption would therefore be a very logical strategy, and the concept of a seasonal atrium has the potential to cut down heating load by about a quarter in the case of a home in Amsterdam. It would therefore be an agent against the highly intensive energy costs of HVAC.

Scientific Relevance

Adaptronics: a new method for adaptive facades

Currently, responsive architectural systems for regulating indoor comfort are largely based on electrical sensors, computer controllers and motors. They can be complex to build, as they require a large number of parts, are prone to failure and they take up a lot of space. This thesis explores the possibility of adaptronic technology in the façade, which replaces all the complex electrical hardware with smart materials integrated into a thoughtfully designed structure. Such a device is able to do the job of sensing, computing and reacting simply by harnessing the properties of the smart material as it responds to external stimuli. This has great potential for façade design, as it has the job of separating the stable zone of human comfort on one side from the constantly fluctuating conditions of the outdoors on the other; it achieves its goals most efficiently when it is able to adapt with the current conditions. Adaptronics would be a new method for adaptive façades. In conventional adaptive facades, the adaptiveness is generally achieved with a set of electrical components that animate the façade elements, like a puppet. In adaptronics, the adaptiveness goes one level deeper, into the materials themselves.

Empowering the designer with Shape Memory Technology

Shape Memory Alloys have not yet been widely used in architecture, yet it has great potential for a range of applications besides using it as an actuator. For example, it can be a very effective connector, solid sealant, dampener and structural healing device. The complexity of its behaviour is one of the major barriers to its design, as virtually all past projects required a deep understanding and modelling of its dynamic phenomena. Throughout the thesis, a constant effort was made to remove that barrier and find methods to incorporate SMAs into the design process of a non-specialist as well as adapting the material to the physical capabilities of the construction industry, which tends to favour conservative approaches. The script produced is able to model the material as it changes with temperature, without needing specialist knowledge. The tool will empower designers to incorporate the shape memory technology into their own projects, and for climate engineers, it makes it possible to track the changing opening sizes with changes in weather, and thereby evaluate the resulting energy and comfort parameters of the indoor condition.

Ethical issues and dilemmas

The study on atria did briefly touch upon the attitude that clients may have when constructing them. For some corporations, atria are a feature which can represent the wealth, sophistication and power of the brand, with little or no regard for the energy-consuming implications from such a structure. It is important to remember that any act of construction is one that could leave decades of carbon contrail in the potentially intensive operating footprint. Even for zero-energy buildings, the energy and carbon cost in the act of building can be immense. The findings regarding the dominance of building-related energy consumption was therefore a reminder of the responsibility one must have when creating built fabric. For a project such as the adaptronic atrium, the responsibility manifests in the intention to make the atrium as an energy-positive architectural element instead of a net energy consumer.

Another issue is the nature of distributing free software. Firstly, with regards to properly acknowledging the sources that it has been built upon. The paper of (Brinson, 1993), which gave the mathematical model for the software, has been credited within the file itself. Secondly, there was a decision to be made regarding how free it would be. In the end, a Creative Commons Attribution 4.0 International License was chosen, which is the most free option and allows the software to be shared and commercially used.

Literature Study: Dynamic Shading and Building Energy Performance

There is no question that for buildings in temperate and hot climates, exterior shading in the summer will drastically reduce the annual cooling load by reducing or preventing solar gain. This is especially true of offices, which can have a high internal heat load from electrical equipment. There are two relevant questions to start off with: 1) the overall energy benefit, taking into account the potential increase in heat load due to reduced solar gain in Winter. 2) The energy saving value of a non-static shading system. Additional questions will arise from dynamic shading systems, for example the nature of user vs automatic control, and the phenomena of user intervention negatively effecting energy consumption. One such example is the scenario of users closing blinds in the winter to reduce glare or for privacy and leaving it in the closed position for long periods, which reduces beneficial solar gain. These issues will be discussed later on.

A study by Palmero-Marrero and Oliveira simulated the overall energy consequences for adding static shading to the East, West and South facades for a building in Mexico, Cairo, Lisbon, Madrid and London. The Southern shading devices in each were optimized for suitable shading in Summer and solar gain the Winter. Whilst ensuring guaranteed indoor comfort all round, the study concluded that significant energy savings were possible in hot climates, but in heating-dominated climates such as London, the energy consumption can actually increase, as shown in Figure 145. This is due to reduction in solar gain in the winter, which would have reduced heating load.

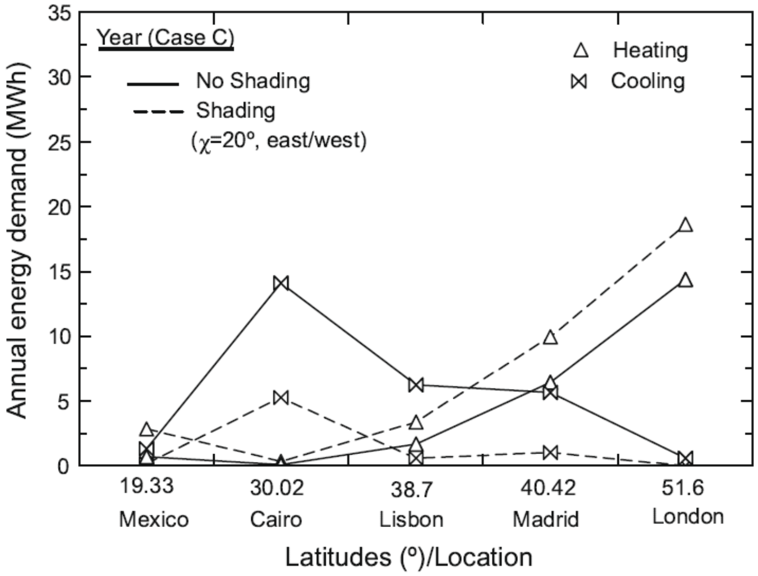

Figure 145: Energy demands with and without shading in various cities[20]

A field measurement and simulation study by Yao looked at the energy benefits of movable external shading in a residential building in temperate Ningbo, compared to no external shading. An overall annual heating/cooling load saving of 30.87% was achieved.[21] A different study by Lee for offices in Oakland, California studied automated Venetian blinds in synchronization with a dimmable electric lighting system to

---

[20] Palmero-Marrero 2009_Effect of louver shading devices on building energy requirements

[21] Yao 2013_An investigation into the impact of movable solar shades on energy, indoor thermal and visual comfort improvements

ensure no direct sun and continuous workplace illuminance. This was compared to static Venetian blinds with the same set-up at various slat angles. Compared to the highest performing static slat-angle, the automated system reduced daily peak cooling loads by 18-32% and average daily cooling loads by 7-15%.[22] Tian et al. simulated the effect of movable solar shades for different residential buildings in different cities of temperate climate using DOE-2 and concluded 17.3 to 22.7% energy saving.[23]

Nielsen simulated and compared three different solar strategies for a typical office located in Denmark: no shading, fixed external shading and dynamic external shading. The dynamic shading was programmed to cut out all direct sunlight according to the temperature, as well as eliminate glare during occupancy hours. The results, shown in Figure 146, indicate that fixed shading increased the total energy consumption in about half the scenarios, but in all cases the dynamic shading had better energy performance than both no shade and fixed shade. At the most extreme, the dynamic shading resulted in about 15% less energy demand than a no-shade scenario (for a Southern façade with a 2m window height), and about 9% less energy demand than a fixed shade (for the same case but for a 1m window height).

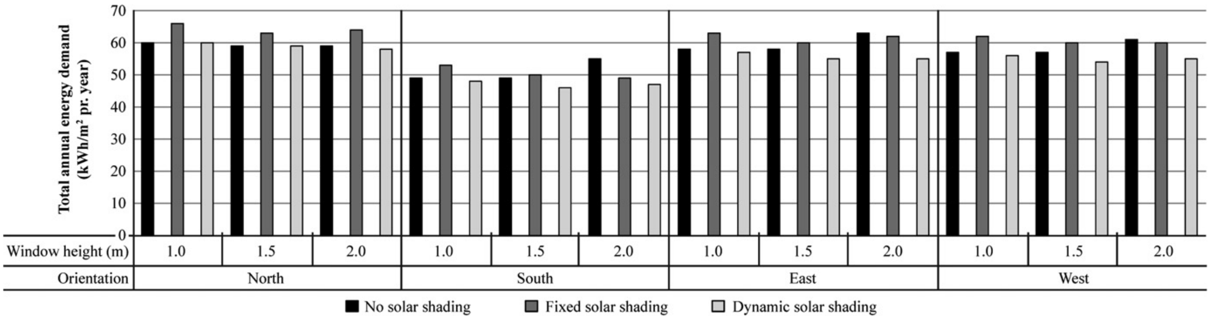

Figure 146: Total annual energy loads for a typical office in Denmark with 3 different solar shading strategies[24]

Finally, Johnsen and Winther demonstrated with simulation that an intelligent dynamic shading system such as variable Venetian blinds can indeed reduce the cooling load to virtually zero. The same paper also advocates the use of intelligently dynamic façade elements in general, including for ventilation, which would result in an overall building energy consumption reduction by half.[25]

Overall, the evidence suggests very worthwhile energy benefits for non-static shading systems, particularly those designed to maximise solar gain in the heating season and minimize in cooling. Additionally, dynamic shading devices can be adjusted to user preferences for functional or comfort reasons. However, there are some drawbacks: the high initial cost of installation, the energy cost of operation and the cost of maintenance and repair in the long term. Another key question is whether dynamic façade elements should be controlled manually or automatically. These issues will be addressed later in the report.

---

[22] Lee 1998_Thermal and daylighting performance of an automated Venetian blind and lighting system in a full-scale private office

[23] Tian HF, Sun DM, Zhou HZ. The energy saving performance of movable solar shading by 65%. Wall Mater Innovation Energy Saving Buildings 2009; 10:48-50 [in Chinese]

[24] Nielsen 2011_Quantifying the potential of automated dynamic solar shading

[25] Johnsen 2015_Dynamic facades- the smart way of meeting the energy requirements

Literature Study: Passive Ventilation Strategies and Building Energy Performance

Ventilation is the act of continuously replacing the air within a building with fresh external air. In 1984, The Dutch Health Council set a minimum ventilation rate of 25 m3/hr per person, corresponding to 2-5 air changes per hour for a standard meeting room.[26] In the Summer time, ventilation can be a powerful sustainable strategy to not only meet this requirement for fresh air, but also to keep the indoor temperature cool. Ventilation strategies can be categorized into three types: mechanical, passive (natural) and hybrid (a combination of the other two). Passive methods are highly favoured in sustainability terms because it consumes virtually zero energy consumption, it has lower construction/installation costs and the maintenance is minimal. CIBSE's guidance gives a rule of thumb that natural ventilation systems can mitigate average total daily heat loads (i.e. solar gains plus internal sources) of 30-40 W/m^2.[27]

Two driving forces can be designed into a building for natural ventilation: the stack effect, which utilises buoyancy to of warm air travelling from lower inlets to upper outlets, and wind. The latter is less reliable, as weather conditions are always changing and both speed and direction of wind need to favour the situation. Therefore, ventilation strategies often favour utilization of the stack effect, which is more predictable and easier to quantify in the design stage.

Gil-Baez et al. conducted experimental investigations on existing school buildings in Southern Spain and found that the replacement of mechanical ventilation with natural (wind and stack) ventilation strategies can result in primary energy savings in the range of 18-33%, even despite some energy loss in Winter passive ventilation.[28] Due the required care to reach this level of improvement, the system needs to be properly designed and controlled, which leads to their preference for automated window controls.

Pfafferott et al. studied the potential for night ventilation to remove thermal energy in the Summer, which could amount to 16% of the thermal load, as shown in Figure 147.[29] The method works by activating the thermal capacity of the concrete ceiling above the central atrium, by passing fresh air between 2am and 8am. Along with the hybrid mechanical-passive day ventilation, this technique helps the building operate without any air conditioning. They also studied a noticeable improvement via the optimization of the night ventilation by controlling the top outlet as a function of operative room temperature and the bottom inlet as a function of air temperature in the atrium. This halved the number of hours of thermal discomfort where $T > 25°C$.

The Concordia University Engineering building in Montreal was also studied regarding its as-built night ventilation benefit. The 17-storey building has a Southwest-facing atrium from the 2nd to the 16th floor, surrounded by functional spaces. By facilitating night ventilation which would activate at temperatures between 15 - 25°C, the cooling load could consequently be reduced by 30% in the months August-October.[30] This saving could potentially be much higher if activation happened at a greater range, for example 8 - 25°C. Again, thermal capacity is given by concrete slabs and there is an emphasis for predictive control intelligence for all the entire ventilation strategy. One pitfall for example is the overcooling from night ventilation, causing thermal discomfort and extra heating load during operation hours.

---

[26] Praktijkgids bouwbesluit ventilatie, 2013

[27] CIBSE 2004_Natural Ventilation in non-Domestic Buildings

[28] Gil-Baez 2017_Natural ventilation systems in 21st-century for near zero energy school buildings

[29] Pfafferot 2004_Design, monitoring and evaluation of a low energy office building with passive cooling by night ventilation

[30] Mouriki 2009 MSc_Solar-Assisted Hybrid Ventilation in an Institutional Building, p109

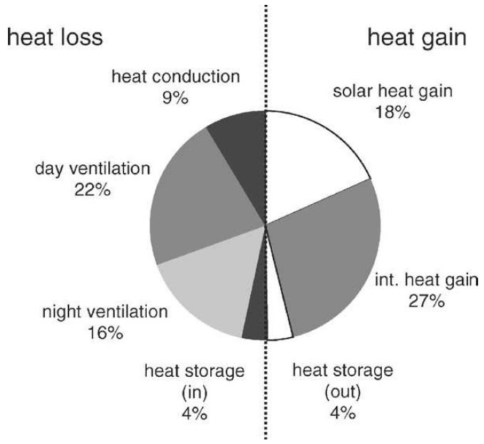

Figure 147: An office building in Hamm, Germany: the Energy balance for thermal gains and losses for a month in the Summer. The night ventilation is entirely buoyancy-driven and can remove 16% of the heat; it is free cooling.[31]

Summary

The energy benefits of passive ventilation can be substantial, especially regarding the stack effect in hot climates. Openings need to be carefully controlled, and preferably automatically, to ensure the most energy efficient operation of the natural ventilation system. Utilizing night ventilation can be advantageous in hot seasons as it can be used to discharge thermal energy from the daytime and store coolth in the building's thermal mass. These findings indicate that not only is passive ventilation beneficial, but an intelligently controlled strategy with dynamic openings can greatly improve the energy savings further. There are however some disadvantages: an automated system is by definition out of control of users, there may be security issues with openings at night and finally, utilization of thermal mass means time is needed to discharge heat and store coolth.

A Note about How We Govern the Devices

It should be noted that various authors have attempted to quantify the energy impact of the rules behind automated control strategies, and to draw conclusions on the ideal algorithms in which to orchestrate their façade movements.[32] [33] [34] [35] [36] They have desirable energy-saving effects but as mentioned above, inhabitants of private or small spaces (residential and office) do prefer and need manual controls as a matter of principle. This is not the case in a large public space such as an atrium, where visitors to the space do not expect or demand individual control of the climatic devices. The next chapter will investigate the energy consumption with regards to atria.

---

[31] Pfafferot 2004_Design, monitoring and evaluation of a low energy office building with passive cooling by night ventilation

[32] Tzempelikos 2013_Comparative control strategies for roller shades with respect to daylighting and energy performance

[33] Moeseke 2007_Impact of control rules on the efficiency of shading devices and free cooling for office buildings

[34] Nielsen 2011_Quantifying the potential of automated dynamic solar shading

[35] Shen 2011_Daylighting and energy analysis of private offices with automated interior roller shades

[36] Tzempelikos 2006_The impact of shading design and control on building cooling and lighting demand

Literature Study: 4D Printing

4D printing and Shape Memory Polymers

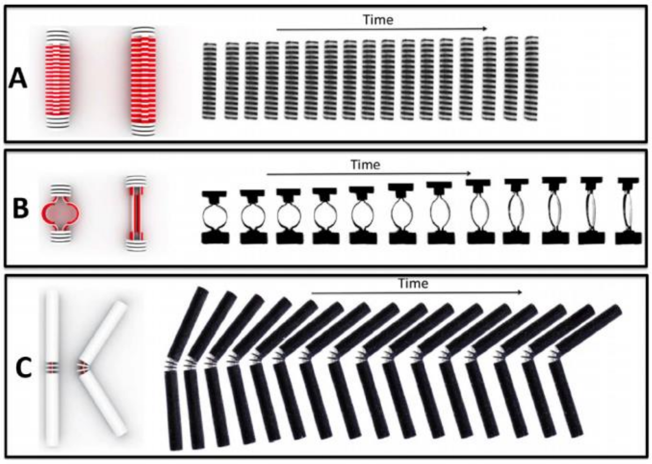

Figure 148: 4D printed objects, made of a polymer that expands in water (red) and a rigid material (white). The frames on the right show a timelapse of the submerged objects. In example A, the amount of red material determines the extent of stretching. In the latter two examples, a two-layer strip of red and white material allows the piece to go from curved to straight (and vice-versa).[37]

One novel and rapidly advancing area of 3D printing technology is that of 4D printing, whose products are endowed with the ability to move in predetermined ways in response to environmental stimuli.[38] The general method relies on the strategic placement of differential rigid or expandable material within the 3D-printed object, thus making it deform in a controlled manner when only the expandable material is made to respond to the environment. Various stimuli are possible depending on the material, such as heat, immersion in water, an electric current[39] and magnetic field (on polymer)[40]. An example of this can be seen in Figure 148, which is expandable polymer immersed in water.

Some materials display a peculiar phenomena of re-shaping itself to a 'remembered' geometry, which fixes any prior deformations, when subjected to stimuli. This is referred to as the Shape Memory Effect, or SME, and is often the active agent that causes the movement. Polymers with this capability are referred to as Shape Memory Polymers, or SMPs, and they are known for having impressive strain recoveries of over 400%, which is why they are used as the active material in 4D prints. They have two solid states, a glassy state which occurs at lower temperatures, and a rubbery state which in the case of heat-induced SME happens at a higher temperature and is the state where the shape is 'remembered'.

In architecture academia, the most visible authority is Skylar Tibbits, who leads the Self-Assembly Lab at MIT. His TED talk of 20 demonstrates a 4D-printed polymer straight rod which changes shape into the letters

---

[37] Raviv 2014_Active Printed Materials for Complex Self-Evolving Deformations

[38] Meng 2010_A Brief Review of Stimulus-active Polymers Responsive to Thermal, Light, Magnetic, Electric, and Water-Solvent Stimuli

[39] Sahoo 2007_Electroactive Shape Memory Effect of Polyurethane Composites Filled with Carbon Nanotubes and Conducting Polymer

[40] Schmidt 2006_Electromagnetic Activation of Shape Memory PolymerNetworks Containing Magnetic Nanoparticles

'MIT' when submerged.[41] One of the goals of the group is to deliver self-building methods in places where it is necessary, for example on Mars and extreme environments.

A great number of synthetic materials, with each type having a multitude of variations, is possible in this field. In Figure 150, Gladman demonstrates the precision and complexity that 4D printing is capable of, by utilizing a hydrogel composite made of stiff cellulose fibrils in a soft acrylamide matrix to produce flat plates, which blossom into petal shapes.[42]

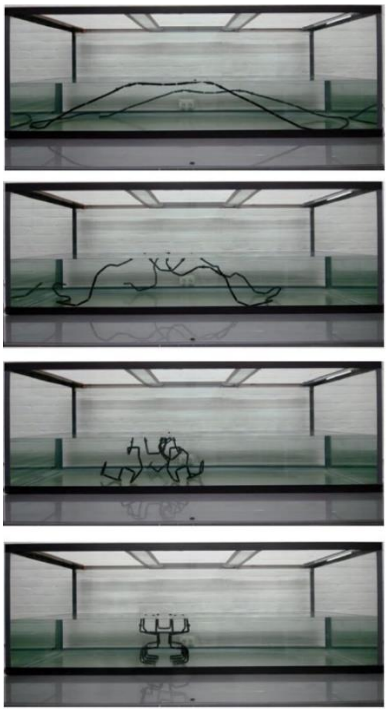

Figure 149: A complex structure emerges from the 4D printed rods when submerged.[43]

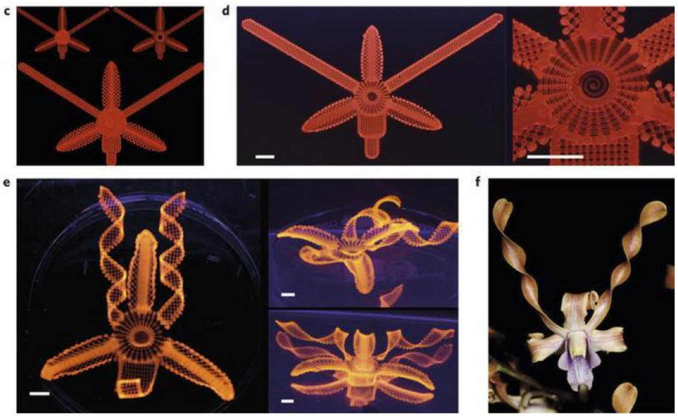

Figure 150: A complex 4D-printed product showing its precision capability[44]

To summarise, 4D-printing is a promising area of innovation, finding uses in smart textiles, space applications, structural adhesion, intelligent medical instruments, artificial muscles, packaging and micro-

---

[41] https://www.ted.com/talks/skylar_tibbits_the_emergence_of_4d_printing

[42] Gladman 2016_Biomimetic 4D Printing

[43] Tibbits 2017_4D printing-multi-material shape change

[44] Gladman 2016_Biomimetic 4D Printing

actuators.[45,46] However, its entry into the mechanical engineering industries has been slow, which is attributed to the lack of structural and functional data that is required for design.[47] It is still a new field that may take decades longer to mature. Other drawbacks for SMPs include the low Young's modulus, which is typically just 2 MPa for the rubbery state, and 827 MPa for the glassy state; the latter is still 200 times less than that of steel.[48] Additionally, the cycle life of SMPs is a concern, especially where large strain recoveries are repeated many times. In some scenarios, just 22 cycles for a 100% strain recovery is considered superior.[49] Despite the impressive strain recoveries that are possible, Rosseau recommends using only 20% to ensure long-term use of an SMP actuator element.[50]

Reference Projects: Dynamic Atria-like and Glazed Spaces

The following reference projects have been selected for their unique design of atria-like and glazed spaces that relate to theme of the literature: intelligent dynamic systems for solar, ventilation and climate control.

Sharifi-ha House by Nextoffice (2014)

Private House in Tehran

Figure 151: time lapse of rooms of Sharifi-ha House being moved.[51]

---

[45] Mather 2009_Shape Memory Polymer Research

[46] Meng 2010_A Brief Review of Stimulus-active Polymers Responsive to Thermal, Light, Magnetic, Electric, and Water-Solvent Stimuli

[47] Mogharebi 2013_On the cyclic material stability of shape memory polymer.pdf

[48] Wei 1998_Review Shape-memory materials and hybrid composites for smart systems

[49] Choong 2017_4D printing of high performance shape memory polymer using stereolithography

[50] Rosseau 2008_Challenges of Shape Memory Polymers- A Review of the Progress Toward Overcoming SMPs Limitations

[51] https://www.archdaily.com/522344/sharifi-ha-house-nextoffice/ accessed 14th January 2018

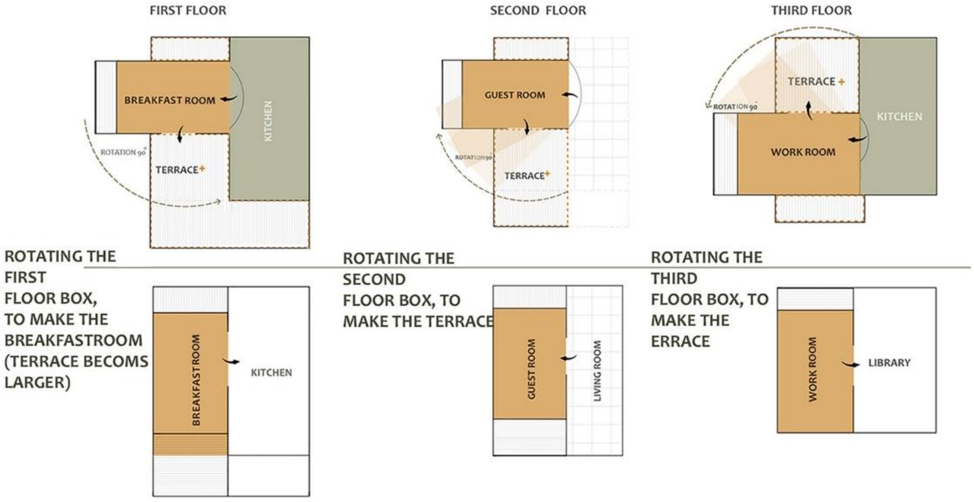

Figure 152: Plan showing how the rooms move[52]

This private house in Iran features three rooms at the façade that are able to rotate as shown above. The idea was to provide seasonal moves of habitation, a reference to traditional Iranian houses, specifically a Zemestan-Neshin (winter living room) and Taabestan-Neshin (summer living room). In the snowy Iranian winters, the rooms can rotate so the façade is closed off, whilst in the hot summer the rooms can rotate open and allow ventilation.[53] Note that this is different to most atria, because it is at its most opaque in the winter, and therefore does not benefit from the added solar gain. The large eaves reduce the summer solar gain to make this strategy work; energy is likely saved, but no energy calculations are publicly available. It is clear that the change of character, from an introverted façade to an extroverted one, is an important consideration in this project.

---

[52] https://www.archdaily.com/522344/sharifi-ha-house-nextoffice/ accessed 14th January 2018

[53] https://www.archdaily.com/522344/sharifi-ha-house-nextoffice accessed 14th January 2018

Office building for a Biotechnology Company by Behnisch & Partner (2003)

Cambridge, USA

An atrium extends through all the floors and forms a central part of the building. It is flooded with natural lighting by the use of seven computer-controlled heliostat reflectors on the roof, which help direct the sunlight through special louvres and into the atrium. The perspex louvres are designed to scatter the light, tracking and rotating in response to the changing light geometry. The building also utilises night time cooling. Energy costs are 42% of US standard.[54]

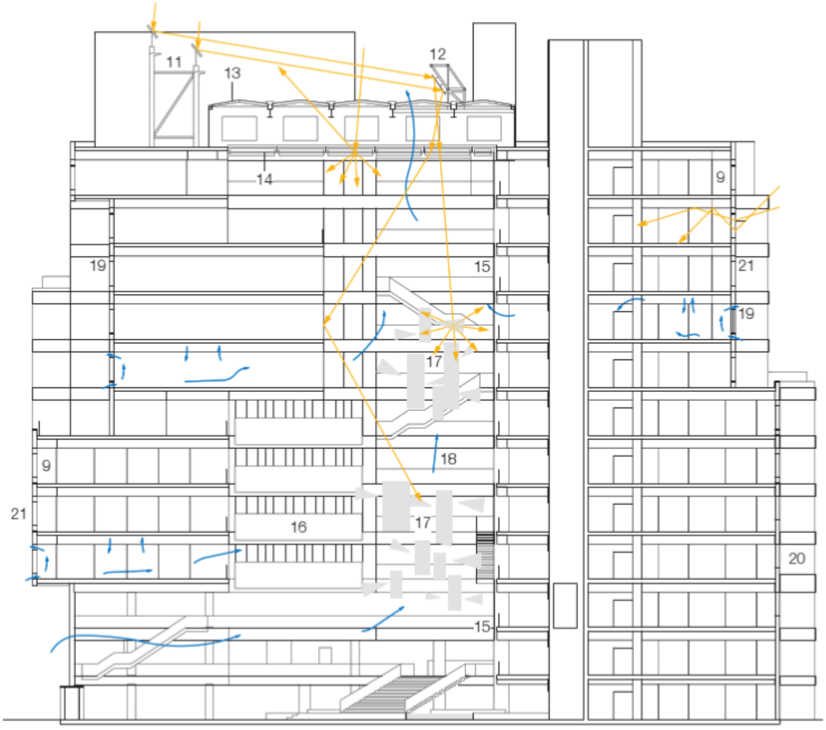

Figure 153: Section of the office building, showing the paths of sunlight being directed down the atrium in the center[55]

---

[54] Energy Manual: Sustainable Architecture by Manfred Hegger, p246

https://ebookcentral-proquest-com.tudelft.idm.oclc.org/lib/delft/reader.action?docID=1075583&query=&ppg=202 p249

[55] Energy Manual: Sustainable Architecture by Manfred Hegger, p246

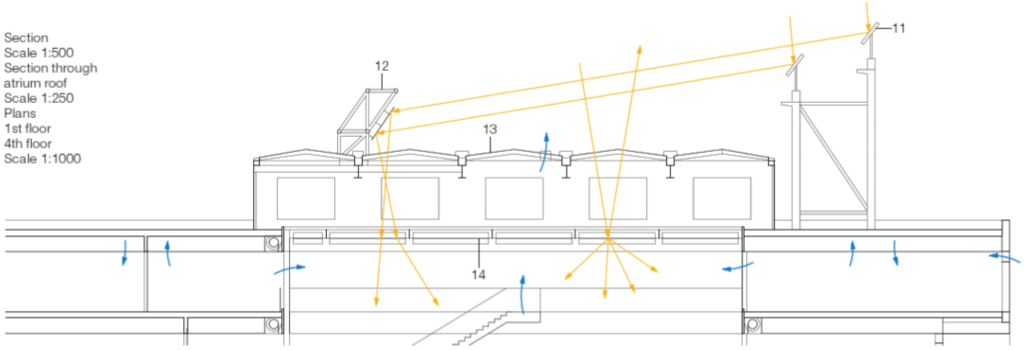

Figure 154: Closeup of the atrium roof and the heliostat hardware. 11) Tracking heliostat with 1600 x 1600 mm mirror 12) Fixed bridge of mirrors 13) Roof light with low-e glazing and extractor fans 14) Prismatic tracking, pivoting louvres, Perspex[56]

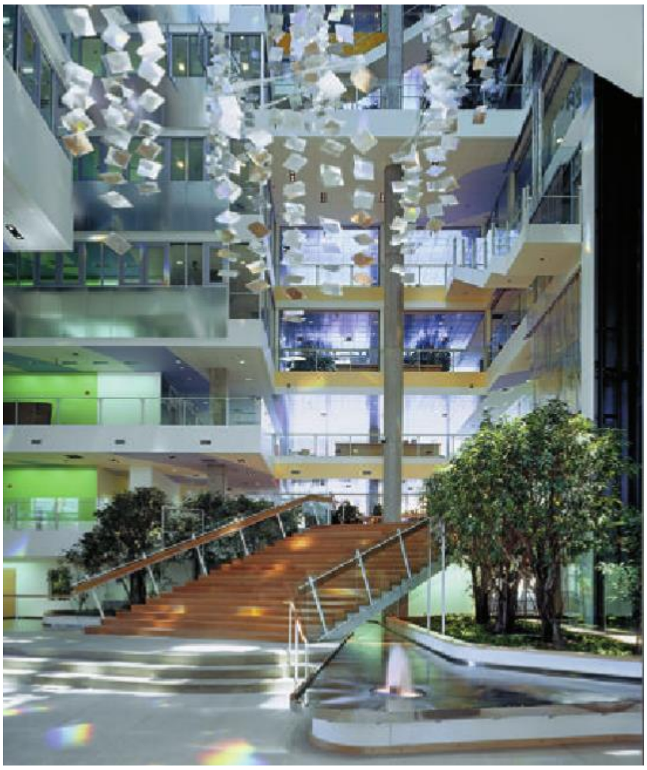

Figure 155: Interior view of atrium[57]

---

[56] nergy Manual: Sustainable Architecture by Manfred Hegger, p247

[57] nergy Manual: Sustainable Architecture by Manfred Hegger, p247

Complete Script of Software Tool

The code to generate the material property topographies and solve for stress strain has been written in Python. It is shown below.

```
import rhinoscriptsyntax as rs
import math

"""

This work is licensed under the Creative Commons Attribution 4.0
International
License. To view a copy of this license, visit
http://creativecommons.org/licenses/by/4.0/

This model is all based on the work of the following paper:
Brinson, L. C. (1993). One-Dimensional Constitutive Behavior of Shape
Memory Alloys:
Thermomechanical Derivation with Non-Constant Material Functions and
Redefined
Martensite Internal Variable. Journal of Intelligent Material Systems and
Structures,
4(2), 229-242. doi:10.1177/1045389X9300400213
"""

#SMA material properties
Mf = SMA[0]
Ms = SMA[1]
As = SMA[2]
Af = SMA[3]
CM = SMA[4]
CA = SMA[5]
ScrS = SMA[6]
ScrF = SMA[7]
Da = SMA[8]
Dm = SMA[9]
rStrain = SMA[10]

#upon reset, the material is cooled down to -20, and then heated back up to
Mf
#and remains fully martensite
if reset == True:
    S00 = 0
    pT = -19
    T00 = -20
    T0 = -20
    T = Mf
    E0 = 1
    pE = 1
    E = 1
    toAus = True

#Useful material parameters to be used for equations
aA = math.pi/(Af-As)
aM = math.pi/(Ms-Mf)
```

```
#Creates evenly spaced series of numbers book-ended by a and b. with c
number of spaces
def increment(a, b, c):
    list = []
    for i in range(c):
        list.append(a + i*((b - a) /c))
    list.append(b)
    return list

#equation for transition zone of Martensite to Austenite
def MtoA(T):
    return E0/2*(math.cos(aA*(T-As-S/CA))+1)

#equation for transition zone of Austenite to Martensite
def AtoM(T):
    cosTerm = math.pi/(ScrS-ScrF)*(S-ScrF-CM*(T-Ms))
    return (1-E0)/2*math.cos(cosTerm)+(1+E0)/2

#make a sine curve between lower and higher point
def genSinCrv(loPt, hiPt):
    loZ = rs.PointCoordinates(loPt)[2]
    hiX = rs.PointCoordinates(hiPt)[0]
    hiY = rs.PointCoordinates(hiPt)[1]
    hiZ = rs.PointCoordinates(hiPt)[2]
    projectedHiPt = rs.AddPoint([hiX, hiY, loZ])
    zDiff = hiZ - loZ
    line = rs.AddLine(loPt, projectedHiPt)
    seedPts = rs.DivideCurve(line, 20)
    seedHeight = []
    for i in range(21):
        h = ((math.sin( i * math.pi / 20 - math.pi / 2))+1)/2 * zDiff
        seedHeight.append(h)
    pts = []
    for i in range(21):
        x = seedPts[i][0]
        y = seedPts[i][1]
        z = seedPts[i][2] + seedHeight[i]
        pts.append(rs.AddPoint([x,y,z]))
    crv = rs.AddCurve(pts)
    return crv

#sine-Loft between a lower and upper line
def sinLoft(lowerLine, upperLine):
    low1 = rs.AddPoint(rs.CurveEditPoints(lowerLine)[0])
    low2 =
rs.AddPoint(rs.CurveEditPoints(lowerLine)[len(rs.CurveEditPoints(lowerLine)
)-1])
    up1 = rs.AddPoint(rs.CurveEditPoints(upperLine)[0])
    up2 =
rs.AddPoint(rs.CurveEditPoints(upperLine)[len(rs.CurveEditPoints(upperLine)
)-1])
    sinCrv1 = genSinCrv(low1, up1)
    sinCrv2 = genSinCrv(low2, up2)
    loft = rs.AddLoftSrf([sinCrv1, sinCrv2])
    return loft

#generate topography for G1 Martensite Fraction, mainly for visualisation
purposes
def genTopo_MF(E0):
    #generate martPlat at E=1
```

```
    x1 = (maxS + CM * Ms - ScrF) / CM
    pt1 = rs.AddPoint([x1, maxS, 1])
    pt2 = rs.AddPoint([Ms, ScrF, 1])
    pt3 = rs.AddPoint([0, ScrF, 1])
    pt4 = rs.AddPoint([0, maxS, 1])
    srf1 = rs.AddSrfPt([pt1, pt2, pt3, pt4])
    #generate martward cliff
    #      generate lower line of martward sinecliff, start point nearer to
origin
    pt1 = rs.AddPoint([Ms, ScrS, E0])
    x2 = ( maxS + CM * Ms - ScrS ) / CM
    pt2 = rs.AddPoint([x2, maxS, E0])
    lowerLine = rs.AddLine(pt1, pt2)
    #       generate upper line of marward sinecliff, start point nearer to
origin
    pt1 = rs.AddPoint([Ms, ScrF, 1])
    x2 = (maxS + CM * Ms - ScrF) / CM
    pt2 = rs.AddPoint([x2, maxS, 1])
    upperLine = rs.AddLine(pt1, pt2)
    #       generate martward sinecliff srf
    srf2 = sinLoft(lowerLine, upperLine)
    #generate middle plateau at E=E0
    x1 = ( maxS + CA * As) / CA
    pt1 = rs.AddPoint([x1, maxS, E0])
    pt2 = rs.AddPoint([As, 0, E0])
    pt3 = rs.AddPoint([Ms, 0, E0])
    pt4 = rs.CurveStartPoint(lowerLine)
    pt5 = rs.CurveEndPoint(lowerLine)
    crv = rs.AddPolyline([pt1, pt2, pt3, pt4, pt5, pt1])
    srf3 = rs.AddPlanarSrf(crv)
    #generate austward cliff
    #       generate lower line of austward sinecliff, start point nearer
to origin
    pt1 = rs.AddPoint([Af, 0, 0])
    x2 = ( maxS + CA * Af) / CA
    pt2 = rs.AddPoint([x2, maxS, 0])
    lowerLine = rs.AddLine(pt1, pt2)
    #       generate upper line of austward sinecliff, start point nearer
to origin
    pt1 = rs.AddPoint([As, 0, E0])
    x2 = ( maxS + CA * As) / CA
    pt2 = rs.AddPoint([x2, maxS, E0])
    upperLine = rs.AddLine(pt1, pt2)
    #       generate austward sinecliff srf
    srf4  = sinLoft(lowerLine, upperLine)
    #generate austenite plateau
    x4 = (maxS + CA * Af) / CA
    pt1 = rs.AddPoint([maxT, maxS, 0])
    pt2 = rs.AddPoint([maxT, 0, 0])
    pt3 = rs.AddPoint([Af, 0, 0])
    pt4 = rs.AddPoint([x4, maxS, 0])
    srf5 = rs.AddSrfPt([pt1, pt2, pt3, pt4])
    #combine all srfs
    return rs.JoinSurfaces([srf1, srf2, srf3, srf4, srf5])

#generate Martward path topo G1
def martwardTopo_MF(E0):
    #generate martPlat at E=1
    x1 = (maxS + CM * Ms - ScrF) / CM
    pt1 = rs.AddPoint([x1, maxS, 1])
```

```
    pt2 = rs.AddPoint([Ms, ScrF, 1])
    pt3 = rs.AddPoint([0, ScrF, 1])
    pt4 = rs.AddPoint([0, maxS, 1])
    srf1 = rs.AddSrfPt([pt1, pt2, pt3, pt4])
    #generate martward cliff
    #      generate lower line of martward sinecliff, start point nearer to
origin
    pt1 = rs.AddPoint([Ms, ScrS, E0])
    x2 = ( maxS + CM * Ms - ScrS ) / CM
    pt2 = rs.AddPoint([x2, maxS, E0])
    lowerLine = rs.AddLine(pt1, pt2)
    #       generate upper line of marward sinecliff, start point nearer to
origin
    pt1 = rs.AddPoint([Ms, ScrF, 1])
    x2 = (maxS + CM * Ms - ScrF) / CM
    pt2 = rs.AddPoint([x2, maxS, 1])
    upperLine = rs.AddLine(pt1, pt2)
    #       generate martward sinecliff srf
    srf2 = sinLoft(lowerLine, upperLine)
    #generate middle plateau at E=E0
    x1 = ( maxS + CA * As) / CA
    pt1 = rs.AddPoint([x1, maxS, E0])
    pt2 = rs.AddPoint([As, 0, E0])
    pt3 = rs.AddPoint([Ms, 0, E0])
    pt4 = rs.CurveStartPoint(lowerLine)
    pt5 = rs.CurveEndPoint(lowerLine)
    crv = rs.AddPolyline([pt1, pt2, pt3, pt4, pt5, pt1])
    srf3 = rs.AddPlanarSrf(crv)
    #generate austward cliff
    #       generate lower line of austward sinecliff, start point nearer
to origin
    pt1 = rs.AddPoint([Af, 0, E0])
    x2 = ( maxS + CA * Af) / CA
    pt2 = rs.AddPoint([x2, maxS, E0])
    lowerLine = rs.AddLine(pt1, pt2)
    #       generate upper line of austward sinecliff, start point nearer
to origin
    pt1 = rs.AddPoint([As, 0, E0])
    x2 = ( maxS + CA * As) / CA
    pt2 = rs.AddPoint([x2, maxS, E0])
    upperLine = rs.AddLine(pt1, pt2)
    #       generate austward sinecliff srf
    srf4  = sinLoft(lowerLine, upperLine)
    #generate austenite plateau
    x4 = (maxS + CA * Af) / CA
    pt1 = rs.AddPoint([maxT, maxS, E0])
    pt2 = rs.AddPoint([maxT, 0, E0])
    pt3 = rs.AddPoint([Af, 0, E0])
    pt4 = rs.AddPoint([x4, maxS, E0])
    srf5 = rs.AddSrfPt([pt1, pt2, pt3, pt4])
    #combine all srfs
    return rs.JoinSurfaces([srf1, srf2, srf3, srf4, srf5])

#generate Austward path topo G1
def austwardTopo_MF(E0):
    #generate martPlat at E=1
    x1 = (maxS + CM * Ms - ScrF) / CM
    pt1 = rs.AddPoint([x1, maxS, E0])
    pt2 = rs.AddPoint([Ms, ScrF, E0])
    pt3 = rs.AddPoint([0, ScrF, E0])
```

```
    pt4 = rs.AddPoint([0, maxS, E0])
    srf1 = rs.AddSrfPt([pt1, pt2, pt3, pt4])
    #generate martward cliff
    #      generate lower line of martward sinecliff, start point nearer to
origin
    pt1 = rs.AddPoint([Ms, ScrS, E0])
    x2 = ( maxS + CM * Ms - ScrS ) / CM
    pt2 = rs.AddPoint([x2, maxS, E0])
    lowerLine = rs.AddLine(pt1, pt2)
    #       generate upper line of marward sinecliff, start point nearer to
origin
    pt1 = rs.AddPoint([Ms, ScrF, E0])
    x2 = (maxS + CM * Ms - ScrF) / CM
    pt2 = rs.AddPoint([x2, maxS, E0])
    upperLine = rs.AddLine(pt1, pt2)
    #       generate martward sinecliff srf
    srf2 = sinLoft(lowerLine, upperLine)
    #generate middle plateau at E=E0
    x1 = ( maxS + CA * As) / CA
    pt1 = rs.AddPoint([x1, maxS, E0])
    pt2 = rs.AddPoint([As, 0, E0])
    pt3 = rs.AddPoint([Ms, 0, E0])
    pt4 = rs.CurveStartPoint(lowerLine)
    pt5 = rs.CurveEndPoint(lowerLine)
    crv = rs.AddPolyline([pt1, pt2, pt3, pt4, pt5, pt1])
    srf3 = rs.AddPlanarSrf(crv)
    #generate austward cliff
    #       generate lower line of austward sinecliff, start point nearer
to origin
    pt1 = rs.AddPoint([Af, 0, 0])
    x2 = ( maxS + CA * Af) / CA
    pt2 = rs.AddPoint([x2, maxS, 0])
    lowerLine = rs.AddLine(pt1, pt2)
    #       generate upper line of austward sinecliff, start point nearer
to origin
    pt1 = rs.AddPoint([As, 0, E0])
    x2 = ( maxS + CA * As) / CA
    pt2 = rs.AddPoint([x2, maxS, E0])
    upperLine = rs.AddLine(pt1, pt2)
    #       generate austward sinecliff srf
    srf4  = sinLoft(lowerLine, upperLine)
    #generate austenite plateau
    x4 = (maxS + CA * Af) / CA
    pt1 = rs.AddPoint([maxT, maxS, 0])
    pt2 = rs.AddPoint([maxT, 0, 0])
    pt3 = rs.AddPoint([Af, 0, 0])
    pt4 = rs.AddPoint([x4, maxS, 0])
    srf5 = rs.AddSrfPt([pt1, pt2, pt3, pt4])
    #combine all srfs
    return rs.JoinSurfaces([srf1, srf2, srf3, srf4, srf5])

#transform a Temp-Stress-MartFrac point for bands 0 to 4 into the resulting
Temp-Force-Strain point
def G1toG2(origPt):
    T = rs.PointCoordinates(origPt)[0]
    S = rs.PointCoordinates(origPt)[1]
    E = rs.PointCoordinates(origPt)[2]
    F = S * A * 1000000
    YoungsMod = Da + E * (Dm - Da)
    strain = E * rStrain + S / YoungsMod
```

```
    disp = strain * L
    return rs.AddPoint(T, F, disp)

#generate 2-way topography for G2 force and strain, mainly for visual
purposes
def genTopo_FD(E0):
    #generate martPlat at E=1
    x1 = (maxS + CM * Ms - ScrF) / CM
    pt1 = rs.AddPoint([x1, maxS, 1])
    pt1 = G1toG2(pt1)
    pt2 = rs.AddPoint([Ms, ScrF, 1])
    pt2 = G1toG2(pt2)
    pt3 = rs.AddPoint([0, ScrF, 1])
    pt3 = G1toG2(pt3)
    pt4 = rs.AddPoint([0, maxS, 1])
    pt4 = G1toG2(pt4)
    srf1 = rs.AddSrfPt([pt1, pt2, pt3, pt4])
    #generate martward cliff
    #       generate lower line of martward sinecliff, start point nearer to
origin
    pt1 = rs.AddPoint([Ms, ScrS, E0])
    pt1 = G1toG2(pt1)
    x2 = ( maxS + CM * Ms - ScrS ) / CM
    pt2 = rs.AddPoint([x2, maxS, E0])
    pt2 = G1toG2(pt2)
    lowerLine = rs.AddLine(pt1, pt2)
    #        generate upper line of marward sinecliff, start point nearer to
origin
    pt1 = rs.AddPoint([Ms, ScrF, 1])
    pt1 = G1toG2(pt1)
    x2 = (maxS + CM * Ms - ScrF) / CM
    pt2 = rs.AddPoint([x2, maxS, 1])
    pt2 = G1toG2(pt2)
    upperLine = rs.AddLine(pt1, pt2)
    #        generate martward sinecliff srf
    srf2 = sinLoft(lowerLine, upperLine)
    #generate middle plateau at E=E0
    x1 = ( maxS + CA * As) / CA
    pt1 = rs.AddPoint([x1, maxS, E0])
    pt1 = G1toG2(pt1)
    pt2 = rs.AddPoint([As, 0, E0])
    pt2 = G1toG2(pt2)
    pt3 = rs.AddPoint([Ms, 0, E0])
    pt3 = G1toG2(pt3)
    pt4 = rs.AddPoint([Ms, ScrS, E0])
    pt4 = G1toG2(pt4)
    x5 = ( maxS + CM * Ms - ScrS ) / CM
    pt5 = rs.AddPoint([x5, maxS, E0])
    pt5 = G1toG2(pt5)
    crv = rs.AddPolyline([pt1, pt2, pt3, pt4, pt5, pt1])
    srf3 = rs.AddPlanarSrf(crv)
    #generate austward cliff
    #        generate lower line of austward sinecliff, start point nearer
to origin
    pt1 = rs.AddPoint([Af, 0, 0])
    pt1 = G1toG2(pt1)
    x2 = ( maxS + CA * Af) / CA
    pt2 = rs.AddPoint([x2, maxS, 0])
    pt2 = G1toG2(pt2)
    lowerLine = rs.AddLine(pt1, pt2)
```

```
    #       generate upper line of austward sinecliff, start point nearer
to origin
    pt1 = rs.AddPoint([As, 0, E0])
    pt1 = G1toG2(pt1)
    x2 = ( maxS + CA * As) / CA
    pt2 = rs.AddPoint([x2, maxS, E0])
    pt2 = G1toG2(pt2)
    upperLine = rs.AddLine(pt1, pt2)
    #       generate austward sinecliff srf
    srf4  = sinLoft(lowerLine, upperLine)
    #generate austenite plateau
    x4 = (maxS + CA * Af) / CA
    pt1 = rs.AddPoint([maxT, maxS, 0])
    pt1 = G1toG2(pt1)
    pt2 = rs.AddPoint([maxT, 0, 0])
    pt2 = G1toG2(pt2)
    pt3 = rs.AddPoint([Af, 0, 0])
    pt3 = G1toG2(pt3)
    pt4 = rs.AddPoint([x4, maxS, 0])
    pt4 = G1toG2(pt4)
    srf5 = rs.AddSrfPt([pt1, pt2, pt3, pt4])
    #combine all srfs
    return rs.JoinSurfaces([srf1, srf2, srf3, srf4, srf5])

#GENERATE MARTWARD PATH TOPO G2
def martwardTopo_FD(E0):
    #generate martPlat at E=1
    x1 = (maxS + CM * Ms - ScrF) / CM
    pt1 = rs.AddPoint([x1, maxS, 1])
    pt1 = G1toG2(pt1)
    pt2 = rs.AddPoint([Ms, ScrF, 1])
    pt2 = G1toG2(pt2)
    pt3 = rs.AddPoint([0, ScrF, 1])
    pt3 = G1toG2(pt3)
    pt4 = rs.AddPoint([0, maxS, 1])
    pt4 = G1toG2(pt4)
    srf1 = rs.AddSrfPt([pt1, pt2, pt3, pt4])
    #generate martward cliff
    #      generate lower line of martward sinecliff, start point nearer to
origin
    pt1 = rs.AddPoint([Ms, ScrS, E0])
    pt1 = G1toG2(pt1)
    x2 = ( maxS + CM * Ms - ScrS ) / CM
    pt2 = rs.AddPoint([x2, maxS, E0])
    pt2 = G1toG2(pt2)
    lowerLine = rs.AddLine(pt1, pt2)
    #       generate upper line of marward sinecliff, start point nearer to
origin
    pt1 = rs.AddPoint([Ms, ScrF, 1])
    pt1 = G1toG2(pt1)
    x2 = (maxS + CM * Ms - ScrF) / CM
    pt2 = rs.AddPoint([x2, maxS, 1])
    pt2 = G1toG2(pt2)
    upperLine = rs.AddLine(pt1, pt2)
    #       generate martward sinecliff srf
    srf2 = sinLoft(lowerLine, upperLine)
    #generate middle plateau at E=E0
    x1 = ( maxS + CA * As) / CA
    pt1 = rs.AddPoint([x1, maxS, E0])
    pt1 = G1toG2(pt1)
```

```
    pt2 = rs.AddPoint([As, 0, E0])
    pt2 = G1toG2(pt2)
    pt3 = rs.AddPoint([Ms, 0, E0])
    pt3 = G1toG2(pt3)
    pt4 = rs.AddPoint([Ms, ScrS, E0])
    pt4 = G1toG2(pt4)
    x5 = ( maxS + CM * Ms - ScrS ) / CM
    pt5 = rs.AddPoint([x5, maxS, E0])
    pt5 = G1toG2(pt5)
    crv = rs.AddPolyline([pt1, pt2, pt3, pt4, pt5, pt1])
    srf3 = rs.AddPlanarSrf(crv)
    #generate austward cliff
    #       generate lower line of austward sinecliff, start point nearer
to origin
    pt1 = rs.AddPoint([Af, 0, E0])
    pt1 = G1toG2(pt1)
    x2 = ( maxS + CA * Af) / CA
    pt2 = rs.AddPoint([x2, maxS, E0])
    pt2 = G1toG2(pt2)
    lowerLine = rs.AddLine(pt1, pt2)
    #       generate upper line of austward sinecliff, start point nearer
to origin
    pt1 = rs.AddPoint([As, 0, E0])
    pt1 = G1toG2(pt1)
    x2 = ( maxS + CA * As) / CA
    pt2 = rs.AddPoint([x2, maxS, E0])
    pt2 = G1toG2(pt2)
    upperLine = rs.AddLine(pt1, pt2)
    #       generate austward sinecliff srf
    srf4  = sinLoft(lowerLine, upperLine)
    #generate austenite plateau
    x4 = (maxS + CA * Af) / CA
    pt1 = rs.AddPoint([maxT, maxS, E0])
    pt1 = G1toG2(pt1)
    pt2 = rs.AddPoint([maxT, 0, E0])
    pt2 = G1toG2(pt2)
    pt3 = rs.AddPoint([Af, 0, E0])
    pt3 = G1toG2(pt3)
    pt4 = rs.AddPoint([x4, maxS, E0])
    pt4 = G1toG2(pt4)
    srf5 = rs.AddSrfPt([pt1, pt2, pt3, pt4])
    #combine all srfs
    return rs.JoinSurfaces([srf1, srf2, srf3, srf4, srf5])

#GENERATE AUSTWARD PATH TOPO G2
def austwardTopo_FD(E0):
    #generate martPlat at E = E0
    x1 = (maxS + CM * Ms - ScrF) / CM
    pt1 = rs.AddPoint([x1, maxS, E0])
    pt1 = G1toG2(pt1)
    pt2 = rs.AddPoint([Ms, ScrF, E0])
    pt2 = G1toG2(pt2)
    pt3 = rs.AddPoint([0, ScrF, E0])
    pt3 = G1toG2(pt3)
    pt4 = rs.AddPoint([0, maxS, E0])
    pt4 = G1toG2(pt4)
    srf1 = rs.AddSrfPt([pt1, pt2, pt3, pt4])
    #generate martward cliff
    #      generate lower line of martward sinecliff, start point nearer to
origin
```

```
    pt1 = rs.AddPoint([Ms, ScrS, E0])
    pt1 = G1toG2(pt1)
    x2 = ( maxS + CM * Ms - ScrS ) / CM
    pt2 = rs.AddPoint([x2, maxS, E0])
    pt2 = G1toG2(pt2)
    lowerLine = rs.AddLine(pt1, pt2)
    #       generate upper line of marward sinecliff, start point nearer to
origin
    pt1 = rs.AddPoint([Ms, ScrF, E0])
    pt1 = G1toG2(pt1)
    x2 = (maxS + CM * Ms - ScrF) / CM
    pt2 = rs.AddPoint([x2, maxS, E0])
    pt2 = G1toG2(pt2)
    upperLine = rs.AddLine(pt1, pt2)
    #       generate martward sinecliff srf
    srf2 = sinLoft(lowerLine, upperLine)
    #generate middle plateau at E=E0
    x1 = ( maxS + CA * As) / CA
    pt1 = rs.AddPoint([x1, maxS, E0])
    pt1 = G1toG2(pt1)
    pt2 = rs.AddPoint([As, 0, E0])
    pt2 = G1toG2(pt2)
    pt3 = rs.AddPoint([Ms, 0, E0])
    pt3 = G1toG2(pt3)
    pt4 = rs.AddPoint([Ms, ScrS, E0])
    pt4 = G1toG2(pt4)
    x5 = ( maxS + CM * Ms - ScrS ) / CM
    pt5 = rs.AddPoint([x5, maxS, E0])
    pt5 = G1toG2(pt5)
    crv = rs.AddPolyline([pt1, pt2, pt3, pt4, pt5, pt1])
    srf3 = rs.AddPlanarSrf(crv)
    #generate austward cliff
    #       generate lower line of austward sinecliff, start point nearer
to origin
    pt1 = rs.AddPoint([Af, 0, 0])
    pt1 = G1toG2(pt1)
    x2 = ( maxS + CA * Af) / CA
    pt2 = rs.AddPoint([x2, maxS, 0])
    pt2 = G1toG2(pt2)
    lowerLine = rs.AddLine(pt1, pt2)
    #       generate upper line of austward sinecliff, start point nearer
to origin
    pt1 = rs.AddPoint([As, 0, E0])
    pt1 = G1toG2(pt1)
    x2 = ( maxS + CA * As) / CA
    pt2 = rs.AddPoint([x2, maxS, E0])
    pt2 = G1toG2(pt2)
    upperLine = rs.AddLine(pt1, pt2)
    #       generate austward sinecliff srf
    srf4  = sinLoft(lowerLine, upperLine)
    #generate austenite plateau
    x4 = (maxS + CA * Af) / CA
    pt1 = rs.AddPoint([maxT, maxS, 0])
    pt1 = G1toG2(pt1)
    pt2 = rs.AddPoint([maxT, 0, 0])
    pt2 = G1toG2(pt2)
    pt3 = rs.AddPoint([Af, 0, 0])
    pt3 = G1toG2(pt3)
    pt4 = rs.AddPoint([x4, maxS, 0])
    pt4 = G1toG2(pt4)
```

```
    srf5 = rs.AddSrfPt([pt1, pt2, pt3, pt4])
    #combine all srfs
    return rs.JoinSurfaces([srf1, srf2, srf3, srf4, srf5])

origDir = (pT >= T0)
newDir = (T >= pT)

if origDir != newDir:   #REVERSAL of the direction of temperature change
    T0 = pT
    pT = T
    E0 = pE
else:                   #NO REVERSAL of the direction of temperature change
    pT = T

if T > T0:
    topo_FD = austwardTopo_FD(E0)
    topo_MF = austwardTopo_MF(E0)
else:
    topo_FD = martwardTopo_FD(E0)
    topo_MF = martwardTopo_MF(E0)

tPlanePt1 = [T, 0, 0]
tPlanePt2 = [T, maxS * 1000000 * A, 0]
tPlanePt3 = [T, maxS * 1000000 * A, 1]
tPlanePt4 = [T, 0, 1]
tPlane = rs.AddSrfPt([tPlanePt1, tPlanePt2, tPlanePt3, tPlanePt4])

springFDcrv = rs.IntersectBreps(tPlane, springFD)
FDpt = rs.CurveBrepIntersect(springFDcrv, topo_FD)[1][0]
force = rs.PointCoordinates(FDpt)[1]
disp = rs.PointCoordinates(FDpt)[2]
S = force / A / 1000000
stressTempCrv = rs.AddLine([T, S, 0], [T, S, 1])
MFpt = rs.CurveBrepIntersect(stressTempCrv, topo_MF)[1][0]
E = rs.PointCoordinates(MFpt)[2]
pE = E

visualTopo_FD = topo_FD
visualTopo_MF = topo_MF
```

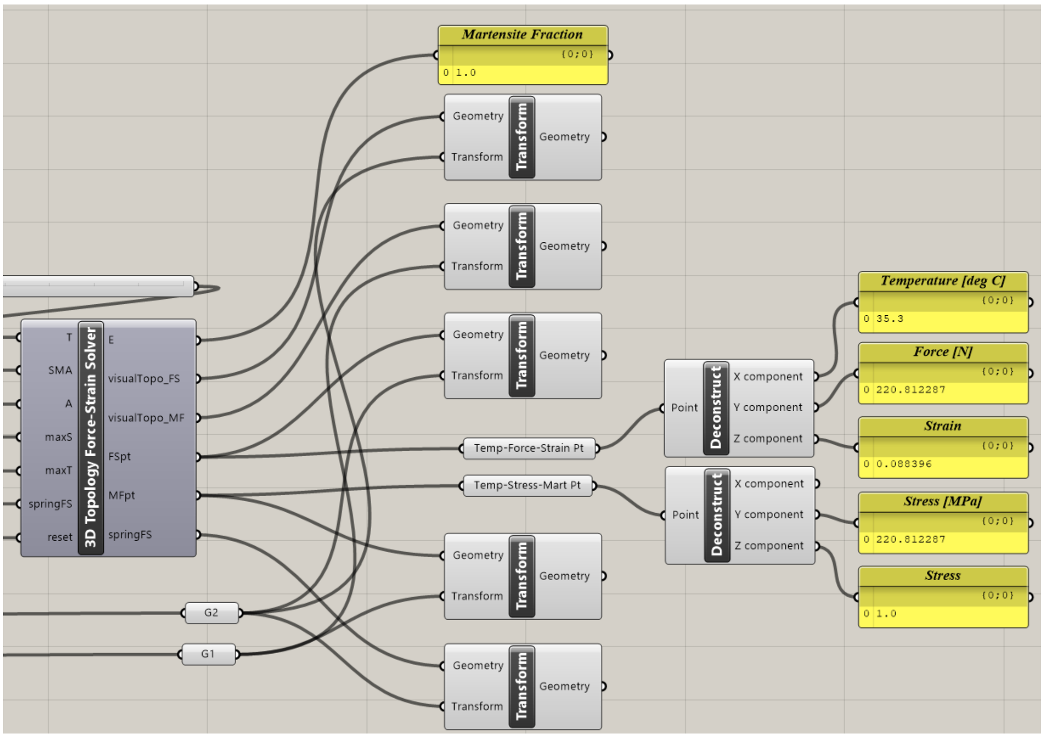
Martensite Fraction
{0;0}
0 1.0
Geometry
Transform
Transform
Geometry
3D Topology Force-Strain Solver
T
SMA
A
maxS
maxT
springFS
reset
E
visualTopo_FS
visualTopo_MF
FSpt
MFpt
springFS
G2
G1
Temp-Force-Strain Pt
Temp-Stress-Mart Pt
Point
Deconstruct
X component
Y component
Z component
Temperature [deg C]
{0;0}
0 35.3
Force [N]
{0;0}
0 220.812287
Strain
{0;0}
0 0.088396
Stress [MPa]
{0;0}
0 220.812287
Stress
{0;0}
0 1.0

Mechanical Cycling Experiment to Find Critical Stress – Detailed results

	True mass kg	Axial force N	Stress Mpa	Tape measure reading mm	Actual SMA Length mm	Strain compared to start of this session	Strain compared to start of 1st session	strain as % of End Residual Strain
1st Loading Session	0.75	7.36	37.49	1000	960	0.00%	0.00%	0.00%
	1.00	9.81	49.99	1001	961	0.10%	0.10%	
	0.75	7.36	37.49	1001	961	0.10%	0.10%	1.18%
	1.25	12.26	62.48	1001	961	0.10%	0.10%	
	0.75	7.36	37.49	1001	961	0.10%	0.10%	1.18%
	1.50	14.72	74.98	1001	961	0.10%	0.10%	
	0.75	7.36	37.49	1001	961	0.10%	0.10%	1.18%
	1.75	17.17	87.48	1002	962	0.21%	0.21%	
	0.75	7.36	37.49	1001	961	0.10%	0.10%	1.18%
	2.00	19.62	99.97	1003	963	0.31%	0.31%	
	0.75	7.36	37.49	1001	961	0.10%	0.10%	1.18%
	2.25	22.07	112.47	1003	963	0.31%	0.31%	
	0.75	7.36	37.49	1001	961	0.10%	0.10%	1.18%
	2.50	24.53	124.97	1018	978	1.88%	1.88%	
	0.75	7.36	37.49	1013	973	1.35%	1.35%	15.29%
	2.75	26.98	137.46	1025	985	2.60%	2.60%	
	0.75	7.36	37.49	1023	983	2.40%	2.40%	27.06%
	3.00	29.43	149.96	1049	1009	5.10%	5.10%	
	0.75	7.36	37.49	1045	1005	4.69%	4.69%	52.94%
	3.25	31.88	162.46	1080	1040	8.33%	8.33%	
	0.75	7.36	37.49	1075	1035	7.81%	7.81%	88.24%
	3.50	34.34	174.96	1088	1048	9.17%	9.17%	
	0.75	7.36	37.49	1082	1042	8.54%	8.54%	96.47%
	3.75	36.79	187.45	1091	1051	9.48%	9.48%	
	0.75	7.36	37.49	1084	1044	8.75%	8.75%	98.82%
	4.00	39.24	199.95	1092	1052	9.58%	9.58%	
	0.75	7.36	37.49	1085	1045	8.85%	8.85%	100.00%

	True mass kg	Axial force N	Stress Mpa	Tape measure reading mm	Actual SMA Length mm	Strain compared to start of this session	Strain compared to start of 1st session	strain as % of End Residual Strain
2nd Loading Session	0.75	7.36	37.49	1010	970	0.00%	1.04%	0.00%
	1.00	9.81	49.99	1010	970	0.00%	1.04%	
	0.75	7.36	37.49	1010	970	0.00%	1.04%	0.00%
	1.25	12.26	62.48	1010	970	0.00%	1.04%	
	0.75	7.36	37.49	1010	970	0.00%	1.04%	0.00%
	1.50	14.72	74.98	1011	971	0.10%	1.15%	
	0.75	7.36	37.49	1010	970	0.00%	1.04%	0.00%
	1.75	17.17	87.48	1011	971	0.10%	1.15%	
	0.75	7.36	37.49	1010	970	0.00%	1.04%	0.00%
	2.00	19.62	99.97	1011	971	0.10%	1.15%	
	0.75	7.36	37.49	1010	970	0.00%	1.04%	0.00%
	2.25	22.07	112.47	1012	972	0.21%	1.25%	
	0.75	7.36	37.49	1010	970	0.00%	1.04%	0.00%
	2.50	24.53	124.97	1012	972	0.21%	1.25%	
	0.75	7.36	37.49	1010	970	0.00%	1.04%	0.00%
	2.75	26.98	137.46	1019	979	0.93%	1.98%	
	0.75	7.36	37.49	1016	976	0.62%	1.67%	7.59%
	3.00	29.43	149.96	1050	1010	4.12%	5.21%	
	0.75	7.36	37.49	1047	1007	3.81%	4.90%	46.84%
	3.25	31.88	162.46	1090	1050	8.25%	9.38%	
	0.75	7.36	37.49	1084	1044	7.63%	8.75%	93.67%
	3.50	34.34	174.96	1095	1055	8.76%	9.90%	
	0.75	7.36	37.49	1088	1048	8.04%	9.17%	98.73%
	3.75	36.79	187.45	1095	1055	8.76%	9.90%	
	0.75	7.36	37.49	1088	1048	8.04%	9.17%	98.73%
	4.00	39.24	199.95	1096	1056	8.87%	10.00%	
	0.75	7.36	37.49	1089	1049	8.14%	9.27%	100.00%

	True mass kg	Axial force N	Stress Mpa	Tape measure reading mm	Actual SMA Length mm	Strain compared to start of this session	Strain compared to start of 1st session	strain as % of End Residual Strain
3rd Loading Session	0.75	7.36	37.49	1015	975	0.00%	1.56%	16.30%
	1.00	9.81	49.99	1016	976	0.10%	1.67%	
	0.75	7.36	37.49	1015	975	0.00%	1.56%	16.30%
	1.25	12.26	62.48	1016	976	0.10%	1.67%	
	0.75	7.36	37.49	1015	975	0.00%	1.56%	16.30%
	1.50	14.72	74.98	1016	976	0.10%	1.67%	
	0.75	7.36	37.49	1015	975	0.00%	1.56%	16.30%
	1.75	17.17	87.48	1017	977	0.21%	1.77%	
	0.75	7.36	37.49	1016	976	0.10%	1.67%	17.39%
	2.00	19.62	99.97	1017	977	0.21%	1.77%	
	0.75	7.36	37.49	1016	976	0.10%	1.67%	17.39%
	2.25	22.07	112.47	1017	977	0.21%	1.77%	
	0.75	7.36	37.49	1016	976	0.10%	1.67%	17.39%
	2.50	24.53	124.97	1018	978	0.31%	1.88%	
	0.75	7.36	37.49	1016	976	0.10%	1.67%	17.39%
	2.75	26.98	137.46	1022	982	0.72%	2.29%	
	0.75	7.36	37.49	1019	979	0.41%	1.98%	20.65%
	3.00	29.43	149.96	1046	1006	3.18%	4.79%	
	0.75	7.36	37.49	1043	1003	2.87%	4.48%	46.74%
	3.25	31.88	162.46	1090	1050	7.69%	9.38%	
	0.75	7.36	37.49	1084	1044	7.08%	8.75%	91.30%
	3.50	34.34	174.96	1098	1058	8.51%	10.21%	
	0.75	7.36	37.49	1091	1051	7.79%	9.48%	98.91%
	3.75	36.79	187.45	1099	1059	8.62%	10.31%	
	0.75	7.36	37.49	1092	1052	7.90%	9.58%	100.00%
	4.00	39.24	199.95	1100	1060	8.72%	10.42%	
	0.75	7.36	37.49	1092	1052	7.90%	9.58%	100.00%

	True mass kg	Axial force N	Stress Mpa	Tape measure reading mm	Actual SMA Length mm	Strain compared to start of this session	Strain compared to start of 1st session	strain as % of End Residual Strain
4th Loading Session	0.75	7.36	37.49	1020	980	0.00%	2.08%	0.00%
	1.00	9.81	49.99	1020	980	0.00%	2.08%	
	0.75	7.36	37.49	1020	980	0.00%	2.08%	0.00%
	1.25	12.26	62.48	1021	981	0.10%	2.19%	
	0.75	7.36	37.49	1020	980	0.00%	2.08%	0.00%
	1.50	14.72	74.98	1021	981	0.10%	2.19%	
	0.75	7.36	37.49	1020	980	0.00%	2.08%	0.00%
	1.75	17.17	87.48	1022	982	0.20%	2.29%	
	0.75	7.36	37.49	1020	980	0.00%	2.08%	0.00%
	2.00	19.62	99.97	1022	982	0.20%	2.29%	
	0.75	7.36	37.49	1020	980	0.00%	2.08%	0.00%
	2.25	22.07	112.47	1022	982	0.20%	2.29%	
	0.75	7.36	37.49	1020	980	0.00%	2.08%	0.00%
	2.50	24.53	124.97	1023	983	0.31%	2.40%	
	0.75	7.36	37.49	1021	981	0.10%	2.19%	1.32%
	2.75	26.98	137.46	1025	985	0.51%	2.60%	
	0.75	7.36	37.49	1022	982	0.20%	2.29%	2.63%
	3.00	29.43	149.96	1065	1025	4.59%	6.77%	
	0.75	7.36	37.49	1061	1021	4.18%	6.35%	53.95%
	3.25	31.88	162.46	1097	1057	7.86%	10.10%	
	0.75	7.36	37.49	1091	1051	7.24%	9.48%	93.42%
	3.50	34.34	174.96	1101	1061	8.27%	10.52%	
	0.75	7.36	37.49	1094	1054	7.55%	9.79%	97.37%
	3.75	36.79	187.45	1101	1061	8.27%	10.52%	
	0.75	7.36	37.49	1096	1056	7.76%	10.00%	100.00%
	4.00	39.24	199.95	1103	1063	8.47%	10.73%	
	0.75	7.36	37.49	1096	1056	7.76%	10.00%	100.00%

	True mass kg	Axial force N	Stress Mpa	Tape measure reading mm	Actual SMA Length mm	Strain compared to start of this session	Strain compared to start of 1st session	strain as % of End Residual Strain
5th Loading Session	0.75	7.36	37.49	1023	983	0.00%	2.40%	0.00%
	1.00	9.81	49.99	1023	983	0.00%	2.40%	
	0.75	7.36	37.49	1023	983	0.00%	2.40%	0.00%
	1.25	12.26	62.48	1024	984	0.10%	2.50%	
	0.75	7.36	37.49	1023	983	0.00%	2.40%	0.00%
	1.50	14.72	74.98	1024	984	0.10%	2.50%	
	0.75	7.36	37.49	1023	983	0.00%	2.40%	0.00%
	1.75	17.17	87.48	1025	985	0.20%	2.60%	
	0.75	7.36	37.49	1023	983	0.00%	2.40%	0.00%
	2.00	19.62	99.97	1026	986	0.31%	2.71%	
	0.75	7.36	37.49	1024	984	0.10%	2.50%	1.35%
	2.25	22.07	112.47	1026	986	0.31%	2.71%	
	0.75	7.36	37.49	1024	984	0.10%	2.50%	1.35%
	2.50	24.53	124.97	1026	986	0.31%	2.71%	
	0.75	7.36	37.49	1024	984	0.10%	2.50%	1.35%
	2.75	26.98	137.46	1030	990	0.71%	3.13%	
	0.75	7.36	37.49	1027	987	0.41%	2.81%	5.41%
	3.00	29.43	149.96	1054	1014	3.15%	5.63%	
	0.75	7.36	37.49	1050	1010	2.75%	5.21%	36.49%
	3.25	31.88	162.46	1096	1056	7.43%	10.00%	
	0.75	7.36	37.49	1091	1051	6.92%	9.48%	91.89%
	3.50	34.34	174.96	1103	1063	8.14%	10.73%	
	0.75	7.36	37.49	1096	1056	7.43%	10.00%	98.65%
	3.75	36.79	187.45	1104	1064	8.24%	10.83%	
	0.75	7.36	37.49	1096	1056	7.43%	10.00%	98.65%
	4.00	39.24	199.95	1105	1065	8.34%	10.94%	
	0.75	7.36	37.49	1097	1057	7.53%	10.10%	100.00%